


12-2011

Synthesis and Characterization of Catalysts for the Selective Transformation of Biomass-Derived Materials

Isaac Tyrone Ghampson

Follow this and additional works at: <http://digitalcommons.library.umaine.edu/etd>

 Part of the [Chemical Engineering Commons](#), [Oil, Gas, and Energy Commons](#), and the [Organic Chemistry Commons](#)

Recommended Citation

Ghampson, Isaac Tyrone, "Synthesis and Characterization of Catalysts for the Selective Transformation of Biomass-Derived Materials" (2011). *Electronic Theses and Dissertations*. 1564.
<http://digitalcommons.library.umaine.edu/etd/1564>

This Open-Access Thesis is brought to you for free and open access by DigitalCommons@UMaine. It has been accepted for inclusion in Electronic Theses and Dissertations by an authorized administrator of DigitalCommons@UMaine.

**SYNTHESIS AND CHARACTERIZATION OF CATALYSTS FOR THE SELECTIVE
TRANSFORMATION OF BIOMASS-DERIVED MATERIALS**

By

Isaac Tyrone Ghampson

B.Sc. Jacobs University Bremen, 2007

A THESIS

Submitted in Partial Fulfillment of the

Requirements for the Degree of

Doctor of Philosophy

(in Chemical Engineering)

The Graduate School

The University of Maine

December 2011

Advisory Committee:

William J. DeSisto, Associate Professor of Chemical and Biological Engineering

Advisor

Adriaan R.P. van Heiningen, Professor of Chemical and Biological Engineering

Brian G. Frederick, Associate Professor of Chemistry

M. Clayton Wheeler, Associate Professor of Chemical and Biological Engineering

Rachel N. Austin, Professor of Chemistry, Bates College

THESIS ACCEPTANCE STATEMENT

On behalf of the Graduate Committee for Isaac Tyrone Ghampson, I affirm that this manuscript is the final and accepted thesis. Signatures of all committee members are on file with the graduate school at the University of Maine, 42 Stodder Hall, Orono, Maine.

William J DeSisto, Associate Professor of Chemical Engineering

Date

LIBRARY RIGHTS STATEMENT

In presenting this thesis in partial fulfillment of the requirements for an advanced degree at The University of Maine, I agree that the Library shall make it freely available for inspection. I further agree that permission for "fair use" copying of this thesis for scholarly purposes may be granted by the Librarian. It is understood that any copying or publication of this thesis for financial gain shall not be allowed without my written permission.

Signature

**SYNTHESIS AND CHARACTERIZATION OF CATALYSTS FOR THE SELECTIVE
TRANSFORMATION OF BIOMASS-DERIVED MATERIALS**

By Isaac Tyrone Ghampson

Thesis Advisor: Dr. William J. DeSisto

An Abstract of the Thesis Presented
in Partial Fulfillment of the Requirements for the
Degree of Doctor of Philosophy
(in Chemical Engineering)
December 2011

The experimental work in this thesis focuses on generating catalysts for two intermediate processes related to the thermal conversion of lignocellulosic biomass: the synthesis and characterization of mesoporous silica supported cobalt catalysts for the Fischer-Tropsch reaction, and an exploration of the reactivity of bulk and supported molybdenum-based nitride catalysts for the hydrodeoxygenation (HDO) of guaiacol, a lignin model compound.

The first section of the work details the synthesis of a series of silica-supported cobalt Fischer-Tropsch catalysts with pore diameters ranging from 2-23 nm. Detailed X-ray diffraction measurements were used to determine the composition and particle diameters of the metal fraction, analyzed as a three-phase system containing Co_{fcc} , Co_{hcp} and CoO particles. Catalyst properties were determined at three stages in catalyst history: (1) after the initial calcination step to thermally decompose the catalyst precursor into Co_3O_4 , (2) after the hydrogen reduction step to activate the catalyst to Co and (3) after the FT reaction. From the

study, it was observed that larger pore diameters supported higher turnover frequency; smaller pore diameters yielded larger mole fraction of CoO; XRD on post-reduction and post-FTS catalyst samples indicated significant changes in dispersivity after reduction.

In the next section, the catalytic behaviors of unsupported, activated carbon-, alumina-, and SBA-15 mesoporous silica-supported molybdenum nitride catalysts were evaluated for the hydrodeoxygenation of guaiacol (2-methoxy phenol) at 300 °C and 5 MPa. The nitride catalysts were prepared by thermal decomposition of bulk and supported ammonium heptamolybdate to form MoO₃ followed by nitridation in either flowing ammonia or a nitrogen/hydrogen mixture. The catalytic properties were strongly affected by the nitriding and purging treatment as well as the physical and chemical properties of support. The overall reaction was influenced by the crystalline phase present in the catalyst, dispersion of molybdenum nitride/oxynitride, and the porosity of the support. The hydrodeoxygenation of guaiacol followed two proposed reaction pathways: demethylation (DME) of guaiacol to form catechol, followed by dehydroxylation to form phenol; or a direct demethoxylation (DMO) to form phenol. The selectivity of the reaction was expressed in terms of the phenol/catechol ratio. Phenol was the predominant product for all the catalysts studied, except for the alumina-supported catalysts (an effect of the alumina support). The results from this thesis are encouraging for the application of Mo nitride based catalysts for hydrodeoxygenation of whole pyrolysis oil.

ACKNOWLEDGMENTS

First and foremost, I am indebted to Prof. William J. DeSisto for his patience, guidance, and for all of the opportunities he has provided for me over the last four years. I am especially grateful to him for inviting me to his home and allowing me to share in his family's experience.

I would like to thank Prof. Brian G. Frederick for his advice, encouragement and for spending a great deal of time with me during my time at the University of Maine. I would also like to acknowledge Prof. Adriaan van Heiningen, Prof. Clayton Wheeler and Prof. Rachel N. Austin for their valuable discussions.

I wish to thank Prof. Nestor Escalona and Prof. Rafael Garcia for the illuminating experience during my time at the Universidad de Concepción. I would also like to thank Catherine Sepúlveda for her assistance.

I would like to acknowledge the generous financial support from the DOE, NSF, CONICYT Chile, and FONDECYT Chile.

I would like to acknowledge Nick Hill for his help in building the experimental apparatus, Prof. J. L. García Fierro for his help with the XPS measurements, David Frankel for his assistance with the X-ray diffractometer, and Kelly Edwards for his help with the TEM measurements.

I would also like to express my gratitude to Rachel Pollock and Timothy Thibodeau for many beneficial discussions.

I am thankful to my family and friends for their encouragement throughout my life.

Finally, I would like to thank Raiha Sagawa Mahmoud for putting up with me.

TABLE OF CONTENTS

ACKNOWLEDGMENTS.....	iii
LIST OF TABLES.....	viii
LIST OF FIGURES.....	x
NOMENCLATURE.....	xiii
Chapter	
1. INTRODUCTION AND BACKGROUND.....	1
1.1. Thermochemical Conversion of Lignocellulosic Biomass.....	1
1.2. Pyrolysis of Woody Biomass.....	3
1.2.1. Hydrodeoxygenation Reaction.....	5
1.2.2. Hydrodeoxygenation of Oxygenated Model Compounds.....	7
1.2.3. HDO Reaction Drawbacks of Conventional Metal Sulfide Catalysts.....	12
1.2.4. Development of Improved Hydrodeoxygenation Catalysts.....	14
1.2.5. Carbon Supports.....	17
1.3. Transition Metal Nitrides and Oxynitrides.....	20
1.3.1. General Properties.....	20
1.3.2. Preparation of Transition Metal Nitride and Oxynitride Catalysts.....	22
1.3.3. Supported Metal Nitride and Oxynitride Catalysts.....	29
1.3.4. HDO Reactions over Molybdenum Nitride and Oxynitride Catalysts.....	33
1.4. Fischer-Tropsch Synthesis.....	35
1.4.1. Fischer-Tropsch Synthesis on Cobalt Catalysts.....	38
1.4.2. Periodic Mesoporous Silica as Supports.....	44
1.5. Objectives and Scope of Thesis.....	46

2. EFFECTS OF PORE DIAMETER ON PARTICLE SIZE, PHASE, AND TURNOVER FREQUENCY IN MESOPOROUS SILICA-SUPPORTED COBALT FISCHER-TROPSCH CATALYSTS	48
2.1. Introduction	48
2.2. Experimental and Methods	51
2.2.1. Synthesis of Mesoporous Silica Supports	51
2.2.2. Preparation of Supported Co Catalyst	53
2.2.3. Catalyst Characterization and Catalytic Testing	54
2.3. Results	61
2.3.1. Materials Characterization	61
2.3.2. Transmission Electron Microscopy/Selected Area Diffraction	69
2.3.3. X-Ray Absorption Spectroscopy	70
2.3.4. Fischer-Tropsch Synthesis	72
2.4. Discussion	73
2.4.1. Dependence of the Reducibility of CoO to Co on Particle Size	75
2.4.2. Relationship between Co _{fcc} and Co _{hcp} phases	76
2.4.3. Relationship between TOF and Pore Diameter	78
2.5. Conclusion	83
3. GUAIACOL HYDRODEOXYGENATION OVER UNSUPPORTED MOLYBDENUM- BASED NITRIDE CATALYSTS	84
3.1. Introduction	84
3.2. Experimental	86

3.2.1. Catalyst Preparation	86
3.2.2. Catalyst Characterization	88
3.2.3. Catalyst Activities	88
3.3. Results and Discussion.....	92
3.3.1. Catalyst Preparation and Characterization.....	92
3.3.2. Catalyst Activity Measurements.....	96
3.4. Conclusion.....	104
4. HYDRODEOXYGENATION OF GUAIACOL OVER CARBON-SUPPORTED MOLYBDENUM NITRIDE CATALYSTS.....	105
4.1. Introduction	105
4.2. Experimental Section.....	110
4.2.1 Catalyst Preparation	110
4.2.2. Catalyst Characterization	112
4.2.3. Catalyst Activity Measurements.....	114
4.3. Results	117
4.3.1. Textural Properties	117
4.3.2. X-ray Diffraction	120
4.3.3. Surface Chemical and Acidic Properties of the Support.....	121
4.3.4. Bulk and Surface Composition of Nitrided Catalysts.....	124
4.3.5. Activity Measurements	127
4.4. Discussion	133
4.4.1. Physico-Chemical Properties of Nitrided Catalysts	133
4.4.2. Correlation of Catalytic Activities and Properties	136

4.4.3. Selectivity	140
4.4.4. Time-on-Stream Behavior	141
4.5. Conclusion	141
5. COMPARISON OF ALUMINA- AND SBA-15-SUPPORTED MOLYBDENUM NITRIDE CATALYSTS FOR HYDRODEOXYGENATION OF GUAIACOL	143
5.1. Introduction	143
5.2. Experimental.....	145
5.2.1. Catalyst Preparation	145
5.2.2. Catalyst Characterization	147
5.2.3. Catalytic Activity Measurements.....	149
5.3. Results and Discussion.....	149
5.3.1. Catalyst Properties	149
5.3.2. Reactivity.....	158
5.4. Conclusion.....	166
6. CONCLUSIONS AND RECOMMENDATIONS.....	168
6.1. Conclusion.....	168
6.2. Recommendation.....	171
REFERENCES.....	174
APPENDIX A X-RAY DIFFRACTION DATA ANALYSIS.....	193
APPENDIX B FISCHER-TROPSCH CALCULATIONS.....	195
APPENDIX C HYDRODEOXYGENATION OF GUAIACOL CALCULATIONS.....	206
BIOGRAPHY OF THE AUTHOR	215

LIST OF TABLES

Table 2.1	Phases analyzed at three stages of catalysts history and their structures and lattice parameters	60
Table 2.2	Nitrogen porosimetry data of support and supported catalysts	61
Table 2.3	Particle size of Co_3O_4 at Stage 1 and predicted metal diameter and dispersion of Co^0 after reduction	62
Table 2.4	Mole fractions, particle sizes, and dispersion of Co_{fcc} and Co_{hcp} for Stage 2.....	66
Table 2.5	Mole ratio, particle size and dispersion of Co_{fcc} and Co_{hcp} for Stage 3.....	67
Table 2.6	Catalysts, metal loading, reaction rate, specific surface areas at each stage, and TOF	73
Table 3.1	Crystallite sizes of bulk different phases present in bulk nitride catalysts	95
Table 3.2	Chemical composition of bulk Mo nitrides	96
Table 3.3	Catalytic activity of unsupported Mo nitrides	98
Table 4.1	Nitrogen porosimetry: activated carbon-related materials	120
Table 4.2	Surface chemical and acidic properties of oxidized supports	123
Table 4.3	Elemental analysis of metal nitride catalysts	124
Table 4.4	Binding energies of core levels and surface atomic ratios of reduced, passivated nitride catalysts	126
Table 4.5	Catalytic activity of carbon-supported Mo nitride catalysts	130
Table 5.1	Adsorption properties of passivated nitride catalysts	152
Table 5.2	Chemical composition of passivated nitride catalysts	155

Table 5.3	XPS binding energies and surface atomic ratios of reduced, passivated nitride catalysts	157
Table 5.4	Reaction rates of catalysts under study	162
Table B.1	Properties of Catalyst	195
Table C.1	Properties of Catalyst	206
Table C.2	Calculated areas from GC spectrum.....	208

LIST OF FIGURES

Figure 1.1	Strategies for production of fuels from biomass.....	3
Figure 1.2	Functional group compositions in bio-oils	6
Figure 1.3	Furanic compounds	8
Figure 1.4	Phenol and substituted phenols	9
Figure 1.5	Hydrodeoxygenation pathways of guaiacol.....	11
Figure 1.6	Crystal structure of γ - Mo_2N	22
Figure 1.7	Acidic sites, metallic sites and dual sites model of MoO_xN_y	22
Figure 1.8	Reaction pathways during reaction of MoO_3 with NH_3	24
Figure 1.9	Reaction pathways to produce low surface area, medium surface area and high surface area bulk Mo_2N	25
Figure 2.1	XRD patterns of selected catalysts after treatment	65
Figure 2.2	Mole fraction of cobalt phases for catalysts after reduction in hydrogen.....	66
Figure 2.3	XRD pattern illustrating the increase in the amount of CoO before and after reaction under FTS conditions for the small pore diameter catalyst Co/MCM-41	68
Figure 2.4	Mole fraction of cobalt phases for catalysts after reaction for 10 h in FTS	68
Figure 2.5	Crystallite size for catalysts from XRD Rietveld refinement of the indicated phases	69
Figure 2.6	TEM image of a region of catalyst Co/silica no. 775 with the corresponding Co_{hcp} diffraction pattern.....	70

Figure 2.7	XANES spectra of cobalt for a selection of catalysts after calcination, reduction and FT reaction compared to reference and theory	71
Figure 2.8	Measured activity for catalysts as a function of pore diameter	72
Figure 2.9	Plot of turnover frequencies vs. pore diameter.....	79
Figure 2.10	Turnover frequency as a function of Co particle sizes	80
Figure 2.11	Relationship between Co metal particle size estimated from Co_3O_4 and particle sizes of fcc and hcp particles determined after reduction or after FT synthesis.....	81
Figure 3.1	Experimental setup	91
Figure 3.2	XRD of bulk oxides and nitrides.	94
Figure 3.3	Variation of the transformation of guaiacol and the yield of products with time	99
Figure 3.4	Hydrodeoxygenation pathways of guaiacol.....	100
Figure 3.5	Distribution and total yield of deoxygenated products versus conversion of guaiacol for CoMoN-A and MoN-A-ii catalysts	103
Figure 3.6	Phenol/catechol ratio for bulk metal nitride catalysts.....	103
Figure 4.1	Hydrodeoxygenation pathways of guaiacol.....	109
Figure 4.2	Experimental set-up for flow reaction.....	116
Figure 4.3	Pore size distribution of HNO_3 treated activated carbon supports	118
Figure 4.4	XRD patterns of CGran carbon- supported nitrides.....	121
Figure 4.5	TPD profiles of the activated carbon supports	123

Figure 4.6	Variation of the transformation of guaiacol and the yield of products with time for GCA- and GCA-supported catalysts.....	128
Figure 4.7	Variation of the transformation of guaiacol and the yield of products with time for CGran- and Darco-supported catalysts	129
Figure 4.8	Reaction rates of carbon-supported Mo nitride catalysts.....	131
Figure 4.9	Phenol/catechol ratio for metal nitride catalysts.....	132
Figure 4.10	Time-on-stream behavior of selected catalysts in terms of total conversion for HDO of guaiacol	133
Figure 4.11	Reaction rates versus XPS Mo/C atomic ratio	138
Figure 5.1	Morphology of alumina- and SBA-15-supported materials.....	151
Figure 5.2	XRD patterns of alumina-supported materials and SBA-15-supported materials.....	154
Figure 5.3	Yield of products and conversion of guaiacol as a function of time	160
Figure 5.4	Hydrodeoxygenation pathways of guaiacol.....	161
Figure 5.5	Phenol/catechol ratio for catalysts under study	164
Figure B.1	Mass Spec signals of reactants during FTS.....	196
Figure C.1	The GC spectrum of products from hydrodeoxygenation of guaiacol on MoN/CGran-NH catalyst	207
Figure C.2	Conversion of guaiacol and the formation of deoxygenated products versus time for MoN/CGran-NH catalyst.....	211
Figure C.3	Yield of phenol and catechol versus guaiacol conversion for MoN/CGran-NH catalyst.....	212

NOMENCLATURE

D	Dispersion
d_{Co^0}	Co metal particle size
$d_{Co_3O_4}$	Co ₃ O ₄ particle size
d_{pore}	average pore diameter
M_w	molecular weight
P	total pressure
$P_{ }$	Co _{hcp} particle size component parallel to the c -axis of a cylindrical particle
P_{\perp}	Co _{hcp} particle size component perpendicular to the c -axis
R	gas constant
R_{rates}	reaction rates
S_{BET}	BET specific surface area
T	temperature
TOF	turnover frequency
TPV	total pore volume
W	weight of catalyst metal percent

CHAPTER 1

INTRODUCTION AND BACKGROUND

1.1. Thermochemical Conversion of Lignocellulosic Biomass

Increase in the dependence on oil and other fossil fuels, rise in energy costs, and the decline in petroleum reserves have made the pursuit of alternative energy sources a world-wide priority. Apart from these economic issues, environmental concerns have also highlighted the need for developing non-fossil energy carriers and chemicals [1]. Production of fuels and a variety of chemicals from biomass has significant potential to reduce dependence on foreign oil, reduce greenhouse gas emissions and pollution, and improve local economies [2]. In fact, biomass are the only renewable source of carbon from which to make liquid transportation fuels [3]. In addition, biofuels generate significantly less greenhouse gas emissions than fossil fuels, and are even considered near CO₂-neutral [1, 3, 4]. According to the DOE "Billion Ton Survey", biomass has surpassed hydropower as the largest domestic source of renewable energy in the United States [4]. However, biomass currently provides only about 3% of the US's overall energy consumption. In an objective to boost the production and consumption of biofuels, the United States and the European Union have targeted a 20-30% displacement of current petroleum consumption with biofuels by 2030 [4, 5]. These mandates have generated considerable interest in biomass conversion technologies [3, 6, 7].

Biomass includes plants and plant-derived materials, agricultural and forestry waste, and oil crops. The chemical composition of lignocellulosic biomass differs significantly from fossil feeds primarily owing to the presence of large

amounts of oxygen (~49 wt %) in plant carbohydrate polymers [2]. The major structural components of lignocellulosic biomass are cellulose, hemicelluloses, lignin, organic extractives and inorganic materials [6]. Cellulose is a linear polymer of D-glucopyranose units linked by β -1-4 glucosidic bonds, and constitute about 40-45% of dry wood [6]. Hemicelluloses molecules are amorphous heterogeneous groups of branched polysaccharides and provide linkage between lignin and cellulose. They account for 25-35% of the mass of dry wood. Lignin is a complex, heterogeneous amorphous polymer of different phenyl propane units, bonded together by ether and carbon-carbon bonds [6]. After appropriate pretreatment and degradation processes, glucose monomers can be obtained from hydrolysis reaction of cellulose. Extracted hemicellulose sugars are feedstock for the production of ethanol, and lignin can be a potential feedstock for higher value fuels and chemicals.

The production of fuels and chemicals from biomass involves significant challenges due to the low energy density and high transportation cost of the feedstock. As a means of energy densification, biomass can be converted to liquids through different conversion routes as shown in Fig. 1.1. The conversion technologies include fermentation of hydrolyzed biomass to ethanol, transesterification of natural oils (plants and algae) to produce biodiesel, and the thermal breakdown of lignocellulosic biomass to produce a variety of hydrocarbon fuels and chemicals [7, 8]. The thermal conversion pathway, which include gasification and pyrolysis, offer particular advantages over the other conversion technologies in terms of flexibility and also with regards to fungibility with existing distribution infrastructure and engines [9]. Gasification results in the production of

non-condensable gases (biosyngas) in the presence of a small amount of oxygen. This is typically followed by other processes such as Methanol Synthesis and Fischer-Tropsch Synthesis (FTS) to convert the biosyngas to alcohols and hydrocarbon fuels.

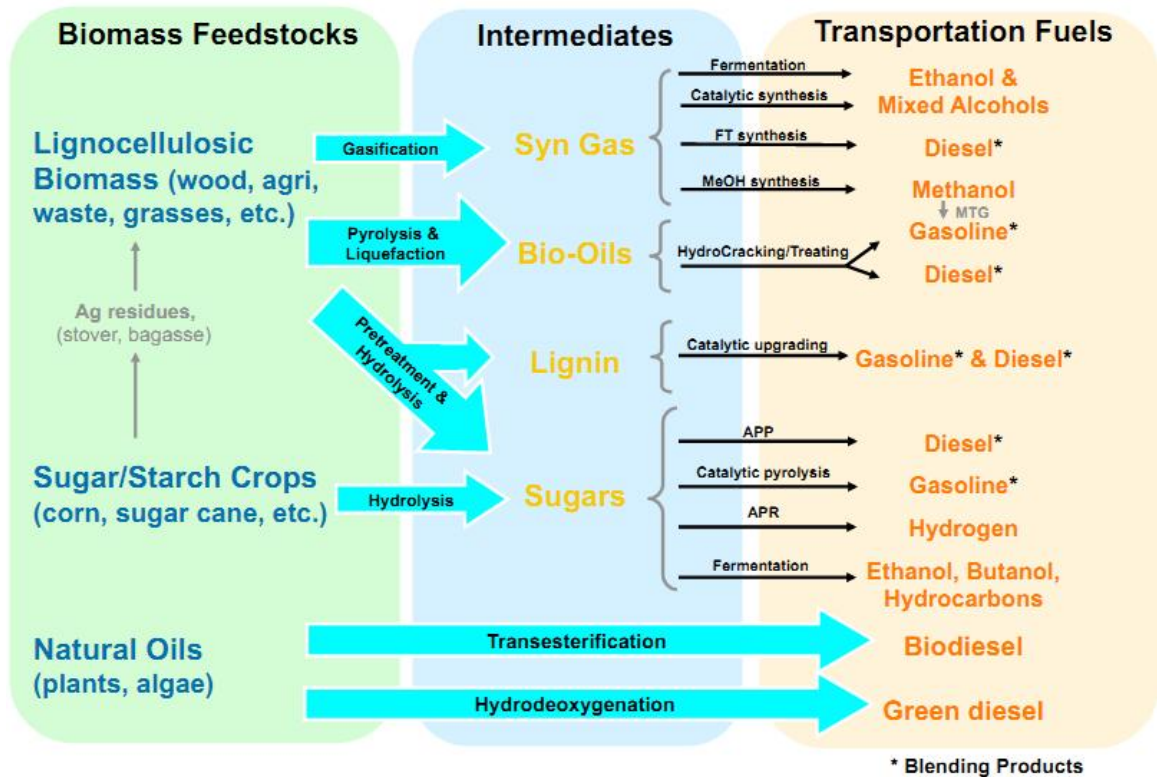


Figure 1.1 Strategies for production of transportation fuels from biomass. Adapted from Jim Frederick's webinar [8].

1.2. Pyrolysis of Woody Biomass

Pyrolysis of biomass is a thermal degradation process in the absence of oxygen which results in the production of bio-oils, char, gases and water. The resulting bio-oil is a complex mixture of large amounts of different molecular weight compounds because of fragmentation reactions of cellulose, hemicelluloses and lignin polymers [10]. Decades of research to optimize yields of liquids and gases

have resulted in the adoption of the fast pyrolysis process. In fast pyrolysis, a very high heating rate (10-200 K/s) and heat transfer, moderate to high temperatures (450-550 °C), and a very short vapor residence time (< 1 s) are used to produce mainly liquid and gaseous products [11, 12]. However, bio-oils possess some undesirable properties that limit their utilization as fuel. Some of these properties include low heating value, high viscosity, corrosivity, incomplete volatility, and thermal instability [13]. These liquid characteristics stem from the presence of water and oxygenated organic compounds in the feed, including phenols, carboxylic acids, aldehydes, ketones, aromatics, carbohydrates, and alcohols [14, 15]. These compounds readily polymerize during storage resulting in an increase in viscosity and average molecular weight. Thus, it is important to chemically or physically upgrade these oils by reducing the content of oxygenates, and thus improving the stability of the oil. Upgrading also includes molecular weight reduction. Physical upgrading methods include blending pyrolysis oil directly with petroleum diesel where they can be emulsified using surfactants [11, 12]. Chemical upgrading processes include hydrodeoxygenation [11, 16, 17] and catalytic cracking of pyrolysis vapors with zeolites which eliminates oxygen as CO and CO₂ [13, 14]. The chemical upgrading processes are comparatively more costly and complex than the physical methods; however, the chemical methods offer significant improvements including better stabilization of different components of products [16]. Hydrodeoxygenation is the most commonly used upgrading process.

1.2.1. Hydrodeoxygenation Reaction

Hydrodeoxygenation (HDO) is the removal of oxygen to produce hydrocarbons and water in feeds characterized by high oxygen content. HDO occurs simultaneously with hydrodesulfurization (HDS) and hydrodenitrogenation (HDN) reactions in petroleum hydrotreating processes to remove heteroatoms such as sulfur and nitrogen. After decades of limited attention, HDO of biomass-derived oils has been receiving a significant level of attention over the past 20 plus years [18].

Direct applications of petroleum hydrotreating technologies to deoxygenate the different chemical groups present in bio-oils have been demonstrated to lead to extensive degradation which results in heavy, coke-like products [14, 15]. This instability was attributed to the various oxygenates in the feed [18]. Thus, a two-stage hydrotreatment method was proposed whereby an initial stabilization stage at low temperatures was performed to improve the storage or transport properties of bio-oils [18, 19]. The oil after partial hydrotreatment could also be used in normal heavy fuel utilization or can be applied in the production of some chemicals [19-21]. After the elimination of the reactive oxygenated chemical groups, a second stage at higher temperatures between 350-425 °C was carried out, aimed at hydrodeoxygenation of phenolic- and furanic-type molecules as well as hydrocracking of larger molecules [18, 19]. This upgrading processes yielded aromatic gasoline with properties comparable to petroleum-based products. In addition, the two-stage hydrotreatment method was reported to consume 13% less hydrogen for equivalent gasoline yield compared to a single-stage process [18]. Although HDO studies of biomass-derived oils have been conducted, model

compounds have been used to simulate studies on HDO reactivities and to provide additional insight into the development of improved catalysts and processes. The primary oxygen functionalities present in bio-oils are shown in Fig. 1.2. The goal of HDO of aromatic oxygenates is to eliminate oxygen while keeping the aromaticity of the feed intact [22]. This increases the overall energy content value and the stability of the liquid while avoiding hydrogen costs and octane losses associated with excessive saturation of aromatics [23]. Elimination of oxygen differs according to the nature of organic compound, depending on the strength of the chemical bonds to be broken. Oxygen can be removed from alcohols, carboxylic acids and esters through thermal decomposition without reducing gases such as hydrogen. Hydrodeoxygenation of ketones requires the use of hydrogen at usually low temperatures. Oxygenates including furans, phenols, and methoxyphenols require both H₂ and an active catalyst. The review in this thesis will include only relevant model compound studies carried over conventional hydrotreating catalysts.

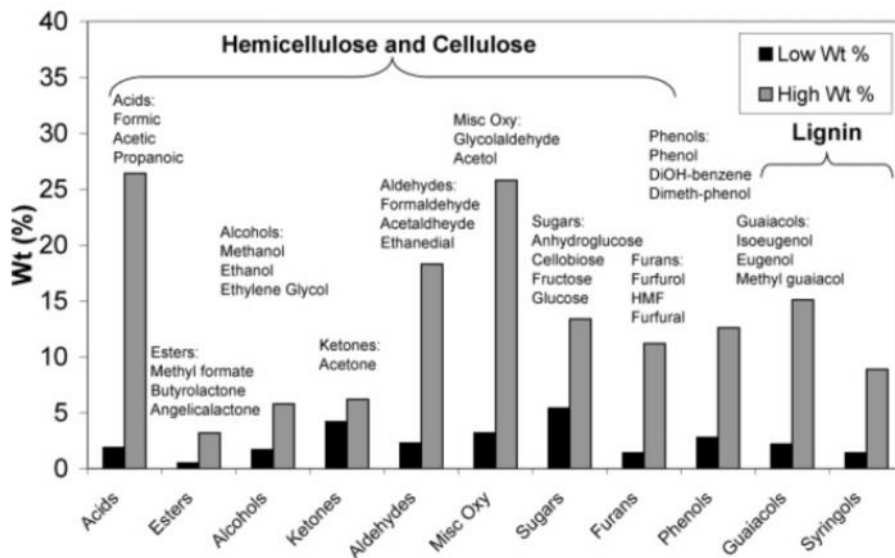


Figure 1.2 Functional group compositions in bio-oils [1, 24]

1.2.2. Hydrodeoxygenation of Oxygenated Model Compounds

Catalyst research and development for HDO reactions of model compounds representative of biomass-derived liquid is of great importance. Selective deoxygenation to minimize hydrogen consumption has been a challenging but central goal during the development of catalysts since it will improve the economics and feasibility of the thermochemical conversion process. The most extensively studied heterogeneous catalysis systems for HDO reactions are conventional HDS and HDN catalysts, sulfided Co(Ni)Mo/Al₂O₃ [16, 20]. The use of metal sulfides was a logical starting point due to the extensive database available for HDS and HDN catalysis. The sulfidation step is a necessary pretreatment procedure to activate the catalysts by creating sulfur vacancies [25]. Molybdenum acts as the main metallic component forming MoS₂ slabs on the Al₂O₃ support. Cobalt or Ni plays the role of promoter with their atoms occupying the edges of MoS₂ slabs according to the Co-Mo-S and Ni-Mo-S model [26]. The promoter creates new sites which enhance catalytic activity compared to unpromoted MoS₂/Al₂O₃. Ferrari et al. [27] proposed four kinds of active sites to explain the HDO activity of the CoMoS catalyst: a) three-fold coordinatively unsaturated Mo atoms responsible for hydrogenation; b) three-fold coordinatively unsaturated Mo atoms with a sulfhydryl group (-SH) neighbor responsible for cleaving C-O bonds; c) acid sites of the alumina support; and d) acid sites on the metal sulfide, sulfhydryl group. These sulfided catalysts have shown significant activity for HDO reactions of furans and phenols. Furanic and phenolic compounds have been studied by many researchers because of their prevalence in biomass-derived liquids, and also because of their low reactivity in HDO [28]. Most

of these studies have included proposed reaction pathways, the effect of catalyst pretreatment on activity, and the development of reaction kinetics.

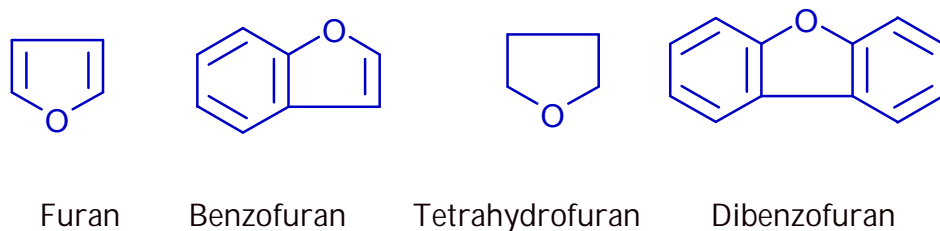


Figure 1.3 Furanic compounds

Hydrodeoxygenation reactions of furanic compounds over sulfided catalysts have been studied by several groups [29-38]. Benzofuran and 2, 3-dihydrobenzofuran have commonly been used by researchers as model compounds for the study of cyclic ether structures found in lignin [16, 23-28]. The products from HDO reactions of these model compounds result from dual path mechanisms which include an initial partial hydrogenation of the oxygen-containing arene ring, followed by cleavage of one of the C-O bonds [23-28]. The other parallel pathway involves direct elimination of oxygen without prior hydrogenation of the heterocyclic ring [33-38]. Thus, catalytic performances have been evaluated based on their selectivity towards one of these transformation routes [22].

The hydrodeoxygenation of phenolic compounds over presulfided commercial hydrotreating catalysts have been investigated by several researchers in the last 30 years [39-44]. Phenol and substituted phenols including *ortho*-, *meta*-, and *para*-cresols, dimethylphenols, methylphenols, and ethylphenol were examined as model compounds at high hydrogen pressure and 300-400 °C reaction

temperature to study the HDO activities of conventional sulfided catalysts. All of the studies resulted in different reactivities and yields in aromatic products including toluene, xylene, ethylbenzene, cyclohexane and substituted cyclohexane. The reaction mechanisms proposed for all the model compounds clearly demonstrated the existence of parallel reaction pathways: 1) prior hydrogenation of aromatic ring followed by rapid cleavage of the C-O bond, 2) direct removal of hydroxyl group [39-45].

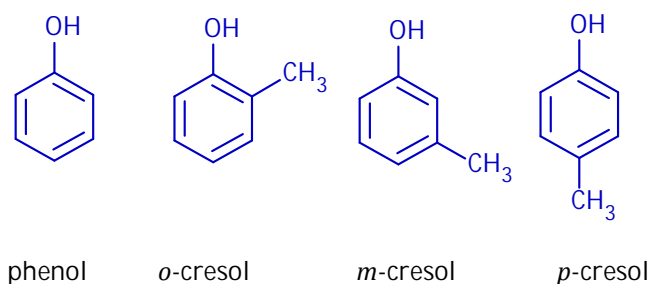


Figure 1.4 Phenol and substituted phenols

Hydrodeoxygenation of methoxyphenols have attracted attention because of their low stability and low reactivity [28]. Most of the work on methoxyphenols have been done with guaiacol and substituted guaiacols [28]. Guaiacol (2-methoxyphenol) resembles a derivative of coniferyl alcohol, a monolignol monomer, and has thus been used as a model compound to evaluate performances of catalysts in HDO reactions. Bredenberg and collaborators [46, 47] studied the effects of reaction temperature on the hydrogenolysis and hydrocracking of guaiacol together with other various methoxyphenols (*o*-cresol and anisole) over sulfided Ni-Mo/SiO₂-Al₂O₃ and Co-Mo/Al₂O₃ catalysts. A mixed oxide supported catalyst (the support is known to be strongly acidic) was chosen for the hydrocracking

experiments while the traditionally used Al_2O_3 -supported catalyst was chosen for the hydrogenolysis study [47]. For both reactions, the authors postulated mechanisms which involved cleavage of the methyl-oxygen bond which resulted in the rapid reaction of guaiacol. The production of phenol was dominant in both reactions and the amount produced increased with an increase in reaction temperature. The investigators also proposed a mechanism for the hydrogenolysis of guaiacol over presulfided Co-Mo/ Al_2O_3 catalysts [46, 47]. The reaction network involved hydrogenolysis of the methoxy group leading to the formation of catechol and methane, followed by C-O bond cleavage to produce phenol. The study also reported the formation of coke through interaction of guaiacol with the catalyst carrier [46]. In a later study, Laurent and Delmon [48] examined HDO activity of mixed oxygenated groups (4-methylacetophenone, diethylsebacate and guaiacol) over sulfided Co-Mo/ Al_2O_3 and Ni-Mo/ Al_2O_3 catalysts. The authors proposed a reaction scheme similar to the one proposed by Bredenberg [47] which began with hydrogenolysis to produce catechol and subsequent conversion to phenol. Co-Mo/ Al_2O_3 and Ni-Mo/ Al_2O_3 catalysts were reported to exhibit comparable activity for these HDO reactions [48]. More recently, Bui and co-workers examined effects on Co promoters on hydrodeoxygenation of guaiacol over sulfided Mo-based catalysts [49]. The presence of Co promoters in bulk Mo-based catalysts greatly enhanced the direct elimination of methoxy group to form phenol and methanol [49]. A reaction mechanism consistent with the scheme proposed by Bredenberg et al. [47] was also reported for the alumina-supported Mo-containing sulfides in this study [49]. In an earlier, related study, Bui et al. [50] also reported more detailed

reaction pathways after studying HDO of guaiacol on sulfided Co-Mo/Al₂O₃ catalyst. The modified form of the reaction scheme is shown in Fig. 1.5. The reaction pathways mainly involved two stages: The first stage involves the removal of the methoxy group on guaiacol to form phenol by either demethylation (DME) and dehydroxylation, or by direct demethoxylation (DMO). The second stage involves parallel pathways for the C-O bond cleavage. One pathway involves direct hydrogenolysis between aromatic carbon and the OH group (DDO) to form benzene, while the alternative pathway proceeds through hydrogenation of the benzene ring to form cyclohexanone (HYD) prior to oxygen removal to form cyclohexene [50]. The authors also reported the formation of heavier compounds which were produced during methylation of aromatic rings [50].

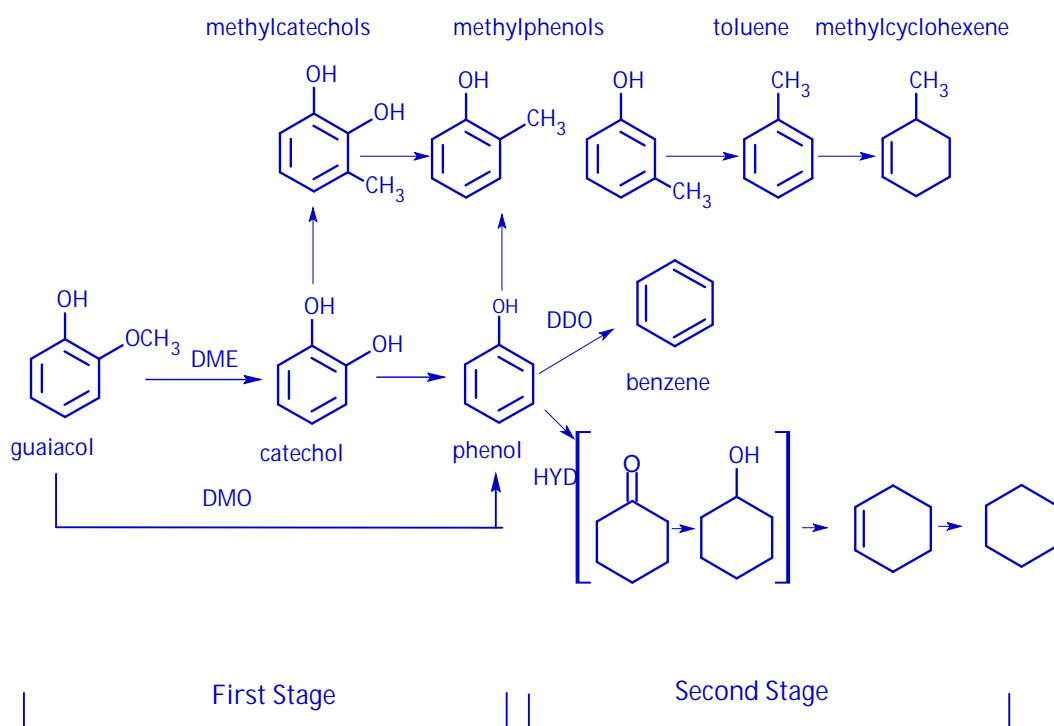


Figure 1.5 Hydrodeoxygenation pathways of guaiacol adapted from Bui et al. [50]

Commercial sulfided hydrotreating catalysts have been used for hydrodeoxygenation studies on other oxygenated model compounds including esters [51, 52] and ethers [53]. However, these model compounds would not be reviewed in this thesis.

1.2.3. HDO Reaction Drawbacks of Conventional Metal Sulfide Catalysts

Despite the discussed usefulness of classical (sulfide form) HDS catalysts, they possess some significant drawbacks for HDO reactions. Unlike petroleum crude, bio-oils have no source of sulfur to replace the one stripped from the catalyst surface during the HDO reaction. To prevent rapid catalyst deactivation owing to diminishing sulfur level, a sulfiding agent is added to the feed to maintain the sulfidation state of the catalysts. Several studies on the effect of the addition of sulfur on HDO reaction processes have shown that H₂S in the feed contaminates the product and catalysts [27, 54-56]. Ferrari and co-workers [27] examined the influence of H₂S partial pressure on the HDO reaction mechanism of a mixture of oxygenated model compounds including guaiacol. The authors observed inhibition of the hydrogenolysis and hydrogenation pathway when the partial pressure of H₂S was increased. Bunch et al. [37] reported similar results, demonstrating that the addition of H₂S to the feed led to a decrease in activity for sulfided and reduced Ni-Mo/ Al₂O₃ during HDO reaction of benzofuran. This effect was attributed mainly to competitive adsorption of H₂S and benzofuran. A study by Senol and co-workers [57] also supported this contention. Therefore, the addition of sulfiding agent to the feed does not appear to be a viable option for commercial application.

The issues arising when using commercial HDS catalysts for HDO are not limited only to the inhibiting effects of H₂S. Alumina supports have been reported to be unstable in the presence of significant amounts of water [58]. Under typical hydrothermal conditions, alumina is known to be metastable by partially transforming into boehmite [58]. A few studies have also attempted to measure the effects of water upon HDO of oxygenates. Laurent and Delmon [48, 59] examined the inhibiting effects of water upon the hydrodeoxygenation of a reaction mixture composed of 4-methylphenol, 2-methylphenol and dibenzofuran. In the study they found that the catalytic activity of sulfided Ni-Mo/Al₂O₃ decreased on addition of water. The authors also reported loss of specific surface area of the alumina-supported catalyst attributed to partial crystallization of the γ -alumina support to boehmite [48, 59]. Furthermore, the alumina support also promotes the formation of coke when it interacts with methoxyphenol compounds due to the presence of weak Lewis-type acidic sites [47, 56]. Deactivation of catalysts in HDO reactions are generally attributed to coke formation [60].

Moreover, C-O bonds are more difficult to break than C-S bonds and using catalysts developed and optimized for the HDS process may be unsuitable for HDO reactions. Thus, there is a substantial incentive to improve existing conventional catalysts, as well as identify and develop alternative catalysts.

1.2.4. Development of Improved Hydrodeoxygenation Catalyst

Rational approaches to overcome the limitations of conventional sulfided Co(Ni)Mo/Al₂O₃ catalysts include adapting the HDS catalytic system to be used with bio-oils, or developing alternative novel HDO catalysts. One opportunity area lies in the modification of alumina (using an acidity modifier e.g. K and Pt) while maintaining the active metal in an attempt to reduce coke formation [55]. Centeno and co-workers [55] have already determined that this approach did not give positive results in controlling coke deposition. Another strategy involves using other supports that are inactive for coke formation. It has been well-established in other HDO studies that the use of supports other than alumina such as carbon, zirconia, or silica can improve catalytic performances in terms of activity and selectivity [55, 60]. Centeno et al. [55] expanded the scope of their HDO studies by investigating the effects of the support on the catalytic performances for HDO of oxygenates. The authors reported promising results using carbon support in terms of selectivity towards direct oxygen removal and reduction in coke formation. Carbon as a support will be discussed in the next section. In a recent study on the support effect for sulfided CoMo catalysts on HDO activity of guaiacol, Bui and co-workers [60] found zirconia as a promising catalyst carrier. The zirconia-supported CoMo catalysts were reported to be selective towards direct elimination of the methoxy group to form phenol. The authors also reported that zirconia is stable under HDO reaction conditions.

Another alternative approach involves exploring different families of active phases [61]. In this regard, noble metals and transition metal compounds including

phosphides, carbides and nitrides have been identified as potential hydrodeoxygenation catalysts. Recent HDO studies over noble metal catalysts by several researchers have shown that some of these catalysts exhibit significant reactivities [62-68]. In a recent paper by Elliot and Hart [63], the hydroprocessing potential of Pd and Ru catalysts over a temperature range of 150 to 300 °C and a H₂ pressure of 4.2 MPa were examined using a model liquid feed mixture containing furfural, guaiacol and acetic acid. For the Ru catalyst, the authors reported phenol to be the primary recoverable product at 300 °C although the catalyst showed a preference for a gasification pathway. On the other hand, the Pd catalyst was only active for hydrogenation at higher temperature, and did not display appreciable deoxygenation capabilities [63]. Gutierrez and collaborators [65] examined noble metal catalysts supported on zirconia for HDO of guaiacol using a batch reactor at 300 °C and 8 MPa of H₂ pressure. A zirconia-supported Rh catalyst had a comparatively better guaiacol conversion than sulfided commercial Co-Mo/Al₂O₃ catalyst. In addition, the noble metal catalysts had a lower carbon deposition than that on the sulfided catalyst. The authors asserted that the decrease in coke formation was due to the change in support, an effect that was confirmed by Bui and co-workers [60]. Recently, Lin et al. [68] compared the catalytic performances of Rh-based catalysts with classical sulfided (Co-Mo and Ni-Mo) catalysts for HDO of guaiacol in terms of activity, selectivity and reaction mechanism. Their investigation indicated that the sulfide catalysts exhibited lower HDO activity and produced significant coke compared to Rh-based catalysts. Additionally, the authors attempted to explain the difference in product distribution in terms of different

reaction mechanisms: conversion of guaiacol over Rh-based catalysts began with hydrogenation of guaiacol's benzene ring (to form 2-methoxycyclohexanol and 2-methoxycyclohexanone), followed by demethylation and dehydroxylation of oxygenates to form cyclohexane as the final product, while guaiacol HDO over classical sulfided catalysts involved initial demethylation (catechol and methane), demethoxylation (to form phenol and methanol), and deoxygenation (to form 2-methylphenol), followed by saturation of the benzene ring [68]. Hydrotreatment of actual bio-oil over noble metal catalysts were carried out at harsher conditions (200-400 °C and 100-200 bar pressure) by Wildschut and co-workers [64]. All the catalysts screened (supported Ru, Pd and Pt) led to higher yields and higher level of deoxygenation than conventional hydrotreatment catalysts, in which the Ru/C catalyst was particularly superior (up to 60 wt% oil yield and 90 wt% deoxygenation level). To summarize, these studies and others make a strong case for the use of noble metals for HDO; however, the improved activity of such catalysts cannot be justified by the significantly higher cost of the noble metals and relatively high hydrogen consumption due to its tendency to hydrogenate aromatic and olefinic compounds [69]. Thus, commercial application appears to be improbable.

Oyama and co-workers [70, 71] have explored the hydrodeoxygenation performance of supported metal phosphides in recent studies. An optimum Ni₂P loading of 18 wt% over silica-support resulted in 80% benzofuran HDO conversion at 3.1 MPa and 370 °C [71]. This conversion was much higher than those observed for commercial sulfided Ni-Mo/Al₂O₃ catalyst. In a recent paper, Oyama and collaborators [70] carried out reactivity studies on gas phase HDO of guaiacol over

transition metal phosphides at a maximum temperature of 300 °C. Major products observed in this study were phenol, benzene and methoxybenzene, with the activity for HDO of guaiacol decreasing in the order: Ni₂P>Co₂P>Fe₂P>WP, MoP. The catalysts screened all displayed superior HDO conversion to the sulfided Co-Mo/Al₂O₃ catalyst which deactivated quickly at the reaction condition studied [70]. In a related study, Li et al. [72] also examined the activity and stability of SiO₂-supported metal phosphide catalysts for HDO of anisole, and found that Ni phosphide-containing catalysts displayed higher activities in comparison to the conventional NiMoS/ -Al₂O₃ catalyst. The authors indicated that the metal sites available on phosphides possessed both Lewis acidity and a metallic property responsible for demethylation, hydrogenolysis, and hydrogenation [72]. These studies show that these materials possess great potential for hydrodeoxygenation reactions. However, for guaiacol conversion, the Lewis acid sites on the surface of the phosphide catalyst could potentially favor the demethylation pathway leading to an indirect production of phenol, and hence more susceptible to coke formation and less hydrogen-efficient reactions.

Transition metal carbides possess similar structural properties to transition metal nitrides, and thus their hydrodeoxygenation properties will be discussed together with those of nitrides in Section 1.3.4.

1.2.5. Carbon Supports

There is a growing interest in the use of carbon as a catalyst support in the literature for a number of hydrotreating reactions. The basic role of a support is to disperse the active phase of the catalyst in order to obtain a large active specific

surface area. The support also facilitates the diffusion of reactants into, and products out of, the internal surface of the pores. Of all the carbon materials, high surface area activated carbons have been used the most as support for various catalytic applications [73]. Activated carbons possess an extensive porous structure that arises from the presence of pores belonging to several groups: micropores (<2 nm pore diameter); mesopores (2-50 nm pore diameter); and macropores (>50 nm pore diameter). Carbon materials are considered relatively inert and thus are weakly interacting supports [74]. Rodriguez-Reinoso [73] wrote an excellent review that highlighted the role of carbon materials in heterogeneous catalysis. In this paper, the author summarized the usefulness of carbon supports for catalysis: resistance to acidic or basic media; tailored pore size distribution for specific reactions; amphoteric character due to the presence of various oxygenated functional groups which enhances metal adsorption and catalyst dispersion; stability at high temperature except in the presence of oxygen >500 K and for hydrogenation reactions >700 K; less expensive compared to alumina and silica supports; and active phase can be recovered by eliminating the support through burning [73].

The use of activated carbon as support for catalytic hydroprocessing has been examined by several researchers. This material has attracted attention as potential support for noble metal catalysts [63]. In addition, carbon-supported sulfided metal catalysts have been reported to exhibit higher HDS activity for dibenzothiophene compared to alumina-supported catalysts [75-77]. Also, the relatively weak interaction between the surface of carbon and the metal causes the

oxidic metal precursor to be completely converted to the sulfide phase, while the strong interaction involving the surface of Al_2O_3 support results in partial conversion to the sulfide form [78]. In a study to determine the influence of the support on HDO of model compounds representing pyrolysis oil, Centeno and co-workers [55] prepared Co-Mo sulfide catalysts supported on alumina, silica and activated carbon. The authors reported that the catalyst supported on carbon led to direct demethoxylation of guaiacol (represented by DMO route in Fig. 1.5), leading to high selectivity in the production of phenol over catechol. Several other studies over carbon-supported catalysts performed over the years by researchers from Université Catholique de Louvain have asserted the usefulness of carbon supports for HDO reactions [27, 56, 79-81]. A study by Chary et al. [82] attempted to compare carbon-supported metal sulfides to conventional Al_2O_3 -supported catalysts towards HDO of furan at near atmospheric pressure. The authors reported that the metal sulfides supported on carbon showed better dispersion and greater HDO activity than the corresponding metal sulfide supported on alumina. Recently, a study by Echeandia et al. [83] also attempted to detect synergistic effects in the HDO of phenol over Ni-W oxide catalysts supported on activated carbon. The study conclusively showed some beneficial effect on using activated carbon supports instead of traditional alumina supports with respect to coke formation on the surface of the support.

1.3. Transition Metal Nitrides and Oxynitrides

1.3.1. General Properties

General catalytic interests in transition metal nitrides arise from their ability to emulate certain catalytic properties similar to the Pt-group metal catalysts. The incorporation of nitrogen atoms into the metal lattice significantly modifies the physical and chemical properties of the parent metal [84]. For example, they possess both acid/and or base sites due to electronegativity differences between the metal and nitrogen atoms. Nitrides can be commonly classified as ionic, covalent, intermediate and metallic depending on the bonding types within the compound and the atomic radii of the constituent elements [85, 86]. Nitrides regarded as classically ionic are formed with nitrogen and the most electropositive elements (Group I, II and III elements). Covalent nitrides are exhibited by nitrides of less electropositive elements. Nitrides of early transition metals are called interstitial nitrides and are formed by a combination of large electronegativity difference and the occupancy of specific interstitial sites of a host atom by nitrogen [84, 85]. Thus, the interstitial structures display a combination of ionic, covalent and metallic characters. They can be arbitrarily classified as binary (monometallic, host metal and nitrogen) and ternary (bimetallic, two metals + nitrogen in the structure) nitrides.

In transition metal nitrides, the simultaneous contributions from ionic, covalent and metallic bonding lead to unique physical and chemical properties. They possess physical properties similar to ceramics but display electronic properties resembling metals [85]. The refractory properties have led to their application as

cutting tools and high-temperature structural materials. They have high melting point, high hardness and tensile strength, and high thermal and chemical stability [84, 85]. Binary-based structures, especially Mo nitrides, have so far been most widely studied and constitute the major part of the published work within transition metal nitrides. In this respect, this thesis will concern itself only with the structure and properties of Mo-based nitrides. In molybdenum nitrides, Mo atoms form lattices of face-centered cubic crystal structure with the nitrogen atoms occupying octahedral interstitial sites in the structure as illustrated in Fig. 1.6. Another non-metallic element such as oxygen is capable of being accommodated into the interstices of nitrogen-deficient crystal structures to form Mo oxynitrides, owing to similarities in their atomic radius. Similarly, in bimetallic nitrides, the metal atoms (e.g. Mo and Co) are located in a face-centered cubic arrangement, and the N and O atoms filling up octahedral interstitial positions [87]. The release of nitrogen from the bulk lattice creates adsorption and catalytic sites [88]. In a study to determine the catalytic sites on transition metal nitrides and oxynitrides, Miga and co-workers [89] proposed a dual-site model where Brønsted groups and transition metal atoms co-existed on the surface of the solid. The dual site model included metallic Mo atom being electronically modified by N atoms, and Brønsted acid sites as shown in Fig. 1.7. The metallic sites were believed to be centers for hydrogenation while the Brønsted acidic sites were believed to be active towards hydrogenolysis of C-heteroatom bonds [90].

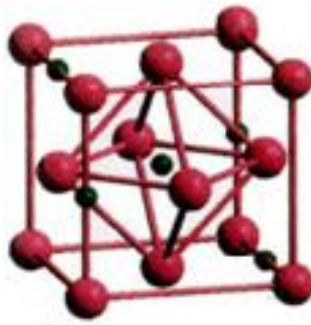


Figure 1.6 Crystal structure of γ - Mo_2N . Large circle represent Mo and the small circle represents nitrogen [91]

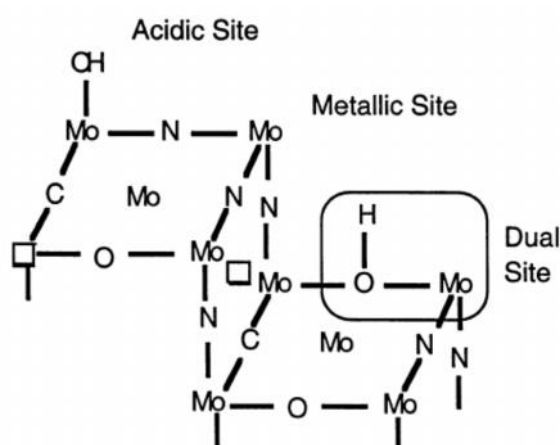


Figure 1.7 Acidic sites, metallic sites and dual sites model of MoO_xN_y [89].

1.3.2. Preparation of Transition Metal Nitride and Oxynitride Catalysts

The surface structure and chemical composition governs the catalytic and adsorptive properties of nitrides. A great impetus for studying transition metal nitrides as heterogeneous catalysts is the ability to prepare high surface area materials. Materials with high surface area contain nanoparticles which exhibit intrinsically higher chemical reactivities, compared to low surface area materials, due to the presence of a large number of defect sites including edges/corners, and a greater concentration of coordinately unsaturated ions [92]. Defect sites located on

the surface of solid catalysts are important because they are usually responsible for many of the catalytic and chemical properties [89]. High surface area Mo nitride powders can be achieved through a temperature-programmed reaction method developed by Volpe and Boudart, or by dispersing the Mo nitrides on high surface area supports [93]. The method developed by Boudart [94] involves flowing a stream of reductive nitriding gas (ammonia) over bulk molybdenum trioxide while linearly heating in a temperature-controlled manner. Volpe and Boudart explained that the reaction involving MoO_3 and NH_3 is topotatic in the sense that there is a crystallographic orientation relationship between the parent material (MoO_3) and the nitride Mo_2N product. Preparing molybdenum nitrides through isothermal reaction of MoO_3 with NH_3 by employing very high temperatures generally produced small surface area Mo nitrides [95].

The surface properties, phase, and composition of Mo-based nitrides are influenced strongly by the synthetic parameters [93]. Choi and co-workers [93] reported that slow heating ramp rates and high space velocities of ammonia led to the generation of high surface area and porous Mo nitride powders. The higher gas space velocity has been suggested to contribute to lowering concentrations of water formed during reduction of the Mo oxide precursor. The accumulated water in the bed may inhibit the transformation from oxide to nitride by limiting contact between NH_3 and MoO_3 [96]. In addition, the presence of water may cause hydrothermal sintering, leading to deterioration of high surface area [97]. The slow heating ramp rates allow the diffusion of nitrogen (and oxygen out) into the metal lattice without substantial reorganization, suppressing sintering of the

intermediates through diffusion [97]. Previous studies by Jagers et al. [98] tracked reaction intermediates and pathways during the solid-state reaction of MoO_3 with ammonia to form $\gamma\text{-Mo}_2\text{N}$. The authors proposed two possible reaction schemes illustrated in Fig. 1.8: the main pathway proceeds through an oxynitride intermediate, and a side reaction which involves partial reduction of MoO_3 to MoO_2 .

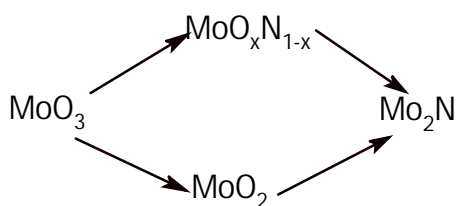


Figure 1.8 Reaction pathway during reaction of MoO_3 with NH_3 [98].

Jagers and collaborators [98] further asserted that proceeding through the oxynitride route led to a large increase in surface area while the alternate route (formation of MoO_2) resulted in the formation of a lower surface area Mo_2N . In a later related study, Choi and co-workers [93] reported more in-depth reaction pathways during temperature-programmed reaction of MoO_3 with NH_3 . The authors also concluded that the generation of low, medium and high surface area Mo nitrides depended on which pathway the reaction proceeded which were invariably dependent on synthesis parameters. In order to produce catalysts with the highest surface area, the authors explained that the reaction should be channeled through H_xMoO_3 ($x \approx 0.34$) and $\gamma\text{-Mo}_2\text{O}_y\text{N}_{1-y}$ intermediates. In their study, Choi et al. [93] employed a three-segment heating program during the reaction of MoO_3 and NH_3 . The authors reported BET surface areas of $116 \text{ m}^2 \text{ g}^{-1}$ and $44 \text{ m}^2 \text{ g}^{-1}$ by varying the early-stage heating rates (40 K h^{-1} and 100 K h^{-1} respectively) while keeping the

space velocity constant at 17 h^{-1} . Furthermore, a BET surface area of $28 \text{ m}^2 \text{ g}^{-1}$ was observed for a molybdenum nitride sample synthesized using a space velocity of 8.5 h^{-1} while employing a similar heating program to that used for the $116 \text{ m}^2 \text{ g}^{-1}$ Mo nitride sample.

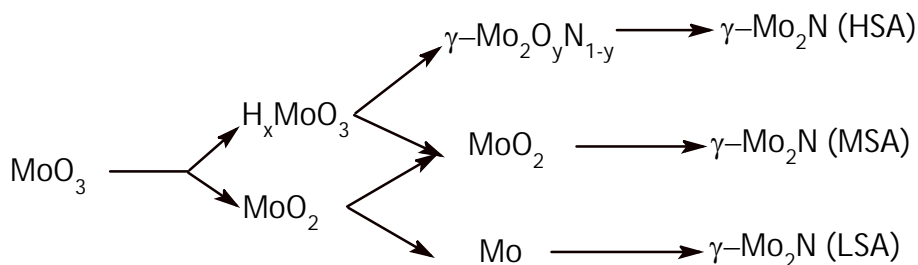


Figure 1.9 Reaction pathways to produce low surface area (LSA), medium surface area (MSA) and high surface area (HSA) bulk Mo_2N . Adapted from Choi et al. [93].

To avoid heat transfer problems due to endothermic decomposition of ammonia gas during temperature-program reaction, Wise and Markel [93] used mixtures of H_2 and N_2 instead of NH_3 gas to produce a $150 \text{ m}^2 \text{ g}^{-1}$ surface area bulk Mo_2N . The authors reported that lower N_2/H_2 space velocities and high temperature ramping rates led to lower product specific surface area, an assertion consistent with earlier results reported by Volpe and Boudart [94]. They attributed this result to increased concentrations of H_2O evolved by the reaction. Other significant aspects of the findings by Wise and Markel [99] involved the effects of the H_2/N_2 ratio on Mo nitride surface area and phase purity. Using nitrogen-rich mixture was found to produce a mixture of low surface area MoO_2 , Mo_2N and Mo . A mixture of 82.3% $\text{H}_2/17.7\% \text{ N}_2$ gas composition produced $\gamma\text{-Mo}_2\text{N}$ with an observed surface area of $119 \text{ m}^2 \text{ g}^{-1}$.

A more recent study by Gong et al. [100] reported the synthesis of β -Mo₂N_{0.78} (tetragonal in contrast to fcc γ -Mo₂N) using hydrogen-rich reaction gas (N₂/H₂: 7/13) or an equimolar mixture of N₂ and H₂. In the study, the authors reported a 8.9 m² g⁻¹ surface area for pure β -Mo₂N_{0.78} and ascribed that to the formation of MoO₂ intermediate. An earlier study by Nagai and co-workers [101] also reported the formation of β -Mo₂N_{0.78} via ammonolysis, with the major difference involving the use of He instead of NH₃ to cool the product to room temperature after nitridation.

Transition metal nitrides are pyrophoric and the surface needs to be passivated through mild thermal oxidation treatment using a dilute stream of oxygen. This passivation treatment forms a protective chemisorbed oxygen monolayer on the surface [102]. Additionally, during passivation oxygen is incorporated into the nitrogen-occupying lattice to form oxynitrides at the surface [97]. Colling and co-workers [103] stated that although the primary bulk crystalline phase for Mo nitride was γ -Mo₂N (fcc), the near-surface which consists of an oxynitride is body-centered. Passivated nitrides are typically pretreated in H₂ at moderate temperature (673 K) prior to use as catalysts in order to remove incorporated oxygen during passivation [93]. In a study, Choi and co-workers [93] attempted to examine the effects of hydrogen reduction temperature and time on the surface area of bulk Mo nitrides. According to the results reported, increasing reduction temperature from 473 K through 673 K (constant reduction time of 4 h) monotonically increased the BET surface area. The authors also reported a maximum surface area when passivated bulk Mo nitride was reduced in H₂ at 673 K for 3-5 h [93]. Although removing the protective oxide layer through H₂ reduction

enhances the surface area, the passivation process was found to cause a loss in surface area of “fresh” Mo nitrides. Thus, the surface area prior to passivation cannot be completely recovered through pretreatment in hydrogen [93]. Choi and collaborators [93] concluded from their study that hydrogen reduction removes the oxygen diffused into the lattice during passivation.

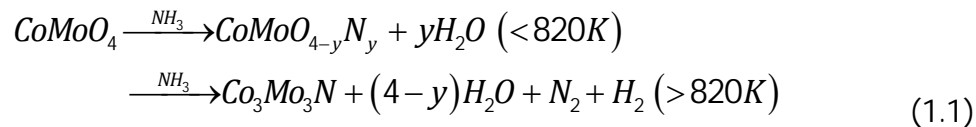
Demczyk and co-workers [104] demonstrated differences in crystal structure and composition of near-surface and bulk structure of high surface area Mo nitride material. From HRTEM and XPS results, the authors found that the presence of $\text{Mo}_2\text{N}_{3-x}\text{O}_x$ accounted for the near-surface structural properties of Mo nitrides. The hypothetical compound was characterized by a primitive cubic structure with nitrogen and oxygen occupying all the octahedral interstices in the structure [104].

Wei et al. [105-107] used XPS, XRD, TPD and TPR to investigate the effect of passivation on surface properties of fresh Mo_2N samples. The authors suggested that passivation leads to the elimination of strongly-bonded NH_x species and the formation of an oxide layer. They based their explanation on the presence of two types of NH_x (weakly- and strongly-adsorbed NH_x species) and H species on freshly prepared Mo_2N , while only a small amount of weakly chemisorbed NH_x species was present on the surface of passivated Mo_2N .

Molybdenum-containing bimetallic (ternary) nitrides and oxynitrides have received comparatively less attention compared to binary nitrides. However, recent advances in the preparation method have been significant, and development of ternary nitrides has thus flourished in their own right. The presence of an additional transition metal may enhance properties relative to monometallic nitrides. These

ternary nitride materials are commonly synthesized by nitridation/reduction of ternary oxide precursors prepared through solid-state synthesis. Bem et al. [108] prepared FeMoO_4 and NiMoO_4 precursors by mixing an aqueous solution of Fe salt (or Ni salt) with aqueous solution of a Mo salt, followed by drying and calcination under nitrogen at 700 °C for 6 h. The bimetallic oxide precursors obtained were placed under flowing ammonia gas and heated at 5 °C min⁻¹ to 700 °C to prepare the corresponding ternary nitrides ($\text{Fe}_3\text{Mo}_3\text{N}$ and $\text{Ni}_3\text{Mo}_3\text{N}$). Yu and co-workers [87, 109-111] synthesized a Mo-containing bimetallic oxide precursor through mechanical mixing of MoO_3 and M-oxide (with M = V, Nb, Cr, Mn, Co), fired in air at various temperature between 948 K - 1058 K for 6 h. The researchers passed an ammonia gas stream over the oxide powders while heating linearly at 5 K min⁻¹ to a final temperature exceeding 892 K. From these methods and temperature profiles, the investigators reported pure phase bimetallic oxynitrides after passivation at room temperature.

Kim and co-workers [112] discussed the changes in phase composition of Co-Mo oxides and corresponding Co-Mo nitrides at different relative Co atomic ratios. Results obtained from XRD patterns indicated that a nominal Co:Mo atomic ratio of 2:8 resulted in mixed nitride phases (Mo_2N and $\text{Co}_3\text{Mo}_3\text{N}$), while 5:5 atomic ratio produced predominantly $\text{Co}_3\text{Mo}_3\text{N}$ phase. The authors further observed the presence of $\text{Co}_3\text{Mo}_3\text{N}$ and Co metal phase at a relative Co mole fraction of 0.7 [112]. In a later study, Hada et al. [113] proposed a reaction pathway during ammonolysis of CoMoO_4 on the basis of XRD and TPR data. Complete nitridation to produce $\text{Co}_3\text{Mo}_3\text{N}$ occurred after a final temperature exceeding 820 K.



In summary, due to the existence of generally applicable synthesis methodologies for Mo-based binary and ternary nitrides and oxynitrides, together with well-documented unique properties, these groups of materials have found application as catalysts for various reactions.

1.3.3. Supported Metal Nitride and Oxynitride Catalysts

The fact that high surface area transition metal nitrides can be prepared through the temperature-programmed reaction method developed by Volpe and Boudart [94] means that the role of the support on catalyst properties has been less examined. The argument in favor of high surface area bulk Mo₂N over supported Mo₂N was that the available surface area of the former was completely occupied by active material while only about 10-15% of the supported catalysts consists of the active material [97]. Thus, the synthesis and applications of metal nitrides in the literature are dominated by the bulk counterpart. However, catalyst supports provide more than just a large surface area to disperse the active phases. The pore structure provided by the support can determine how rapidly reactants are transported into the interior surface of the catalyst. The physical and chemical properties of the support may also influence properties including metal dispersion and resistance to sintering.

Supported Mo nitride catalysts are commonly prepared using the impregnation technique. Nagai and co-workers [114, 115] studied the HDS and HDN activities of Mo nitrides supported on alumina (11.7 wt% and 97.1 wt% Mo). The

authors demonstrated that the HDN activity of carbazole over these materials were significantly higher compared with conventional sulfided and reduced catalysts [114]. The same group of authors also found a similar relationship when they prepared and tested alumina-supported Mo nitrides for dibenzothiophene HDS [115]. They reported that the nitride catalysts consumed less hydrogen owing to being extremely active towards direct sulfur removal from dibenzothiophene. The group of Nagai [101, 116-120] carried out more research on alumina-supported molybdenum nitrides by using techniques such as TPD, XPS and Temperature-programmed surface reaction (TPSR) to investigate the surface properties of these materials. Results from the TPD studies of nitrated 12.5% Mo/Al₂O₃ indicated the presence of NH_x species on the surface which is formed when the catalyst is cooled to room temperature under NH₃ after nitridation [117]. XPS measurements were used to study the deactivation and regeneration mechanism of nitrated 12.5% Mo/Al₂O₃ during HDS of dibenzothiophene [116]. The authors observed a decrease in HDS activity and an increase in hydrogenation selectivity for their reaction system and attributed it to the accumulation of sulfur on the nitride catalysts. The aged and deactivated catalysts were re-nitrated by ammonia retreatment which regenerated unsaturated Mo species and reduced sulfur species on the near-surface of the catalyst [116]. In a more recent study, Nagai et al. [120] determined from XPS the active sites of nitrated 12.5% Mo/Al₂O₃ for hydrogenation in the HDN of carbazole. Their study showed that the presence of metallic Mo and Mo²⁺ on the catalyst surface were responsible for hydrogenation of the benzene rings in carbazole to tetrahydrocarbazole and perhydrocarbazole [120].

Colling and Thompson [121] investigated the structures and compositions of γ -Al₂O₃-supported Mo nitrides and its dependence on metal loading, heating rates, and space velocities. Their study showed a strong relationship between the properties of the supported species and the preparation conditions. Particularly, using low (4 and 8 wt% Mo) loadings led to the formation of highly dispersed, raft-like molybdate domains, while high Mo loadings (16 wt% Mo) resulted in the formation of γ -Mo₂N crystallites. The authors also reported a decrease in pyridine HDN activities with increasing Mo loading and their explanation for this behavior was the existence of two types of active sites on the catalyst surface [121]. The activities of the supported Mo nitrides were comparable to unsupported Mo nitrides but superior to conventional sulfided Ni-Mo catalysts. Bussell and co-workers [120-123] used a variety of conventional and spectroscopic techniques to investigate the bulk and surface properties of alumina-supported Mo nitrides. The HDS activities of these materials were measured for thiophene. From IR spectroscopy results, Bussell et al. [122] proposed a model for the structure of the active catalytic surface of a Mo₂N/Al₂O₃ under reaction conditions. The model involved the formation of a thin layer of highly dispersed MoS₂ on the surfaces of the nitrated particles treated in thiophene/H₂ mixtures, while the bulk structure of γ -Mo₂N was retained. Bussell and co-workers [123] also found correlations between thiophene HDS activities and the densities of active sites of alumina-supported γ -Mo₂N catalysts. They reported that the higher activity of Mo₂N/Al₂O₃ catalysts over Mo/Al₂O₃ sulfide catalyst stem from higher density of active sites of the former. In a fairly recent study, Bussell and co-workers [124] described the synthesis of bulk and alumina-supported Mo-based

bimetallic nitrides ($\text{Ni}_2\text{Mo}_3\text{N}/\text{Al}_2\text{O}_3$, $\text{Co}_3\text{Mo}_3\text{N}/\text{Al}_2\text{O}_3$). The studies reported the preparation of supported nitrides possessing high active surface areas and high oxygen chemisorption capacities. In a follow-up study, Bussell and collaborators [125] reported that alumina-supported bimetallic nitrides were significantly more active than monometallic Mo nitrides ($\text{Mo}_2\text{N}/\text{Al}_2\text{O}_3$) for thiophene HDS. The authors attributed the higher activity of former to the presence of bimetallic sulfides on the catalyst surface [125].

Catalytic applications of supported Mo-based nitrides in the literature have been overwhelmingly dominated by the nitrides supported on alumina. There have only been a handful of papers reporting the use of other supports such as titania (TiO_2) [126], carbon [127] and silica [128]. Guerrero-Ruiz et al. [127] reported the gas-phase hydrogenation of crotonaldehyde over unsupported bulk and activated carbon-supported Mo_2N catalysts. The authors suggested an affiliation between selectivity to crotyl alcohol and the abundance of (200) planes of the Mo_2N crystallites indicating the structure-sensitivity of this reaction over Mo nitride catalysts. Lee and collaborators prepared, characterized and compared CO hydrogenation reaction of alumina-, silica-, zirconia-, and titania-supported Mo_2N prepared via nitridation of MoS_2 [129]. Based on H_2 uptake measurements, the authors reported turnover frequency decreasing in the order: alumina > silica > zirconia > titania. Another study comparing different supports was carried out by Trawczynski [130] who investigated thiophene and vacuum gas oil HDS over alumina and activated carbon supported Mo nitrides. The author reported that activated carbon supported- Mo_2N displayed a higher HDS activity compared to the

alumina-supported counterpart. The study also indicated that the acidity of the catalysts was determined by the support properties [130]. Since, the performance of Mo nitrides for HDO catalysis is one of the focus of this thesis, other alternatives to alumina supports should be explored due to the limitations of this material for HDO reactions.

1.3.4. HDO Reactions over Molybdenum Nitride and Oxynitride Catalysts

Hydrotreating catalytic reaction studies of transition metal nitrides and oxynitrides have mainly concentrated on HDS [97, 112, 113, 115, 116, 118, 122, 123, 125, 126, 131-137], HDN [89, 101, 114, 117, 120, 138-143] and simultaneous HDS, HDN and HDO reactions [96, 134, 144-148]. Most of these studies were conducted to investigate relationships between catalyst's properties and catalytic activities. The studies were performed using HDS model compounds such as thiophene, benzothiophene and dibenzothiophene, and HDN model compounds such as pyridine, indole, quinoline and carbazole. The performances of these catalysts in most of the studies were superior to conventional sulfided catalysts. However, there are only a few examples in the literature where transition metal nitrides were employed as catalysts for HDO reactions. Here, only the HDO performances of transition metal nitrides will be briefly reviewed.

Abe and Bell [149] reported the catalytic HDN of indole, HDS of benzothiophene and HDO of benzofuran over bulk Mo_2N . They observed nearly equivalent amounts of benzene, toluene and ethylbenzene produced during the HDO of benzofuran at atmospheric pressure and 673 K. The authors demonstrated a mechanism which proceeded through rapid hydrogenation of the O-containing ring

prior to C-O bond scissions in the saturated O-containing ring. Another interesting finding from this study was that the removal of oxygen in the form of water (and hence the presence of H₂O in the reactant feed) had a lesser effect on suppressing the activity of Mo₂N for hydrogenation and dealkylation in comparison to the presence in the feed of H₂S and NH₃ for HDS and HDN reactions respectively. Similar to the studies by Abe and Bell, a series of moderate surface area transition metal carbides and nitrides (which included nitrides of titanium, vanadium and molybdenum) were tested for their catalytic activity in HDN, HDS, HDO and hydrogenation by Ramanathan and Oyama [145]. Benzofuran was the model HDO compound used. VN was found to exhibit excellent activity and selectivity in HDO of benzofuran while WC was found to be comparable in activity to commercial sulfided Ni-Mo/Al₂O₃ catalyst in HDN reaction [145]. In a recent study, Monnier and co-workers [150] prepared -Al₂O₃-supported Mo, W, and V nitride catalysts and tested them for HDO of oleic acid and canola oil. The authors observed superior performances for HDO of oleic acid over Mo₂N/ -Al₂O₃ compared to VN/ -Al₂O₃ and W₂N/ -Al₂O₃ in terms of conversion, oxygen elimination and production of normal alkanes.

The examples of alternative supports (such as carbon, silica and zirconia) and Mo nitrides discussed in this chapter demonstrated two major points in developing commercially attractive HDO catalysts. The first is the clear advantage that carbon supports have over alumina supports in terms of less formation of coke, selectivity towards direct deoxygenated products, and relative stability in water. The review also showed the importance of non-sulfide metal catalysts in HDO

reactions. Since metal nitrides combine the properties of being less difficult to prepare (compared to metal carbides [90]) with their bifunctional catalytic character [89], relatively low cost (compared to noble metal catalysts), their lower susceptibility to oxidation (compared to metal phosphides [72]), and their unique catalytic pathways leading to minimum hydrogen consumption, they can become a very attractive alternative to classical Co(Ni)-Mo/ -Al₂O₃ sulfide catalysts for hydrodeoxygenation reactions. In conclusion, it can be said that despite the catalytically desired properties of a Mo₂N catalysts they have so far received very little attention for hydrodeoxygenation catalytic processes.

1.4. Fischer Tropsch Synthesis

Fischer Tropsch synthesis is the hydrogenation of carbon monoxide (CO) over metal catalysts to produce hydrocarbons. Important progress in FTS research has been made ever since Hans Fischer and Franz Tropsch developed the Synthol process in 1922. The Synthol process involves the production of a mixture of oxygenated hydrocarbons, olefins and paraffins via the reaction of carbon monoxide and hydrogen at high pressure and 673 K temperature over alkalized iron chips [151]. The process was expanded to include low pressure reactions to produce heavy molecular weight hydrocarbons over Co catalysts. Commercial applications of the FT process were operated in Germany by Ruhrchemie AG in 1937. From 1938 through World War II, different reactor configurations and processes were developed for large scale FTS applications. Between the 1950s and 1970s, interest in FTS waned due to world energy dependence on cheap oil supply except in South Africa. Interests in FTS were rekindled after Arab members of OPEC (Organization

of Petroleum Exporting Countries) proclaimed an oil embargo in 1973 and 1979. Recently, FTS has received renewed attention driven by problems associated with the utilization of stranded gas, changes in fossil fuel reserves, and environmental concerns [151].

Gasification of coal, natural gas or biomass produces synthesis gas (syngas), a mixture of CO and H₂, which is utilized as feedstock for the production of liquid transportation fuels and chemicals. After initial gas clean-up and CO/H₂ ratio adjustments, FTS is carried out over Group VIII metal catalysts to produce a broad distribution of highly linear hydrocarbons and a relatively small fraction of oxygenated compounds under typical reaction conditions. This synthesis proceeds through a sequence of chain-growth polymerization reactions on the surface of the catalyst whereby -CH₂- monomers are inserted into the hydrocarbon growth chain [152]. These polymerization reactions results in a broad spectrum of products, with the mix of primary products being predominated by alkanes and alkenes.

The reaction stoichiometry of CO hydrogenation to produce hydrocarbons can be represented by two main equations (1.2 and 1.3). The primary products from these equations are linear alkenes and alkanes respectively.



The water gas shift (WGS) reaction (Eq. 1.4) is a side reaction which may occur concurrently, particularly over FTS iron catalysts. This involves reaction of FTS

reactant and product, CO and H₂O respectively, to generate CO₂ and H₂. The WGS reaction is important in adjusting the CO/H₂ usage ratio. There are some other secondary reactions which accompany the main reactions above and that include undesired reaction pathways such as methanation and Boudouard reactions depicted in Eq. 1.5 and 1.6 respectively



These highly exothermic reactions proceed on Group VIII metals. Metals such as Ru, Fe, Co and Ni have been reported to exhibit demonstrable activities for FTS. Ruthenium catalysts have not been utilized commercially despite its high activity and selectivity towards higher molecular weight hydrocarbons. This is because of the relatively high cost and limited availability worldwide. They have generally been used as promoters for Co catalysts. Nickel-based materials have the disadvantage of being highly selective towards the formation of methane at increasing reaction temperature, as well as forming nickel carbonyls which results in loss of metal at elevated pressure [153]. Iron and cobalt are presently the only industrially used FTS catalysts.

There are trade-offs involving the use of iron and cobalt catalysts. Iron catalysts are relatively cheaper than Co catalysts and typically produce lower molecular weight hydrocarbons and alcohol. Iron catalysts are significant towards WGS reactions (Eq. 1.4) and thus operable at a lower syngas H₂/CO usage ratio. Thus, iron catalysts appear to be desirable for biomass-produced syngas which has

a low H₂/CO ratio as a result of preferential conversion of carbon to CO₂ by the high oxygen content of biomass materials [154]. These catalysts are also suitable for both high- and low-temperature FT processes [151]. Cobalt catalysts, despite being relatively more expensive than Fe, have a longer catalytic life, and also possess higher activity at high conversions. Water-gas shift reactions are negligible over Co catalysts and therefore require an H₂/CO usage ratio of ~2.0 [155]. Due to Co catalysts favoring the production of long-chain hydrocarbons, its general resistance to deactivation as well the absence of the competing water-gas shift reactions, Co represents the catalyst of interest in this study. Thus, this part of the thesis will review only cobalt-based catalytic systems.

1.4.1. Fischer Tropsch Synthesis on Cobalt Catalysts

Because the activity of the metal catalysts is a complex function of many factors, gaining insights into the relationships between methods of catalyst preparation, catalyst properties and catalyst performances for FTS have been the focus of intense research for many years. The catalysts preparation methods have strong effects on catalytic performances. Methods such as impregnation [156], sol-gel technique [157], and co-precipitation [158] have been used to synthesize catalysts with demonstrable FT activity. A great majority of FTS catalyst research has focused on supported Co catalysts where oxidized Co species were dispersed on zeolites [159, 160] and various inorganic oxides such as Al₂O₃ [161, 162], titania (TiO₂) [163, 164], and silica (SiO₂) [165, 166]. The active Co metal atom is then produced from reduction of the oxidic Co precursor. Zeolites, typically used in the petroleum industry, are stable under Fischer Tropsch (FT) conditions [167].

Previous work on FT zeolite catalysts involved preparing cobalt-containing ZSM-5 zeolites using various methods by Jong and Cheng [159]. One of the methods involved incorporating Co into the framework of ZSM-5 zeolites while the other method was via precipitating/impregnation of Co_3O_4 on ZSM-5. These two methods revealed the different chemical/structural nature of Co species. The former showed the modification of ZSM-5 framework by the incorporated cobalt (Co-ZSM-5) as well as the existence of a small amount of cobalt oxide. The precipitation/impregnation method (Co/ZSM-5) revealed the presence of cobalt silicate in the sample. Bessel [160] investigated the influence of pore structure of ZSM zeolite family-supported Co catalysts on FT activity. The author correlated activity with the channel size of the zeolite supports and attributed it to increased cobalt dispersion. Another carrier that has been widely used for FT Co catalysts is alumina. The support forms a strong interaction with cobalt oxide surface species and this lead to the formation of cobalt aluminates, an inactive cobalt species only reducible at temperatures above 900 °C [161]. Various methods such as chemical pretreatment of the alumina support (before Co introduction) [168] or the addition of promoters [169] have been utilized to improve support properties and hence the overall activity of the catalysts. The major challenge for Al_2O_3 -supported FT Co catalysts is reducibility of Co species to obtain the active Co metal sites in the catalysts. Alumina is also known to be unstable in the presence of water. For silica-supported Co catalysts, the cobalt metal-support interaction is relatively weaker compared to that of Al_2O_3 supports. The weak interaction leads to low dispersion and that represents the biggest challenge for silica-supported catalysts. The interaction, however, is still strong

enough to lead to the formation of inactive cobalt silicate which could only be reduced at temperature above 600 °C [170]. One major advantage of silica over alumina supports is the effects of water (a product of FTS) on the FTS rates. The addition of water has been reported to significantly enhance CO conversion and FTS rates of Co/SiO₂ [171]. The interaction of water with Co/Al₂O₃ catalysts results in mostly negative effects on CO conversion. Other supports such as TiO₂ and carbon have been rarely used with only a handful of published reports. Due to the inertness of carbon it has the potential to overcome problems associated with inactive, hard-to-reduce cobalt silicate and aluminates present in Al₂O₃ and SiO₂-supported Co catalysts respectively [151]. However, for the FT study in this thesis silica was chosen as the catalyst support.

The impregnation method is the most widely used technique to prepare silica-supported Co FT catalysts. It consists of contacting the support with a volume of solution containing the Co precursor salts (cobalt nitrate, cobalt acetate, cobalt chloride etc). Solvents commonly used include deionized water, methanol, ethanol, or propanol. The mixture is typically aged at room temperature for a certain period to aid in capillary aspiration of the salt solution into the pores. The system is then dried in an oven to drive off volatile components of the solution. This is followed by calcination to prepare a silica-supported Co₃O₄ catalyst. The choice of Co salt and solvent used have been reported to influence the extent of reduction and dispersion [170, 172]. Wang and co-workers [172] reported that regardless of the solvent used, using Co(NO₃)₂ as the Co precursor salt resulted in larger Co₃O₄ in a silica support of 3.4 nm pore diameter. In comparison between different Co salts, van Steen and

co-workers [170] reported the formation of cobalt silicates when using cobalt acetate. The authors concluded that the amount of cobalt silicates formed related to the polarity of the solvent. A study by Ohtsuka et al. [173] was conducted to compare FT performances of Co supported on SBA-15 prepared using an ethanol solution of Co acetate, nitrate, or an equimolar mixture of both compounds. The authors reported that the catalysts prepared using a Co acetate precursor compound was almost inactive while catalysts prepared from nitrate and the equimolar mixture resulted in 85-90% conversion. The inactivity of Co acetate-prepared catalysts was ascribed to the formation of hard-to-reduce cobalt species, consistent with the presence of cobalt silicates as reported by van Steen et al. [170].

The influences of catalyst's properties such as pore diameter of silica-supported catalysts [156, 165, 174-179] and metal particle size [180-182] on overall reactivity of the catalysts have been described extensively in the literature. Several studies on the relationship between FT activity and support pore diameter have reported increasing FT reaction rates with increasing support pore diameter [156, 175-177, 183]. Studies by Khodakov and co-workers [156, 175] have shown that activity and C_{5+} selectivity of Co supported on mesoporous silica increases with pore diameter, and attributed the results to different Co particle size and reducibility in the narrow and wide pore silica. Li et al. [183] reported that Co/SiO₂ with the largest average pore diameter of 10.4 nm displayed the highest activity for FTS followed by Co/SBA-15 (5.3 nm pore diameter) and then Co/MCM-48 (2.6 nm). The authors however observed the highest selectivity to C_{5+} by the Co/SBA-15 catalyst. The activities of the three catalysts were interpreted in terms of

reducibility of cobalt oxides while the formation of C₅₊ hydrocarbons was explained by the Co particle size. Based on a very similar interpretation to the work reported by Khodakov et al. and Li et al., Ohtsuka and co-workers [176] studied FTS performances of Co catalysts loaded on mesoporous molecular sieves with different pore diameter. They suggested that the highest activity shown by the Co/SBA-15 catalyst was as a result of dispersion and reducibility of the oxide species. Most recently, González et al. [177] observed high activity and selectivity towards the diesel fraction using wide pore silica supported Co catalysts.

In general, metal particle size influences FT turnover frequency (TOF) only below a critical threshold of 6- 8 nm [184]. Bezemer et al. [184] investigating the effect of cobalt particle size on CO hydrogenation reported the insensitivity of TOF on particle size larger than 6 nm using carbon nanofiber-supported Co catalysts. The authors also observed much lower FT reaction rates and C₅₊ selectivity for smaller cobalt particle sizes (2.6 nm). These phenomena have been explained by either different surficial character of small particles or by strong metal-support interactions which leads to a certain level of electronic modification [156]. Smaller particles might result in less effective catalysts because they contain fewer edge defects for catalysis [184], or because they are more susceptible to deactivation by reoxidation [151], or because they interact strongly with the support to impede reduction [174, 175], or because they slow reaction rates by binding reactants more strongly [185].

The presence of multiple Co phases has been cited as a factor affecting FTS catalytic activity, and a justification for general research into the significant impact

of the fraction of the different phases [186, 187]. However, there are still relatively few reports of an actual influence on catalytic activity, and detailed investigations into the intrinsic activity of each phase are particularly lacking. Reduction of the Co_3O_4 precursor under hydrogen proceeds in two steps [188]: the first involves complete reduction of Co_3O_4 to CoO ; the second step involves partial reduction of CoO to metallic Co . In the bulk form cobalt undergoes a martensitic transformation from hexagonal-closed packed (hcp) structure to face-centered cubic (fcc) structure when heated at temperatures above $420\text{ }^\circ\text{C}$ [189]. Kitakami and collaborators [189] found that the Co_{fcc} phase is thermodynamically stable at temperature above $420\text{ }^\circ\text{C}$ while the Co_{hcp} phase is more stable at lower temperature in the bulk form. Cobalt metal particles may however exist as a two-phase mixture in the nanometer scale [186, 190]. The existence of the multiple crystal phases have been reported to depend on surface energy contributions to the bulk chemical potential. In an earlier study, Srinivasan et al. [186] employed *in situ* XRD to characterize the structure of silica-supported Co catalysts reduced in H_2 at $350\text{ }^\circ\text{C}$. The authors found the presence of Co_{hcp} and Co_{fcc} metallic phases, with 17% of the Co_{hcp} phase being faulted. Consequently, attempts have been made by a handful of researchers to investigate the influence of the characteristics of the metallic phase (fcc or hcp) on FTS behavior of supported Co catalysts [187]. Enache et al. [187] noted a higher turnover frequency with materials that contained more quantities of amorphous and poorly crystalline Co_{hcp} metallic phase than materials which yielded more Co_{fcc} metallic phase. This result suggested that the reaction was catalyzed by the crystallographic defects of the Co_{hcp} phase. Ducreax et al. [190] used CO-H_2

treatment to decompose Co_2C in order to selectively form the Co_{hcp} phase which greatly enhanced FTS catalytic activity. The results were also interpreted in terms of the predominant formation of hcp stacking [190].

The review from this section indicates that a large number of papers in the literature so far focus on the effect of support pore structure on FT reaction rates and selectivity to long-chain aliphatic hydrocarbons. Less attention has been given to the influence of multiple Co phases. The intent of the Fisher-Tropsch study in this thesis is to try to gain insights into the effect of pore diameter of mesoporous silica supported Co catalysts on particle size, cobalt crystal phase and turnover frequency. The information from this study would add to efforts devoted to the understanding of fundamental catalyst parameters which influences FT reactivity. The insights gained will aid in the design and production of improved catalysts for FTS.

1.4.2. Periodic Mesoporous Silica as Supports

Conventional mesoporous silica supports possess broad pore size distributions and are irregularly spaced. For that reason, novel mesoporous silica materials with controllable pore size have been widely used as supports to disperse Co metal catalysts [175, 176, 183, 191]. In other words, they represent a new class of materials showing remarkable potential for a range of applications. Pioneering work in the early 1990s by Mobil researchers resulted in the synthesis of silica-based mesoporous molecular sieves [192]. This included hexagonal phase MCM-41 and cubic structured MCM-48. These two materials were synthesized via electrostatic assembly between ionic surfactants (as structure-directing agent) and anionic inorganic species. New routes to synthesize these materials and other

mesoporous molecular sieves have been published and are principally governed by the pH of the reaction medium. Tanev and Pinnavaia [193] developed a neutral templating route to synthesize hexagonal mesoporous silica (HMS) via hydrogen-bonding interactions between neutral primary amine micelles and neutral inorganic precursors. Stucky and co-workers [194] reported a significant advancement on the synthesis of this material by using non-ionic tri-block copolymers to template well-ordered hexagonal mesoporous silica structures in acidic media (named SBA-15). Generally, these novel mesoporous silica materials are formed following polymerization of a silica precursor after reaction with micelles of surfactants. The surfactant is then removed by calcination or solvent extraction which leads to the formation of a highly ordered porous structure [195]. The ability to adjust the pore diameter by using different sizes of templating molecules makes them promising materials to investigate the effects of pore sizes on properties of Co/SiO₂ [196]. This will lead to the design of supported catalysts with improved activities and selectivities. Considerable interests in these materials are driven, in part, by significant strides that have been made in utilizing periodic mesoporous silica in catalyst design and development during the past decade. These periodic mesoporous silicas are characterized by their high surface areas (500-1500 m² g⁻¹), narrow pore size distributions and large pore volumes (1-2 cm³ g⁻¹) [197]. MCM-41 [156], MCM-48 [174], HMS [198] and SBA-15 [173] have been applied for FTS. In particular, SBA-15 type materials has been widely studied because of its higher hydrothermal stability (due to thicker inorganic walls), high structure regularity, low-cost, and nontoxic template [199]. The ordered wide pores of SBA-15 (from 5 to

30 nm) may facilitate the flow of reactants to, and products from, the catalytic sites. The difference in hydrothermal stabilities and pore structures of these materials result in different structural properties of the impregnated Co metal as well as mass transfer kinetics. For that reason periodic mesoporous silica were utilized as supports for FTS study.

1.5. Objectives and Scope of Thesis

The purpose of the studies in this thesis was the preparation, characterization and evaluation of catalysts for intermediate processes related to the thermal conversion of lignocellulosic biomass. This dissertation dealt with two processes: Fischer-Tropsch synthesis (FTS) and hydrodeoxygenation (HDO) of a model compound of bio-oil. For FTS, a feed stream consisting of carbon monoxide and hydrogen gas mixtures were passed over silica-supported cobalt catalysts. Guaiacol (2-methoxyphenol) was chosen as a model compound to evaluate the HDO performances of transition metal nitrides. The study had two principal objectives:

- I. To investigate the effects of pore diameter of mesoporous silica-supported cobalt catalysts for the Fischer-Tropsch reaction. The influence of pore diameter on key parameters such as cobalt particle size, multiple cobalt phases and the overall reactivity of the catalysts were determined from these studies.

- II. To undertake hydrodeoxygenation catalyst research using guaiacol as the model compound. Experiments were conducted over monometallic and bimetallic molybdenum nitride catalysts.

The experiments conducted in this thesis gave us an insight into fundamental factors affecting catalytic activities and selectivities in reactions relevant to the renewable production of fuels, chemicals and energy. This can facilitate optimum design and efficient utilization of catalysts which is critical to their eventual commercial applications.

Chapter 1 describes the thermochemical conversion of lignocellulosic biomass and provides a review of traditional and non-traditional catalysts employed for hydrodeoxygenation of guaiacol. The chapter continues with a review of the physical and catalytic properties of transition metal nitrides and finally concludes with a review of the Fischer-Tropsch synthesis and catalysts.

Chapter 2 presents a study on the influence on FTS activity by cobalt catalysts supported on mesoporous silica with variable pore diameter.

Chapters 3 to 5 report on HDO of guaiacol tested over a series Mo and CoMo nitride catalysts. The first part of the series touches on unsupported Mo and CoMo nitride catalysts (Chapter 3). The work was then extended to supported metal nitride catalysts: activated carbons (Chapter 4), alumina and mesoporous silica (Chapter 5).

Chapter 6 presents the conclusions of the research and general recommendations.

CHAPTER 2

**EFFECTS OF PORE DIAMETER ON PARTICLE SIZE, PHASE, AND
TURNOVER FREQUENCY IN MESOPOROUS SILICA-SUPPORTED COBALT
FISHER-TROPSCH CATALYST***

2.1. Introduction

Fischer-Tropsch synthesis (FTS) is receiving renewed attention, driven by the global need to convert non-petroleum based energy resources into fuels and chemicals. Cobalt catalysts are known to favor the production of higher molecular weight hydrocarbons in FTS and hence the characterization of cobalt-based catalysts supported on relatively high surface area materials has recently been the focus of intense research [151, 174, 176, 180, 200-202]. These materials have several key parameters that can be varied. Determining the influence of any one parameter on the overall reactivity of the catalysts has been challenging. The two factors that have received the most attention are the influence of metal particle size [151, 175, 180, 181, 184, 203] and pore diameter. Less attention has been focused on the influence of multiple Co phases. In this chapter we characterize a series of Co catalysts on porous silicas and demonstrate the presence of a substantial number of small Co_{hcp} particles. We suggest that a failure to account for cobalt in small particles can lead to an overestimation of the effectiveness of a catalyst and conclude that by

* A portion of this chapter has been published as: I.T. Ghampson, C. Newman, L. Kong, E. Pier, K.D. Hurley, R.A. Pollock, B.R. Walsh, B. Goundie, J. Wright, M.C. Wheeler, R.W. Meulenberg, W.J. DeSisto, B.G. Frederick, and R.N. Austin, *Applied Catalysis A: General* 388 (2010) 57-67

accounting for both Co_{hcp} and Co_{fcc} surface areas, there is a clear correlation between turnover frequencies (TOF) and pore diameters between 2 and 13 nm.

Turnover frequencies (moles of product produced - or substrate consumed - per surface metal per unit time) provide insight into which fundamental factors affect catalytic activity and can facilitate rational catalyst design. TOFs depend on estimates of surficial metal area, which are calculated using experimentally-measured average particle size [156, 165, 174-179, 183, 202, 204]. Many authors calculate the surface area of Co FT catalysts based on the size of the Co_3O_4 particles (determined by XRD [151, 175]) on as-prepared catalysts. However there is evidence that particle size and hence surface area may change during pretreatment. Prieto et al. found larger particles (18-71% larger) when looking at reduced catalysts (using chemisorption) relative to oxidized material (by XRD) which they attribute to sintering of particles during reduction [205]. Song and Li showed that estimates of particle diameters vary dramatically when incomplete reduction of Co_3O_4 particles is taken into account [179].

In general, FTS has been thought to be insensitive to structure [202] but there are some data that suggest that very small metal particles (below a critical threshold of approximately 7-10 nm) lead to less effective catalysts [184, 185, 202, 203]. Small particles might be less active because they contain fewer edge defects where catalysis can more easily occur [184], or because they contain more low coordinate Co that might bind reactants more tightly and slow reaction rates [185], or because the high surface area could destabilize the particles and prevent reduction [174, 175, 204] or promote reoxidation [151]. Some experiments suggest

a particle size threshold (approximately 10 nm) above which TOF are unchanged [200].

Furthermore, several researchers have noted that after reduction multiple metal phases can exist, which could affect reactivity [184]. Srinivasan et al. [186] and Enache et al. [187] found both fcc and hcp phases after reduction. Enache noted higher TOF with materials that contained more Co_{hcp} than materials with more Co_{fcc} [187], but thought that this might be due to defects and disorder [187]. Ducreux et al. were able to preferentially prepare the hcp phase by reducing Co_2C precursors and found that predominantly hcp material converted almost two times as much CO as the predominantly fcp material [190].

In this chapter, we describe the characterization of cobalt metal catalysts analyzed with XRD as CoO and two metal phases: Co_{fcc} and Co_{hcp} and report on the relationships between metal phases, particle diameters, support pore diameters, and turnover frequencies for nine different catalysts. Additional characterization with nitrogen porosimetry, x-ray absorption near edge structure (XANES), and transmission electron microscopy/selected area diffraction (TEM/SAD) supports our materials analysis. Cobalt catalysts were impregnated onto silica supports with different pore diameters and calcined to yield Co_3O_4 particles, reduced with hydrogen to produce CoO and Co metal, and then exposed to FTS conditions for 10 hours. We characterized the catalyst properties at three different stages in catalyst history: (1) after calcination; (2) after H_2 reduction; and (3) after FT reaction. X-ray diffraction data was used to determine the particle diameters of Co_3O_4 (Stage 1) and

Co_{hcp}, Co_{fcc} and CoO (Stages 2 and 3) as well as the relative amounts of Co_{hcp}, Co_{fcc} and CoO at Stages 2 and 3.

The most notable relationship we find is that turnover frequencies, based upon total metal surface areas determined after FTS, are very well correlated with pore diameter. We also note that significant changes in dispersion occurred during the ten hour time under reaction conditions. Hence a failure to account for cobalt in small particles can lead to an overestimation of the effectiveness of a catalyst. We also find evidence that solid supports with extensive networks of small micropores may decrease the overall efficiency of FT catalysts.

2.2. Experimental and Methods

2.2.1. Synthesis of Mesoporous Silica Supports

MCM-41. MCM-41 was synthesized following a literature procedure [206], in which 1 g ammonium hydroxide (NH₄OH, Fischer Scientific, 28% in water) was mixed with 21 g of the surfactant, cetyltrimethylammonium chloride (CTMACI, Aldrich, 25% in water). The solution was then added to 5 g tetramethylammonium hydroxide pentahydrate (Acros Organics, 97%). 5 g of Cabo-sil M-5 fumed silica (SiO₂, Cabot, >99.8 %) and 11.4 g of deionized water were subsequently added to the mixture, and the solution was stirred at room temperature for 30 min. The mixture was then transferred to a polymer flask, sealed and heated at 100 °C for 24 h in an oven. After filtration and washing with deionized water, the solid product recovered was air-dried at room temperature for 24 h. The sample was then calcined in air by a ramp of 1 °C min⁻¹ to 500 °C and held at 500 °C for 6 h.

MCM-48. MCM-48 was synthesized by a conventional hydrothermal method [197]. Cetyltrimethylammonium bromide (CTMABr, 2.4 g, Aldrich, 99%) was dissolved in 50 mL Milli-Q water. Ethanol (EtOH, 50 mL, Acros Organics, 99.5%) and 12 mL, 5N NH₄OH were then added, and the solution stirred for 10 min. Tetraethylorthosilicate (TEOS, 3.6 mL, Aldrich, 99%) was added and the reaction stirred for 2 h. The solid product was recovered by filtration, rinsed with Milli-Q water and then calcined for 6 h at 550 °C.

HMS. For the preparation of HMS [207], 0.80 g of hexadecylamine (HDA, Aldrich, 98%) was added, at room temperature, to a 6.3 mL solution of Milli-Q water and 4.1 mL EtOH. The mixture was stirred until a homogenous mixture was obtained. TEOS (2.23 mL) was then added under vigorous stirring. The reaction was continuously stirred overnight and the solid product was recovered by centrifugation. The product was then washed with Milli-Q water during vacuum filtration, air dried at room temperature and calcined at 550 °C for 10 h.

SBA-15. SBA-15 was synthesized using a non-ionic surfactant as the structure-directing agent according to reported procedure [208, 209] as follows: 6 g of Amphiphilic difunctional block copolymer, (Mr=5750, EO₂₀PO₇₀EO₂₀, Pluronic P123, BASF) was dissolved in 45 g of deionized water and 180 g, 2 M hydrochloric acid solution (HCl, Fisher Scientific, 37%) with stirring. Then, 12.75 g of TEOS was added to the solution with stirring at 40 °C for 24 h. The homogeneous gel mixture was then transferred into a polymer flask, sealed and heated at 100 °C for 48 h. After filtration and washing with water, the white solid product recovered was air-dried

at room temperature for 24 h. The sample was then calcined in air by a ramp of 1 °C min⁻¹ to 500 °C and held for 10 h.

Co-MCM-48. The synthesis of cobalt incorporated MCM-48 (Co-MCM-18) used the same procedure as that used to prepare MCM-48 except that 0.47 g cobalt(II)nitrate hexahydrate ($\text{Co}(\text{NO}_3)_2 \cdot 6\text{H}_2\text{O}$, Acros Organics, 99%) was added before the addition of EtOH and NH_4OH .

Co-HMS. Cobalt modified HMS (Co-HMS) was prepared by following the same procedure used to prepare HMS except 0.291 g of $\text{Co}(\text{NO}_3)_2 \cdot 6\text{H}_2\text{O}$ was added before the addition of TEOS.

Co-SBA-15. Cobalt modified SBA-15 (Co-SBA-15) was prepared using the same procedure used to prepare SBA-15 except that that 1.866 g of $\text{Co}(\text{NO}_3)_2 \cdot 6\text{H}_2\text{O}$ was added with TEOS.

The synthesis of MCM-48, HMS, Co-MCM-48 and Co-HMS supports were performed by partner students at Bates College, Maine.

Conventional Mesoporous Silica. Two sources of commercial silica gel were also used as supports: silica gels from Qingdao Haiyang Chemical Ltd. (silica gel no. 775, 30-50 mesh, 300-700 μm particle size) and silica gel granules from Grace Davison (silica gel no. 646, 35-60 mesh).

2.2.2. Preparation of Supported Co Catalysts

Cobalt was introduced to all of the supports using wetness impregnation method where the required amount of $\text{Co}(\text{NO}_3)_2 \cdot 6\text{H}_2\text{O}$, to yield 9.1% Co nominal weight-loading in the final catalysts, was dissolved in excess of water and added to the support. The mixture was then left overnight at ambient temperature. After

impregnation, the samples were dried at 100 °C for 12 h, and subsequently calcined in flowing dry air by a ramp of 1 °C min⁻¹ to 500 °C and held for 5 h.

Data for the following catalysts are reported in this chapter: Co/MCM-41, Co/MCM-48, Co/Co-MCM-48, Co/HMS, Co/Co-HMS , Co/SBA-15, Co/Co-SBA-15, Co/silica gel no. 775, Co/silica gel no. 646, where the "/Co-XX" indicates cobalt incorporation into the framework.

2.2.3. Catalyst Characterization and Catalytic Testing

Overall, the supports have very similar chemical properties. Silica MCM-41 [210-212], MCM-48 [213], SBA-15 [214], and HMS [215] are minimally acidic, especially in comparison to alumina or alumina-doped supports. Silica gel has also been shown to be less acidic than HZSM-5 and tungsten-doped silica gels [216]. Incorporation of heteroatoms into a silica framework has been reported to increase thermal stability [217-220] and may also increase the acidity of the supports [201, 207].

Cobalt Content Analysis. Cobalt metal loading in the calcined catalysts was determined in-house (at Bates College) by ICP-OES or by Galbraith Laboratories using ICP-MS. Samples analyzed in-house were digested in a microwave digester using concentrated HNO₃ and HCl before analysis in a Perkin Elmer Optima 3000 XL. In-house results gave good agreement with those from Galbraith.

Nitrogen Porosimetry. Nitrogen sorption isotherms were measured at -196 °C using a Micromeritics ASAP-2020. Prior to analysis the samples were outgassed under vacuum. MCM-41 was outgassed at 350 °C for 10 h while all other

mesoporous silica supports and Co impregnated supports were outgassed at 250 °C for 8 h.

The surface area, pore size, pore volume, and micropore analyses were estimated using standard approaches. The BET specific surface area [221] was calculated using the adsorption branch of the nitrogen sorption isotherm in the relative pressure range of 0.05-0.25 (P/P_0), and the total pore volume was recorded at $P/P_0 = 0.995$. Pore size distributions were calculated via the adsorption branch of the nitrogen sorption isotherm using the BJH method [222], based on the Kelvin equation. However, the Kelvin equation and statistical film thickness curve used for analysis were modified by those reported by Kruk et al. [223] (Eq. 2.1 and 2.2 respectively):

$$r\left(\frac{P}{P_0}\right) = \frac{2\gamma V_L}{RT \ln\left(\frac{P}{P_0}\right)} + t\left(\frac{P}{P_0}\right) + 0.3nm \quad (2.1)$$

$$t\left(\frac{P}{P_0}\right) = 0.1 \left[\frac{60.65}{0.030701 - \log\left(\frac{P}{P_0}\right)} \right]^{0.3968} \quad (2.2)$$

Catalysts Treatment. Catalyst material properties are reported in this chapter in relation to three different stages in the catalyst history. This is done to gain insights into how these materials change in the presence of high temperatures and H₂ pressures, and in the course of catalyzing FTS:

- Stage 1 is the as-prepared catalyst after calcination in air.
- Stage 2 is after the catalysts were reduced in H₂ but prior to FT synthesis.
- Stage 3 is after Fischer-Tropsch synthesis.

All treatments were carried out in an Altamira AMI-200 R-HP catalyst characterization instrument. Typically, 100-200 mg of the catalyst (pressed and sieved to obtain 180-450 μm particle size) was supported between glass wool plugs in a ¼-in o.d. glass-lined, stainless steel reactor tube connected via Swagelock fittings. Gas and gas mixtures were fed to the reactor in an up-flow mode. The thermocouple probe is in contact with the top of the catalyst bed to control the reactor temperature.

For Stage 1, 200 mg of each catalyst was calcined in air at 500 °C for 5 h before characterization with XRD and BET. For Stage 2, 100 mg of catalyst was calcined in air at 500 °C for 5 h, followed by reduction in 10% H₂ in Ar (Matheson, certified mixture grade) at 500 °C for 5 h at atmospheric pressure. The sample was cooled down to ambient temperature in Ar (Boc Gases, Grade 5), and then characterized. Stage 3 of the catalyst history is described below.

Fischer-Tropsch Synthesis. The Fischer-Tropsch synthesis test was carried out in an Altamira AMI-200 R-HP characterization instrument. Prior to the catalytic tests, about 100 mg of catalyst was calcined in air at 500 °C for 5 h, followed by reduction in 10% H₂ in Ar at 500 °C for 5 h. The sample was cooled down to ambient temperature in Ar. The reactor was pressurized to 10 bar and the temperature was then ramped from ambient to 270 °C at a rate of 10 °C min⁻¹ under two independently controlled gas mixtures, 10% CO in He (Matheson, certified mixture grade) and 10 % H₂ in Ar (with a 1:2.1 mole ratio). The final conditions were maintained for 10 h, after which the reactor was cooled down to ambient temperature in the reactant gas mixtures (10%CO/He and 10%H₂/Ar). The product

stream was sampled through a 1m long 50 μ m ID capillary into a turbo-molecular pump station (AMATEK) and analyzed with an SRS RGA-300 Mass Spectrometer, which was interfaced with a computer. The moles of reactants consumed were calculated from the change in CO/He and H₂/Ar ratios, using the inert gases as internal standards (an example can be found in Appendix B). High flow rates of reactants were employed to decrease contact time which limited conversion to <10%. This was done to minimize heat and mass transfer effects in order to perform quantitative analysis of reaction rates. The conversion of CO typically increased over a period of several hours; the steady state reaction rates reported correspond to activity after 10 h on-stream. After reaction, separate portions of the catalysts were taken immediately for XRD measurement or stored in glass ampoules under vacuum for XANES measurements at the beamline.

X-Ray Diffraction. Wide angle θ - 2θ x-ray diffraction patterns for Co, CoO and Co₃O₄ phase identification and particle size determination were acquired at room temperature on a PANalytical X'PertPro X-Ray diffractometer utilizing Cu-K α radiation (45 kV, 40 mA) in a parallel beam optical configuration. The incident beam was focused in line mode through a 0.145 mm Ni automatic attenuator to reduce the intensity of the beam, a 1/2 $^\circ$ divergence slit to control the equatorial divergence of the beam, and a 15 mm beam mask to control the axial width of the beam following reflection off a parabolic W/Si mirror. To eliminate spurious lines and reduce the effect of sample fluorescence, the diffracted beam was directed sequentially through a 0.27 $^\circ$ parallel plate collimator, a 0.04 radian Söller slit assembly and a (002) graphite monochromator before reaching the proportional detector. The standard

scan parameters for Co_3O_4 (Stage 1) were to scan from 15 to $70^\circ 2\theta$ with a step size of 0.03° and a counting time of 1 s per step. For Co and CoO (determined at Stages 2 and 3, respectively) the samples were scanned from 30 to $160^\circ 2\theta$, with a step size of 0.03° and a counting time of 7 s per step. The powder catalyst samples (100 mg) were cast onto zero background single crystal quartz plates cut 6° off (001) as slurries in 2-propanol and, to avoid air oxidation, measured immediately following reduction or exposure to Fischer-Tropsch conditions. There was no evidence of initial oxidation of the catalysts during XRD measurements. However, if the catalysts were exposed to air for several days, slow oxidation of the cobalt was visible by XRD. This observation is consistent with other studies in which a surface wax product layer is thought to build up after several hours of FTS, protecting the cobalt particles from oxidation [224-226].

The instrumental contribution to line broadening was accounted for by measuring a LaB_6 standard (NIST SRM 660) from 20 - $140^\circ 2\theta$ using an identical optical configuration to that used for data collection on the catalyst samples, followed by Rietveld structural refinement on the entire spectrum using *EXPGUI* graphical interface for General Structural Analysis System (GSAS) package [227, 228]. In the GSAS program, the diffraction line positions and intensities are calculated directly from the unit cell and the lineshape accounts for particle size, strain, and preferential orientation effects. The contributions of the silica support to the diffraction pattern were accounted for by measuring wide angle XRD patterns of SBA-15, HMS and MCM-48 silica materials and using them as background by fitting the amorphous scattering with a non-linear function (a 12-term shifted Chebyshev

polynomial). The symmetry and lattice parameters of the phases analyzed are shown in Table 2.1. Further details on the Rietveld analysis used to obtain quantitative values of phase fractions and profile parameters are discussed in Appendix A.

Quantification of the relative amount of each phase present in the catalyst samples at Stages 2 and 3 were determined from XRD data. The peak intensity of the k^{th} line of phase α was calculated using $I_k = S_\alpha M_k L_k |F_k|^2$, where S_α is the scale factor for phase α , M_k is the multiplicity, L_k is the Lorentz Polarization Factor and F_k is the structure factor of the k^{th} diffraction line. The weight fraction of phase α was calculated using $W_\alpha = (S_\alpha Z_\alpha MW_\alpha V_\alpha) / \sum_i (S_i Z_i MW_i V_i)$ where S is the scale factor, Z is the number of formula units per unit cell, MW is the molecular weight and V is the unit cell volume. This method was validated by analyzing the ratio of Co_{hcp}/Co_{fcc} in a standard (Alfa-Aesar, 22 mesh, 99.9998%). Our results were in excellent agreement with the published ratio [229].

Quantitative XRD analysis allows us to determine both the particle size and relative amounts of each phase. It gives significantly different total surface areas from stage to stage in catalyst history; consequently, the calculated TOF varies significantly depending on the stage in catalyst history upon which the specific metal surface area is based.

Transmission Electron Microscopy and Selected Area Diffraction. Freshly prepared catalysts were examined using TEM and selected area diffraction (SAD) with a Phillips CM 10 microscope at 100 keV. Samples were ground and

electrostatically transferred onto carbon-coated grids. Images were recorded on Kodak 4489 electron image film.

Table 2.1 Phases analyzed at three stages of catalysts history and their structures and lattice parameters

Phases/Stages	Space Group	Lattice parameters/(Å)		
		<i>a</i>	<i>b</i>	<i>c</i>
Co ₃ O ₄ /Stage 1	<i>Fd-3m</i>	8.084	8.084	8.084
Co _{fcc} /Stages 2&3	<i>Fm-3m</i>	3.545	3.545	3.545
Co _{hcp} /Stages 2&3	<i>P63/mmc</i>	2.503	2.503	4.060
CoO/Stages 2&3	<i>Fm-3m</i>	4.260	4.260	4.260

X-Ray Absorption Spectroscopy (XAS). For the characterization of the local electronic structure of cobalt in the catalysts, synchrotron based x-ray absorption near edge spectroscopy (XANES) measurements were performed by Ben Goundie, Jeff Wright and Prof. R.W. Meulenberg. The XANES spectra were acquired at the bend magnet beamline 8-2 at the Stanford Synchrotron Radiation Laboratory. The powder catalyst samples were deposited on carbon tape onto a stainless steel sample holder. A consistent powder thickness was maintained from sample to sample. For analysis of post-temperature programmed reduction (TPR) or post-FT samples, the reacted materials were vacuum-sealed in an ampoule upon completion of the reaction. The vacuum-sealed samples were unpacked under ambient conditions at the synchrotron beamline, mounted onto carbon tape and immediately loaded into the UHV chamber. Total time of exposure to air was less than one minute (less than the time exposed to air during the XRD experiments). Experimental measurements were taken at base pressures of less than 5×10^{-9} torr. XAS experiments were conducted using the total electron yield (TEY) detection method where the total photocurrent is measured as the photon energy is scanned

through the absorption edges. All spectra are normalized to the photocurrent from a gold grid. The experimental energy resolution is ~ 0.15 eV at the cobalt L_3 -edge.

2.3. Results

2.3.1. Materials Characterization

Table 2.2 provides the characterization data of the silica supports used in this study. The surface areas of the support ranged 300-1400 $\text{m}^2 \text{g}^{-1}$ and the total pore volumes (TPV) ranged from 0.67-1.21 $\text{cm}^3 \text{g}^{-1}$. The primary pore diameters were estimated from the maximum in the BJH pore size distribution. For these support the primary pore diameter varied from 3.2-22 nm. After impregnation and calcination, the surface areas decreased.

Table 2.2 Nitrogen porosimetry data of support and supported catalysts

Sample	Silica Support (without cobalt)			Silica supported cobalt catalysts		
	S_{BET} (m^2/g)	TPV (cm^3/g)	d_{pore} (nm)	S_{BET} (m^2/g)	TPV (cm^3/g)	d_{pore} (nm)
Co/MCM-41	978	0.67	3.2	510	0.49	3.8
Co/MCM-48	1392	0.83	3.3	1152	0.62	3.1
Co/Co-MCM-48	941	0.71	3.5	495	0.49	2.9
Co/HMS	1001	1.31	4.6	783	0.88	4.3
Co/Co-HMS	515	0.63	3.8	431	0.62	3.7
Co/SBA-15	885	1.21	10.0	613	1.02	10.4
Co/Co-SBA-15	933	1.07	9.4	632	0.89	9.8
Co/silica gel no. 775	464	1.07	13.0	343	0.87	14.2
Co/silica gel no. 646	307	1.20	22.3	302	1.18	21.7

For particle size determination and phase identification, a detailed peak shape analysis of the XRD pattern was performed after all three stages of the catalyst history. These were done by Rietveld refinements of the scale factor, background coefficients, unit cell lattice constants and profile-function coefficients in GSAS. Atomic coordinates within the cell, site fractions, and thermal motion

parameters were kept fixed during the refinement. Effects of preferred orientation and shape anisotropy were significant in the hcp phase. For comparison with previous studies [175, 180, 230, 231], XRD patterns after air-calcination were measured to estimate Co_3O_4 particle size at Stage 1. Table 2.3 provides the particle size and dispersion of the cobalt metal, along with the percent reduction observed at Stage 2, to calculate specific surface areas that would be expected after reduction. The Co_3O_4 particle diameter was calculated from the GSAS fit to the XRD data. The cobalt metal particle size expected after reduction was calculated from Co_3O_4 particle size, ($d_{\text{Co}^0} = 0.75 \times d_{\text{Co}_3\text{O}_4}$) [177]. The cobalt metal particle diameter (d) was then used to calculate the dispersion using the relation $D(\%) = 96/d_{\text{Co}^0}(\text{nm})$ for spherical cobalt particles, assuming a site density of $14.6 \text{ atoms nm}^{-2}$ [177]. The dispersion values calculated from Stage 1 data were fairly constant for all the catalysts used in our study.

Table 2.3 Particle size of Co_3O_4 at Stage 1 and predicted metal diameter and dispersion of Co^0 after reduction

Catalyst	Particle Size (nm)		Percent Reduction (%) in Stage 2	Expected Dispersion (%)
	Co_3O_4	$\text{Co}(0)$		
Co/MCM-41	10.4	7.8	86.3	12.3
Co/MCM-48	4.8	3.6	28.4	26.6
Co/Co-MCM-48	30.9	23.2	53.9	4.1
Co/HMS	19.9	14.9	48.2	6.4
Co/Co-HMS	32.5	24.4	58.5	4.0
Co/SBA-15	10.0	7.5	83.4	12.9
Co/Co-SBA-15	14.9	11.1	78.5	8.6
Co/silica gel no. 775	12.4	9.3	96.4	10.4
Co/silica gel no. 646	17.9	13.5	94.7	7.1

Analysis of the XRD data after hydrogen reduction (pre-reaction Stage 2) and post-reaction (Stage 3) revealed the presence of two cobalt phases (Co_{fcc} and Co_{hcp}) as well as a CoO phase. The particle sizes of all the three phases after H_2 reduction and FT catalytic testing were determined from profile parameters after Rietveld refinement over the entire range of the XRD data. Fig. 2.1A shows the entire XRD pattern after FT testing of $\text{Co}/\text{Co-HMS}$ from 30 to $160^\circ 2\theta$ along with the Rietveld refinement fit and residuals. For CoO and Co_{fcc} , there was no significant particle size anisotropy or preferential orientation. For Co_{hcp} , refinement of both particle size anisotropy and preferential orientation parameters significantly improved the fit. For the Co_{hcp} particles, the dispersion was calculated from the components parallel, d_{\parallel} , and perpendicular, d_{\perp} , to the c axis of a cylindrical particle using the relation:

$$D_{\text{cyl}} = \frac{0.321d_{\perp}(\text{nm}) + 0.642d_{\parallel}(\text{nm})}{d_{\perp}(\text{nm}) \cdot d_{\parallel}(\text{nm})} \quad (2.3)$$

Figures 2.1B and 2.1C show expanded regions of the XRD patterns of Co/silica gel no. 646 and $\text{Co}/\text{SBA-15}$ taken after Stage 3. The fitted profiles for each individual phase are shown along with the sum to fit the entire diffraction data. For Co/silica gel no. 646, the intense peak at 44.3° corresponds to the Co_{fcc} phase; all of the fcc lines are narrow indicating relatively large particle sizes. The Co_{hcp} peak at 47.0° and all related hcp lines are substantially broader, indicating much smaller particle sizes. By contrast, in the $\text{Co}/\text{SBA-15}$, the broad Co_{hcp} peak at 47° is not as apparent, because it is so broad and is masked by the tails of the adjacent CoO and Co_{fcc} peaks.

The relative amounts of each phase in each supported catalyst at Stage 2 (also plotted in Fig. 2.2 against support pore diameter) are presented in Table 2.4. The relative amounts of Co_{hcp} and Co_{fcc} for the different supported catalysts at this stage show no relationship to pore diameter. Apart from the Co/MCM-41 catalyst, the CoO mole fraction decreases monotonically with pore diameter. Particle sizes and dispersion, calculated from the XRD data, are also given in Table 2.4. The Co_{hcp} particle size remains small and fairly constant while the Co_{fcc} particle size decreases with decreasing support pore diameter. The CoO particle size does not show a dependence on support pore diameter.

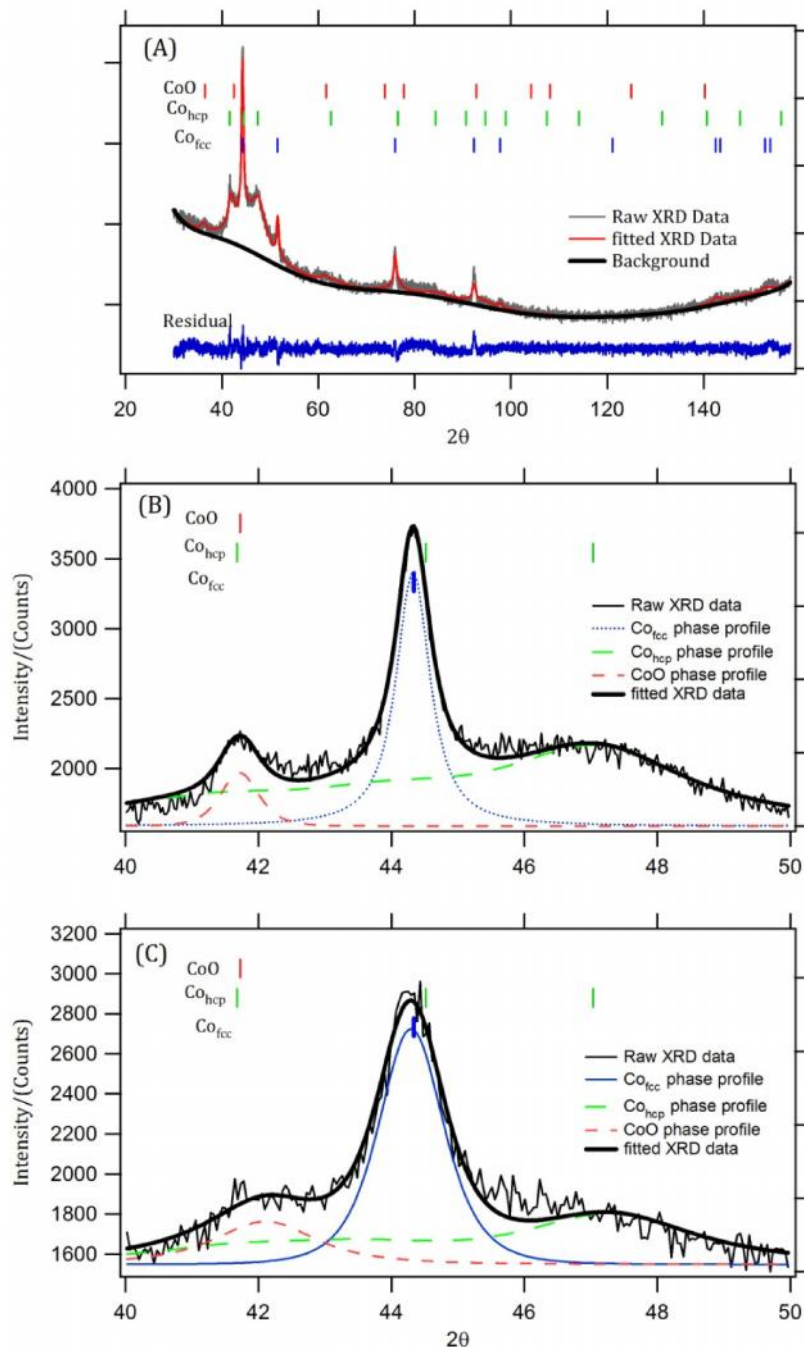


Figure 2.1 XRD patterns of selected catalysts after treatment. A) The full XRD pattern for Co/Co-HMS post FT, fit using Rietveld refinement of the three phases CoO, Co(hcp), and Co(fcc) and a Chebyshev background determined from the amorphous silica support, showing sharp Co(fcc) lines and broad CoO and Co(hcp) lines corresponding to smaller particles. Markers indicate the positions of lines unique to each phase. Expanded region showing the fcc, hcp and CoO lines for B) Co/Silica no. 646 and C) Co/SBA-15.

Table 2.4 Mole fractions, particle sizes, and dispersion of Co_{fcc} and Co_{hcp} for Stage 2

Catalyst	Mole Ratio			Particle Size (nm)				Dispersion (%)		
	FCC	HCP	CoO	FCC	HCP Co^0		CoO	FCC	HCP	Wtd
	Co^0	Co^0		Co^0	P_{\parallel}	P_{\perp}		Co^0	Co^0	Sum
Co/MCM-41	0.80	0.13	0.07	7.5	3.6	7.2	3.9	12.8	17.7	15.3
Co/MCM-48	0.20	0.08	0.72	4.7	1.2	4.4	6.6	20.4	41.7	26.8
Co/Co-MCM-48	0.24	0.30	0.46	29.8	1.2	4.2	5.2	3.2	42.2	24.8
Co/HMS	0.35	0.13	0.52	8.1	3.8	6.3	7.5	12.0	18.5	13.7
Co/Co-HMS	0.20	0.39	0.41	3.0	1.6	7.5	8.9	3.3	27.8	19.9
Co/SBA-15	0.21	0.63	0.17	8.2	4.0	8.3	8.9	11.7	15.8	14.8
Co/Co-SBA-15	0.07	0.72	0.21	9.4	1.4	4.1	8.1	10.2	39.4	37.7
Co/silica gel no. 775	0.68	0.28	0.04	9.5	3.8	6.6	9.5	10.1	18.1	12.4
Co/silica gel no. 646	0.45	0.50	0.05	22.0	3.7	6.2	7.8	4.3	19.0	12.0

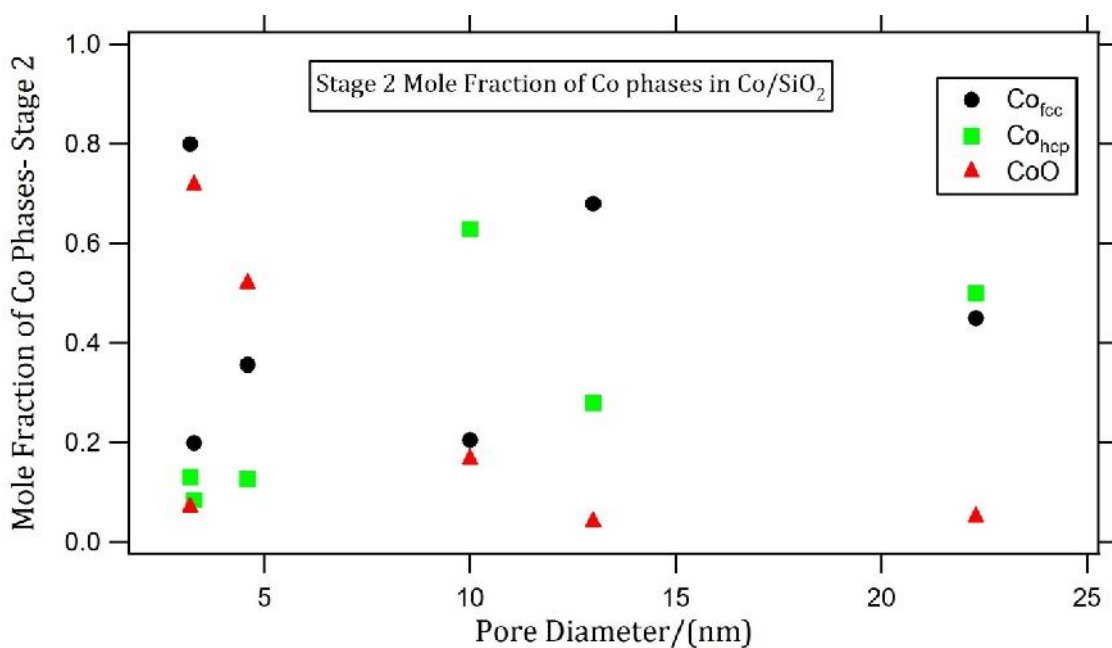
**Figure 2.2** Mole fraction of cobalt phases for catalysts after reduction in hydrogen (stage 2)

Table 2.5 shows the relative amounts of each phase in each supported catalyst at Stage 3. The relative amount of CoO present after 10 hrs under FTS conditions still generally decreases with increasing pore diameter. In the larger pore size catalysts, the relative amount of CoO decrease, while in the smaller pore diameter supports, it decrease. Figure 2.3 shows the expanded region of XRD data

showing the evolution of CoO. In this case, the CoO peak at 42° grows while the Co_{fcc} peak at 44.3° diminishes. The Co_{hcp} peak at 47° remains fairly constant. Although the mole fraction of CoO varies with pore diameter, the relative amounts of Co_{fcc} and Co_{hcp} do not show any clear dependence on the support pore diameter, as shown in Fig. 2.3. XRD data used to calculate particle sizes and dispersion at Stage 3 are given in Table 2.5 and shown in Fig. 2.4. Similar to the Stage 2 data, the Co_{hcp} particle size remains small and fairly constant while the Co_{fcc} particle size decreases with decreasing support pore diameter. The CoO particle size is also relatively insensitive to pore diameter and generally smaller than the Co_{fcc} particles. The Co_{hcp} and Co_{fcc} dispersion values are calculated from the particle sizes and mole fraction determined from the XRD data.

Table 2.5 Mole ratio, particle size and dispersion of Co_{fcc} and Co_{hcp} for Stage 3

Catalyst	Mole Ratio			Particle Size (nm)				Dispersion (%)		
	FCC Co ⁰	HCP Co ⁰	CoO	FCC Co ⁰	HCP P	Co ⁰ P _⊥	CoO	FCC Co ⁰	HCP Co ⁰	Wtd Sum
Co/MCM-41	0.31	0.54	0.15	6.7	3.4	5.4	8.4	14.4	21.5	18.9
Co/MCM-48	0.23	0.14	0.63	5.1	1.2	3.3	4.8	18.9	46.0	29.0
Co/Co-MCM-48	0.22	0.62	0.16	46.7	1.5	4.6	6.0	2.1	35.8	27.1
Co/HMS	0.41	0.14	0.45	6.7	3.0	6.3	5.5	14.4	21.0	16.1
Co/Co-HMS	0.20	0.77	0.03	2.8	1.9	10.5	7.2	3.4	23.5	19.3
Co/SBA-15	0.21	0.53	0.26	7.8	2.8	8.5	5.7	12.4	18.9	17.0
Co/Co-SBA-15	0.18	0.72	0.09	7.8	1.6	4.9	6.2	12.4	32.6	28.5
Co/silica gel no. 775	0.42	0.44	0.14	17.2	3.1	6.2	6.4	5.6	20.7	12.7
Co/silica gel no. 646	0.35	0.64	0.01	18.5	3.1	5.8	4.2	5.2	21.5	15.8

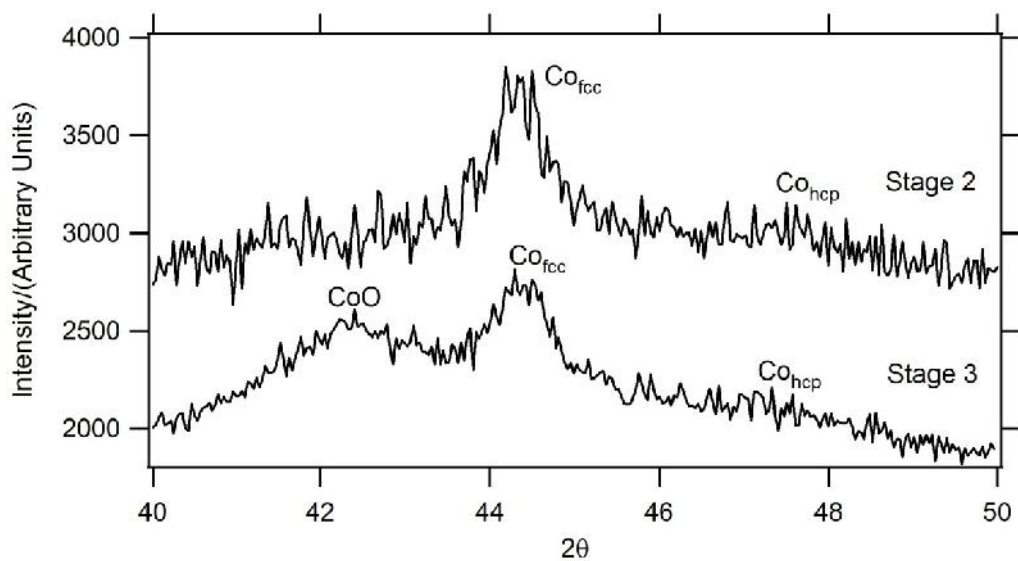


Figure 2.3 XRD pattern illustrating the increase in the amount of CoO before (Stage 2) and after (Stage 3) reaction under FTS conditions for the small pore diameter catalyst Co/MCM-41.

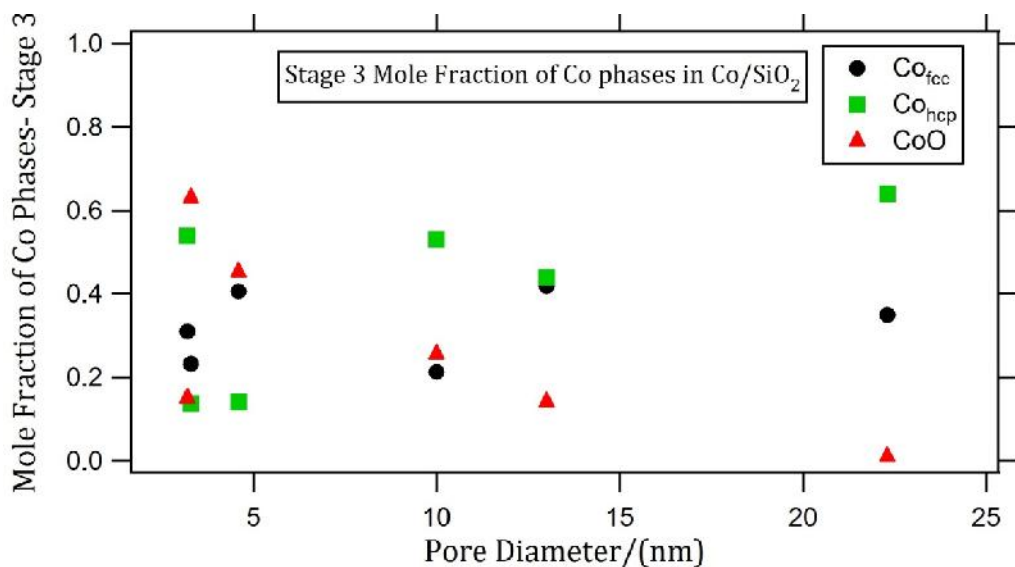


Figure 2.4 Mole fraction of cobalt phases for catalysts after reaction for 10 h in FTS (Stage 3).

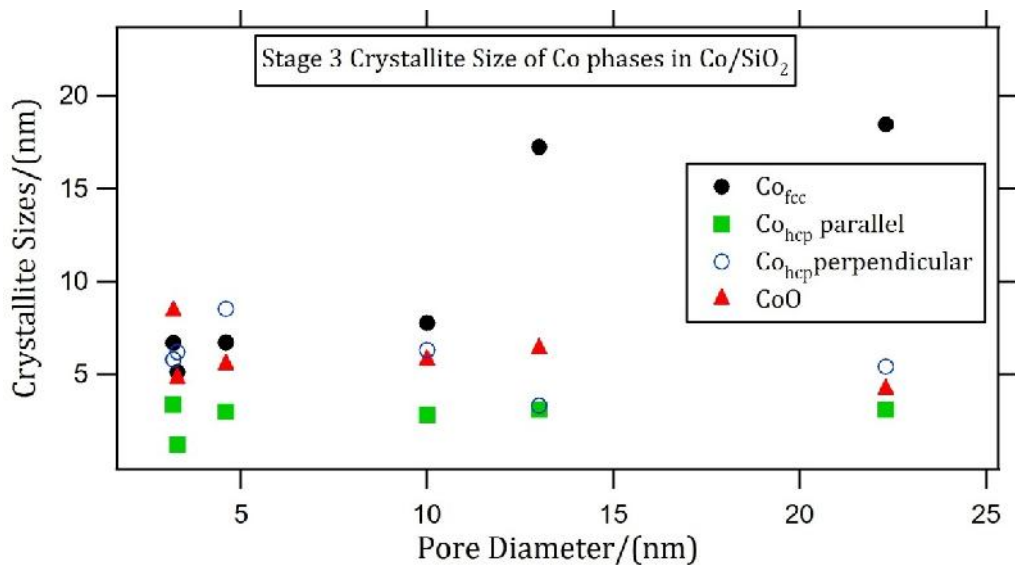


Figure 2.5 Crystallite size for catalysts from XRD Rietveld refinement of the indicated phases. The plot shows the small and constant size of Co_{hcp} particles while the size of Co_{fcc} particles increased with support pore diameter.

2.3.2. Transmission Electron Microscopy/Selected Area Diffraction

TEM measurements were made on the Co/silica gel no. 775 catalyst at Stage 2 and the data obtained from this technique supports the phases observed in the XRD data. Figure 2.6 shows a TEM image revealing darker striations suggesting the presence of cobalt within the pore structure, although individual particles could not be resolved. Analysis of the corresponding selected area diffraction pattern gave all of the major lines in XRD for the Co_{hcp} phase. The *d*-spacings correlated closely with those determined by XRD ($R^2=0.9992$). The diffraction patterns obtained were always identified as the hcp phase. Large metal particles or diffraction patterns associated with the fcc phase were not evident from the measurement, but the relative number of fcc particles should be small compared to the number of hcp particles.

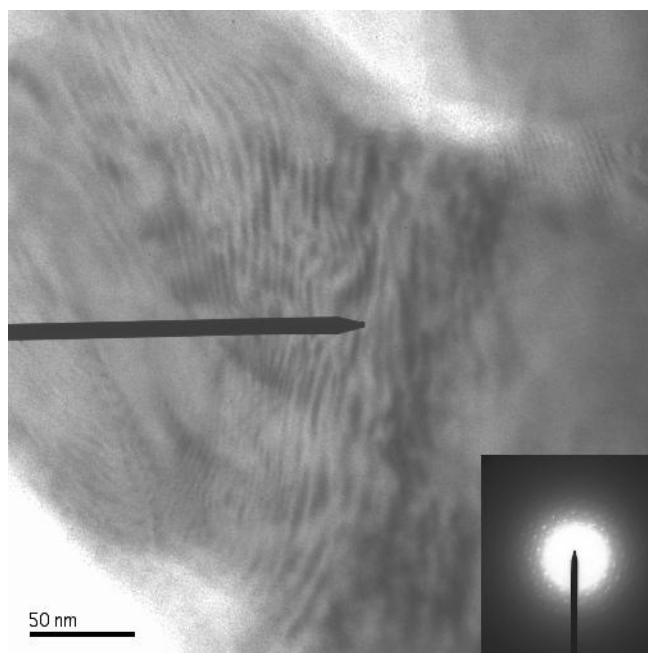


Figure 2.6 TEM image of a region of catalyst Co/silica no. 775 with the corresponding Co_{hcp} diffraction pattern.

2.3.3. X-Ray Absorption Spectroscopy

Because our XRD analysis only quantified the material in ordered crystalline cobalt phases, XANES measurements were made to provide complementary information regarding the presence of any additional amorphous cobalt species. Figure 2.7A displays Co $L_{3,2}$ -edge XANES spectra for a selection of catalysts at Stage 1. Irrespective of the support used, the data suggests that the cobalt species observed via XANES is Co_3O_4 , with little to no contribution from other cobalt species. In particular, there is no significant difference between the impregnated catalysts with and without cobalt in the framework. Selected area diffraction patterns in TEM also confirmed the Co_3O_4 phase.

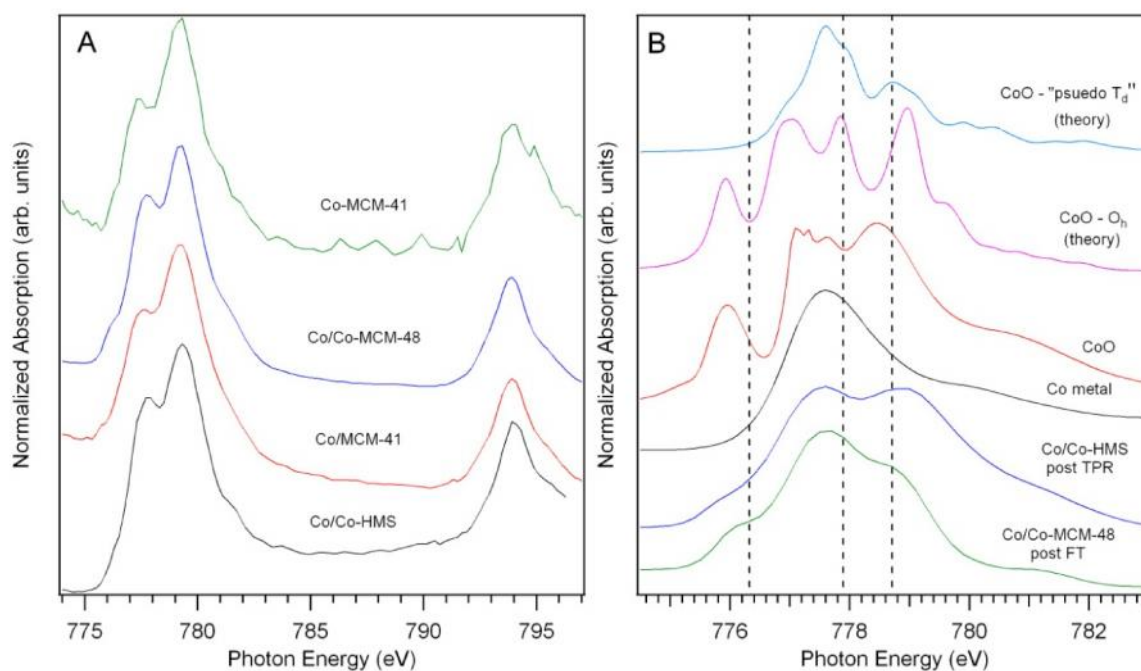


Figure 2.7 XANES spectra of cobalt for a selection of catalysts after calcination, reduction and FT reaction compared to reference and theory. (A) Cobalt $L_{3,2}$ - after calcination to Co_3O_4 and (B) cobalt L_3 -edge after reduction and FT reaction. All the spectra are normalized to unity at 777.6 eV (L_3 peak maximum for metallic cobalt). The spectra for metallic cobalt and CoO were taken from [232].

Figure 2.10B compares L_3 -edge XANES spectra for selected catalysts at Stages 2 and 3 with reference spectra and theoretical spectra. We expect the XANES data to be a linear combination of both metallic Co and CoO. The L_3 edge for the metal appears at 777.5 eV, while that for CoO is shifted to 779 eV with a pre-edge shoulder at 776 eV. The XANES spectra are qualitatively consistent with the XRD data analysis. For example, in the cobalt-HMS catalyst tested after reduction (Stage 2), a large peak appears at 779 eV which, when compared to the CoO standard, is in the energy range for CoO. The strength of this peak suggests a nearly equal amounts of both metallic Co and CoO were present in our samples, similar to what was observed via XRD (Table 2.4). XANES simulations for CoO in both octahedral and tetrahedral coordination environments [233-235] were undertaken to see if there

was any evidence for tetrahedrally-coordinated cobalt as might occur on surfaces. Fairly broad absorption edges in our samples were observed, which might reflect some cobalt oxide in a non-octahedral coordination environment.

2.3.4. Fischer-Tropsch Synthesis

The results of cobalt loading measured by inductively coupled plasma-mass spectrometry (ICP-MS), measured reaction rates, cobalt specific surface areas (assuming 14.6 Co atoms nm⁻²), and calculated turnover frequencies for each supported catalyst are shown in Table 2.6. The reaction rates decrease with decreasing support pore diameter as shown in Fig. 2.8.

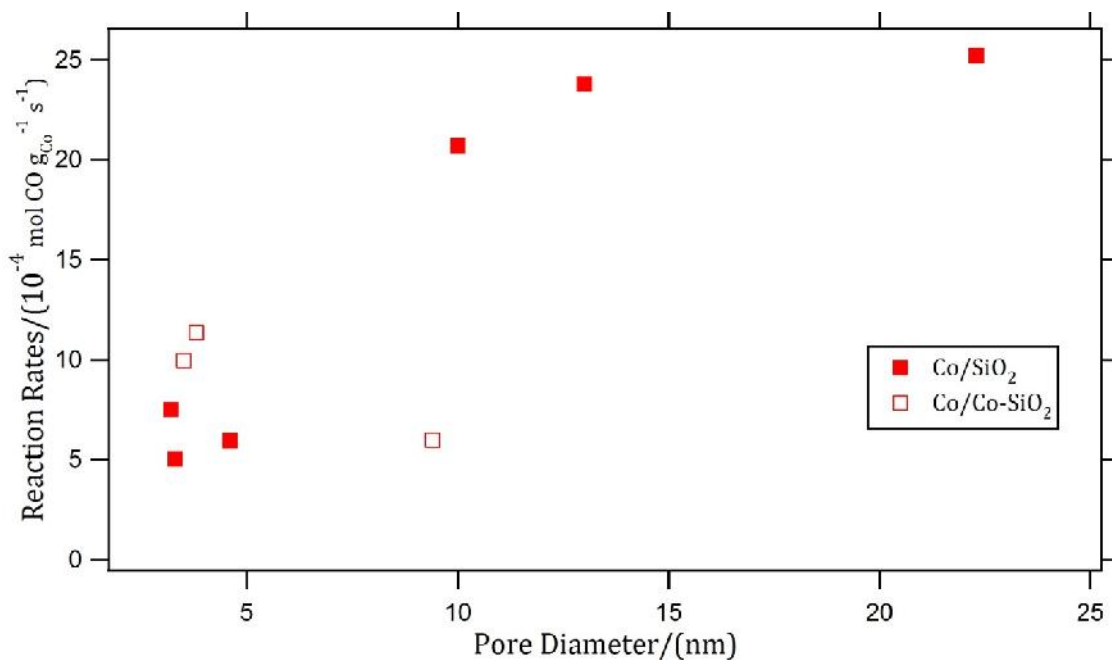


Figure 2.8 Measured activity for catalysts as a function of pore diameter

Table 2.6 Catalysts, metal loading, reaction rate, specific surface areas (SSA) at each stage, and TOF

Catalyst	ML [*]	RA [†]	Co Specific surface area (m ² /g)					TOF [‡]
			Co Stage 1	Co _{fcc} Stage 2	Co _{hcp} Stage 2	Co _{fcc} Stage 3	Co _{hcp} Stage 3	
Co/MCM-41	8.90	7.5	80	72	16	31	81	27.6
Co/MCM-48	7.50	5.04	52	29	23	30	45	27.7
Co/Co-MCM-48	8.25	9.95	15	5	89	3	155	25.9
Co/HMS	7.79	5.95	22	29	17	41	21	39.9
Co/Co-HMS	10.20	11.35	17	5	76	5	127	35.7
Co/SBA-15	9.38	20.7	76	17	70	18	70	99.1
Co/Co-SBA-15	10.10	5.97	48	5	199	16	164	13.7
Co/silica gel no. 775	9.11	23.8	70	48	35	16	64	139.7
Co/silica gel no. 646	9.06	25.2	47	14	67	13	96	95.2

2.4. Discussion

The relationships between reactivity and catalyst support pore structure [165, 174, 175, 183], cobalt particle size [181, 184, 185, 203], cobalt particle reducibility [174, 175], and transport properties [175, 236-238] have been discussed extensively in the literature. In this work, we note a correlation between the specific activity of the catalysts examined and their pore diameter. We also observe a significant amount of Co_{hcp} phase, consisting entirely of small cylindrical particles. Others have noted a relationship between pore diameter and CO conversion, frequently attributing it to the formation of larger, more easily reduced Co particles in larger pore materials [156, 175-178, 239], but also invoking mass transport limitations [175, 240] or CO adsorption properties [241]. To try to better understand the relationship between pore diameter and activity, we converted the specific activity data to turnover frequencies (TOF) by dividing the number of moles

* Metal Loading: (%)

† Reaction rates: (10⁻⁶ mol g_{Co}⁻¹ s⁻¹)

‡ Turnover frequency: (10⁻⁴ s⁻¹)

of carbon monoxide consumed by the number of surficial Co atoms and then examined the relationships between TOF and pore diameter, Co phase composition, and Co_{hcp} and Co_{fcc} particle size.

We utilized a three-phase system to determine the specific surface area of metallic cobalt in each catalyst, which was then used to calculate TOFs. After activation and reduction (Stage 2) and after FTS (Stage 3), the catalyst properties (particle size and extent of reduction) were determined by XRD. In both Stages 2 and 3 all three cobalt phases were identified: Co_{fcc} , Co_{hcp} and CoO. We rely, in our analysis, primarily on data from XRD, with complementary information from nitrogen porosimetry, TEM/SAD, and XANES. XRD provides clear information on crystallites and their sizes but does not provide information on non-crystalline particles. XANES, on the other hand, is a local probe of electronic structure and does not require crystalline order for a signal. Therefore, cobalt $L_{3,2}$ -edge XANES is a sensitive probe for analyzing non-crystalline cobalt species that may be present in our samples. XANES can also be used to qualitatively probe the level of reduction from Co_3O_4 to CoO and Co metal upon both TPR and FTS. Taken as a whole, the similarity in interpretations derived from our XRD and XANES measurements gives us confidence that relying on data from diffracting particles captures most of the cobalt chemistry occurring in these materials.

These results raise four key questions. First- how does the support pore size control the amount of CoO and the ease of reducibility of the Co_3O_4 catalyst precursor particles? Second - why are small hcp particles present and what impact do they have on the reactivity? Third – why are the turnover frequencies smaller in

materials with small pore diameters? In addressing these questions, we review published information on pore diameters, particle size, reducibility and reactivity as well as on particle size and hcp/fcc formation and reactivity and then offer additional comments based on the novel observations reported here.

2.4.1 Dependence of the Reducibility of CoO to Co on Particle Size

Smaller pore diameter supports show more CoO in both Stage 2 and Stage 3, with the striking exception of Co/MCM-41. While, oxidation has been postulated as a possible deactivation mechanism for FTS [175, 183, 224, 242], in our materials we believe the presence of high mole fractions of CoO reflects the materials' intransigence to reduction. In fact, from Stage 2 to Stage 3, the materials that had the highest mole fractions of CoO show reduction of CoO during FTS while materials that initially had less CoO show some oxidation. Formation of CoO between Stages 2 and 3 also correlates with the Co_{fcc} surface area: materials with more Co_{fcc} surface area in Stage 2 show an increase in mole fraction of CoO during FTS.

For small catalyst crystallites, particle size is known to alter the chemical equilibrium. As Co crystallites become smaller (i.e. ~ 10 nm), the contribution of surface energy to the chemical potential of the bulk material becomes significant, making reduction more difficult [243]. Additionally, for smaller pore diameter supports, diffusive effects may be important. Even at pressures of 7500 torr, as in our experiments, the Knudsen number (defined as $K_n = \lambda/d$ where λ is the mean free path of the gas molecule and d is the pore diameter) is approximately six, indicating a Knudsen diffusion regime. For Knudsen diffusion the diffusivity of a gas molecule scales with the root of molecular weight, thus $p_{\text{H}_2\text{O}}/p_{\text{H}_2}$ could increase by

a factor of three. Given these facts, it is plausible that nanosized Co_3O_4 particles in mesopores could be more difficult to reduce beyond CoO [174, 180]. Thus, the main trend in the mole fraction of CoO with pore diameter appears to be well explained by the size of clusters and the constraint of the pores. We see no evidence in the XANES data for non-crystallized cobalt silicate, whose presence has been postulated to decrease the reducibility of cobalt ions [166].

2.4.2. Relationship between Co_{fcc} and Co_{hcp} Phases

At room temperature, the hcp phase should be the preferred phase, but under our treatment and reaction conditions, metastable fcc particles commonly occur [189, 244]. Bulk cobalt metal undergoes a martensitic transformation, changing from hcp to fcc when heated above $420\text{ }^\circ\text{C}$ [189, 245]. For smaller particles, phase transformation becomes more difficult because the increased surface energy of hcp particles favors the fcc structure [189]. Experimental results indicated that Co_{fcc} particles as large as 200 nm remained stable upon cooling to room temperature [245]. In our catalysts we see Co_{fcc} particles with diameters less than 20 nm, consistent with calculations of Kitakami *et al.* [189]. However, we also find small Co_{hcp} particles after the $500\text{ }^\circ\text{C}$ reduction step, which is not predicted. These Co_{hcp} particles remain stable through both Stages 2 and 3. The Co_{hcp} particles could form upon heating up to the transition temperature in hydrogen (cobalt oxide reduction) and remain in the Co_{hcp} phase at elevated temperatures, stabilized by their environment. An alternative could be that the particles form as Co_{fcc} then transition to Co_{hcp} upon cooling and during FT reaction. In either case, we postulate that the environment surrounding the Co_{hcp} particles is energetically favorable for

stabilization. The driving force for the bulk transformation is small, $-16 \text{ J} \cdot \text{mol}^{-1}$, therefore it is plausible that subtle changes in environment could provide the required energy to stabilize a particular phase [245]. We note that the mole fraction of Co_{hcp} is particularly high in the MCM-41, suggesting that the environment stabilizes the hcp phase so strongly that it is even favored over the CoO phase, perhaps accounting for the low amount of CoO.

The highly reproducible particle shape anisotropy and preferential orientation is another indication that abnormally small Co_{hcp} particles are stabilized in the silica pores. The XRD analysis is consistent with disc-shaped particles (i.e. cylinders whose diameter is twice its height) which, in comparison to spherical particles, have a 21% increase in surface to volume ratio. Observation of preferential orientation suggests that the high index facets are in contact with pore walls in order to lower surface energies. The connection between Co_{hcp} stabilization and secondary meso/micropores in silica supports requires further investigation.

Prior work has suggested Co nanocrystals can contain hcp domains within a larger particle [187, 190, 246-248]. Our TEM data is inconsistent with that interpretation for the catalysts described in this chapter. We observe that the hcp particle size is relatively indifferent to the size of the fcc particles in the various materials synthesized, which also seems unlikely to be consistent with the interpretation that the hcp particles are embedded in larger fcc particles.

2.4.3. Relationship between TOF and Pore Diameter

The turnover frequencies were calculated using the cobalt loading, measured reaction rate at the end of the FT reaction, and a mole fraction weighted sum of the dispersions of each Co metal phase (Stage 3). There is a linear relationship between TOF and pore diameter up to a pore diameter of 13 nm, as shown in Fig. 2.9. At pore diameters larger than 13 nm, it appears that TOF is insensitive to pore diameter (see Fig. 2.9), or perhaps that it even decreases. This analysis suggests three possibilities: (1) the Co phase is intrinsically more active in the larger pore materials to the extent that larger pores contain larger metal particles, which have higher activity; (2) wide pore catalysts have more CO adsorption sites [241] or (3) the diffusion of reactants and products is faster with larger pore materials [249]. We favor the latter interpretation because the majority of the surface area comes from hcp particles, whose size doesn't vary much (Fig 2.5), and the amount of it shows no correlation with pore size (Fig. 2.5). The size of fcc particles does generally increase with pore diameter, but the mole fraction of fcc is similar in magnitude to that of the hcp. This data argues against a particle size effect. Iglesia et al. point out that CO diffusion can limit reaction rates for 1-3 mm particles [241] and that particles smaller than 200 microns are necessary to avoid diffusional limitations. Our particles range in size from 180-400 microns. However it is possible that a combination of factors contribute to the reactivity reported here. We note also that there is an inverse relationship between TOFs and surface area.

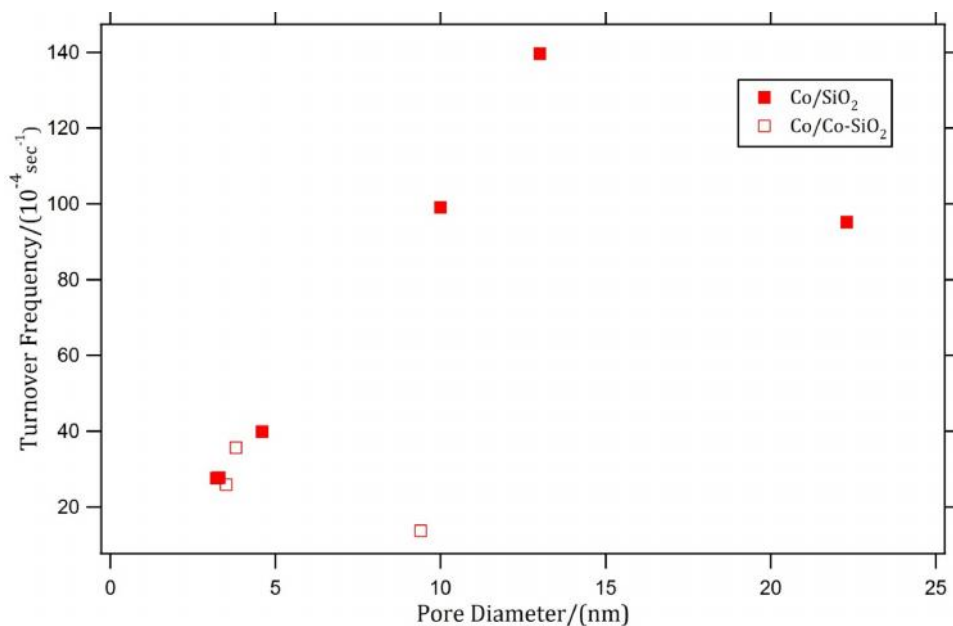


Figure 2.9 Plot of turnover frequencies vs. pore diameter.

A decrease in TOF below a critical particle size has been interpreted to mean that the reaction is sensitive to the structure of the cobalt metal, whereas if the TOF is independent of particle size then neither electronic effects nor defect sites affect the intrinsic reaction rate of the catalyst particle. In a number of FT studies, the TOF decreases below a particle size of about 8 nm [175, 184, 203]. Because our catalysts are comprised of two phases – a Co_{fcc} phase in which particle size does scale with pore diameter and a Co_{hcp} phase that is uniformly made up of small particles whose size does not vary with pore diameter – it is not surprising that there is no clear correlation between particle diameter and TOF. We plot TOF v. particle size for both the Co_{fcc} and Co_{hcp} particles (Fig. 2.10) and see no trend between TOF and the size of the Co_{hcp} particles. We do, however, see a correlation between Co_{fcc} particle size and TOF, but the Co_{fcc} particles make a small contribution to the overall surface area of metallic cobalt so it is unlikely that Co_{fcc} particles are determining reactivity. Rather

the relationship between Co_{fcc} particle size and TOF is likely to be simply a function of the fact that the Co_{fcc} particle size scales with pore diameter and pore diameters and TOFs are correlated.

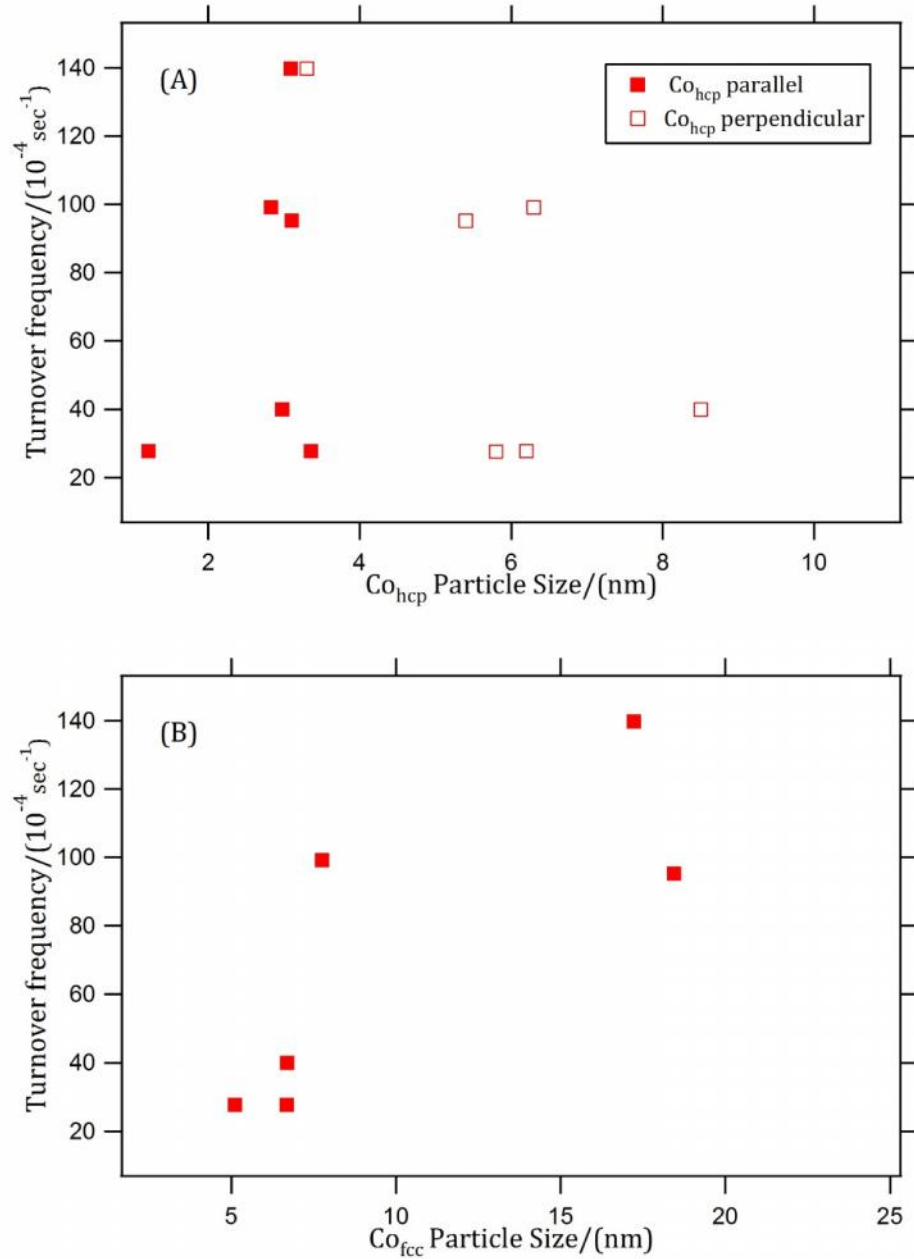


Figure 2.10 Turnover frequency as a function of Co particle sizes (A) Co_{hcp} particle size and (B) Co_{fcc} particle size

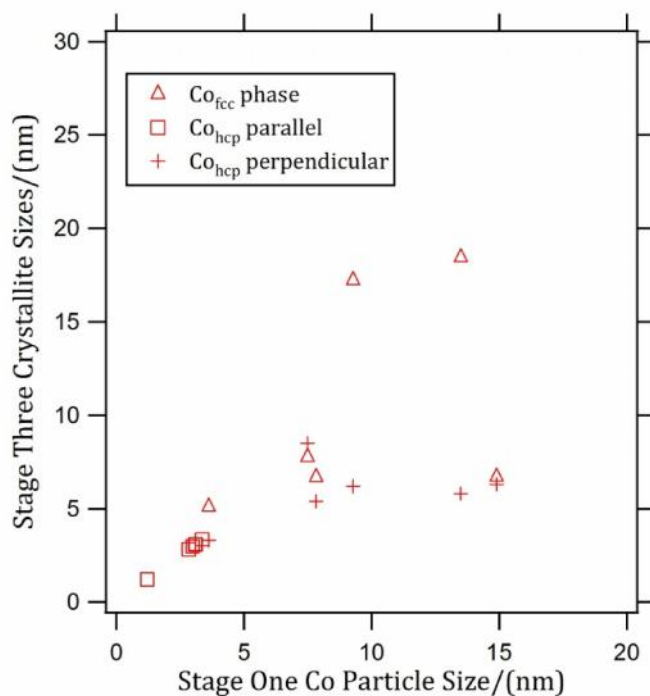
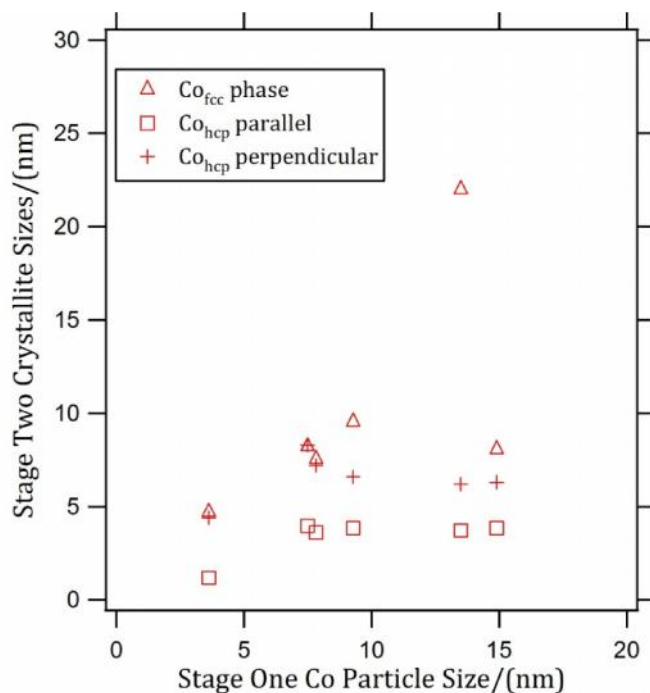


Figure 2.11 Relationship between Co metal particle size estimated from Co_3O_4 and particle sizes of fcc and hcp particles determined A) after reduction (Stage 2) or B) after FT synthesis (Stage 3). The plot shows that there is a strong correlation between Co_3O_4 particle size and Co_{fcc} particle size, but no correlation with Co_{hcp} size.

A number of groups have determined dispersion from either the Co_3O_4 particle size after calcination [175, 250] or the Co_{fcc} particle size after reduction or post reaction [190]. In Fig. 2.11, we plot the Co_{fcc} and Co_{hcp} particle sizes determined at Stages 2 and 3 from XRD against the particle size estimated from Co_3O_4 particles at Stage 1. Co_{fcc} and Co_3O_4 particle sizes are correlated but there is essentially no correlation between Co_{hcp} particle sizes and Co_3O_4 particles size estimates. The large mole fraction and high dispersion of the Co_{hcp} phase (dispersions of 20-50% in our catalysts) produces large hcp specific surface areas. If the hcp phase is as active as the fcc phase, then our specific surface areas would suggest that as much as 95% of the reaction could take place on the hcp phase. Thus, calculations of TOF that neglect the Co_{hcp} content and base dispersion on total (reduced) metal content and the Co_{fcc} dispersion (from XRD), could generate overly optimistic estimates of intrinsic reaction rates.

Annealing Co-containing materials at high temperature under a hydrogen atmosphere has been shown to change the cobalt dispersion [205]. Whether the particles become larger or smaller (as well as the extent of any phase changes) is likely to depend on the precise conditions of FTS. We provide evidence that both particle size and Co phases depend on treatment conditions [190]. Our data are consistent with a model in which small hcp particles can be stabilized in mesoporous materials, despite high thermal treatment and these small particles can, when present, contribute significantly to the total fraction of Co in a catalyst. Our data is also consistent with a model in which the Co_{fcc} particles also contribute to the catalytic activity. In some materials, a fraction of these particles may be on the

exterior surfaces of the silicas and not inside the pores, although our data shows no clear consequence of the presence of a small fraction of surface particles.

The post-reaction characterization of the materials shows a strong correlation between TOF and pore diameter (see Fig. 2.10). It seems likely that the larger pores (up to approximately 13 nm) facilitate diffusion of reactants and products, thereby speeding up reaction rates. Larger pores are also less prone to occlusion and oxidative inactivation.

2.5. Conclusion

We have synthesized and characterized silica supported cobalt catalysts with different pore diameters for evaluation in the Fischer-Tropsch reaction. Our characterization included determining detailed catalyst properties at three stages of catalyst history: (1) after the initial oxidation step to thermally decompose the catalyst precursor; (2) after the hydrogen reduction step to activate the catalyst; and (3) after FT reaction. The careful use of XRD analysis allowed the particle size of each Co phase, fcc and hcp, to be determined as well as the quantification of the amounts of each phase. The particle sizes of the Co_{fcc} decreased with decreasing support pore size whereas the particle size of Co_{hcp} remained constant and anisotropic in shape for Stages 2 and 3. The Co_{hcp} particle size was consistently smaller than the Co_{fcc} particle size. The CoO mole fraction is larger with smaller pore materials, indicating that those materials are more difficult to fully reduce. We find a very good correlation between pore diameter and TOF with a maximum TOF occurring at materials with a pore diameter around 13 nm.

CHAPTER 3

GUAIACOL HYDRODEOXYGENATION OVER UNSUPPORTED MOLYBDENUM-BASED NITRIDE CATALYSTS*

3.1. Introduction

Legislation stipulating increases in the production of fuels, chemicals and energy from renewable resources such as biomass have been passed by the United States and the European Union, owing to issues related to increases in total energy consumption, depletion of fossil fuels, and environmental concerns [4, 5, 22]. For that reason, processes for the transformation of biomass into fuels and value-added chemicals are being extensively investigated by researchers worldwide. Catalytic hydrodeoxygenation (HDO) is an important reaction, which partially or completely removes oxygenates from biomass-derived oil, or pyrolysis oil, in order to improve its fungibility as a fuel. For this reason, several HDO studies of model oxygenates observed in pyrolysis oils have been conducted to gain valuable insights into reaction mechanisms of different functional groups present in bio-oil, as well as the development of improved catalysts and processes.

Most HDO studies have been conducted over classical sulfided catalysts originally developed for hydrodesulfurization (HDS) and hydrodenitrogenation (HDN) reactions in petroleum refining processes. Despite the high activity of these catalysts for HDO of model compounds such as guaiacol, they require the addition of sulfur to the feed to prolong the catalyst lifetime, which leads to contamination of

* A portion of this chapter has been accepted for publication in *Applied Catalysis A: General*

products. Another principal disadvantage of sulfided catalysts is the high level of hydrogen consumption due to the consecutive transformation of guaiacol to catechol and to phenol. These limitations have led to the study of new active phases, which will eliminate the necessity to add a sulfur source to the feed, potentially consume less hydrogen, and lower the formation of coke by permitting the rapid conversion of guaiacol into phenol. Transition metal nitrides [251] and phosphides [70] have been identified as phases that show promising activities for HDO of guaiacol.

Bulk transition metal nitrides prepared from the temperature-programmed reaction of a metal oxide precursor and NH_3 [94] or N_2/H_2 mixtures [99] have compared favorably to traditional catalysts for HDS and HDN reactions [97, 148, 252]. However, only very few studies have been reported demonstrating the performance of bulk metal nitrides for HDO catalysis [145, 149]. In those previous HDO studies, the oxygen-containing model compound used was benzofuran, a representative compound of crude and coal-derived oil. To our knowledge, no common oxygenates present in bio-oil have been used to evaluate the efficacy of bulk nitride catalysts. Guaiacol (2-methoxyphenol) is an excellent model compound in HDO studies of bio-oil because of its low stability [28], and has been used to evaluate various catalytic systems such as metal sulfides and noble metals catalysts [49, 50, 60, 65, 68, 253, 254]. In this chapter, comparative examination of guaiacol HDO activities of bulk Mo nitrides with varying surface area are described. Specific activities (activity normalized to the surface area) of unsupported Mo nitrides prepared using different reducing/nitriding gases, as well as at two different space

velocities, were compared. The principal objective of the work in this study was to identify an optimal synthesis condition for Mo nitrides with respect to activities and selectivities. Furthermore, the addition of Co has been observed to enhance the activity of Mo-based bulk nitride catalysts for HDS [137] and HDN [112] reactions, as well as Mo sulfide catalysts for HDO reactions [49]. For this purpose, we synthesized cobalt-promoted molybdenum nitride and examined the effect of Co addition on metal nitride HDO activity and selectivity.

3.2. Experimental

3.2.1. Catalyst Preparation

Bulk molybdenum trioxide was prepared by thermally decomposing ammonium heptamolybdate (Fischer Scientific, AHM, $(\text{NH}_4)_6\text{Mo}_7\text{O}_{24}\cdot 4\text{H}_2\text{O}$, A.C.S. grade) in a flow of dry air at 500 °C for 4 h with a heating rate of 1 °C min⁻¹. The bimetallic oxide precursor was prepared following a procedure similar to one reported by Korlann et al. [124] by adding an aqueous solution of cobalt (II) nitrate hexahydrate (Acros Organics, $\text{Co}(\text{NO}_3)_2\cdot 6\text{H}_2\text{O}$, 99%, 16.472 g, 100 mL of H₂O) dropwise to a second solution consisting of AHM dissolved in deionized water (10 g, 80 mL of H₂O) under stirring. This was done to obtain a 1:1 Co/Mo mole ratio. The solution was vaporized to dryness in a water bath, and a purple, solid precipitate was collected by vacuum filtration. The product was rinsed with two washings of water followed by a single washing with ethanol. The solid was dried overnight at 120 °C and calcined in air at 500 °C for 4 h with a heating rate of 1 °C min⁻¹.

Molybdenum nitrides were prepared following previously reported procedures by flowing NH₃ (Matheson, 99.99%) [94] or N₂/H₂ mixtures (N₂, BOC

Gases, Grade 5; H₂, Matheson, 99.99%) [99] over the sample. The experimental set-up included a 10 mm i.d. × 12 mm o.d. × 1 m long quartz reactor fitted with a quartz wool plug. The reactor tube was placed inside a MELLEN tubular resistance furnace. The temperature was monitored using a chromel-alumel thermocouple which was controlled by a programmable temperature controller (Omega Series CN- 4321) connected to the furnace. High purity gases were connected to the reactor via stainless steel tubings. The gas flow rates were controlled using needle valves and measured with a soap bubble flow meter. For a typical synthesis, the reactor loaded with 4 g of the oxidic precursor was purged with nitrogen prior to nitridation for 30 min and switched to NH₃ or N₂/H₂ mixtures (N₂/H₂ = 5/1 (v/v)). The temperature was linearly increased from ambient temperature to 300 °C within 30 min (9.33 °C min⁻¹), then from 300 °C to 500 °C by a heating rate of 0.6 °C min⁻¹, and from 500 °C to 700 °C by a heating rate of 2 °C min⁻¹. Then, the temperature was maintained at 700 °C for another 2 h. The nitrides prepared using NH₃ were cooled down to room temperature using the same flow rate of NH₃, while the nitrides prepared using the N₂/H₂ mixtures were cooled down in N₂. The materials were then passivated in 1% O₂/N₂ (Boc Gases, UHP grade) for 12 h at room temperature to avoid violent oxidation upon exposure to air. The monometallic nitrides were either prepared with molar hourly space velocities (MHSV) of 19 and 29 h⁻¹ and the bimetallic nitride was prepared with an NH₃ MHSV of 29 h⁻¹. For notation, Mo nitrides prepared using ammonia have suffix "A", while nitrides prepared using N₂/H₂ mixture has suffix "NH". For example, MoN-A-i and MoN-A-ii are molybdenum nitrides prepared via ammonolysis using MHSV of 19 and 29 hr⁻¹, respectively.

3.2.2. Catalyst Characterization

X-ray diffraction (XRD). XRD patterns of powdered samples were recorded on a PANalytical X'Pert PRO X-ray diffractometer equipped with a graphite monochromator and $\text{CuK}\alpha$ radiation (45 kV, 40 mA) in a parallel beam optical geometry. The standard scan parameters were $15\text{-}85^\circ 2\theta$ with a step size of 0.02° and a counting time of 1 s per step for bulk metal oxides and 10 s per step for bulk nitrides. Identification of the phases was achieved by reference to JCPDS diffraction file data. Details of the XRD instrumental set-up are given in Chapter 2.

BET surface area. Nitrogen adsorption/desorption isotherms were measured at 77 K using Micromeritics ASAP-2020 instrument to determine the BET specific surface area (S_{BET}). Prior to the analysis, the samples were degassed at 200°C for 2 h.

Elemental analysis. Metal and nitrogen contents in the Mo nitride samples were determined by the Analytical Laboratory of the Department of Plant, Soil and Environmental Sciences at the University of Maine or by Galbraith Laboratory using ICP-AES for the metal analysis and combustion method for the nitrogen analysis.

3.2.3. Catalyst Activities

Prior to catalytic testing, the passivated samples were activated *ex situ*, under a flow of H_2 (AGA Chile, 99.99%) at atmospheric pressure, in a vertical Pyrex reactor tube (6.4 mm i.d. and 25 cm long) placed inside a programmable furnace. Hydrogen, flowing at 60 mL min^{-1} (at STP), was passed over approximately 0.35 g of the passivated catalyst, while the temperature of the system was increased from room temperature to 450°C at a heating rate of $10^\circ\text{C min}^{-1}$. The temperature was

maintained at 450 °C for 6 h and subsequently cooled down to room temperature under N₂ flow (AGA Chile, Grade 5).

All HDO experiments were carried out in a 300 mL stainless steel batch autoclave (Parr Model 4841) operated at 300 °C and under a H₂ pressure of 5 MPa. A schematic of the reaction set-up is shown in Fig. 3.1. The reactor was equipped with a magnetic drive stirrer and a heating plate which were both controlled by a Parr Model 4841 reactor controller. The magnetic stirrer was set at 1000 rpm during catalytic testing to ensure good stirring. The heating plate was placed around the reactor together with a jacket to ensure isothermal conditions. A thermocouple placed inside a thermowell was used to measure the internal temperature of the reactant solution. About 0.25 g of freshly pretreated catalyst was added to the reactor, charged with 80 mL decalin (Merck, 99.5 %), 2.53 mL guaiacol (0.232 mol L⁻¹, Merck, 99%), and 700 μL of hexadecane (Merck, 99%) as internal standard for quantitative GC analysis. The sealed reactor was flushed with nitrogen to evacuate air from the system by pressurization-depressurization cycles. While continuously stirring the mixture, the reactor was heated to 300 °C under N₂. Once the reaction temperature was attained, N₂ was replaced with H₂ and then pressurized to 5 MPa. This pressure was maintained for the entire duration of the experiment by adding H₂ to the reactor whenever necessary. Samples were periodically withdrawn from the reactor through a $\frac{1}{16}$ -in. diameter tube (incorporated with a stainless steel filter at one end) after the sampling line has been purged with small amounts of the reactant mixture. The liquid samples were collected in sealed septum vials and analyzed using a Perkin Elmer (Clarus 400) gas chromatograph equipped with a

flame ionization detector (FID) and a CP-Sil 5 CB column (Agilent, 30 m × 0.53 mm × 1.0 μm film thickness). The injector and FID were held at 275 °C and 180 °C respectively. The GC oven program consisted of an initial isothermal operation at 30 °C for 6 min, followed by a heating rate of 30 °C min⁻¹ to 70 °C which was held for 22 min, and a subsequent heating rate of 30 °C min⁻¹ to 275 °C. The product distributions were identified by their column retention time in comparison with available standards at the same conditions. The concentration of guaiacol at the start of the reaction was taken as 100% in order to ignore small conversion due to heating of the system. The catalytic activity was expressed by the initial reaction rate which was calculated from the slopes of the conversion vs. reaction time plot, assuming pseudo first order kinetic expression as shown in Eq. 3.1 [54], and by the intrinsic activity (i.e. the reaction rates per unit area). The phenol/catechol ratios were determined at 10 % conversion of guaiacol to exclude contributions from internal and external mass transfers. A number of repeated runs under the same conditions were performed to ensure satisfactory reproducibility of the data. The uncertainty in the calculation of reaction rates from GC peaks is 3 %.

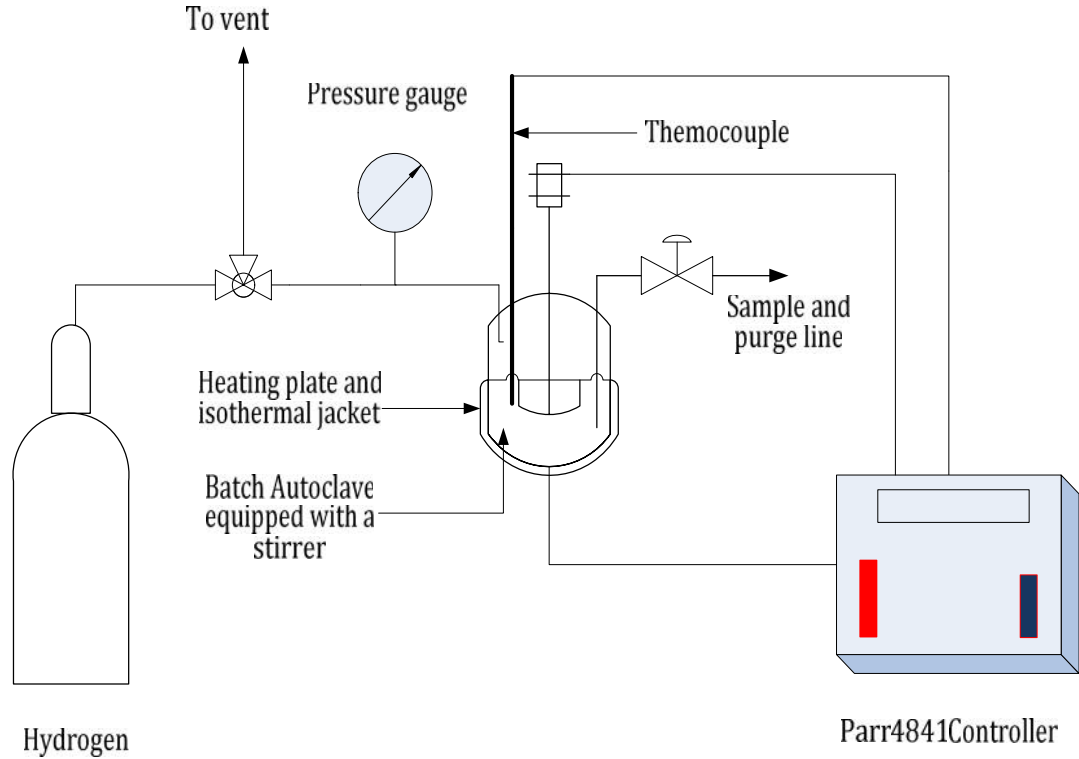


Figure 3.1 Experimental setup

$$-\ln \frac{C_i}{C_0} = kWt \quad (3.1)$$

where C_i and C_0 are the concentration of the reactant in sample i and at time zero of the reaction, k is the rate constant in $\text{min}^{-1} \text{g}_{\text{catalyst}}^{-1}$, W is the weight of the catalyst in g and t is the time of the reaction in min. From equation 3.1 the reaction rate R_{rates} in $\text{mol min}^{-1} \text{g}_{\text{catalyst}}^{-1}$ can be expressed by:

$$R_{\text{rates}} = n_{\text{guaiacol},0} \left[\frac{\Delta \left(\frac{-\ln X_i}{W} \right)}{\Delta t} \right] \quad (3.2)$$

where $n_{\text{guaiacol},0}$ is the initial moles of guaiacol in the reactant solution and $\Delta \left(\frac{-\ln X_i}{W} \right) / \Delta t$ is the initial slope from the first-order logarithmic plot (where X_i is the

conversion in sample *i*). The reaction rate was calculated from the initial reaction (at low conversion) of the transformation of guaiacol because of deviations from a first order kinetic occurring at higher conversions [54].

3.3. Results and Discussion

3.3.1. Catalyst Preparation and Characterization

Wide-angle XRD patterns for bulk molybdates, pre-and post nitridation, are shown in Fig 3.2. The patterns obtained were compared to JCPDS data files for phase identification (MoO_3 : 35-0609, $\gamma\text{-Mo}_2\text{N}$: 25-1366, $\beta\text{-Mo}_2\text{N}_{0.78}$: 25-1368, MoO_2 : 32-0671, Mo: 42-1120, $\beta\text{-CoMoO}_4$: 021-0868, $\text{Co}_3\text{Mo}_3\text{N}$: 04 008 1301). The MoO_3 phase was observed for the bulk Mo oxide precursor samples. The result presented indicated a complete thermal decomposition in air of AHM to MoO_3 . XRD patterns of the bulk nitrides indicated that the nitridation procedure affected the phases present in the final metal nitride catalyst. XRD patterns of the MoN-A-i and MoN-A-ii catalysts revealed characteristic peaks of $\gamma\text{-Mo}_2\text{N}$ ($2\theta = 37.25, 43.37, 63.11, 75.65,$ and 79.69). However, the diffraction patterns of the MoN-A-i catalyst also exhibited crystalline MoO_2 peaks ($2\theta = 26.03, 53.45,$ and 66.63), indicating incomplete nitridation. The XRD patterns of the MoN-NH-i catalyst revealed peaks that corresponded to $\beta\text{-Mo}_2\text{N}_{0.78}$ ($2\theta = 37.57, 43.09, 45.03, 62.45, 64.05, 75.35, 78.17,$ and 80.23). The $\beta\text{-Mo}_2\text{N}_{0.78}$ phase is a tetragonal Mo nitride phase which results from the transformation of $\gamma\text{-Mo}_2\text{N}$ [105]. The formation of the $\beta\text{-Mo}_2\text{N}_{0.78}$ phase in MoN-NH-i was consistent with work published by Gong et al. [100] who reported the synthesis of $\beta\text{-Mo}_2\text{N}_{0.78}$ under similar synthesis conditions. Nagai and co-workers [101] also reported the synthesis of bulk $\beta\text{-Mo}_2\text{N}_{0.78}$ when they cooled NH_3 -nitrided products in

He to room temperature prior to passivation. However, the diffraction pattern of the MoN-NH-ii catalyst revealed the additional presence of MoO₂ (2 θ = 26.03, 31.79, 37.39, 41.45, 41.97, 49.51, 53.11, 53.57, 53.99, 60.57, 66.67, 67.75, 72.53, and 78.71), Mo metal (2 θ = 40.51, 73.41), and γ -Mo₂N (2 θ = 37.09, 43.45, 63.23, 75.45, and 79.75) phases. According to Choi et al. [93], MoO₂ and Mo metal are potential reaction intermediates to produce low surface area Mo nitride material. Thus, the XRD result of MoN-NH-ii suggests incomplete conversion of MoO₃ to γ -Mo₂N.

Thermal decomposition of the cobalt molybdate precursor in air formed MoO₃ and β -CoMoO₄ phases, as observed by XRD. Although the theoretical Co/Mo ratio for the CoMo oxide is 1, there was no evidence by XRD of Co₃O₄. Peak locations and relative intensities of the XRD pattern of the CoMoN-A catalyst revealed the presence of Co₃Mo₃N (2 θ = 32.29, 35.51, 40.05, 42.57, 46.53, 49.49, 55.21, 59.83, 64.93, 69.79, 72.77) and γ -Mo₂N (2 θ = 37.37, 43.37, 63.09, 75.67, 79.51). Given that monometallic and bimetallic oxides are precursors for monometallic and bimetallic nitrides respectively, the presence of both γ -Mo₂N and Co₃Mo₃N in the CoMoN-A catalyst could have been due to the direct transformation of MoO₃ and β -CoMoO₄ during temperature-programmed reaction with NH₃.

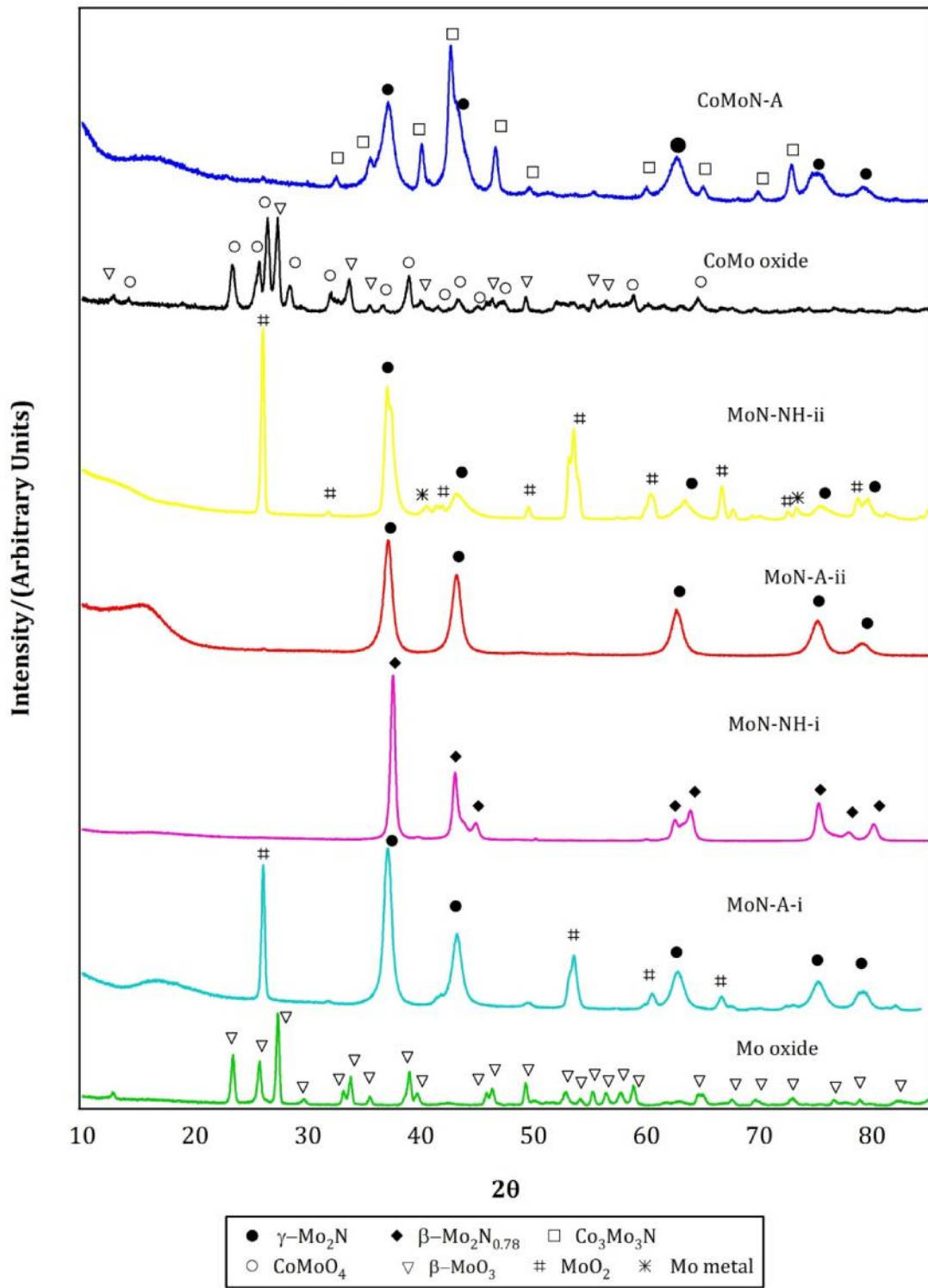


Figure 3.2 XRD of bulk oxides and nitrides

Crystallite sizes of the different molybdenum crystal phases of bulk Mo nitrides calculated from peak widths using the Scherrer equation are presented in Table 3.1. The full width at half-maximum (FWHM) data was corrected for instrumental contribution to the line broadening by using Warren's formula ($\beta^2 = B^2 - b_0^2$), where B is FWHM of the measured peak, b_0 is the FWHM of LaB₆ standard (NIST SRM 660) interpolated to the angle of interest, and β is the corrected FWHM. The calculated particle diameter of Mo₂N in the samples ranged from 5.7 to 9.3 nm, while the MoO₂ present in MoN-A-i and MoN-NH-ii had much larger crystallite sizes of 43.3 nm and 78.6 nm, respectively. Crystallite sizes of 21.2 nm were calculated for the Co₃Mo₃N phase present in CoMoN-A catalyst.

Table 3.1. Crystallite sizes of bulk different phases present in bulk nitride catalysts

Sample	Space Velocity (h ⁻¹)	Crystallite size (nm)				
		γ -Mo ₂ N (200)	β -Mo ₂ N _{0.78} (200)	MoO ₂ (111)	Mo (110)	Co ₃ Mo ₃ N (411)
MoN-A-i	19	5.7	-	43.3	-	-
MoN-A-ii	29	9.3	-	-	-	-
MoN-NH-i	19	-	29.3	-	-	-
MoN-NH-ii	29	6.2	-	78.6	13.8	-
CoMoN-A	29	7.1	-	-	-	21.2

The elemental analysis of passivated Mo nitrides is shown in Table 3.2. The catalyst containing the highest atomic N/Mo was also comprised of single phase γ -Mo₂N. The catalyst containing the lowest atomic N/Mo contained oxides and molybdenum metal in addition to the metal nitride. While the theoretical N/Mo is 0.5 for γ -Mo₂N, it is plausible that excess N could reside in interstitial sites and defects like grain boundaries.

Table 3.2 Chemical composition of bulk Mo nitrides

Catalyst	Elemental Analysis (wt %)		N/Mo atomic ratio	
	Mo	N	Actual	Theoretical
MoN-A-i	67.10	6.24	0.64	<0.5
MoN-A-ii	76.20	9.62	0.86	0.5
MoN-NH-i	79.40	6.63	0.57	0.39
MoN-NH-ii	93.20	3.16	0.23	<<0.5

The BET surface areas of the passivated nitride catalysts are summarized in Table 3.3. Comparison of bulk oxidic precursors and corresponding nitrides shows a significant increase in textural properties after nitridation. The BET surface area of the bulk Mo oxide precursor was $2 \text{ m}^2 \text{ g}^{-1}$, while the corresponding nitrides ranged from 9 to $115 \text{ m}^2 \text{ g}^{-1}$. The BET surface area of the bulk Co-Mo oxide precursor and the corresponding bulk Co-Mo nitride were $17 \text{ m}^2 \text{ g}^{-1}$ and $50 \text{ m}^2 \text{ g}^{-1}$, respectively. The significant increase in surface area upon nitridation may be due to an increase in density during the transformation of the oxide to the nitride, which caused the evolution of cracks [93]. Differences in surface areas of individual catalysts can be attributed to differences in synthesis parameters including nitridation gas, temperature profile, and gas space velocity [93]. A model, based on reaction pathways from the oxide to nitride, has been proposed by Choi, et al. to explain the effect of synthesis conditions on the surface area of nitrides [93].

3.3.2. Catalyst Activity Measurements

The evolution of the transformation of guaiacol and the yield of products for the unsupported nitride catalysts are shown in Fig. 3.3. The products formed from the reaction over all the catalysts were similar, with guaiacol yielding principally phenol. Minor amounts of catechol, benzene, cyclohexene and cyclohexane were

also detected, with the deoxygenated products appearing at longer reaction times. The variation of the reactant and products with time can be explained by the schematic in Fig. 3.4. On the basis of this reaction scheme, the majority of the reaction proceeded through the direct demethoxylation route (DMO) to form phenol via hydrogenolysis of the aromatic carbon-oxygen bond. The second reaction pathway involved hydrogenolysis of the O-CH₃ bond (demethylation route, DME) on guaiacol to form catechol, which was then transformed to phenol. Continuous production of catechol, as evident in Fig. 3.3, indicated that the conversion of catechol to phenol was not prominent over the time scale used in this study, consistent with our earlier work [251]. Therefore, the demethylation pathway appeared to be the minor route to phenol production.

The reaction rate results of the nitride catalysts for guaiacol conversion are summarized in Table 3.3. Intrinsic activities normalized to molybdenum content and S_{BET} are also shown in Table 3.3. It can be seen from Table 3.3 that the MoN-A-ii and MoN-NH-ii catalysts displayed higher intrinsic activities and total reaction rates than the MoN-A-i and MoN-NH-i catalysts, respectively. Table 3.3 also shows a certain level of structure-sensitivity, with lower surface area catalysts having higher intrinsic activities. However, the change in the reaction rate is not proportional to the surface area of the catalyst, suggesting that the conversion of guaiacol is not directly dependent of the BET surface area and the Mo content of the catalysts. In other words, the changes in the conversion of guaiacol observed in Table 3.3 are not due to an increase in the active sites produced by an increase in the specific surface

area or Mo content. These results suggest that the conversion of guaiacol depends on the different phases present in the unsupported catalysts.

The catalyst with the highest reaction rate for guaiacol conversion was MoN-A-ii. This catalyst had the highest atomic N/Mo and consisted of single-phase γ - Mo_2N , as determined by XRD. The MoN-A-i catalyst contained predominantly γ - Mo_2N and some unconverted molybdenum oxide, which resulted in a slightly lower reaction rate. The MoN-NH-i catalyst contained β - $\text{Mo}_2\text{N}_{0.78}$ suggesting that this phase of molybdenum nitride is less active than the gamma phase for hydrodeoxygenation (demethoxylation). The MoN-NH-ii catalyst contained significant impurities of molybdenum oxide and molybdenum metal which could have resulted in a relatively lower reaction rate. Our data is consistent with Nagai et al. [101] who demonstrated that the C-N hydrogenolysis activity decreased according to the order γ - $\text{Mo}_2\text{N} > \beta$ - $\text{Mo}_2\text{N}_{0.78} \gg \text{Mo}$ metal.

Table 3.3. Catalytic activity of Unsupported Mo nitrides

Catalyst	S_{BET} ($\text{m}^2 \text{g}^{-1}$)	Reaction Rate $\left(\begin{array}{c} \times 10^6 \\ \text{mol} \cdot \text{g}_{\text{catalyst}}^{-1} \cdot \text{s}^{-1} \end{array} \right)$	Intrinsic Activity	
			Reaction Rate/Mo atoms $\left(\begin{array}{c} \times 10^4 \\ \text{molec. Moat}^{-1} \text{s}^{-1} \end{array} \right)$	Reaction Rate/Mo atoms $\cdot S_{\text{BET}}$ $\left(\begin{array}{c} \times 10^5 \\ \text{g} \cdot \text{molec. Moat}^{-1} \cdot \text{m}^{-2} \text{s} \end{array} \right)$
MoN-A-i	115	4.98	7.12	0.62
MoN-A-ii	40	6.23	7.84	1.96
MoN-NH-i	9	1.54	1.85	2.09
MoN-NH-ii	10	1.81	1.86	1.86
CoMoN-A	50	5.21	-	-

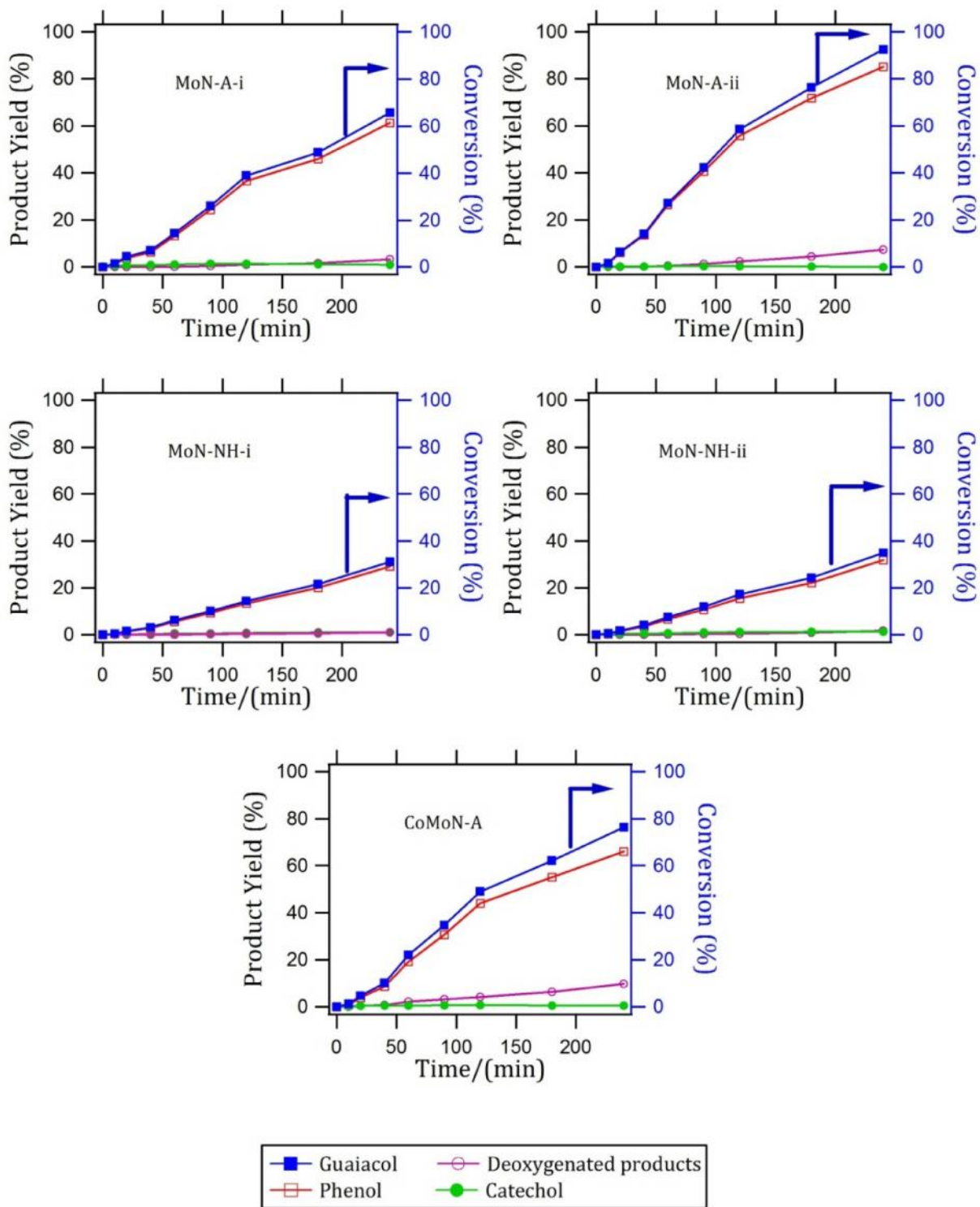


Figure 3.3 Variation of the transformation of guaiacol and the yield of products with time.

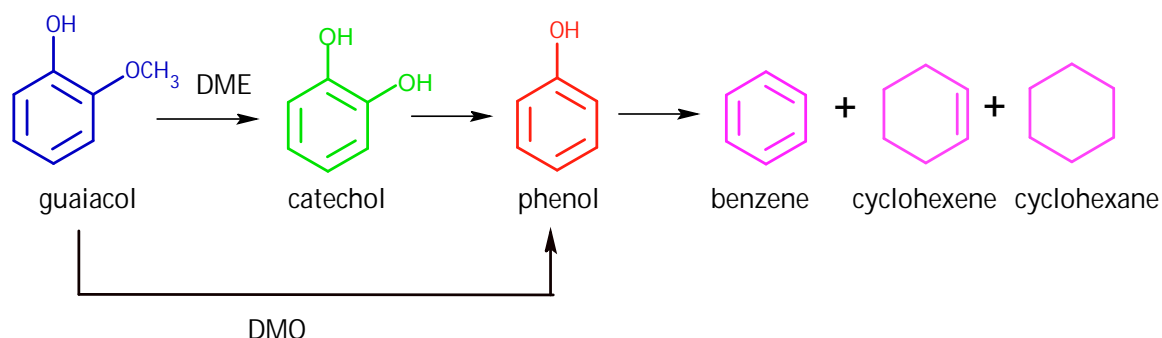


Figure 3.4 Hydrodeoxygenation pathways of guaiacol. Adapted from Ferrari et al. [81]

The catalytic performance of the CoMo bimetallic nitride catalyst relative to the Mo monometallic nitride indicated that the addition of Co did not enhance the activity of the catalyst. Our observation is inconsistent with the positive effects of Co promoters on bulk Mo nitrides reported for HDS and HDN catalysis [112, 255]. This result may be attributed to incomplete formation of the bimetallic nitride, $\text{Co}_3\text{Mo}_3\text{N}$, as evident by the presence of Mo_2N . Particle sizes calculated from the XRD data in Table 3.1 indicated that $\text{Co}_3\text{Mo}_3\text{N}$ particles were three times larger than Mo_2N particles in the CoMoN-A catalyst. It is possible that the Mo_2N particles were embedded within $\text{Co}_3\text{Mo}_3\text{N}$ crystallites, and hence, only a portion of the bimetallic nitride was accessible for catalysis.

However, the addition of Co increased the yield of deoxygenated products such as benzene, cyclohexene and cyclohexane as illustrated in Fig. 3.5. Figure 3.5A shows that appreciable quantities of different deoxygenated products such as benzene, cyclohexene and cyclohexane were formed during reaction over the CoMoN-A catalyst. Figure 3.5B shows that cyclohexene was the principal deoxygenated product formed during reactions involving the MoN-A-ii catalyst. The

result in Fig. 3.5B indicated that hydrogen is conserved and double bond hydrogenation is minimized over MoN-A-ii catalyst relative to data in Figure 3.5A for CoMoN-A catalyst. A plot of the total yield of deoxygenated products vs. conversion (Fig. 3.5C) clearly shows a higher yield for reactions catalyzed by CoMoN-A compared to that catalyzed by MoN-A-ii. Thus, it appears that the addition of cobalt created new, or modified, active sites related to the $\text{Co}_3\text{Mo}_3\text{N}$ phase which enhanced the elimination of oxygen from phenol to form benzene, as well as increased the hydrogenation of the aromatic ring of benzene to form cyclohexene and cyclohexane. Figure 3.5 also shows that the yields of the deoxygenated compounds produced by both catalysts increased at high conversions. The results indicate that further studies to optimize the Co composition in order to produce single-phase $\text{Co}_3\text{Mo}_3\text{N}$ in the Co-Mo-N catalyst, as well as studies focusing on the nature of the surface of the catalyst for HDO catalysis are warranted.

The selectivity in the transformation of guaiacol is expressed in terms of the phenol/catechol (Phe/Cat) ratio, calculated at 10% guaiacol conversion, and shown in Fig. 3.6. The results in Fig. 3.6 show that, for most of the experiments, except for reactions over the MoN-A-ii catalyst, the Phe/Cat ratios calculated were similar, suggesting that the active sites were the same. The yield of formation of phenol at 10 % guaiacol conversion for all the catalysts ranged from 8.7 – 9.7 %, while the production of catechol by all the catalysts ranged from 0.2 – 1%. For the MoN-A-ii catalyst, 9.7 % phenol and 0.2 % catechol were produced at 10 % guaiacol conversion which corresponded to the highest Phe/Cat ratio. The low value of catechol produced resulted in a very high Phe/Cat ratio of 49 ± 9 . The lowest

Phe/Cat ratio was obtained for the MoN-A-i catalyst which produced 8.9 % phenol and 1 % catechol at 10 % guaiacol conversion. The reason for the surprisingly high Phe/Cat ratio of the MoN-A-ii catalyst could be attributed to the presence of single-phase Mo₂N, with high activity for the direct demethoxylation route. The other monometallic catalysts contained other phases, such as MoO₂, β-Mo₂N_{0.78} or Mo. The presence of the MoO₂ phase decreased the ability of the active Mo₂N to rapidly remove the oxygen atom, while the presence of Mo metal increased the hydrogenation character of the catalysts and hence channeled some of the reaction through the demethylation route to form catechol. A closer look at the Phe/Cat ratio differences between the catalysts agrees with this assertion. The difference in the Phe/Cat ratio between the MoN-NH-i and the MoN-NH-ii catalysts indicated that the MoN-NH-i catalyst containing only the β-Mo₂N_{0.78} phase was more selective towards phenol than the catalyst containing the nitride, Mo metal and MoO₂ phases. Despite these differences, the phenol/catechol ratios for all the catalysts tested which ranged from 9 to 48 were substantially higher than values reported for sulfided catalysts [55]. The higher amount of phenol produced at low conversion has implications in terms of the prevention of excessive hydrogen consumption [22]. Additionally, the rapid transformation of guaiacol to phenol will lead to less formation of coke due to the propensity of guaiacol and catechol to form polycondensation products and coke [22]. The reduction in hydrogen consumption and negligible coke formation will be critical for the ultimate commercial success of an HDO catalyst.

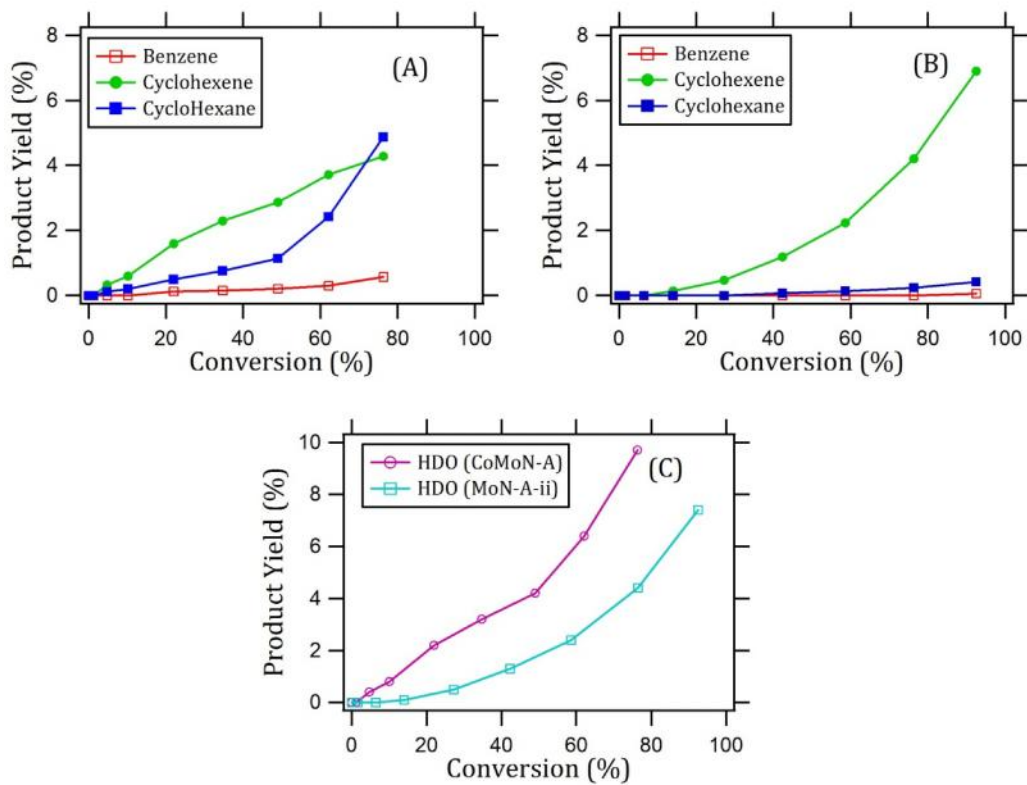


Figure 3.5 Distribution and total yield of deoxygenated products versus conversion of guaiacol for (A) CoMoN-A and (B) MoN-A-ii catalysts.

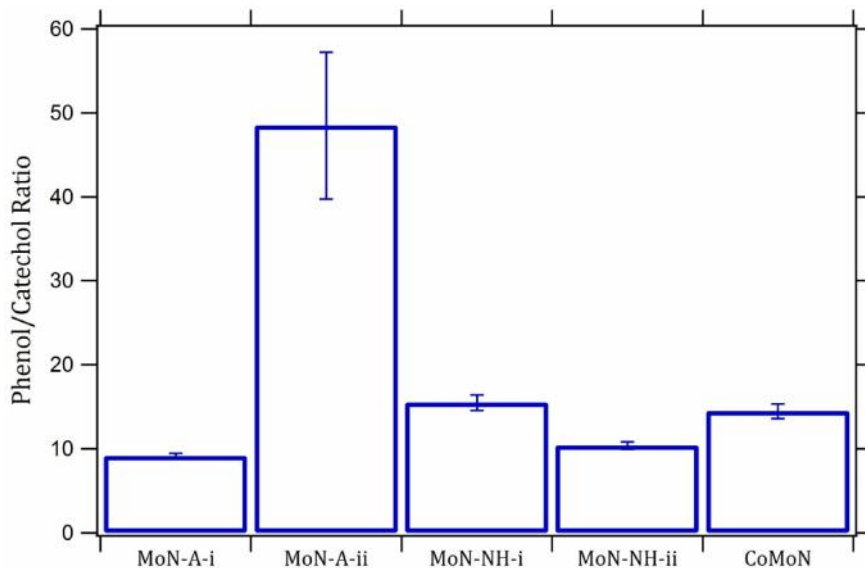


Figure 3.8 Phenol/catechol ratio for bulk metal nitride catalysts

3.4. Conclusion

All the metal nitride catalysts prepared and characterized in this study demonstrated high activity and rapid production of significant amounts of phenol, indicating that the transformation of guaiacol mostly proceeded through the direct demethoxylation route, bypassing the formation of catechol. The activity trends indicated that the Mo nitride catalyst with the highest degree of nitridation contained only the γ -Mo₂N phase and was the most active. The presence of another Mo nitride phase (β -Mo₂N_{0.78}) and other molybdenum compounds such as MoO₂ and Mo metal, decreased the activities of the catalysts. Furthermore, comparison of phenol/catechol ratios indicated that the catalysts possessing only the γ -Mo₂N phase displayed the highest selectivity towards the production of phenol. The addition of Co did not enhance the overall activity of the Mo nitride catalysts. This may have been due to the lack of single phase Co₃Mo₃N. However, the bimetallic nitride produced higher yields of deoxygenated products compared to monometallic nitride prepared using the same synthesis condition, and this result was also attributed to the presence of Co₃Mo₃N particles.

CHAPTER 4
HYDRODEOXYGENATION OF GUAIACOL OVER CARBON-SUPPORTED
MOLYBDENUM NITRIDE CATALYSTS*

4.1. Introduction

Bio-oils derived from pyrolysis of woody biomass have received considerable attention as an alternative renewable feedstock to crude oil for the production of fuels and value-added chemicals due to long-term economic and environmental concerns [11]. Their utilization as fuel is, however, limited by their high viscosity, low heating value, incomplete volatility and thermal instability, which stem from the presence of oxygenated organic compounds in the feed [18]. Catalytic hydrodeoxygenation (HDO) reactions are typically performed to upgrade bio-oils in order to increase its quality as transportation fuel. There are two significant challenges in catalytic HDO upgrading of bio-oil: the prevention of coke formation/catalyst deactivation and the selective removal of oxygen without over hydrogenating aromatic and olefinic compounds [18, 22].

Model compounds have been used to mimic HDO studies of bio-oil components in an effort to understand characteristics of the reactions of different functional groups present in the feed, as well as provide additional insight into the development of improved catalysts and processes [28]. Guaiacol (2-methoxyphenol) is commonly used as a model compound for HDO studies to represent the large number of mono- and dimethoxy phenols present in bio-oil [63]. Guaiacol is known

* A portion of this chapter is in preparation to be submitted for publication in *Applied Catalysis A: General*

as a precursor to catechol and subsequently to coke [22, 48]. Also, guaiacol possesses two different oxygenated functional groups (-OCH₃ and -OH) which makes it challenging to completely deoxygenate [70].

Heterogeneous catalysts commonly studied for HDO of guaiacol (and many other model compounds) are conventional sulfided Co(Ni)Mo/ -Al₂O₃ [48, 49] and supported noble metal catalysts such as Ru, Rh and Pd [65, 68]. The initial interest in the metal sulfides was driven by high cost and lack of selective HDO activity of the noble metal catalysts. The proposed reaction scheme during HDO of guaiacol over the alumina-supported sulfide catalysts begins with initial demethylation of the methoxy group (-O-CH₃) to form catechol, followed by elimination of one of the hydroxyl groups to form phenol (Fig. 4.1) [48, 54, 70]. Further conversion leads to the formation of benzene, cyclohexene and cyclohexane. Despite high catalytic activity for guaiacol conversion, there are some drawbacks associated with these sulfide catalysts. The alumina support can be unstable in water at processing conditions. Also, the sulfide catalyst can oxidize under processing conditions, requiring regeneration with a sulfiding agent during reaction to prolong catalyst activity. This regeneration can contaminate products [22, 48, 54, 256]. In addition, the acidic nature of the alumina support was found to be prone to substantial coke formation through strong interaction with guaiacol, forming doubly anchored phenates leading to rapid catalyst deactivation [257]. These drawbacks prompted interests in neutral materials such as silica [55], zirconia [65, 254] and activated carbon [27, 81] as catalytic supports. Centeno et al. [55] reported that despite lower activity of metal sulfides supported on silica and carbon compared with the

conventional alumina-supported counterpart, the use of the alternative supports led to negligible coke formation. Furthermore, studies involving activated carbon- and zirconia- supported catalysts indicated direct elimination of the methoxy group which favored direct production of phenol from guaiacol [55, 60]. Particularly, carbons are believed to be promising supports for the HDO of bio-oils and have been further explored by several researchers [79, 258, 259].

Interest in carbon supports has increased mainly due to its flexibility and the ability to recover active metal after catalyst deactivation [258]. For HDO reactions, deactivation of metal catalysts by water produced could be limited due to the hydrophobic character of the surface of the carbon support [83]. However, the weak interaction between the support surface and the active metal results in low dispersion of the sulfide phase [55, 258]. In a later study, activated carbon surfaces were functionalized with oxygen species in an attempt to improve activity by improving dispersion of the active sulfide phase [56]. The oxidative treatments with HNO_3 modified the surface chemistry of the support and promoted the formation of small, well-dispersed crystals of the molybdenum precursor on the support [259, 260]. However, this led to lower yields of phenol during HDO of guaiacol [56]. Additional studies further confirmed that HDO chemistry can be controlled through modification of the surface chemistry of the carbon support and consequently the dispersion [16, 22]. This adds to the potential use of carbon-supported catalytic systems for rational catalyst design [79, 81].

To address issues related to the use of sulfided catalysts, other active phases such as noble metals [63, 65, 68, 253], transition metal phosphides [70] and

transition metal nitrides [251] have been employed for HDO reactions in order to eliminate the need to add sulfur to the feed. In particular, transition metal nitrides show great potential as catalysts which arise from ceramic-like physical properties coupled with chemical properties resembling platinum-group materials [84]. These materials have also demonstrated unique catalytic pathways, leading to desirable product selectivities [84, 261]. Consequently, they could provide a cheaper and more selective alternative to noble-metal catalysts such as Ru, Pd and Pt. Our previous study showed high activities and significantly high phenol/catechol ratio for bulk molybdenum nitride catalysts in HDO of guaiacol [262]. However, for commercial applications, catalyst supports are widely used due to their influence on the physical and chemical properties of the catalyst such as its mechanical and morphological properties. In addition, the use of support reduces cost of the active phase and increases the catalyst's resistance to sintering. Thus, catalytic studies involving carbon supports with different textural, structural and acidic properties will generate fundamental information relevant not only to the significance of this material under HDO reaction conditions but also to catalyst design strategies for HDO catalysts.

The addition of Co as a promoter has been reported to improve the activity of bulk and supported Mo_2N catalysts for HDS and HDN reactions [135, 255]. In addition, Co-promoted MoS_2 catalysts exhibited significantly higher HDO activity compared to non-promoted MoS_2 catalysts for HDO of guaiacol [49]. However, in our previous study for HDO of guaiacol over bulk nitrides, we found that although the addition of Co improved the yield of deoxygenated products, the overall activity

was not enhanced compared to the monometallic nitride [262]. This motivated us to investigate the effect of Co promoters on the catalytic properties of supported nitrides in HDO reactions.

In this chapter, we report the synthesis and characterization of molybdenum nitrides dispersed on four different activated carbon supports. The supports were both microporous/mesoporous carbons and mesoporous/macroporous carbons. The molybdenum nitride catalysts were synthesized by impregnation of an aqueous salt, and subsequent thermal conversion to the nitride. Thermal conversion was achieved by two different procedures: ammonolysis and reduction/nitridation using a hydrogen/nitrogen mixture. The catalysts were characterized and evaluated in the HDO of guaiacol. The effects of the synthesis procedure, carbon support properties, and the addition of Co as a promoter on the HDO of guaiacol were examined in terms of reaction rate and the phenol/catechol selectivity.

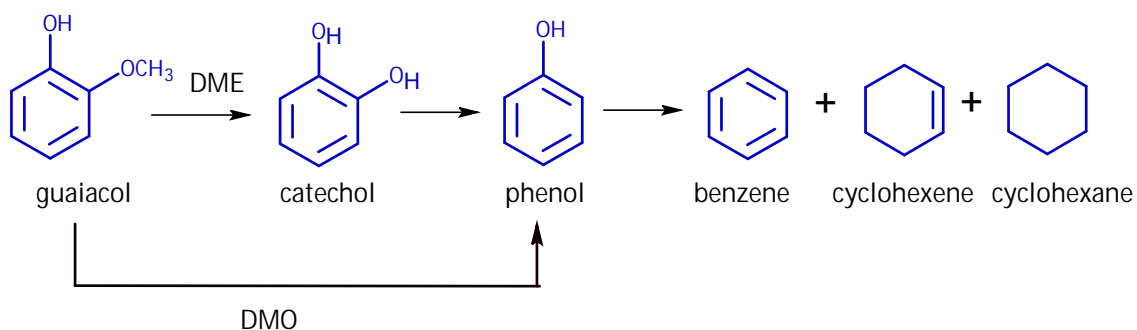


Figure 4.1 Hydrodeoxygenation pathways of guaiacol. Adapted from Ferrari et al. [81]

4.2. Experimental Section

4.2.1. Catalyst Preparation

Four commercial activated carbons obtained from Norit Americas Inc were used as supports. NORIT **GAC** 1240 Plus (0.42-2.00 mm particle size, $S_{BET} = 976 \text{ m}^2 \text{ g}^{-1}$, $TPV = 0.56 \text{ cm}^3 \text{ g}^{-1}$) and NORIT **GCA** 1240 Plus (0.42-1.70 mm particle size, $S_{BET} = 1132 \text{ m}^2 \text{ g}^{-1}$, $TPV = 0.51 \text{ cm}^3 \text{ g}^{-1}$) are acid washed granular activated carbons of high purity produced by steam activation of select grades of coal and coconut shells respectively. **Darco** MRX (0.60-2.00 mm particle size, $S_{BET} = 613 \text{ m}^2 \text{ g}^{-1}$, $TPV = 0.62 \text{ cm}^3 \text{ g}^{-1}$) is an acid washed specialty grade of granular activated carbon produced by steam activation of lignite coal. NORIT **C Gran** (0.50-1.70 mm particle size, $S_{BET} = 1402 \text{ m}^2 \text{ g}^{-1}$, $TPV = 1.15 \text{ cm}^3 \text{ g}^{-1}$) is a granular activated carbon produced by chemical activation using the phosphoric acid process. Prior to their use as support, the activated carbon materials were treated with 1 M HNO_3 at 90 °C for 6 h. Then, the solution was filtered and extensively washed with distilled water to bring the pH to 7. The samples were dried overnight under vacuum conditions at 120 °C. The supported molybdenum oxide precursors were prepared by incipient wetness impregnation using aqueous solutions of ammonium heptamolybdate (Fischer, AHM, $(\text{NH}_4)_6\text{Mo}_7\text{O}_{24} \cdot 4\text{H}_2\text{O}$, A.C.S. grade). After impregnation, the samples were kept at room temperature for 24 h, followed by drying overnight at 110 °C. The bimetallic oxide precursors were prepared by sequential impregnation of Mo and Co into the support. Firstly, Mo-loaded samples were prepared using the same drying-calcination procedure described above. These samples were then impregnated with aqueous solution of cobalt (II) nitrate hexahydrate (Acros Organics, $\text{Co}(\text{NO}_3)_2 \cdot 6\text{H}_2\text{O}$,

99%) and kept overnight at room temperature. The samples were further dried overnight at 110 °C. The supported oxides were prepared to obtain nominal loading of 8.1 wt% Mo metal content for monometallic samples, 8.1 wt% Mo metal and 2.4 wt% Co metal content for the bimetallic samples. All oxide precursors were sieved to obtain a 180-450 µm particle size.

Molybdenum nitrides were prepared using the same set-up described previously in Chapter 3. The quartz reactor tube was loaded with about 2.5 g of the oxidic precursor, while flowing NH₃ (Matheson, NH₃, 99.99 %) or a N₂/H₂ mixture (N₂: BOC Gases, Grade 5; H₂: Matheson, 99.99%) over the sample [94, 99]. The reactor was purged with nitrogen prior to nitridation for 30 min and switched to NH₃ (300 mL min⁻¹) or a N₂/H₂ mixture (300 mL min⁻¹, N₂/H₂ = 5/1 (v/v)). The temperature was linearly increased from ambient temperature to 300 °C within 30 min (9.33 °C min⁻¹), then from 300 °C to 500 °C by a heating rate of 0.6 °C min⁻¹, and from 500 °C to 700 °C by a heating rate of 2 °C min⁻¹. Then, the temperature was maintained at 700 °C for 2 h. The nitrides prepared using NH₃ were cooled down to room temperature using the same flow rate of NH₃ while the nitrides prepared using the N₂/H₂ mixture were cooled down in 300 mL min⁻¹ of nitrogen. The materials were then passivated in a 1% O₂/N₂ (Boc Gases, UHP grade) for 12 h at room temperature. Preparation of metal nitride catalysts using ammonia and nitrogen-hydrogen mixtures were referred to as method 1 and method 2 respectively. For notation, Mo nitrides prepared using method 1 has suffix "A", while method 2 have suffix "NH": e.g. MoN/Darco-A and MoN/Darco-NH are Darco activated carbon-supported Mo nitride using NH₃ and a N₂/H₂ mixture respectively.

4.2.2. Catalyst Characterization

Nitrogen Porosimetry. Nitrogen adsorption/desorption isotherms were measured at 77 K using a Micromeritics ASAP-2020 instrument to evaluate the pore structure of the catalyst samples. Prior to the measurements, the samples were outgassed under vacuum at 200 °C for 12 h. The nitrogen adsorption isotherms were collected within a broader relative pressure range of $10^{-6} < P/P_0 < 0.995$, and a low pressure incremental dosing of $3 \text{ cm}^3 \text{ g}^{-1}$ STP were also used to obtain adequate characterization of the micropore region. The isotherms were used to calculate BET specific surface area (S_{BET}), total pore volume (TPV), average pore diameter (d_{pore}), and micropore volume (V_{μ}). S_{BET} was calculated using the adsorption branch of the nitrogen isotherm in the relative pressure range of $0.04 < P/P_0 < 0.14$ and TPV was recorded at $P/P_0 = 0.995$. Average pore diameters were calculated from the equation, $d_{pore} = 2 \cdot TPV / S_{BET}$ (assuming slit-shaped pores). The pore size distributions (PSD) for pores varying from 0.4 to 100 nm were determined from the adsorption branch of the isotherm using the nonlocal density functional theory (NLDFT) method [263, 264]. Micropore volume was calculated from NLDFT cumulative pore volumes of pores of the size below 2 nm.

X-ray diffraction. Wide angle θ - 2θ x-ray diffraction patterns of powdered samples were obtained using a PANalytical X'Pert Pro X-ray diffractometer equipped with a graphite monochromator and $\text{CuK}\alpha$ radiation (45 kV, 40 mA) in a parallel beam optical geometry. The standard scan parameters were $15-85^\circ 2\theta$ with a step size of 0.02° and a counting time of 10 s per step. Identification of the phases was achieved by reference to JCPDS diffraction file data.

Chemical analysis. Molybdenum, cobalt and nitrogen contents in the metal nitride samples were performed by Galbraith Laboratories using ICP-AES for the metal analyses and combustion method for nitrogen analyses.

X-ray photoelectron spectroscopy (XPS). X-ray photoelectron spectra of reduced catalysts were obtained on a VG Escalab 200R electron spectrometer using a Mg K (1253.6 eV) photon source. The catalyst samples were pre-reduced *ex situ* with H₂ at 450 °C for 6 h. After reduction, the samples were cooled to room temperature, flushed with nitrogen and stored in flasks containing isooctane (Merck, 99.8 %), then transferred to the pre-treatment chamber of the spectrometer. The binding energies (BE) were referenced to the C 1s level of the carbon support at 284.9 eV. An estimated error of ± 0.1 eV can be assumed for all measurements. Intensities of the peaks (I_{Mo3d} and I_{C1s}) were calculated from the respective peak areas after background subtraction and spectrum fitting by a combination of Gaussian/Lorentzian functions. Relative surface atomic ratios (Mo/C) were determined from the corresponding peak areas, normalized by tabulated atomic sensitivity factors (S_{Mo3d} and S_{C1s}) [265] as shown in Eq. 4.1. The errors in the quantitative estimation were similar in each sample with a precision of 7%.

$$Mo/C = \frac{\left(\frac{I_{Mo}}{S_{Mo}} \right)_{3d}}{\left(\frac{I_C}{S_C} \right)_{1s}} \quad (4.1)$$

Temperature program desorption-mass spectroscopy (TPD-MS). TPD analyses of the carbon supports were carried out in an in-house built set-up which consisted of a U-shaped quartz tube micro-reactor, placed inside a programmable electrical furnace. The TPD profiles were obtained from room temperature to 1040 °C, at a

heating rate of 10 °C min⁻¹ and under helium (AGA Chile, 99.995%), flow of 50 mL min⁻¹. The evolutions of the gases desorbed were monitored by a thermal conductivity detector (TCD). In addition, to quantify the gases produced during thermal decomposition of the surface, TPD was coupled with MS and carried out using Altamira AMI-200 R-HP characterization instrument. About 0.2 g of the activated carbon sample was first pretreated at 100 °C for 4 h in He (50 mL min⁻¹) to remove most of the weakly adsorbed water, and cooled to room temperature in He. The pretreated sample was then heated in a flow of He (50 mL min⁻¹) from room temperature to 800 °C at a heating rate of 10 °C min⁻¹. The following effluent gases were monitored with an SRS RGA-300 Mass Spectrometer: H₂O (18), CO (28) and CO₂ (44).

Acidity Measurements. Acid site concentration and the acid strength measurements of the carbon supports and some selected catalysts were determined using a potentiometric method [266], whereby a suspension of the carbon support in acetonitrile (Merck, 99.9%) was titrated with *n*-butylamine (Merck, 99%). The variation in electric potential was registered on a Denver Instrument UltraBasic pH/mV meter.

4.2.3. Catalytic Activity Measurements

Reactivity studies were performed in a 300 mL stirred-batch autoclave reactor set-up (Parr Model 4841) at 300 °C and under a hydrogen pressure of 5 MPa. Details of the catalyst activation and reaction measurements are given in 3.2.3. The catalytic activity was expressed by the initial reaction rate which was calculated

from the slopes of the conversion vs. reaction time plot, and by the intrinsic activity (i.e. the reaction rates per molybdenum atom).

The stability of some selected nitride catalysts during the hydrodeoxygenation reaction was compared to a commercial reference catalyst in a continuous-flow micro-reactor. The experimental set-up is shown in Fig. 4.2. The reactor was a stainless steel tube with an inside diameter of 8 mm and a total height of 300 mm placed inside a programmable furnace. The internal reactor temperature was measured by a thermocouple placed inside a thermowell, and controlled by a temperature controller. The liquid reactant mixture was fed to the reactor by a high pressure HPLC pump (LabAlliance Series I) through stainless steel tubing with Variac-controlled heating tapes wrapped around it. The temperature of the liquid feed lines was monitored by a thermocouple. Hydrogen was similarly connected to the reactor inlet where it flows downward through the catalyst bed after mixing with the liquid feed. The flow rate of hydrogen was controlled by a metering valve and measured with a soap bubble flowmeter connected to the gas exit stream. The reactor tube was divided into three vertical zones: 150 mm thermowell-occupied preheated zone, 20 mm catalyst zone filled with catalyst particles physically mixed 1:1 with SiC (Soviquim, Chile), and a 130 mm bottom zone packed with SiC. The catalyst and bottom zones were supported on a plug of quartz wool. The effluents from the reactor were cooled down to room temperature and passed through a gas-liquid separator. The liquid products were then collected downstream in small vials by sampling through a valve. A back pressure regulator connected to the exit stream reduces the system pressure.

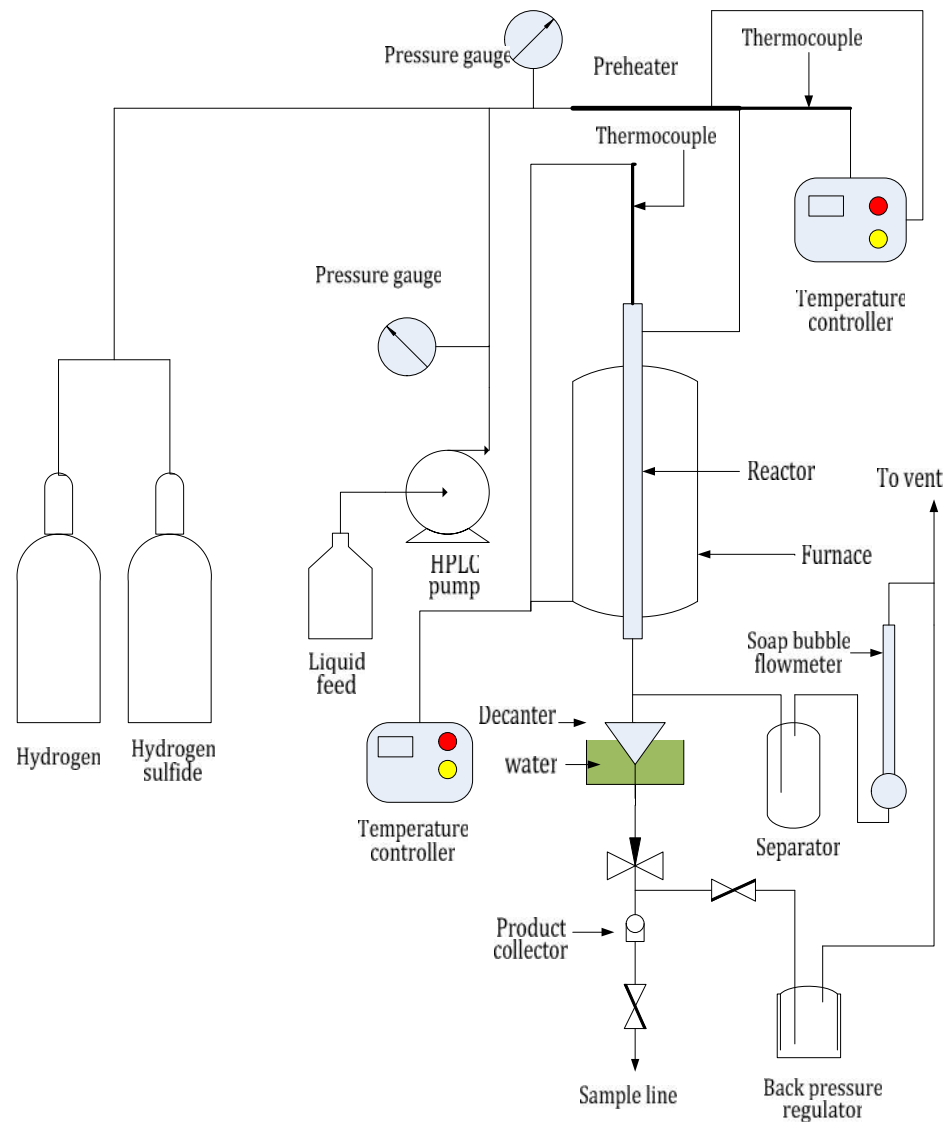


Figure 4.2 Experimental set-up for flow reaction

For a typical reaction, approximately 0.2 g of catalyst loading (180 – 420 μm) was used. Prior to the reaction, the nitride catalysts were reduced *in situ* in H_2 flow (60 mL min^{-1}) at 450 $^\circ\text{C}$ for 6 h, while the commercial Ni-Mo/ Al_2O_3 catalyst (Procatalyse, HR 346, $S_{\text{BET}} = 256 \text{ m}^2\text{g}^{-1}$) was sulfided *in situ* using a 10 vol. % H_2S (AGA Chile, 99.99%) in H_2 mixture, at a flow rate of 67.5 mL min^{-1} and a temperature of 350 $^\circ\text{C}$ held for 3 h. The reactor was then first pressurized with

hydrogen to 3 MPa and set to the desired flow rate. The reactor and liquid feed lines were then heated to their respective desired temperatures (300 and 120 °C respectively), while the liquid feed was simultaneously fed to the reactor at a flow rate of 1 mL min⁻¹. The liquid feed mixture consisted of 2.53 mL guaiacol (0.232 mol L⁻¹), and 700 µL hexadecane dissolved in 80 mL decalin. The initial high flow rate of liquid feed was used to ensure complete wetting of the catalyst bed. After collecting the first liquid drop, the liquid flow rate was decreased to 0.1 mL min⁻¹. The conditions for HDO reactions were as follows: reaction temperature of 300 °C, 3 MPa total pressure, liquid feed flow of 5.4 g h⁻¹ corresponding to liquid hourly space velocity (LHSV) of 27 h⁻¹, H₂ gas hourly space velocity (GHSV) of 3600 h⁻¹, H₂/guaiacol molar ratio of 23. The liquid flow rate was chosen to obtain low conversion. After about 0.5 h, the liquid used to flush the catalyst bed were collected downstream. This was done at least three times to remove any residual liquid. Fresh samples were then collected at an hourly interval for 8-9 h with regular flushing preceding each collection. The liquid products were then analyzed by GC-FID.

4.3. Results

4.3.1. Textural Properties

The pore size distributions (PSD) for the activated carbon supports calculated from the adsorption branch of the isotherm using the NLDFIT method are shown in Fig. 4.3. All the activated carbon materials have non-uniform, wide pore size distributions (PSD). All of the supports revealed the presence of micropores in the range 0.4-2.0 nm. However, the PSD of CGran and Darco indicated a predominance of larger mesopores up to 100 nm in these materials. On the

contrary, the pores of GCA and GAC carbon materials were mainly located in the microporous region of pore widths between 0.4-2.0 nm. The GAC carbon material also possessed an appreciable amount of larger mesopores between 3-100 nm which were clearly demonstrated by pores in the mesopore size range.

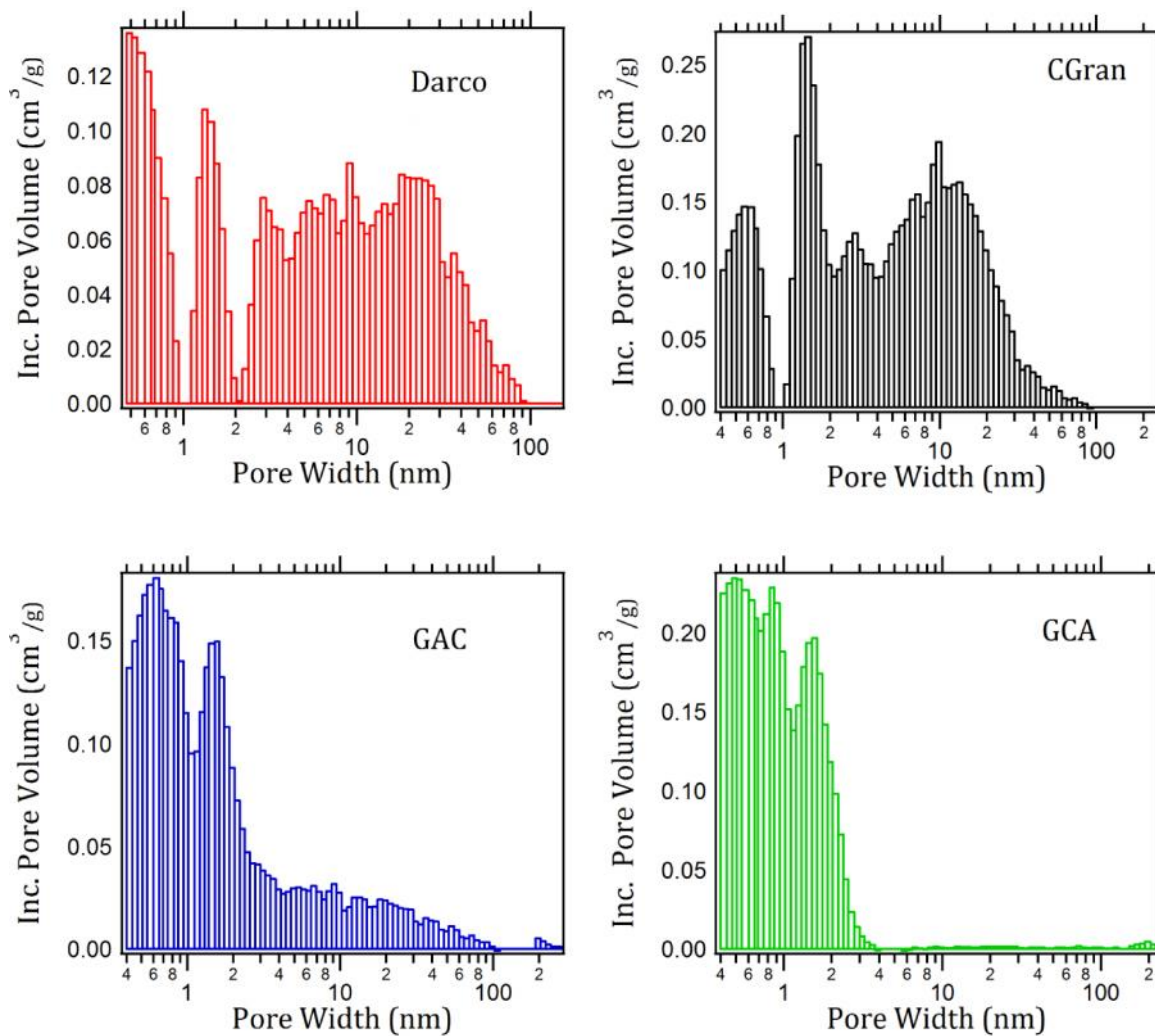


Figure 4.3 Pore size distribution of HNO₃ treated activated carbon supports

The BET specific surface area, total and micropore volume of the activated carbon supports, Mo and CoMo nitride catalysts are presented in Table 4.1. The BET surface areas of the materials under study ranged from 461 to 1402 m² g⁻¹. There were some differences in textural parameters of the four supports. The CGran and

GCA carbons were characterized by higher surface areas; however, both supports differed in their microporous and mesoporous volumes. The GCA support had a larger fraction of micropores than the CGran support (about 76% and 32% respectively). On the other hand, Darco carbon possessed the lowest S_{BET} while GAC carbon had a moderately high surface area. The lowest S_{BET} displayed by the Darco support is consistent with this material having the lowest microporosity (19%) of all the carbon supports. The PSD of GAC carbon support indicated that approximately 57% mesoporosity and 43% microporosity contributed to the total surface area of this material. Oxidation pretreatment of activated carbon supports with HNO_3 produced changes in the textural properties of the original samples. As seen in Table 4.1, significant losses of specific surface area (26 %), total pore volume (25 %) and micropore volume (24 %) were obtained for CGran activated carbon after treatment with HNO_3 . The treatment also brought about a moderate loss of micropore volume for the GAC carbon (5 %) which resulted in a 4 % loss of specific surface area. In contrast, oxidation with HNO_3 increased the specific surface area and total pore volume of the Darco and GCA activated carbons compared to the as-received samples. The pore size distributions of the carbon materials were not significantly modified after the treatment. Results summarized in Table 4.1 also show that impregnation of Mo (and Co for bimetallic nitrides) into carbon supports, followed by thermal conversion to the nitride led to general decreases in BET surface area, total and micropore volume of the support. The percent loss in S_{BET} and TPV after impregnation and nitridation were more evident for CGran materials.

Table 4.1 Nitrogen porosimetry of activated carbon-related materials

Sample	S_{BET} ($m^2 g^{-1}$)	d_{pore} (nm)	Pore Volume ($cm^3 g^{-1}$)		
			TPV	V_{μ}	$(TPV - V_{\mu})$
Darco _{as-received}	612	2.0	0.62	0.12	0.50
Darco _{pretreated}	664	2.0	0.68	0.14	0.54
MoN/Darco-A	561	2.1	0.58	0.13	0.45
MoN/Darco-NH	560	2.1	0.60	0.14	0.46
CoMoN/Darco-A	475	2.3	0.54	0.10	0.44
CGran _{as-received}	1402	1.6	1.15	0.37	0.78
CGran _{pretreated}	1014	1.7	0.86	0.28	0.58
MoN/CGran-A	566	1.6	0.46	0.15	0.31
MoN/CGran-NH	571	1.6	0.47	0.15	0.32
CoMoN/CGran-A	461	1.9	0.44	0.11	0.33
GAC _{as-received}	976	1.1	0.56	0.32	0.24
GAC _{pretreated}	942	1.2	0.55	0.31	0.24
MoN/GAC-A	775	1.2	0.46	0.25	0.21
MoN/GAC-NH	752	1.2	0.45	0.24	0.21
CoMoN/GAC-A	706	1.5	0.52	0.21	0.31
GCA _{as-received}	1132	0.9	0.51	0.39	0.12
GCA _{pretreated}	1202	0.9	0.55	0.42	0.13
MoN/GCA-A	995	0.9	0.45	0.35	0.10
MoN/GCA-NH	1066	0.9	0.49	0.35	0.14
CoMoN/GCA-A	950	0.9	0.44	0.33	0.11

4.3.2. X-ray Diffraction

X-ray diffraction patterns of metal nitrides supported on GCA, GAC and Darco carbon revealed only peaks associated with the original carbon supports. The absence of Mo nitride diffraction peaks suggests that the catalysts likely contained small crystallites of Mo nitrides below the XRD detection limit. XRD data where catalyst phases were identified are shown in Fig. 4.4. The XRD results of the MoN/CGran-NH catalyst showed characteristic peaks for β -Mo₂N_{0.78} ($2\theta = 37.61^\circ$, 62.53° , 75.53°) together with broad features ($2\theta = 26^\circ$ and 43°) associated with the carbon supports. Also shown in Fig. 4.4 is the diffraction pattern for CoMoN/CGran-A which indicated the presence of Co₃Mo₃N crystallites ($2\theta = 40.09^\circ$, 42.59° , 46.59°).

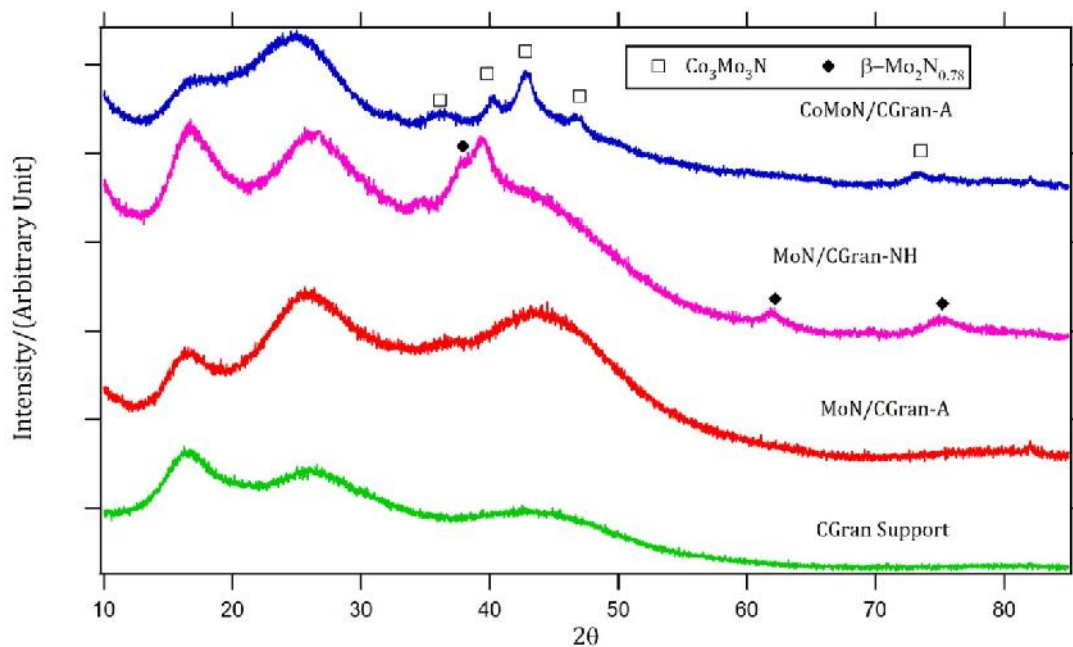


Figure 4.4 XRD patterns of CGran carbon- supported nitrides

4.3.3. Surface Chemical and Acidic Properties of the Support

The chemical nature of the surface groups of the activated carbon supports after HNO_3 treatment were determined from TPD/MS measurements and shown in Fig. 4.5. Observed peaks during decomposition of carbons have been assigned to various surface groups such as lactonic (190 – 650 °C) [267-270], carboxylic (200-300 °C) [268-270], phenolic (600-700 °C) [267, 269, 270], carbonyls (800-980 °C) [267, 269, 270], and quinone groups (700-1000 °C) [269-271]. Decomposition of groups where carbon is bonded to two oxygen atoms (carboxylic acids, lactones, and carboxylic anhydrides) releases CO_2 which is indicative of the presence of strong acidic sites [259, 269, 272, 273]. Figure 4.5 shows that all the supports exhibited pronounced peaks at low temperatures (250–400 °C) which is indicative of strong acidic sites. The relative intensities of the lower temperature peaks of the carbon materials as well as comparison of the integrated area of desorbed CO_2 as monitored

by MS (summarized in Table 4.2) show that CGran contained the greatest amount of acidic groups. In the high temperature region, the GCA, GAC and Darco carbon supports presented broader shoulders between 515–1000 °C which is indicative of the presence of phenolic, carbonyls and quinone groups. The CGran carbon support exhibited a peak between 415–730 °C which is suggestive of the presence of mostly phenolic groups. The decomposition of these functional groups, which lead to desorption of CO, indicated the presence of weakly acidic, neutral and basic groups where carbon is bonded to an oxygen atom [259, 269, 272, 273]. In addition, integration of the evolved CO peak shows that CGran contained the greatest amount CO₂- and CO-desorbing groups among the activated carbon supports. The results in Table 4.2 also show that the GCA and Darco carbons had similar quantities of CO₂ and CO releasing functional groups. Furthermore, comparison of TPD/MS results of acid-pretreated and as-received reference activated carbon supports shows greater amounts of CO₂- and CO-desorbing groups in the former. This is consistent with the creation of surface oxygen groups on the activated carbon surface during HNO₃ treatment [259].

The surface acidity of the activated carbon supports were estimated from potentiometric titration curves with *n*-butylamine as the probe molecule. The results include the maximum acid strength of the surface sites (derived from the initial electrode potential, E_0) and the total number of acid sites normalized by the surface area (acid site density). The HNO₃-pretreatment created stronger acid sites in comparison to the as-received reference activated carbon supports. Table 4.2 shows acidity results of oxidized carbon supports. On the basis of the results, CGran,

Darco and GAC carbon supports displayed strong acid sites with $E_0 > 100$ mV, whereas GCA carbon displayed weak acid sites with $0 < E_0 < 100$ mV [266]. Comparison of the density of acid sites in Table 4.2 indicated that the Darco carbon had the highest acid density, while the GAC and CGran carbons presented similar acid densities. The lowest density of acid sites was measured for the GCA Carbon.

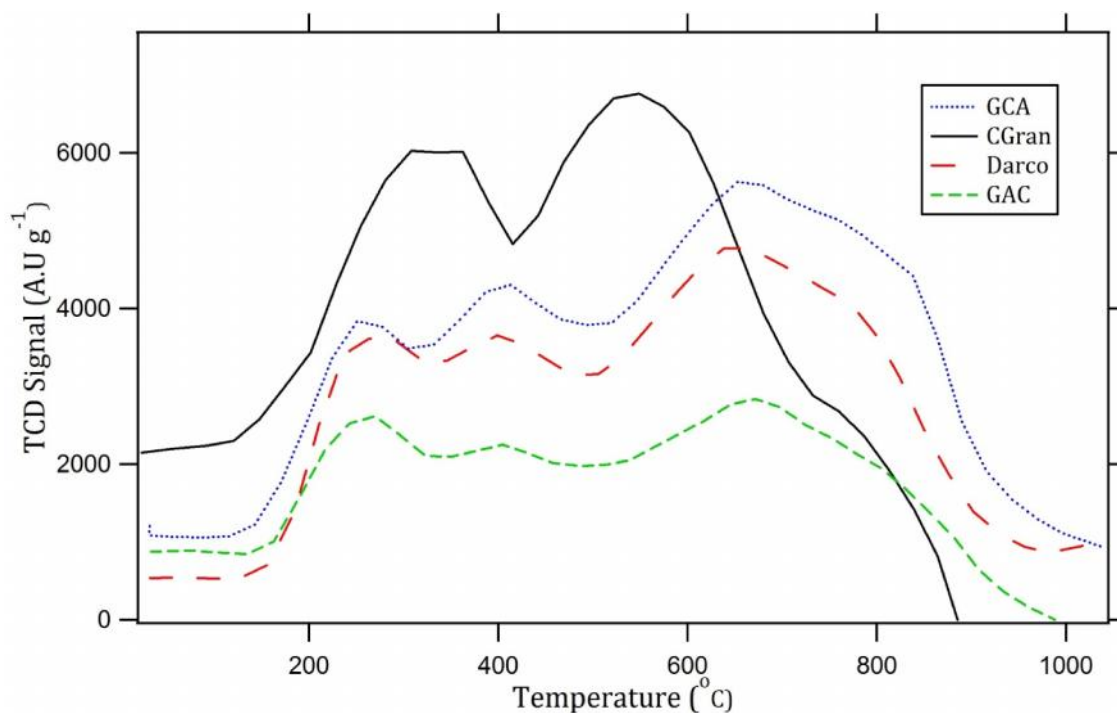


Figure 4.5 TPD profiles of the activated carbon supports

Table 4.2 Surface chemical and acidic properties of oxidized supports

Support	TPD (Area of MS Signal per g of support)		Acidity measurements	
	CO ₂	CO	Acid strength (mV)	Total acidity (meq/m ²)
GCA	12	8	61	1.2
GAC	16	16	119	1.6
CGran	26	29	290	1.5
Darco	12	8	127	2.3

4.3.4. Bulk and Surface Composition of Nitrided Catalysts

Bulk molybdenum, cobalt and nitrogen weight contents of passivated supported nitride catalysts are listed in Table 4.3. The nitrogen contents for the nitride samples prepared via method 1 were consistently higher compared to samples prepared via method 2. The nitrogen content, in large part, could be associated with nitrogen functional groups on the carbon support surface produced after nitridation with ammonia or a nitrogen/hydrogen mixture [274]. Thus, method 1 was more effective in nitriding the support.

Table 4.3 Elemental analysis of metal nitride catalysts

Catalyst	Elemental Composition (wt %)			N/Mo atomic ratio
	Mo	Co	N	
MoN/GCA-A	9.93	-	2.09	1.44
MoN/GCA-NH	8.79	-	1.16	0.91
CoMoN/GCA	8.44	2.03	2.54	2.06
MoN/GAC-A	7.60	-	2.14	1.93
MoN/GAC-NH	10.70	-	1.58	1.01
CoMoN/GAC	9.48	1.97	2.35	1.70
MoN/CGran-A	9.62	-	5.58	3.98
MoN/CGran-NH	11.25	-	1.26	0.77
CoMoN/CGran	12.60	2.87	4.55	2.47
MoN/Darco-A	10.20	-	3.70	2.49
MoN/Darco-NH	9.57	-	1.59	1.14
CoMoN/Darco	8.53	2.05	4.10	3.29

The surface species of the reduced, supported Mo nitride catalysts were determined by XPS and summarized in Table 4.4. The XPS binding energies of C 1s consisted of four peaks between binding energy (BE) values of 284.8 and 289.2 eV. The peak with BE of 284.8 eV was assigned to C-C and/or C=C bonds of aromatic and aliphatic carbon [269, 275], while the BE of 286.3 eV is indicative of C-O bonds in phenolic or ether groups [276, 277], or may be as a result of the presence of C=N bonds [278]. The peak with BE of 287.7 eV is consistent with quinone-type groups or C=N species [278, 279], and the BE of 289.3 eV is consistent with carboxyl groups

and esters [277]. The relative abundance (shown in parentheses) of the C 1s spectra shows a predominance of aromatic and aliphatic carbons on the surface of all of the catalysts.

Table 4.4 shows that after reduction of the passivated catalysts, only the Mo⁶⁺ species, with a binding energy of Mo 3d_{5/2} of ~232.5 eV, was present on the surface of the catalyst. The Mo⁶⁺ can be assigned to either non-nitrided MoO₃ or Mo oxynitrides [280]. The XPS result for the CoMo nitride samples also shows the Co 2p_{3/2} binding energy of 781.5 eV for the Co³⁺ species [113]. The result indicated that despite reduction of the passivated nitride catalysts at 450 °C, the surface of catalysts were mainly oxynitrides rather than nitrides [280]. The three binding energies of the N 1s region indicated the presence of different species on the surface of the catalyst. The peaks with BEs of ~398.3, 399.6 and 400.1 eV can be ascribed to pyridine, amide and nitrile functional groups respectively [276, 281]. The component at ~396.5 eV is attributed to N 1s from Mo-N bond [113].

The atomic ratios of Mo/C, N/C and Co/C of the catalysts calculated from XPS data are also listed in Table 4.4. There were clear differences in the Mo/C surface atomic ratios, indicative of catalyst dispersion, for the catalysts prepared under different conditions. In Table 4.4, the XPS analysis showed that Mo nitride catalysts prepared via method 2 displayed higher Mo/C ratio as compared to the catalysts prepared via method 1. Thus, it can be interpreted from Table 4.4 that the thermal conversion of activated carbon-supported Mo oxide using a N₂/H₂ mixture led to more highly dispersed Mo nitride particles.

Table 4.4 Binding energies (eV) of core levels and surface atomic ratios of reduced, passivated nitride catalysts

Catalyst	C 1s (eV)	Mo3d _{5/2} (eV)	N1s (eV)	Co2p _{3/2} (eV)	Mo/C at.	N/C at.	Co/C at.
MoN/GCA-A	284.8 (77)	232.4	396.3 (15) 398.3 (56) 399.6 (29)	-	0.0139	0.0436	-
	286.2 (15)						
	287.7 (5)						
	289.2 (3)						
MoN/GCA-NH	284.8 (76)	232.5	396.8 (19) 398.4 (62) 400.1 (19)	-	0.0146	0.0379	-
	286.3 (15)						
	287.7 (5)						
	289.2 (4)						
CoMoN/GCA	284.8 (72)	232.5	396.3 (38) 398.3 (40) 399.6 (22)	781.5	0.0104	0.0421	0.0045
	286.2 (17)						
	287.7 (6)						
	289.2 (5)						
MoN/GAC-A	284.8 (76)	232.5	396.3 (15) 398.3 (56) 399.6 (29)	-	0.0128	0.0380	-
	286.3 (16)						
	287.7 (5)						
	289.2 (3)						
MoN/GAC-NH	284.8 (76)	232.5	396.8 (19) 398.4 (62) 400.1 (19)	-	0.0157	0.0410	-
	286.3 (15)						
	287.7 (5)						
	289.2 (4)						
CoMoN/GAC	284.8 (73)	232.5	396.3 (38) 398.3 (40) 399.6 (22)	781.3	0.0143	0.0485	0.075
	286.2 (16)						
	287.7 (6)						
	289.3 (5)						
MoN/CGran-A	284.8 (77)	232.8	396.8 (7) 398.4 (63) 400.1 (30)	-	0.0088	0.0531	-
	286.3 (14)						
	287.7 (5)						
	289.3 (4)						
MoN/CGran-NH	284.8 (79)	233.0	396.9 (12) 398.6 (55) 400.1 (33)	-	0.0176	0.0529	-
	286.3 (13)						
	287.7 (4)						
	289.3 (4)						
CoMoN/CGran	284.8 (80)	232.7	396.6 (17) 398.5 (57) 400.2 (26)	781.5	0.0182	0.0088	0.0095
	286.3 (12)						
	287.7 (4)						
	289.2 (4)						
MoN/Darco-A	284.8 (72)	232.7	396.5 (19) 398.4 (55) 400.1 (26)	-	0.0140	0.0506	-
	286.2 (16)						
	287.7 (6)						
	289.3 (6)						
MoN/Darco-NH	284.8 (73)	232.7	396.9 (21) 398.5 (59) 400.1 (20)	-	0.0159	0.0400	-
	286.2 (16)						
	287.7 (6)						
	289.3 (5)						
CoMoN/Darco	284.8 (72)	232.6	396.5 (19) 398.4 (54) 400.1 (27)	781.4	0.0102	0.0468	0.0061
	286.2 (16)						
	287.7 (6)						
	289.3 (6)						

4.3.5. Activity Measurements

The conversion of guaiacol and the evolution of the reaction products are illustrated in Figs. 4.6 and 4.7. Periodic samplings of the liquid mixture in the reactor were analyzed by GC, from which the concentration of the reactant and the product yields were determined relative to a hexadecane reference internal standard. The main reaction products from the HDO of guaiacol were phenol, catechol, cyclohexene, cyclohexane and benzene. The hydrodeoxygenation of guaiacol followed two proposed reaction pathways (Fig. 4.1) [81]: the first was an initial demethylation (DME) to form catechol, followed by dehydroxylation to form phenol; the second was a direct demethoxylation (DMO) of guaiacol to form phenol. Methane and methanol could not be separated by the column used although they are expected byproducts of DME and DMO respectively. Further deoxygenation of phenol produced benzene, cyclohexene and cyclohexane. Figures 4.6 and 4.7 show that the product distributions from the HDO of guaiacol over all the catalysts were similar. The major product observed was phenol, while catechol and deoxygenated products were observed in relatively smaller amounts. Continuous production of catechol at longer reaction time indicated that the conversion of catechol to phenol was not prominent over the time scale used in this study. In addition, the continuous production of phenol and catechol indicated that both demethylation and direct demethoxylation occurred over these supported catalysts. The same tendency was observed for bulk metal nitrides [262]. Possible hydrocarbon products such benzene, cyclohexene and cyclohexane were limited.

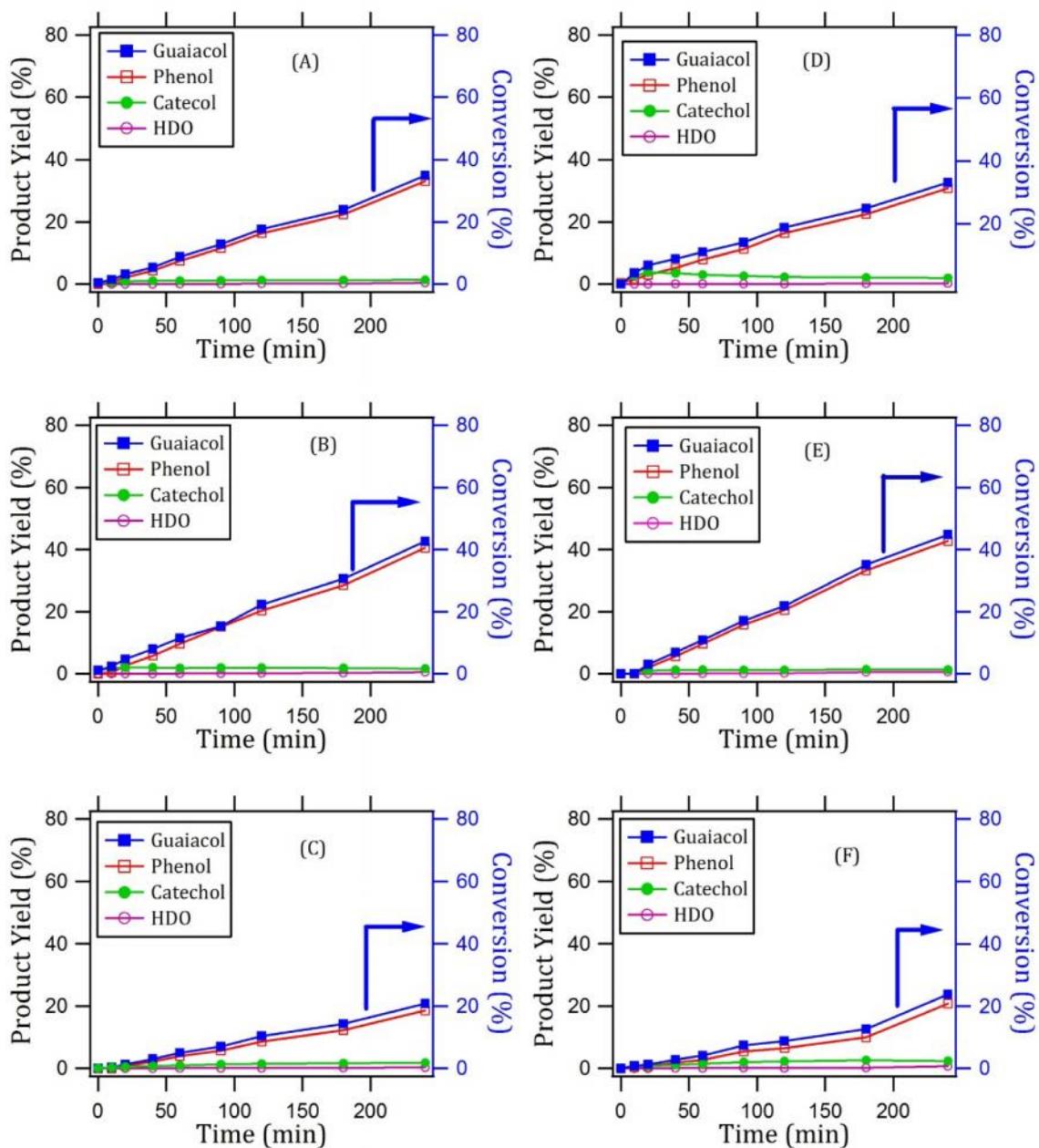


Figure 4.6 Variation of the transformation of guaiacol and the yield of products with time for GCA- and GCA-supported catalysts. (A) MoN/GCA-A, (B) MoN/GCA-NH, (C) CoMoN/GCA-A, (D) MoN/GAC-A, (E) MoN/GAC-NH, and (F) CoMoN/GAC-A catalysts.

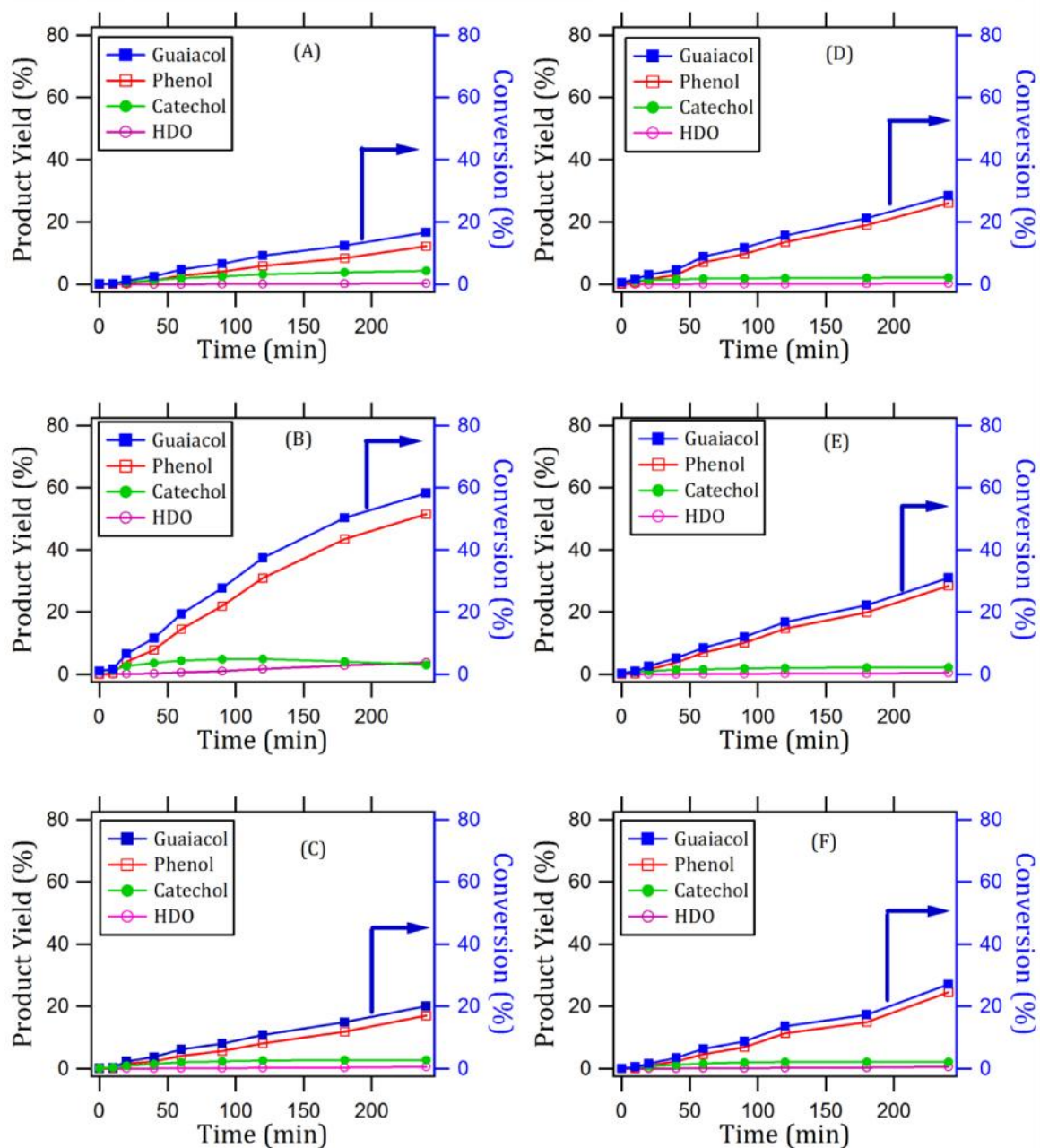


Figure 4.7 Variation of the transformation of guaiacol and the yield of products with time for CGran- and Darco-supported catalysts. (A) MoN/CGran-A, (B) MoN/CGran-NH, (C) CoMoN/CGran-A, (D) MoN/Darco-A, (E) MoN/Darco-NH, and (F) CoMoN/Darco-A catalysts.

Table 4.5 displays catalytic activities expressed in terms of reaction rates and intrinsic activities (reaction rates normalized by the molybdenum content). The initial reaction rates calculated from the slopes of the guaiacol conversion curve are further illustrated in Fig. 4.8. It can be observed from Fig. 4.8 that the reaction rates were strongly affected by the method of nitridation: for the same carbon support, the catalysts prepared by method 2 had higher activities than catalysts prepared by method 1. Other trends can be observed in Fig. 4.9 when focusing on catalysts prepared using the same method but dispersed on different carbon supports. The reaction rates of the method 1 catalysts decreased in the order (Fig. 4.8): MoN/GCA-A > MoN/GAC-A > MoN/Darco > MoN/CGran-A while reaction rates of the method 2 catalysts decreased in the order (Fig. 4.8): MoN/CGran-NH > MoN/GAC-NH > MoN/GCA-NH > MoN/Dacro-NH. The intrinsic activities based on the molybdenum content are also given in Table 4.5. The intrinsic activity trends were similar to the observed reaction rates.

Table 4.5 Catalytic activity of carbon-supported Mo nitride catalysts

Catalyst	Activity ($\times 10^6 \text{ mol } g_{\text{catalyst}}^{-1} \text{ s}^{-1}$)	Intrinsic Activity ($\times 10^4 \text{ molec. Moat}^{-1} \text{ s}^{-1}$)
MoN/GCA-A	1.78	15.47
MoN/GCA-NH	2.12	23.22
CoMoN/GCA	1.06	12.07
MoN/GAC-A	1.67	21.08
MoN/GAC-NH	2.38	21.30
CoMoN/GAC	0.84	8.50
MoN/CGran-A	0.87	8.72
MoN/CGran-NH	3.55	30.28
CoMoN/CGran	1.03	7.82
MoN/Darco-A	1.44	13.57
MoN/Darco-NH	1.58	15.83
CoMoN/Darco	1.37	15.36

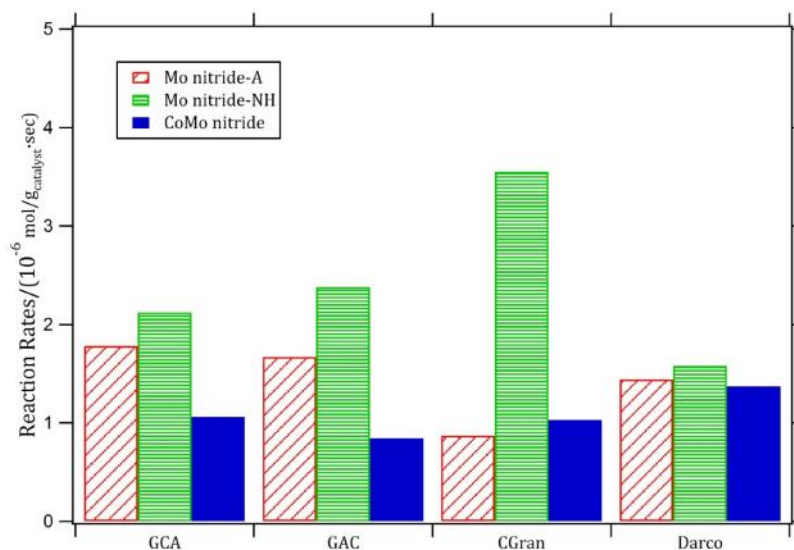


Figure 4.8 Reaction rates of carbon-supported Mo nitride catalysts

Figure 4.8 also shows that the addition of Co did not increase the activity of the catalysts. In fact, the reaction rates of the CoMoN catalysts supported on GCA and GAC carbons were lower than similarly supported monometallic catalysts. For the samples supported on Darco carbon, the reaction rates were similar for the Mo and Co-promoted catalysts.

The selectivity in the transformation of guaiacol was expressed in terms of the phenol/catechol (Phe/Cat) ratio, determined at 10% guaiacol conversion and shown in Fig. 4.9. Molybdenum and CoMo nitride catalysts supported on Darco carbon displayed the highest Phe/Cat ratio. MoN/Darco-NH and CoMoN/Darco-A catalysts displayed similar Phe/Cat ratio which were higher than that for the MoN/Darco-A catalyst. The results also show no observed clear differences in Phe/Cat ratios for the three nitride catalysts supported on the CGran carbon. However, differences in Phe/Cat ratios were observed for the nitrides supported on

GAC and GCA carbons. For nitrides supported on GAC carbon, the highest Phe/Cat ratio was observed for the MoN/GAC-NH catalyst, followed by the CoMoN/GAC-A catalyst and then the MoN/GAC-A catalyst. The trend in Phe/Cat ratios of nitrides supported on GCA carbon was in the reverse order with MoN/GCA-NH catalyst displaying the lowest Phe/Cat ratio.

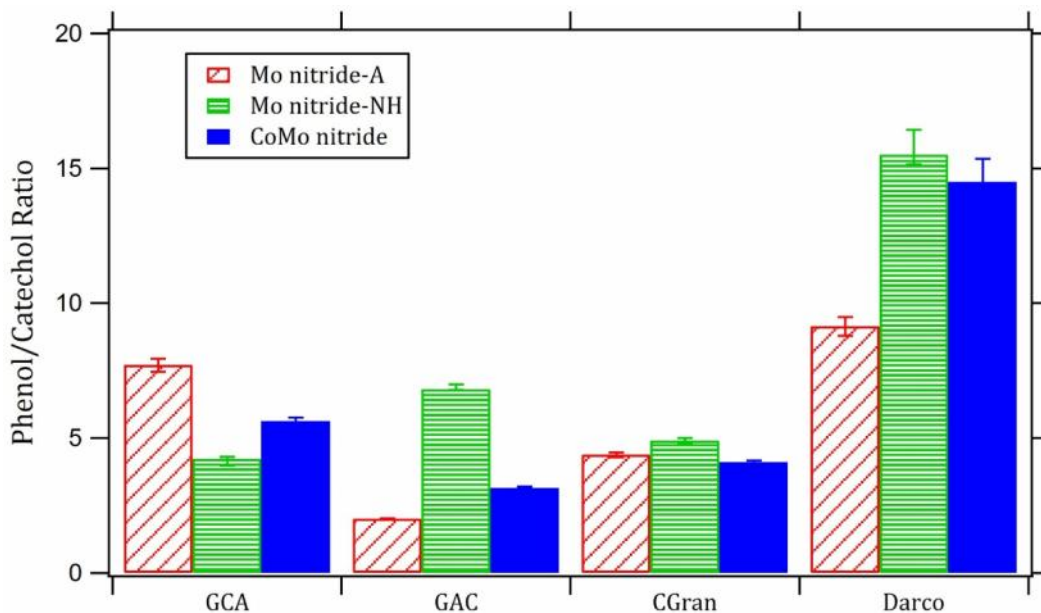


Figure 4.9: Phenol/catechol ratio for metal nitride catalysts

Preliminary investigation of time-on-stream behavior of nitride catalysts compared to a reference commercial sulfided NiMo/Al₂O₃ catalyst was conducted in a continuous flow reactor and shown in Fig. 4.10. The liquid flow rate was chosen to obtain low conversion. The nitride catalysts showed a lower activity relative to the sulfide catalyst during the initial hours on stream. However, the nitride catalysts displayed a higher stability after 4 h on stream. The reference unsupported Mo₂N

catalyst displayed a higher conversion in comparison to the GAC carbon-supported catalyst.

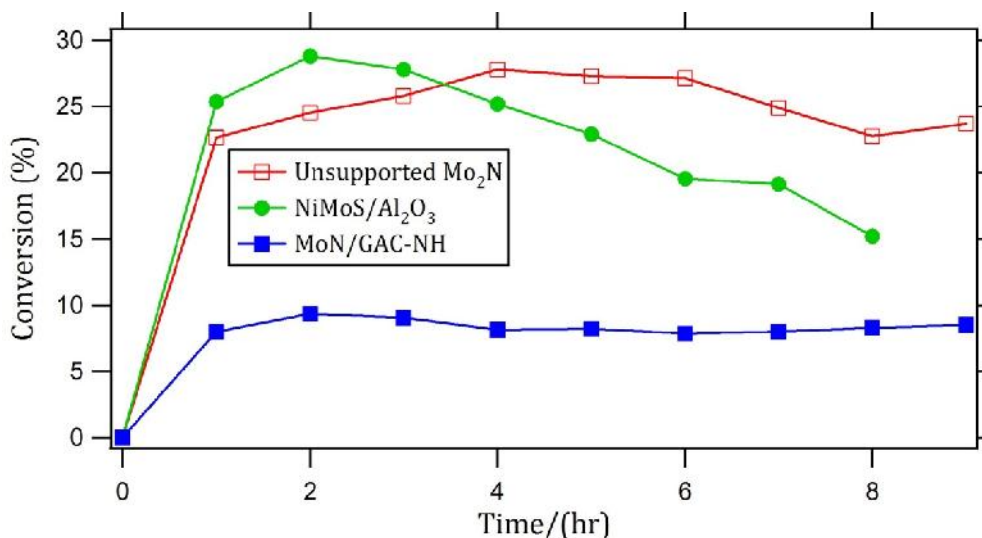


Figure 4.10 Time-on-stream behavior of selected catalysts in terms of total conversion for HDO of guaiacol. The reaction conditions were 300 °C temperature, 3 MPa H₂ pressure, and H₂/Guaiacol ratio of 23.

4.4. Discussion

4.4.1. Physico-Chemical Properties of Nitride Catalysts

The oxidative treatment with HNO₃ influences the concentration and nature of oxygen-containing groups on the surface of the carbon support, which plays an important role in enhancing dispersion [260]. The differences in the textural characteristics of the non-modified and pretreated carbon supports reported in Table 4.1 shows the effects of the oxidation treatment on the carbon support. The loss in the textural properties of CGran and GAC carbon supports may be due to the formation of oxygen groups on the walls of the pores which makes them inaccessible for nitrogen adsorption [272]. On the contrary, improvements in textural properties of Darco and GCA carbon supports suggested the removal of

matter from the pore canals after HNO₃ treatment [282]. Additionally, the variation in the microporous and mesoporous volumes of the Darco carbon support after impregnation and nitridation suggests that the nitride species were preferentially deposited inside the mesopores of the Darco support. On the contrary, textural properties results for the other supports suggest that the Mo₂N species were deposited homogeneously inside the microporous and mesoporous structure of the support.

Aside from the influence on support porosity, surface oxidation of the carbon support also modified the chemical nature of the surface. Comparison of TPD/MS results and total acidity measurements of as-received and pretreated activated carbon supports indicated that the concentration of oxygen-containing surface groups and the surface acidity increased upon HNO₃ pretreatment. The oxidation of the support has been reported to enhance metal dispersion [56, 259, 283].

X-ray diffraction analyses of the metal nitrides supported on carbon were unable to confirm the presence of Mo and CoMo nitride phases in most cases. The XRD patterns of the GCA, GAC and Darco carbon supports presented peaks attributed to metal oxide crystalline impurities like CaCO₃ (JSPDS ref no: 00-041-1475). Since the diffraction patterns of supported metal nitride catalysts were similar to their respective activated carbon supports, the phases of the unidentified impurities may have masked low intensity Mo nitride peaks. However, the XRD patterns of metal nitrides supported on CGran showed evidence of some nitride phases. The tetragonal γ -Mo₂N_{0.78} phase detected on the pattern of the MoN/CGran-

NH catalyst was similarly observed by Gong et al. [284], who reported the preparation of β - $\text{Mo}_2\text{N}_{0.78}/\text{Al}_2\text{O}_3$ materials using a procedure similar to method 2.

The bulk nitrogen compositions of the passivated catalysts prepared via method 1 are compared to the catalysts prepared via method 2. The catalysts prepared via ammonolysis contained higher atomic N/Mo than those prepared via reduction/nitridation using the N_2/H_2 mixture. A similar trend was obtained for N/C atomic surface ratio calculated from XPS data. This may indicate that ammonia is a better nitrogen source than nitrogen for the synthesis of molybdenum nitride catalysts. However, the atomic N/Mo ratios which ranged from 0.77-3.98 were far greater than the theoretical N/Mo ratio (0.5 for Mo_2N and 0.39 for $\text{Mo}_2\text{N}_{0.78}$), suggesting that the values reported in Table 4.3 were not indicative of Mo nitride formation because of significant contributions from nitrogen functions produced after HNO_3 treatment and nitridation of the activated carbon support. This interpretation is consistent with other reports in the literature [274, 281]. The surface Mo and Co species of the reduced, passivated Mo nitride catalysts from XPS data shows the presence of either non-nitrided oxide precursors or oxynitrides. The preferential formation of Mo^{6+} species and/or the absence of Mo^{2+} ($2 < \text{oxidation state} < 4$) could be due to a higher concentration of oxygen-containing surface groups on the carbon support as a result of oxidative treatment. Stronger interactions between Mo species and oxidized carbon supports may have inhibited the formation of fully nitrided groups [251]. In addition, the presence of mixed oxide impurities such as CaMoO_4 on the carbon support may contribute to the formation of Mo^{6+} species [80]. On the other hand, XRD results showed the formation of detectable amounts of nitrides on

the CGran support. These results are in contrast to the XPS results. The differences between the nature of the bulk crystalline structure and the surface structure may be suggestive of the formation of nitrides inside the pores of the support rather than on the surface of the catalyst. This is consistent with the decrease in specific surface area of the support after impregnation and thermal conversion. Another possibility could be that the nitride particles were superficially oxidized when briefly exposed to the environment before XPS measurements. Hence the Mo₂N species located in core of the particles were not detected by XPS, but rather by XRD.

4.4.2. Correlation of Catalytic Activities and Properties

All the molybdenum nitride-based catalysts prepared in this study were active for the HDO of guaiacol. Under the current reaction conditions, phenol was the primary reaction product. Catechol, benzene, cyclohexene and cyclohexane were minor products. The reaction rate data for the molybdenum nitride catalysts, correlated with the dispersion (represented by the Mo/C XPS data), is shown in Figure 4.11. The correlation of HDO activity with dispersion has similarly been reported for sulfided Co-Mo/Carbon and reduced Ni-W/Carbon catalysts [56, 83]. The nitridation procedure influenced the dispersion of Mo oxynitride. From Table 4.4 we show that using two different synthesis methods, dispersion can be varied on carbon supports. Based on the data, synthesis method 2 which involved reduction/nitridation with the N₂/H₂ mixture resulted in more highly dispersed catalysts. This could be related to differences in the amount of nitrogen species on the carbon surface due to cooling to room temperature in either NH₃ or in N₂ following nitridation. Nagai et al. [117] found that cooling in flowing He led to the

desorption of NH_x ($x < 3$) species on the surface of the catalyst, while cooling in flowing NH_3 led to more nitrogen species on the surface of the catalyst. Consequently, in method 2, the nitrogen-cooled catalysts contained more exposed Mo oxynitride on the surface compared to the ammonia-cooled catalysts employed for method 1. The higher HDO activity for method 2 catalysts has further implications in their potential industrial applications where the use of a N_2/H_2 mixture for nitridation offer particular advantages in terms of economic recycling of the nitridation gas used, as well as the elimination of heat transfer problems associated with the large-scale use of NH_3 [99].

The textural and chemical properties of the support could also influence the dispersion of Mo oxynitride. The difference in dispersion between the catalysts supported on the different carbon materials but prepared via method 2 can be explained by the interplay between the mesoporosity ($TPV-V_\mu$) of the support and its surface acidity as a consequence of the concentration of oxygen surface groups. The highest dispersion displayed by MoN/CGran-NH catalyst can be ascribed to the CGran carbon support possessing the most abundant oxygen surface groups and the highest mesoporosity. The large amount of oxygen functional groups on the CGran support (more hydrophilic character), as well as its high mesoporosity, aid in the access of aqueous solution to its internal pore structure which allow homogenous radial distribution of the metal precursor within the pores of the support [251]. This promotes good dispersion of the Mo oxynitride phase [56]. Conversely, the lowest dispersion of the MoN/GCA-NH catalyst could be attributed to the lowest

concentration of oxygen surface (more hydrophobic character) groups as well as the predominance of micropores in the support.

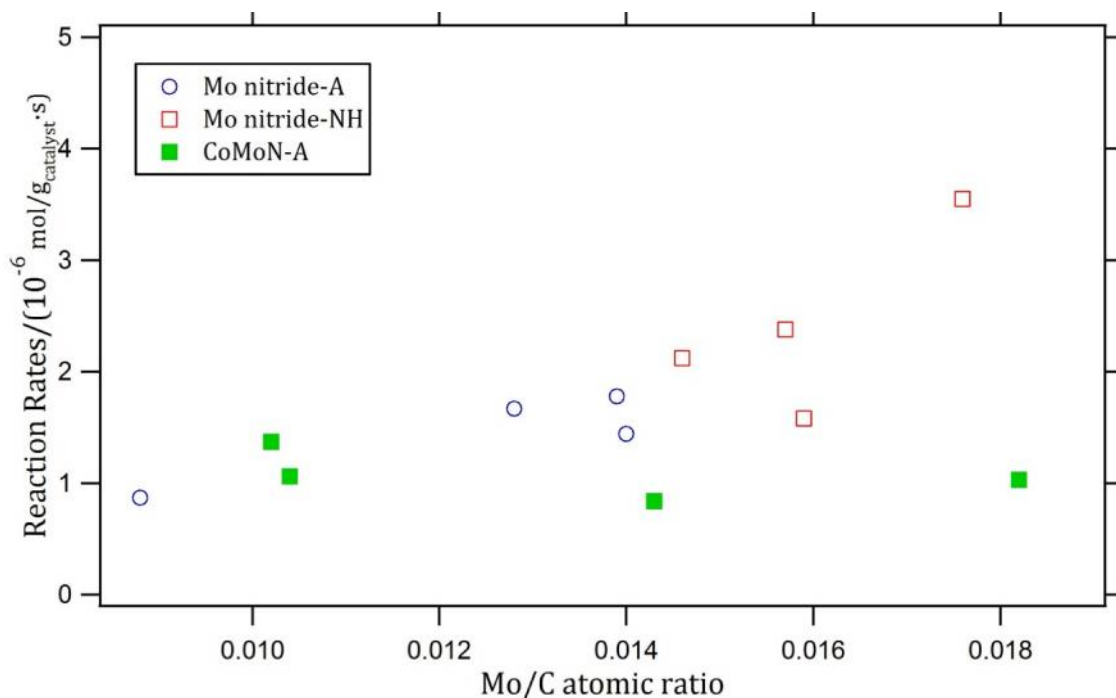


Figure 4.11 Reaction rates vs. XPS Mo/C atomic ratio

The specific activity trend of the different activated carbon-supported nitride catalysts can be related to one or more of these catalysts properties: Mo dispersion, porosity and the surface acidity of the support. Focusing on catalysts which were prepared using the method 2 procedure, the reaction rate appears to be favored by a combination of higher dispersion and higher mesoporosity of the catalyst, as well as the surface acidity of the support (with MoN/Darco-NH being the exception). The higher dispersion of Mo oxynitride and the ease of accessibility of reactants into the mesoporous structure resulted in the observed highest HDO activity for MoN/CGran-NH catalyst. For the catalysts which were prepared by ammonolysis, the reaction rate for guaiacol conversion correlates with dispersion of Mo oxynitride

as shown in Fig. 4.11. However, Mo nitrides supported on Darco carbon catalysts exhibited inferior activity in comparison to Mo nitrides supported on GAC and GCA carbon despite their relatively higher dispersion and higher mesoporosity. This anomaly could be due to an overestimation of the Mo signal obtained by XPS. Considering that the Darco support had the lowest specific surface area of all carbon supports, and that all the catalysts were impregnated with a similar Mo content, this catalyst should contain the largest Mo nitride particle sizes. However, the measured Mo/C atomic surface ratios for Mo nitrides supported on Darco were high probably due to the inability of X-ray photons to penetrate large Mo nitride particles, leading to high intensity of the Mo 3d XPS signal and therefore an overestimation of the Mo/C atomic surface ratios. A similar behavior was previously observed by Lagos et al. [270]. Therefore, this might indicate that the low activity of Mo nitrides supported on Darco carbon catalysts was linked to possible loss of active sites through the formation of aggregates. The discrepancy in the result of this study, however, suggests that atomic scale knowledge of the active phase is needed.

When cobalt was incorporated to form CoMo bimetallic nitride catalysts, the catalysts were not nearly as active as their comparable Mo nitride catalysts as shown in Fig. 4.11. We have previously shown that the addition of Co did not enhance the activity of unsupported Mo nitride catalyst relative to the Mo monometallic nitride [262]. For the bulk nitride catalysts, the diminishing effect of Co was attributed to incomplete formation of the bimetallic nitride, $\text{Co}_3\text{Mo}_3\text{N}$, phase. It is our opinion that this behavior extends to supported nitrides as well.

4.4.3. Selectivity

In contrast to metal hydrogenation catalysts like Ru [63], metal sulfide and metal nitride hydrotreating catalysts have a higher selectivity for HDO reactions relative to hydrogenation of aromatic and olefinic compounds [49, 262]. During the conversion of guaiacol over Mo nitride/carbon catalysts, both demethylation and demethoxylation reactions take place only on the active sites situated on the metal nitrides due to the inertness of the carbon support for this reaction. Blank reactions with only the carbon supports resulted in minimal conversion identical to the thermal conversion with no solid material in the feed. The high production of phenol displayed by all catalysts cannot be ascribed to the acid strength of support or the catalysts. Recently, Sepulveda et al. [285] showed that strong acid sites favor the formation of catechol. On the other hand, the trend displayed by carbon-supported nitride catalysts was similar to results observed for unsupported nitride catalysts (high production of phenol) [262]. These results suggest that the active sites of nitrides or/and oxynitrides were not modified by the support, and that these active sites are very selective to the demethoxylation routes. Figure 4.9 shows that the method of nitridation used to prepare the catalyst slightly changed the phenol/catechol ratio in all the catalysts. Also, the CoMo nitride catalysts displayed different phenol/catechol ratios for each of the supports used. These changes in phenol/catechol ratio are not yet clear. However, we postulate that the active sites of DME and DMO were slightly modified by the nitridation procedure. Figure 4.9 also shows that the nitride supported on Darco carbon displayed the highest

phenol/catechol ratio, indicating that Darco-supported nitride catalysts contained the most DMO sites.

4.4.4. Time-On-Stream Behavior

Developing a robust HDO catalyst for pyrolysis oil upgrading is a considerable challenge. Possible reasons for catalyst deactivation during HDO include coking, poisoning, and loss of active sites through surface chemistry changes [54, 256]. As shown in Fig. 4.10 the nitride catalysts displayed higher stability than the reference sulfided catalyst after 4 h on stream under continuous operation. The gradual deactivation of the sulfided NiMo/Al₂O₃ catalyst could be due to loss of the sulfided phase during HDO reaction. This result provides preliminary evidence to support studies by Monnier et al. [150] which established the relative stability of nitride catalysts under hydrodeoxygenation conditions. However, additional studies on the HDO stabilities of these catalysts at different conditions (i.e. contact time, temperature, pressure, longer time-on-stream) are warranted.

4.5. Conclusion

Four different activated carbon materials with different textural properties were used as supports to prepare Mo nitride catalysts. The supports were acid-pretreated to increase the concentration of surface oxygen groups and enhance catalyst dispersion. The catalysts were prepared by temperature-programmed reaction of the oxidic precursor and either NH₃ or a N₂/H₂ mixture, and evaluated for use in HDO of guaiacol. All the prepared catalysts were active for the HDO of guaiacol, demonstrating rapid production of significant amounts of phenol, indicating that the transformation of guaiacol mostly proceeded through the direct

demethoxylation route, bypassing the formation of catechol. The higher activity per gram of catalyst of carbon-supported Mo nitrides prepared by nitridation/reduction using the N_2/H_2 mixture than similarly supported Mo nitrides prepared by ammonolysis was attributed to higher dispersion of Mo oxynitride. Catalyst dispersion was further influenced by the textural and chemical properties of the support. Over the MoN/CGran-NH catalyst, highly exposed Mo species and high mesoporosity of support led to the most active HDO catalyst. A general diminishing influence on activity was observed after incorporation of Co to prepare bimetallic nitrided catalyst.

CHAPTER 5

COMPARISON OF ALUMINA- AND SBA-15-SUPPORTED MOLYBDENUM NITRIDE CATALYSTS FOR HYDRODEOXYGENATION OF GUAIACOL*

5.1. Introduction

The removal of oxygen from biomass-derived oils through catalytic hydrodeoxygenation (HDO) is receiving considerable attention because of its potential as feedstock for the production of fuels and value-added chemicals. Most of the initial studies on HDO reactions have been conducted over metal sulfides supported on alumina [1, 2]. However, recently there have been significant efforts on the development of catalysts, based on new or modified supports and new active phases, with lower hydrogen consumption and high selectivity towards direct oxygen removal [22]. Guaiacol (2-methoxyphenol) has commonly been used as a model compound for the HDO studies because it is known to exist significantly in bio-oils, because of its propensity for coke formation, and also because of its intransigence to deoxygenation [28]. Several of the studies have reported that the HDO activity and selective transformation of guaiacol to phenol is distinctively influenced by the nature of the support [55, 60]. Catalysts supported on alumina (Al_2O_3) displayed higher activity compared with alternative supports such as silica and carbon owing to higher dispersion of the active phase [55]. However, alumina-supported catalysts suffer from coke formation which limits the lifetime of the catalyst [55]. The benefits of using silica and carbon supports lie in the negligible

* A portion of this chapter has been submitted for publication in *Catalysis Letters*

formation of coke and greater selectivity towards the production of phenol over catechol [55].

Interests in exploring non-sulfided catalysts for HDO have increased due to issues related to contamination of the feed by the sulfiding agent [27, 54]. Novel active phases such as metal nitrides have been shown to be an effective catalyst for HDS [286] and HDN [139] reactions. However, only a limited number of studies have reported their performance for HDO reactions. Recently, Monnier et al. [150] reported activity on γ -Al₂O₃-supported Mo, W, and V nitride catalysts for HDO of oleic acid and canola oil. In a recent study, we demonstrated high activity and rapid demethoxylation of guaiacol to phenol using unsupported Mo nitride catalysts [262]. It is the purpose of this chapter to extend our investigations from bulk nitrides to alumina- and silica-supported nitrides for HDO of guaiacol.

Mesoporous silica materials have generated interests as catalysts support in heterogeneous catalysis owing to their very high specific surface areas, controllable pore diameters, narrow pore size distributions, and large pore volumes. These unique physical properties have made them a more desirable alternative to conventional silica supports enabling the control of catalyst particle size and influencing product selectivity through transport effects [287, 288]. In particular, SBA-15 is of general interest because of its high structure regularity, low-cost and nontoxicity [199]. Studies to extend our understanding of the SBA-15 pore structure and its relationship to transport properties [289], and the hydrothermal stability of SBA-15 [290] have been examined to generate fundamental information relevant to the use of this material as a support in developments of catalysts for production of

biofuels. We focus here on demonstrating the reactivity of SBA-15 silica supported molybdenum nitride catalysts for the HDO of a biomass-derived compound.

In the present study, we report on the synthesis and characterization of molybdenum nitride dispersed on SBA-15 mesoporous silica and γ -alumina. The molybdenum nitride was synthesized by impregnation, oxidation and thermal conversion to the nitride. Thermal conversion was achieved by two different procedures: ammonolysis and reduction/nitridation using hydrogen/nitrogen mixtures. The resulting materials were characterized using nitrogen adsorption-desorption (surface area, porosity), XRD, elemental analysis and XPS, and their activity was compared with commercial sulfided NiMo/Al₂O₃ catalysts for HDO of guaiacol.

5.2. Experimental

5.2.1. Catalyst Preparation

SBA-15 mesoporous silica was synthesized following a reported procedure [208]. In a typical synthesis, 6 g of Pluronic P123 block copolymer (BASF, $M_{avg}=5800$, EO₂₀PO₇₀EO₂₀) was dissolved with stirring in 45 g of deionized water and 180 g of 2 mol L⁻¹ HCl. Then, 12.75 g of tetraethyl orthosilicate (Aldrich, TEOS, 99%) was added to the solution with stirring at 40 °C for 24 h. The homogeneous sol-gel mixture was then transferred into a polymer flask, sealed and heated at 100 °C for 48 h. After filtration and washing with water, the white solid product recovered was air-dried at room temperature for 24 h. The sample was then calcined in air with a heating rate of 1 °C min⁻¹ to 500 °C and held for 10 h. The

alumina support was obtained commercially (Alfa Aesar, γ - Al_2O_3 , 1/8" pellets) and used without any further purification.

The supported molybdenum oxide precursors were prepared by incipient wetness impregnation using aqueous solutions of ammonium heptamolybdate (Fischer Scientific, $(\text{NH}_4)_6\text{Mo}_7\text{O}_{24}\cdot 4\text{H}_2\text{O}$, A.C.S. grade). The mixture was then left overnight at ambient temperature. After impregnation, the samples were dried for 12 h at 110 °C and 120 °C for SBA-15- and alumina-supported samples respectively, and subsequently calcined in a flow of dry air with a heating rate of 1 °C min^{-1} at 500 °C and held for 3 h. The bimetallic oxide precursors were prepared by impregnating the Mo oxide supported materials with an aqueous solution of cobalt (II) nitrate hexahydrate (Acros Organics, $\text{Co}(\text{NO}_3)_2\cdot 6\text{H}_2\text{O}$, 99%), followed by the same drying-calcination procedure described above. The supported oxides were prepared to obtain nominal loading of 8.1 wt% Mo metal content for monometallic samples, 8.1 wt% Mo metal and 2.4 wt% Co metal content for the bimetallic samples. All oxide precursors were sieved to obtain a 180-450 μm particle size. Supported molybdenum nitrides were prepared using the same set-up described previously in Chapter 3: temperature-programmed reaction of the oxidic precursors with NH_3 (Matheson, 99.99 %), or a N_2/H_2 mixture (N_2 , BOC Gases, Grade 5; H_2 , Matheson, 99.99%). The synthesis procedure involved flowing 300 mL min^{-1} of either NH_3 or N_2/H_2 ($\text{N}_2/\text{H}_2 = 5/1$ (v/v)) over the 2.5 g of the supported Mo oxide precursor while the temperature was increased from room temperature to 300 °C in 30 min, then from 300 °C to 500 °C within 5.6 h, and from 500 °C to 700 °C within 1.7 h. The temperature was maintained at 700 °C for 2 h, and then cooled to room temperature

under NH_3 flow for the nitrides prepared via ammonolysis or cooled under nitrogen flow for the nitrides prepared using the N_2/H_2 mixture. Finally, the sample was passivated in a 1 % O_2/N_2 for 12 h at room temperature. For notation, nitrides prepared using ammonia (method 1) have suffix "A", while nitrides prepared using nitrogen-hydrogen mixture (method 2) have suffix "NH".

5.2.2. Catalyst Characterization

Nitrogen sorption isotherms of the nitrides were measured at 77 K using a Micromeritics ASAP-2020 instrument to evaluate the BET specific surface area (S_{BET}), total pore volume (TPV) and average pore diameter (d_{pore}). Prior to the measurements, the samples were outgassed under vacuum following conditions common for these materials: SBA-15-supported materials were outgassed at 200 °C for 8 h, and alumina-supported materials were outgassed at 250 °C for 2 h. S_{BET} was calculated using the adsorption branch of the nitrogen isotherm in the relative pressure range of 0.05 P/P_0 0.25 and the TPV was recorded at $P/P_0 = 0.995$. The primary pore diameter was estimated from the maximum in the BJH pore size distribution.

X-ray diffraction (XRD) patterns of powdered samples were recorded on a PANalytical X'Pert PRO X-ray diffractometer equipped with a graphite monochromator and $\text{CuK}\alpha$ radiation (45 kV, 40 mA) in a parallel beam optical geometry. The standard scan parameters were 15-85° 2θ with a step size of 0.02° and a counting time of 10 s per step. Identification of the phases was achieved by reference to JCPDS diffraction file data.

Elemental analyses of the nitrides were performed by the Analytical Laboratory of the Department of Plant, Soil and Environmental Sciences at the University of Maine, and by Galbraith Laboratory. Mo and Co contents were determined by ICP-AES while nitrogen analyses were determined by a combustion method.

X-ray photoelectron spectra of reduced catalysts were obtained on a VG Escalab 200R electron spectrometer using a Mg K (1253.6 eV) photon source. The passivated catalysts were activated *ex situ* with H₂ at 450 °C for 6 h. After reduction, the samples were cooled to room temperature, flushed with nitrogen and stored in flasks containing isooctane (Merck, 99.8 %), then transferred to the pre-treatment chamber of the spectrometer. The binding energies (BE) were referenced to the C 1s level of the carbon support at 284.9 eV. Intensities of the peaks were calculated from the respective peak areas after background subtraction and spectrum fitting by a combination of Gaussian/Lorentzian functions. Relative surface atomic ratios (Mo/Al or Mo/Si) were determined from the corresponding peak areas, normalized by tabulated atomic sensitivity factors (S_{Mo3d} , S_{Al2p} and S_{Si2p}) [265] as shown in Eq. 4.1. The errors in the quantitative estimation were similar in each sample with a precision of 7%.

$$\frac{Mo}{Si} = \frac{\left(\frac{I_{Mo}}{S_{Mo}} \right)_{3d}}{\left(\frac{I_{Si}}{S_{Si}} \right)_{2p}} ; \quad \frac{Mo}{Al} = \frac{\left(\frac{I_{Mo}}{S_{Mo}} \right)_{3d}}{\left(\frac{I_{Al}}{S_{Al}} \right)_{2p}} \quad (5.1)$$

The acid strength and acid site concentration of some selected catalysts were measured using a potentiometric method [266], whereby a suspension of the

material in acetonitrile was titrated with *n*-butylamine. The variation in electric potential was registered on a Denver Instrument UltraBasic pH/mV meter.

5.2.3. Catalytic Activity Measurements

Guaiacol HDO activity measurements were carried out in a 300 mL stainless steel batch reactor (Parr Model 4841), at 300 °C and under a hydrogen pressure of 5 MPa. Details of the catalyst activation and reaction measurements are given in 3.2.3. As a basis for comparison, commercial Ni-Mo/Al₂O₃ catalyst (Procatalyse HR 346) was pre-sulfided using a 10 vol. % H₂S in H₂ mixture at 350 °C for 3 h and tested for the conversion of guaiacol. The catalytic activity was expressed by the initial reaction rate which was calculated from the slopes of the conversion vs. reaction time plot, and by the intrinsic activity (i.e. the reaction rates per molybdenum atom).

5.3. Results and Discussion

5.3.1. Catalyst Properties

Nitrogen sorption analyses were performed to determine the difference in support morphology between -Al₂O₃ and SBA-15 materials. The N₂ adsorption-desorption isotherms and pore size distribution (PSD) of alumina and SBA-15 materials are shown in Fig. 5.1. The isotherm and PSD for the as-prepared SBA-15 support were consistent with previously reported results for this material [208, 209]. According to IUPAC classifications, the N₂ isotherms (Figs. 5.1A and 5.1B) belong to a type IV isotherm which is typical of mesoporous materials [291]. The isotherms for the SBA-15 materials in Fig. 5.1B show a sharp inflection in the relative pressure (P/P₀) range from 0.7 to 0.8, indicative of the presence of uniform

pore size distribution [177]. The isotherms of γ - Al_2O_3 -based materials revealed a sharp inflection in the P/P_0 range from 0.8 to 1.0, suggestive of wide pore size distribution. Figures 5.1A and B also show that the quantity of nitrogen adsorbed and the P/P_0 position of the inflection point on the isotherm of the support decreased after impregnation and nitridation.

The BJH pore size distributions (PSD), as derived from the desorption branch of the N_2 isotherm of the materials under study, are shown in Fig. 5.1C and 5.1D. As seen in Fig. 5.1C and 5.1D, the SBA-15 mesoporous silica support yielded a narrow pore size distribution centered at 8.3 nm, while the alumina support yielded a broad pore size distribution centered at 9.3 nm. In addition, PSD curves of metal nitrides supported on SBA-15 mesoporous silica revealed a bimodal pore distribution system with peaks at 4.5 nm and 7.2 nm, suggesting the presence of small complementary pores and ordered mesoporous pores respectively [288, 292].

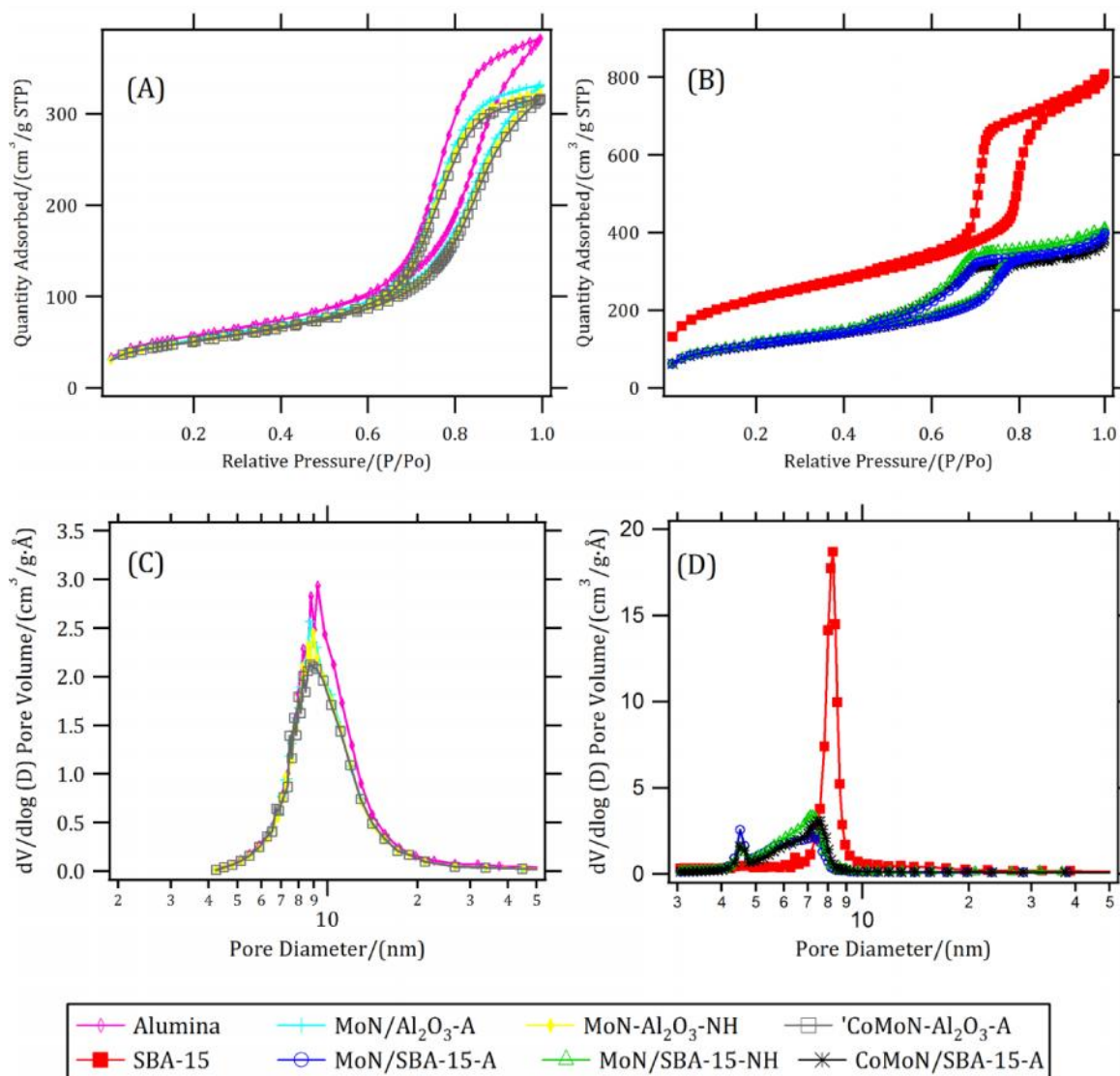


Figure 5.1 Morphology of alumina- and SBA-15-supported materials. N_2 adsorption-desorption isotherms of (A) alumina-supported materials and (B) SBA-15-supported materials; BJH pore size distributions (C) alumina-supported materials (D) SBA-15-supported materials

The BET surface areas, total and micropore volumes, and primary pore diameters are summarized in Table 5.1. The SBA-15 silica support had the higher surface area (S_{BET}) and higher total pore volume (TPV) compared to the γ - Al_2O_3 support. After Mo impregnation and thermal conversion, the surface areas, pore diameters and total pore volumes in both supports decreased. These decreases may

generally be attributed to partial blockage of the pores of the support and a dilution effect due to the presence of Mo species inside the channels of the support [175]. The partial blockage of the pores was more intense for SBA-15 than for γ -Al₂O₃ support. This difference in behavior could be due to the narrower pores of the SBA-15 silica support which is relatively easier to block.

Table 5.1 Adsorption properties of passivated nitride catalysts

Sample	S_{BET} (m ² g ⁻¹)	TPV (cm ³ g ⁻¹)	d_{pore} (nm)
-Al ₂ O ₃	207	0.62	9.3
MoN/Al ₂ O ₃ -A	191	0.51	8.6
MoN/Al ₂ O ₃ -NH	183	0.50	8.9
CoMoN/Al ₂ O ₃ -A	182	0.49	8.9
SBA-15	818	1.25	8.3
MoN/SBA15-A	418	0.75	7.3
MoN/SBA15-NH	397	0.70	7.2
CoMoN/SBA15-A	387	0.62	7.5

Figure 5.2 shows the x-ray diffraction profiles of the supports and catalysts used in this study. Examination of the XRD patterns of Mo and CoMo nitrides supported on alumina revealed only diffraction peaks associated with the supports. Broad diffraction peaks characteristic of γ -Al₂O₃ (JSPDS ref no: 010-0425) may have masked the nitride peaks. The XRD patterns of MoN/SBA-15-A and MoN/SBA-15-NH catalysts showed broad peaks for crystalline γ -Mo₂N ($2\theta = 37.13, 43.41,$ and 63.03) and β -Mo₂N_{0.78} ($2\theta = 37.51, 43.11, 62.89,$ and 75.45) respectively. The estimated average diameter of the Mo nitride crystals from the diffraction peaks of the MoN/SBA-15-A and MoN/SBA-15-NH catalysts were 2 and 3 nm respectively. The XRD pattern collected for the CoMoN/SBA-15-A catalyst revealed the formation of Mo₂N but no evidence of Co₃Mo₃N phase. The presence of Mo₂N as the only phase

observed in this catalyst may suggest that the particle size of the $\text{Co}_3\text{Mo}_3\text{N}$ phase was small and below the XRD detection limit. It is evident from the XRD results that the crystal structure of supported Mo nitride particles are closely related to their nitridation and purging treatment during the formation of the particles: catalysts prepared by method 1 resulted in $\gamma\text{-Mo}_2\text{N}$ particles and those prepared by method 2 resulted in $\beta\text{-Mo}_2\text{N}_{0.78}$.

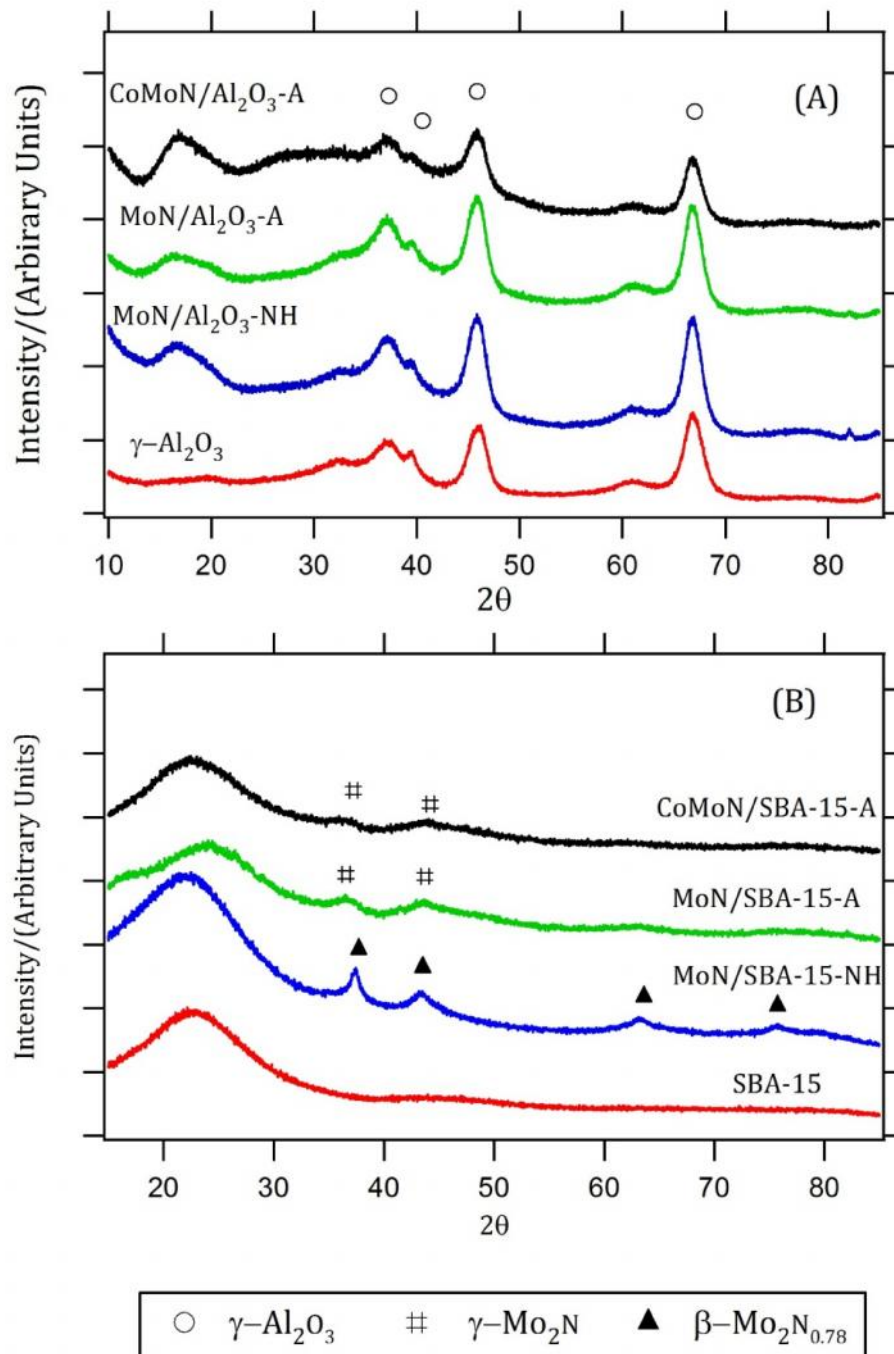


Figure 5.2 XRD patterns of (A) alumina-supported materials and (B) SBA-15-supported materials

Elemental analyses of passivated, supported Mo and CoMo nitrides are listed in Table 5.2. The nitrogen contents for nitride samples from method 1 were higher compared to samples prepared from method 2 in both supports. The lower nitrogen content for the method 2 samples may be due to purging the samples in flowing nitrogen after nitridation which removed weakly-bonded NH_x species [117]. The atomic N/Mo ratios of the nitride catalysts are presented in Table 5.2. While the theoretical N/Mo is 0.5 and 0.39 for $\gamma\text{-Mo}_2\text{N}$ and $\beta\text{-Mo}_2\text{N}_{0.78}$ respectively, it is plausible that excess N could reside in interstitial sites and defects like grain boundaries. These findings, in addition to the absence of diffraction peaks for crystalline Mo nitride phase on the alumina-supported catalyst, suggest that small crystallites of Mo nitrides below the XRD detection limit were formed on the catalysts. This is consistent with other report in the literature for $\text{Mo}_2\text{N}/\text{Al}_2\text{O}_3$ catalysts [293].

Table 5.2 Chemical composition of passivated nitride catalysts

Catalyst	Mo (wt %)	Co (wt %)	N (wt %)	N/Mo atomic ratio
MoN/ Al_2O_3 -A	8.39	-	1.76	1.44
MoN/ Al_2O_3 -NH	8.74	-	0.49	0.38
CoMoN/ Al_2O_3 -A	8.33	1.87	1.66	1.54
MoN/SBA15-A	7.22	-	2.26	2.15
MoN/SBA15-NH	6.67	-	0.92	0.95
CoMoN/SBA15-A	7.34	1.95	1.42	1.32

Table 5.3 lists a summary of XPS results of the surface composition and oxidation states of the components in the reduced, passivated Mo nitride catalysts. The BE values of the Mo $3d_{5/2}$, N 1s, Co $2p_{3/2}$, Si 2p and Al 2p core levels and the surface atomic ratios are presented in Table 5.3. The XPS binding energies of Mo 3d

for all the samples contains BE values near 229.0, 230.5 and 232.6 eV. The Mo 3d energy of 229.0 ± 0.2 eV is typical of Mo⁺ ($2 < < 4$) assigned to Mo₂N species [294]. The binding energies of 230.5 ± 0.1 eV and 232.6 ± 0.3 eV are typical of Mo⁴⁺ and Mo⁶⁺ respectively in molybdenum oxynitrides [280]. This result indicates that Mo₂N and Mo oxynitrides coexist on the surface of all the catalysts. The surface distribution of the Mo oxidation states in the Mo 3d (compiled in parentheses in Table 5.3) shows that molybdenum oxynitride was the dominant surface phase, while Mo₂N particles were distributed from 9 to 30 %. This result indicates that despite reduction of the passivated nitride catalysts at 450 °C, the sample surfaces were mainly oxynitrides rather than nitrides. Table 5.3 also shows that higher amount of Mo₂N (Mo⁺) were formed on the surface of the SBA-15 silica support than on the γ -Al₂O₃ support, indicating that more nitrogen-deficient patches of Mo were on the surface of the former. This behavior is attributed to weaker metal-support interactions of the SBA-15 silica support which leads to relatively easier reducibility of the MoO₃ precursor. The XPS results also show that the Mo⁺ content on the method 2 catalysts surface were higher than the method 1 catalyst. The Co 2p_{3/2} binding energy for the supported-CoMo nitrated samples of 778.4 ± 0.1 eV is within the range of the reported BE of Co⁰ for cobalt-nitride species [113], while the BE = 781.5 ± 0.2 eV compares well with Co³⁺ cation of Co-Mo oxynitrides [113]. The amount of Co³⁺ species in the bimetallic nitrides was higher than the amount of zero-valent cobalt. Thus, the most abundant surface metal species in the bimetallic nitrides were the oxynitrides. The N 1s core-level spectra made three contributions: the BE = 394.4 ± 0.3 eV could be attributed to the Me-O-N bond (Me: Mo, Co etc.)

[295]; the BE = 396.7 ± 0.3 eV is close to Mo-N bond [113]; the BE near 398.5 ± 0.3 eV has been reported to be assigned to nitrogen atoms trapped in the grain boundary of Mo nitrides [126]. Finally, the BEs of 103.4 eV obtained for SBA-15-supported catalysts and 74.5 eV obtained for alumina-supported catalysts were identical to the Si 2p and Al 2p of the parent SiO₂ [296] and Al₂O₃ respectively [119]. This suggests that the alumina and SBA-15 silica supports were not nitrated under the synthesis condition.

Table 5.3 XPS binding energies (eV) and surface atomic ratios of reduced, passivated nitride catalysts

Catalyst	Mo3d _{5/2}	N1s	Co2p _{3/2}	Si2p or Al2p	Mo/ Si(Al)	N/ Si(Al)	Co/ Si(Al)
MoN/SBA15-A	229.0 (25)	394.4 (26)	-	103.4	0.033	0.084	-
	230.5 (29)	396.5 (35)					
	232.9 (46)	398.7 (39)					
MoN/SBA15-NH	228.9 (27)	394.4 (28)	-	103.4	0.035	0.086	-
	230.4 (31)	396.4 (38)					
	232.6 (42)	398.5 (34)					
CoMoN/SBA15-A	228.9 (30)	394.4 (33)	778.4 (19) 781.7 (81)	103.4	0.034	0.108	0.013
	230.5 (28)	396.5 (38)					
	232.6 (42)	398.6 (29)					
MoN/Al ₂ O ₃ -A	228.9 (9)	394.7 (17)	-	74.5	0.099	0.236	-
	230.5 (22)	396.7 (36)					
	232.7 (69)	398.7 (47)					
MoN/Al ₂ O ₃ -NH	229.0 (15)	394.5 (19)	-	74.5	0.133	0.349	-
	230.5 (25)	396.3 (34)					
	232.6 (60)	398.4 (47)					
CoMoN/Al ₂ O ₃ -A	228.9 (19)	394.5 (29)	778.5 (18) 781.5 (82)	74.5	0.108	0.386	0.038
	230.5 (30)	396.5 (35)					
	232.6 (51)	398.3 (36)					

The XPS Mo 3d/Al 2p (or Si 2p), N 1s/Al 2p (or Si 2p), and Co/Al 2p (or Si 2p) atomic ratios for the reduced, passivated catalysts are shown in Table 5.3. The Mo/Al surface atomic ratio was greater than the Mo/Si atomic ratio in all the catalysts. This indicates that SBA-15-supported catalysts possess their molybdenum species located inside the inner silica porous structure while the Al₂O₃-supported

catalysts had their molybdenum species located on the external support surface of the catalyst. This is in good agreement with their N₂ adsorption-desorption isotherms of the passivated catalysts (shown in Fig. 5.1) which shows a more pronounced decrease in the quantity of N₂ adsorbed and a shift of the hysteresis loop to lower P/P₀ values of the SBA-15-supported catalysts, indicating the presence of particles in the porous structure. Table 5.3 also shows that catalysts prepared by reduction/nitridation using a N₂/H₂ mixture produced more exposed Mo and N species on the surface of the support than catalysts prepared by ammonolysis. This is consistent with our work on carbon-supported nitrides in chapter 4 [297]. However, this behavior is inconsistent with the estimates of dispersion based on particle sizes determined by XRD of SBA-15-silica supported catalysts. These results suggest that the nitride species deposited on the surface were different from those deposited inside the pores of the support. In other words, the SBA-15 silica support promoted the formation of nitrogen-deficient patches of Mo on the nitride surface, while the formation of nitrides with higher amount of nitrogen was preferentially located inside the silica pore.

5.3.2. Reactivity

Activity of supported metal nitride catalysts: Al₂O₃ vs. SBA-15. In the present study, we evaluated and compared the catalytic properties of Mo nitrides supported on SBA-15 mesoporous silica and Mo nitrides supported on conventional alumina. Figure 5.3 shows the evolution of reactants and products during the HDO of guaiacol on supported Mo nitride catalysts. The transformation of guaiacol during HDO reactions follows the reaction scheme shown in Fig. 5.4. According to this scheme,

guaiacol either undergoes demethylation (DME) to form catechol, which can then be transformed to phenol, or direct demethoxylation (DMO) to form phenol. Further deoxygenation could occur to produce benzene, cyclohexene and cyclohexane. Figure 5.3 shows that there were significant differences between alumina- and SBA-15-supported catalysts in terms of the changes in products concentrations with time. Over the alumina-supported catalysts, catechol was the major early product while phenol surpassed catechol at longer reaction time. The SBA-15-supported catalysts produced more phenol than catechol at both lower and higher conversions. On the basis of the catalytic mechanism shown in Fig. 5.4, alumina-supported catalysts proceeded through both the DME and DMO pathways, while the mesoporous silica-supported catalysts mainly proceeded through the DMO pathway. These results are consistent with previously published work by Centeno et al. [55] on metal sulfide catalysts. Trace amounts of deoxygenated products (denoted HDO in Fig. 5.3) such as benzene, cyclohexene and cyclohexane were also observed.

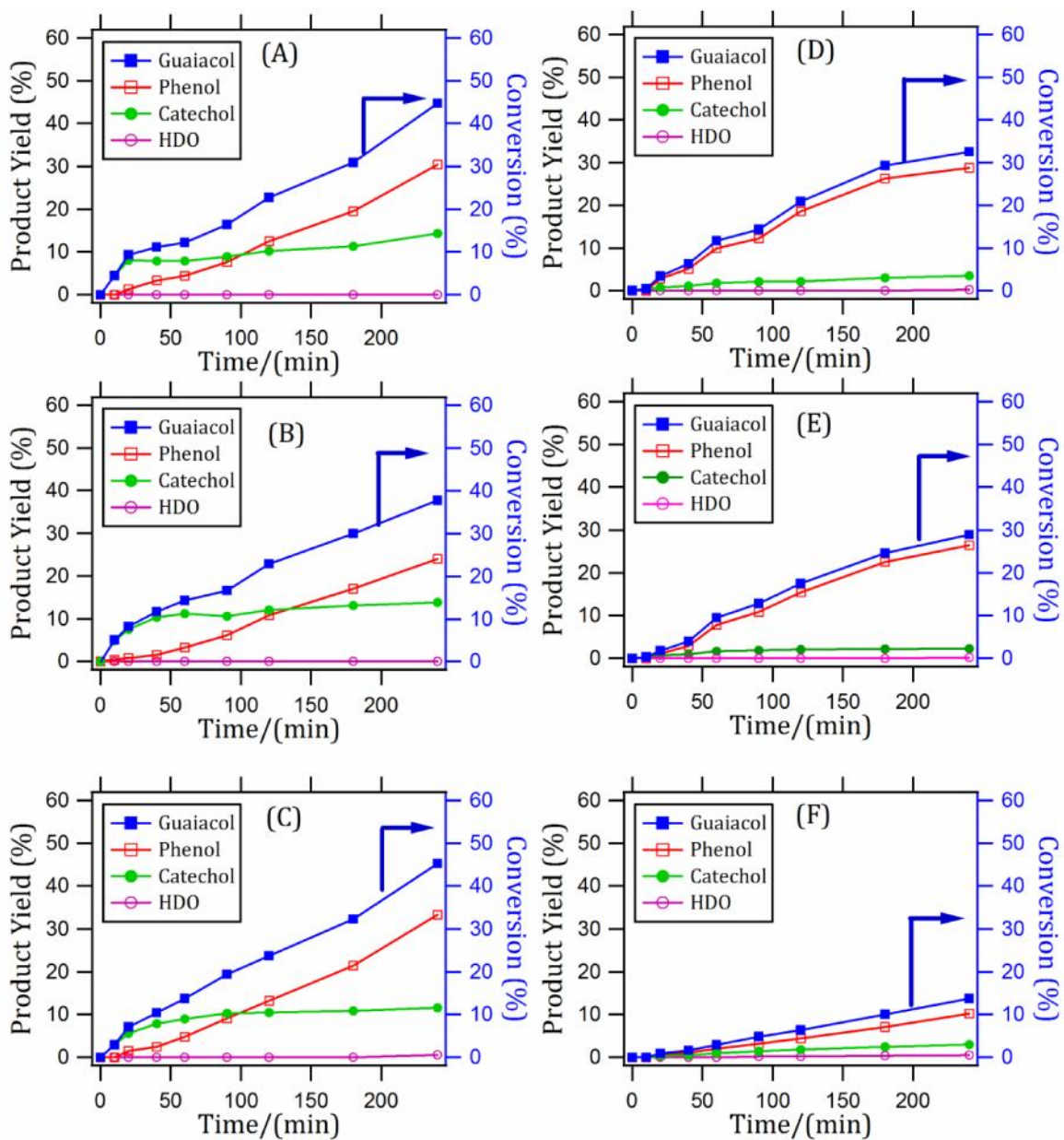


Figure 5.3 Yield of products and conversion of guaiacol as a function of time for (A) MoN/Al₂O₃-A (B) MoN/Al₂O₃-NH (C) CoMoN/Al₂O₃-A (D) MoN/SBA-15-A (E) MoN/SBA-15-NH, and (F) CoMoN/SBA-15-A catalysts

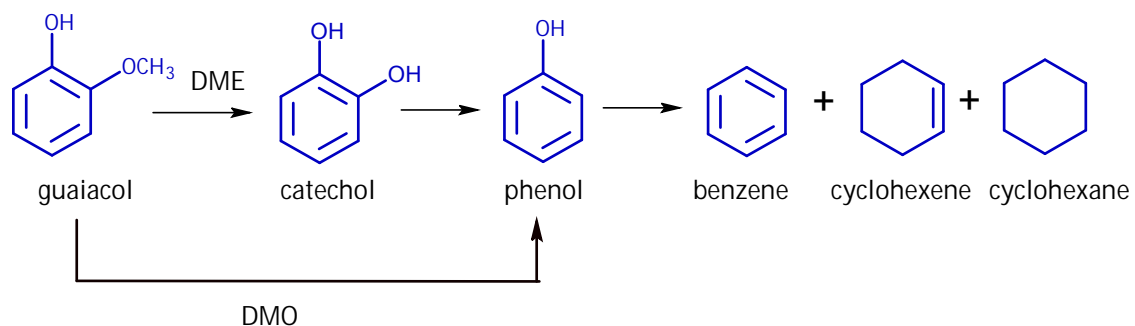


Figure 5.4: Hydrodeoxygenation pathways of guaiacol. Adapted from Ferrari et al. [81]

The activities of the catalysts expressed as the reaction rates, as well as the calculated intrinsic activities are presented in Table 5.4. The reaction rates were calculated from the initial reaction during the transformation of guaiacol shown in Fig. 5.3. Blank reactions with the Al_2O_3 and SBA-15 silica supports alone showed an appreciable conversion of guaiacol to catechol by the former while no significant conversion was observed for the latter. The reaction rates of the Al_2O_3 -supported catalysts were about three times higher than the SBA-15-supported catalysts. The differences in catalytic activity between Mo nitride supported on alumina and SBA-15 in this study was not related to the acid strength of the metal nitride/support catalytic system. The acid strength of MoN/ Al_2O_3 -A and MoN/SBA-15-A catalysts, estimated from potentiometric titration of the catalyst in acetonitrile with *n*-butylamine [266], were identical with the initial electrode potential of 120 mV and 115 mV respectively. Thus, the higher reaction rates displayed by the alumina-supported nitride catalysts could be explained by their faster conversion of guaiacol to catechol and coke [54]. To support this assertion, reaction rates of alumina-supported catalysts were also determined at higher guaiacol conversion after the

rate of production of catechol had slowed down (these values are reported in parentheses in Table 5.4). Laurent and Delmon also reported that the conversion of guaiacol over the alumina-supported metal sulfided catalysts produced two ranges of conversion rates, and interpreted this observation as due to the formation of coke [48, 54]. The authors speculated that at 30-60 % guaiacol conversion, the active sites responsible for coking would be deactivated and the calculated reaction rates corresponded well to the activity of the catalyst [48, 54]. However, the slowing down of the conversion rate of guaiacol over the alumina-supported catalyst could also be due to inhibition of the active sites caused by coke deposition. From Table 5.4, the reaction rates of the Al₂O₃-supported nitride catalysts in parentheses were similar to that of the SBA-15-supported nitride catalysts, further proving that the differences in reactivities between the two supports were due to catechol formation.

Table 5.4 Reaction rates of catalysts under study

Catalyst	Reaction Rate $\left(\begin{array}{c} \times 10^6 \\ mol\ g_{catalyst}^{-1} s^{-1} \end{array} \right)$	Intrinsic Activity $\left(\begin{array}{c} \times 10^4 \\ molec. Moat^{-1} s^{-1} \end{array} \right)$
MoN/Al ₂ O ₃ -A	5.75 (2.20)*	65.8
MoN/Al ₂ O ₃ -NH	5.13 (1.63)	56.4
CoMoN/Al ₂ O ₃ -A	4.39 (2.09)	50.6
MoN/SBA15-A	2.08	27.7
MoN/SBA15-NH	1.60	23.0
CoMoN/SBA15-A	0.72	9.4
NiMoS/Al ₂ O ₃	2.50 (2.22)	25.7

The intrinsic activities, calculated using experimental reaction rate data normalized by the molybdenum content of the catalyst, are presented in Table 5.4.

* Reaction rates determined from slopes at higher conversions

The trend in the initial intrinsic activities was similar to that of the initial reaction rates.

Figure 5.5 shows the selectivity in the conversion of guaiacol, expressed by the phenol/catechol ratio which was calculated at 10 % conversion of guaiacol. SBA-15-supported catalysts produced significantly more phenol than catechol, while the alumina-supported catalysts produced more catechol than phenol. These results indicate a higher selectivity of the nitrides supported on alumina towards the demethylation pathway compared to that of nitrides supported on SBA-15 which had a higher capacity for aromatic carbon-oxygen hydrogenolysis. The results confirm that both support modified the active sites of the nitrides. Hydrogenolysis of the methyl-oxygen bond, as well as hydrogenolysis of the $C_{\text{aromatic}}\text{-OCH}_3$ bond, has been suggested to take place on both the support surface and on the active species [56]. However, since the bare SBA-15 silica support was catalytically inert for HDO reaction the higher phenol/catechol ratio displayed by these catalysts may be attributed primarily to the DMO sites on the Mo nitride and oxynitride.

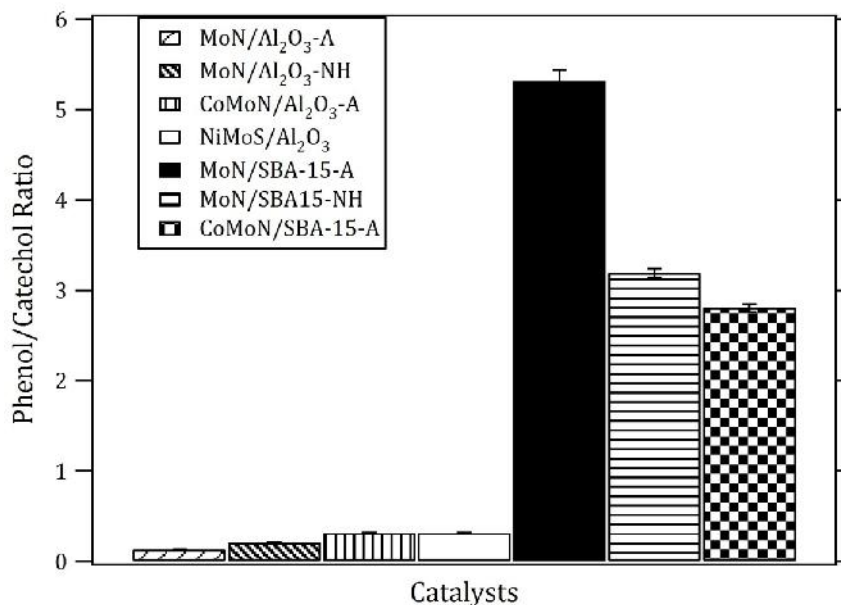


Figure 5.5 Phenol/catechol ratio for catalysts under study

Activity of differently-synthesized Mo nitride catalysts: Method 1 vs. Method 2. It can be observed in Table 5.4 that the nitride catalysts prepared using method 1 displayed higher reaction rates than the nitride catalysts prepared using method 2. In general, it was concluded that the higher bulk N/Mo ratio (shown in Table 5.2) and the formation of γ -Mo₂N phase (deduced from XRD) by the method 1 synthesis procedure led to a more favorable conversion of guaiacol than the formation of β -Mo₂N_{0.78} by the method 2 procedure. This is consistent with the results of unsupported Mo nitrides in chapter 3, which revealed higher guaiacol conversion for catalysts that contain predominantly γ -Mo₂N in comparison to catalysts that contain β -Mo₂N_{0.78} particles [262]. There is no observable relationship between the activity and the distribution of surface Mo nitride and oxynitride species, suggesting that there might be multiple active phases with differing activities for guaiacol conversion in the molybdenum-oxygen-nitrogen system. A

study on the atomic scale knowledge of the active phase of Mo nitride and oxynitride for HDO catalysis is warranted.

Figure 5.5 shows differences in phenol/catechol ratios for the SBA-15-supported nitride catalysts prepared using different nitridation procedures. The higher phenol/catechol ratio obtained for the MoN/SBA-15-A catalyst could also be due the presence of the γ -Mo₂N crystalline phase which has a greater capacity to directly cleave the C_{aromatic}-OCH₃ bond [262]. Also from Fig. 5.5, it can be observed that the alumina-supported catalysts displayed similar phenol/catechol ratio. This behavior is not clear. However, it could be due to the dominant effect of the Lewis acidity of the alumina support (forming catechol) which slightly modified the active sites.

The addition of Co to the supported Mo nitrides did not enhance the conversion rate of guaiacol. In fact, the reaction rate was 1.3 times lower for CoMoN/Al₂O₃-A catalyst as compared to non-promoted MoN/Al₂O₃ catalysts, while the CoMoN/SBA-15-A catalyst was about three times less active as compared to non-promoted MoN/SBA-15-A catalysts. This could be explained by the incomplete formation of Co₃Mo₃N phase (from XRD and XPS results) which typically have a higher C-X (X: S or N) hydrogenolysis rate than monometallic Mo nitride catalyst [135, 255].

Comparison of nitrides to commercial sulfided NiMo/Al₂O₃ catalyst. The activity of a commercial sulfided NiMo/Al₂O₃ catalyst was also tested for the HDO of guaiacol and given in Table 5.4. The activity per gram of catalyst obtained with the commercial reference catalyst was two times lower as compared to the Mo nitrides

supported on alumina. Furthermore, the alumina-supported nitrides showed more than two times higher activity per Mo atoms than the sulfided NiMo/Al₂O₃ catalyst. On the contrary, the sulfided catalyst was more active than the most active metal nitride supported on SBA-15 mesoporous silica. This preliminary comparison of results is encouraging for the application of nitrides for HDO catalysis.

The phenol/catechol ratio as shown in Fig. 5.5 of the sulfided NiMo/Al₂O₃ catalyst was comparable to the Mo nitrides supported on alumina. This result further proves the overall capacity of alumina-supported catalysts for demethylation of guaiacol, regardless of the active phase [48]. This is in good agreement with other reported findings which indicated that Lewis acid sites of the alumina support were mainly responsible for the conversion of guaiacol to catechol [48, 54]. Although the Mo nitride catalysts supported on SBA-15 mesoporous silica showed lower activity, they have particular advantages over the alumina-supported nitride and sulfide catalysts in terms of the higher specificity for phenol over catechol. This has implications with regards to lower consumption of hydrogen and less formation of coke in HDO applications. In addition, the ability to finely tune pore sizes in ordered mesoporous silica supports offers other opportunities to influence activity and selectivity by controlling catalyst dispersion and the diffusion of reactants and products from the active catalyst site.

5.4. Conclusion

We have prepared alumina- and SBA-15-supported Mo nitride catalysts and showed their reactivity for the HDO of guaiacol in terms of reaction rates and phenol/catechol ratio. Catalysts were synthesized by nitridation using two

procedures: thermal conversion in ammonia and thermal conversion in nitrogen/hydrogen mixtures. Nitridation using ammonia resulted in higher activities in both supports and correlated with the formation of γ -Mo₂N and a higher N/Mo ratio in the catalyst. Nitridation using nitrogen/hydrogen resulted in the formation of β -Mo₂N_{0.78}. Consistent with findings for MoS₂-based catalysts on alumina, the alumina supported nitrides resulted in significant conversion of guaiacol to catechol. The silica supported catalysts resulted in minimal catechol production, and maximum phenol production. For the catalysts studied here, the major factor influencing activity was the active phase whereas the major factor influencing phenol production over catechol production was the support which modified the nature of the active sites of nitrides. All nitride catalysts compared favorably to a conventional sulfided NiMo/Al₂O₃ catalyst. The addition of cobalt did not have a promoting effect on HDO activity. These results are encouraging for the application of ordered mesoporous silicas as supports for molybdenum nitride based catalysts in HDO applications.

CHAPTER 6

CONCLUSIONS AND RECOMMENDATIONS

6.1. Conclusion

In this thesis, the synthesis, characterization and reactivity of various catalysts for reactions related to the thermochemical conversion of woody biomass to fuels and chemicals were described. The experimental work was divided into two main sections. The first section dealt with the development of a suite of mesoporous silica-supported cobalt catalysts with different pore diameters for evaluation in the Fischer-Tropsch reaction. The main difference between our approach and other previously reported silica-supported FT Co catalysts was the thorough characterization of the structure and reactivity of all catalysts at three different stages in the catalytic process. This approach was important to investigate the effects of variable pore diameters on relative mole fractions of the different phases, on particle diameters, and on turnover frequency (TOF) at various stages of catalyst thermal history.

The key results from the first sections are summarized below:

- All the materials contained three cobalt phases including two metal phases (Co_{hcp} and Co_{fcc}) with significantly different particle size distributions.
- Detailed analyses from TEM, XRD and XANES were consistent with an interpretation in which the Co_{hcp} phase consisted of small metal particles while the Co_{fcc} particles were larger and more closely correlated with the pore size of the supports.

- The presence of CoO reflects the material's difficulty to fully reduce. Smaller pore diameter supports yielded a larger mole fraction of CoO which was explained by significant contributions of surface energy and hindered diffusion in and out of the pores.
- Calculated turn-over frequency based upon our more extensive three-phase cobalt dispersion analysis of the catalysts characterized after the FT reaction led to substantial improvement in the correlation between TOF and pore diameter over the 3-13 nm range. The increase in catalytic effectiveness with increasing pore diameter was attributed to facilitated diffusion of reactants and products in larger pore materials.

The second section detailed the HDO of guaiacol over unsupported and supported molybdenum nitride catalysts at 300 °C and 5 MPa. The reaction conditions and model compound used have been demonstrated previously in the literature as a test reaction to improve the processing and storage properties of bio-oil. The main novelty of this research was the evaluation of the performance of nitride catalysts, prepared using different synthesis procedure, for the hydrodeoxygenation of a lignin model compound. The research highlights from this section are:

- Nitridation of MoO₃ in either flowing ammonia or a nitrogen/hydrogen mixture resulted in Mo₂N catalyst with different phases present, as were determined by XRD. The nitriding and purging treatment procedures also slightly modified the active sites for demethylation and demethoxylation reaction.

- For unsupported nitride catalysts, the activity (guaiacol conversion) and phenol/catechol ratio within the products indicative of HDO activity was related to the purity of crystalline phase initially present in the catalyst. The highest activity was obtained by the catalyst containing only γ -Mo₂N phase and having the highest N/Mo atomic ratio.
- The results were consistent with hydrodeoxygenation proceeding predominantly by demethylation on the alumina supports. However, all the other catalysts (unsupported, carbon- and SBA-15-supported catalysts) showed the ability to catalyze the hydrodeoxygenation of guaiacol to phenol through direct demethoxylation. This observation shows that the active sites of nitrides and/or oxynitrides were not modified by the support, and that they are very selective to the demethoxylation route. This has potential impact in improving the economics of bio-oil upgrading by minimizing hydrogen consumption through selective deoxygenation. The lack of catechol production using the unsupported nitride catalysts and the carbon- and SBA-15-supported nitride catalysts is important in minimizing coking reactions, preventing rapid catalyst deactivation. This opens up possibilities for utilizing silica supports with highly controlled pore sizes to possibly influence product distribution in HDO of more diverse feed streams derived from biomass conversion processes.
- For carbon-supported nitride catalysts, Mo nitrides prepared using a N₂/H₂ mixture resulted in more highly dispersed catalysts and consequently more active catalysts relative to those prepared using ammonolysis.

- The HDO activity of the carbon-supported catalyst was related to interplay between dispersion of Mo species and the pore size distribution of the different carbon supports.
- The alumina-supported catalysts displayed higher activities compared to the SBA-15 silica-supported catalysts which were due to catechol production, an effect of the alumina support.
- The addition of cobalt generally did not have a promoting effect on catalytic activity. However, unsupported bimetallic nitride catalyst with both $\text{Co}_3\text{Mo}_3\text{N}$ and Mo_2N present displayed an improvement in the production of hydrocarbons.

6.2. Recommendation

The research work done in the first section provided additional insights into which fundamental factors affect Fischer-Tropsch catalytic activity. A significant finding from this study was the importance of accounting for surface areas of multiple cobalt phases in the estimation of the effectiveness of the catalyst. This led to a more reliable correlation between catalytic properties and turnover frequency, which would help in rational catalyst design. However, the knowledge gained from the FT work could be built upon to develop other metal-based hydrodeoxygenation catalysts in mesoporous supports.

- Determination of the structure and phase of metal-based catalysts under hydrodeoxygenation working conditions will provide an understanding of the active sites and the deactivation mechanism relevant for HDO catalyst development.

- Determining the role of micropores in mesoporous silica catalyst supports on transport and hydrothermal stability will provide fundamental understanding of the structural features of the support which are of general interest to catalysis.

The potential of nitride/oxy-nitride catalysts for hydrodeoxygenation has been demonstrated in this thesis. Continued studies in these catalysts could prove beneficial for the ultimate industrial application for the HDO of bio-oils.

- The synthesis methods should be extended to create materials with higher surface area. In addition, the synthesis of pure-phase bimetallic nitride catalysts ($\text{Co}_3\text{Mo}_3\text{N}$ and $\text{Ni}_2\text{Mo}_3\text{N}$) must be emphasized, and its HDO catalysis, with diverse feed streams must be further investigated.
- Characterization of the post-reduction and post-reaction catalysts under different conditions must be performed to obtain information on the changes in catalysts properties in order to determine the optimal conditions for these materials.
- Studies geared towards atomic scale knowledge of the active phase must be conducted to develop a model of the active sites of these catalysts.
- Continuous flow experiments under HDO reaction conditions in order to determine long-term stability of these catalysts and possible catalyst regeneration methods would be useful.
- Studies on growing nitride/oxy-nitride on zirconia and mesoporous silica supports using various synthesis techniques including impregnation and chemical vapor deposition (CVD) will be beneficial. In addition to its HDO catalysis, the

influence of the nitride/oxy-nitride layers on the hydrothermal stability and transport properties of the supports must be studied.

REFERENCES

- [1] G.W. Huber, S. Iborra, and A. Corma, Chem. Rev. 106 **(2006)** 4044-4098.
- [2] D.L. Klass, Biomass for renewable energy, fuels and chemicals, Academic Press, San Diego. 29-50.
- [3] A.V. Bridgwater, Chem. Eng. J. 91 **(2003)** 87-102.
- [4] R.D. Perlack, L.L. Wright, A.F. Turhollow, R.L. Graham, B.J. Stokes, and D.C. Erbach. **(2005)**. Biomass as Feedstock for a Bioenergy and Bioproducts Industry: The Technical Feasibility of a Billion-Ton Annual Supply. In DOE/GO-102005-2135. Oak Ridge National Laboratory, Oak Ridge, Tennessee.
- [5] **(2007)**. Renewable Energy Road Map. In http://ec.europa.eu/energy/energy_policy/doc/03_renewable_energy_road_map_en.pdf.
- [6] E. Sjostrom, Wood Chemistry: Fundamentals and Applications. Academic Press, San Diego, **(1993)**.
- [7] A.V. Bridgwater, and J.M. Double, Fuel 70 **(1991)** 1209-1224.
- [8] J. Frederick, Advancing Beyond Ethanol: Future Supply, Demand, and Technology Development for Alternative Transportation Fuels, National Renewable Energy Laboratory. **(2010)**.
- [9] A. Demirbas, Energy. Convers. Manage. 42 **(2001)** 1357-1378.
- [10] D. Mohan, C.U. Pittman, and P.H. Steele, Energy Fuels 20 **(2006)** 848-889.
- [11] A.V. Bridgwater, D. Meier, and D. Radlein, Org. Geochem. 30 **(1999)** 1479-1493.
- [12] W.J. DeSisto, N. Hill, S.H. Beis, S. Mukkamala, J. Joseph, C. Baker, T.-H. Ong, E.A. Stemmler, M.C. Wheeler, B.G. Frederick, and A. van Heiningen, Energy Fuels 24 **(2010)** 2642-2651.
- [13] A.V. Bridgwater, Chem. Eng. J. 91 **(2003)** 87-102.
- [14] L. Ingram, D. Mohan, M. Bricka, P. Steele, D. Strobel, D. Crocker, B. Mitchell, J. Mohammad, K. Cantrell, and C.U. Pittman, Energy Fuels 22 **(2007)** 614-625.

- [15] C.A. Mullen, G.D. Strahan, and A.A. Boateng, *Energy Fuels* 23 **(2009)** 2707-2718.
- [16] R. Maggi, and D.C. Elliot, in: A.V. Bridgwater, and D.G.B. Boocock, (Eds.), Blackie, London. 575-588.
- [17] T.V. Choudhary, and C.B. Phillips, *Appl. Catal., A* 397 **(2011)** 1-12.
- [18] D.C. Elliott, *Energy Fuels* 21 **(2007)** 1792-1815.
- [19] P. Grange, E. Laurent, R. Maggi, A. Centeno, and B. Delmon, *Catal. Today* 29 **(1996)** 297-301.
- [20] A.V. Bridgwater, *Appl. Catal., A* 116 **(1994)** 5-47.
- [21] D.C. Elliot, and G.G. Neuenschwander, in: A.V. Bridgwater, and D.G.B. Boocock, (Eds.), In *Developments in thermochemical biomass conversion*, Blackie Academic and Professional London.
- [22] J. Zakzeski, P.C.A. Bruijnincx, A.L. Jongerius, and B.M. Weckhuysen, *Chem. Rev.* 110 **(2010)** 3552-3599.
- [23] R. French, *Upgrading, Mild Hydroprocessing of Biomass Pyrolysis Oil: Effect of Catalyst Type on Oxygenates and Refinery Use*, Chicago, IL. **(2011)**, 109-130.
- [24] T. Milne, F. Agblevor, M. Davis, S. Deutch, and D. Johnson, in: A.V. Bridgwater, (Ed.), *Developments in thermochemical biomass conversion*, Blackie Academic & Professional, London. 409-424.
- [25] H. Topsøe, B.S. Clausen, N.Y. Topsøe, and E. Pedersen, *Ind. Eng. Chem. Fund.* 25 **(1986)** 25-36.
- [26] N.-Y. Topsøe, and H. Topsøe, *J. Catal.* 84 **(1983)** 386-401.
- [27] M. Ferrari, R. Maggi, B. Delmon, and P. Grange, *J. Catal.* 198 **(2001)** 47-55.
- [28] E. Furimsky, *Appl. Catal., A* 199 **(2000)** 147-190.
- [29] E. Furimsky, *Appl. Catal.* 6 **(1983)** 159-164.
- [30] E. Furimsky, *Ind. Eng. Chem. Prod. Rd.* 22 **(1983)** 31-34.

- [31] S. Krishnamurthy, S. Panvelker, and Y.T. Shah, *AIChE J.* 27 **(1981)** 994-1001.
- [32] V. Lavopa, and C.N. Satterfield, *Energy Fuels* 1 **(1987)** 323-331.
- [33] C.L. Lee, and D.F. Ollis, *J. Catal.* 87 **(1984)** 325-331.
- [34] M.C. Edelman, M.K. Maholland, R.M. Baldwin, and S.W. Cowley, *J. Catal.* 111 **(1988)** 243-253.
- [35] A.Y. Bunch, and U.S. Ozkan, *J. Catal.* 206 **(2002)** 177-187.
- [36] A.Y. Bunch, X.Q. Wang, and U.S. Ozkan, *Appl. Catal., A* 346 **(2008)** 96-103.
- [37] A.Y. Bunch, X.Q. Wang, and U.S. Ozkan, *J. Mol. Catal. A: Chem.* 270 **(2007)** 264-272.
- [38] Y. Romero, F. Richard, Y. Reneme, and S. Brunet, *Appl. Catal., A* 353 **(2009)** 46-53.
- [39] H. Weigold, *Fuel* 61 **(1982)** 1021-1026.
- [40] E.O. Odebunmi, and D.F. Ollis, *J. Catal.* 80 **(1983)** 56-64.
- [41] E. Laurent, and B. Delmon, *Ind. Eng. Chem. Res.* 32 **(1993)** 2516-2524.
- [42] S.B. Gevert, M. Eriksson, P. Eriksson, and F.E. Massoth, *Appl. Catal., A* 117 **(1994)** 151-162.
- [43] F.E. Massoth, P. Politzer, M.C. Concha, J.S. Murray, J. Jakowski, and J. Simons, *J. Phys. Chem. B* 110 **(2006)** 14283-14291.
- [44] E.-M. Ryymin, M.L. Honkela, T.-R. Viljava, and A.O.I. Krause, *Appl. Catal., A* 389 **(2010)** 114-121.
- [45] Y. Romero, F. Richard, and S. Brunet, *Appl. Catal., B* 98 **(2010)** 213-223.
- [46] J.B.s. Bredenberg, M. Huuska, J. Rätty, and M. Korpio, *J. Catal.* 77 **(1982)** 242-247.
- [47] J.B. Bredenberg, M. Huuska, and P. Toropainen, *J. Catal.* 120 **(1989)** 401-408.
- [48] E. Laurent, and B. Delmon, *Appl. Catal., A* 109 **(1994)** 77-96.

- [49] V.N. Bui, D. Laurenti, P. Afanasiev, and C. Geantet, *Appl. Catal., B* 101 **(2011)** 239-245.
- [50] V.N. Bui, G. Toussaint, D. Laurenti, C. Mirodatos, and C. Geantet, *Catal. Today* 143 **(2009)** 172-178.
- [51] O.I. Senol, E.M. Ryymin, T.R. Viljava, and A.O.I. Krause, *J. Mol. Catal. A: Chem.* 268 **(2007)** 1-8.
- [52] E.-M. Ryymin, M.L. Honkela, T.-R. Viljava, and A.O.I. Krause, *Appl. Catal., A* 358 **(2009)** 42-48.
- [53] F.P. Petrocelli, and M.T. Klein, *Fuel Sci. Techn. Int.* 5 **(1987)** 25-62.
- [54] E. Laurent, and B. Delmon, *Appl. Catal., A* 109 **(1994)** 97-115.
- [55] A. Centeno, E. Laurent, and B. Delmon, *J. Catal.* 154 **(1995)** 288-298.
- [56] G. de la Puente, A. Gil, J.J. Pis, and P. Grange, *Langmuir* 15 **(1999)** 5800-5806.
- [57] O.I. Senol, E.M. Ryymin, T.R. Viljava, and A.O.I. Krause, *J. Mol. Catal. A: Chem.* 277 **(2007)** 107-112.
- [58] E. Furimsky, and F.E. Massoth, *Catal. Today* 52 **(1999)** 381-495.
- [59] E. Furimsky, and F.E. Massoth, *Catal. Today* 52 **(1999)** 381-495.
- [60] V.N. Bui, D. Laurenti, P. Delichère, and C. Geantet, *Appl. Catal., B* 101 **(2011)** 246-255.
- [61] E. Furimsky, *Appl. Catal., A* 171 **(1998)** 177-206.
- [62] D. Procházková, P. Zámotný, M. Bejblová, L. Cervený, and J. Cejka, *Appl. Catal., A* 332 **(2007)** 56-64.
- [63] D.C. Elliott, and T.R. Hart, *Energy Fuels* 23 **(2008)** 631-637.
- [64] J. Wildschut, F.H. Mahfud, R.H. Venderbosch, and H.J. Heeres, *Ind. Eng. Chem. Res.* 48 **(2009)** 10324-10334.
- [65] A. Gutierrez, R.K. Kaila, M.L. Honkela, R. Slioor, and A.O.I. Krause, *Catal. Today* 147 **(2009)** 239-246.

- [66] C. Zhao, Y. Kou, A.A. Lemonidou, X. Li, and J.A. Lercher, *Angew. Chem.* 121 **(2009)** 4047-4050.
- [67] T.T. Pham, L.L. Lobban, D.E. Resasco, and R.G. Mallinson, *J. Catal.* 266 **(2009)** 9-14.
- [68] Y.-C. Lin, C.-L. Li, H.-P. Wan, H.-T. Lee, and C.-F. Liu, *Energy Fuels* 25 **(2011)** 890-896.
- [69] V.M.L. Whiffen, and K.J. Smith, *Energy Fuels* 24 **(2010)** 4728-4737.
- [70] H.Y. Zhao, D. Li, P. Bui, and S.T. Oyama, *Appl. Catal., A* 391 **(2011)** 305-310.
- [71] S.T. Oyama, X. Wang, Y.K. Lee, and W.J. Chun, *J. Catal.* 221 **(2004)** 263-273.
- [72] K. Li, R. Wang, and J. Chen, *Energy Fuels* 25 **(2011)** 854-863.
- [73] F. Rodriguez-Reinoso, *Carbon* 36 **(1998)** 159-175.
- [74] S. Rondon, W.R. Wilkinson, A. Proctor, M. Houalla, and D.M. Hercules, *J. Phys. Chem.* 99 **(1995)** 16709-16713.
- [75] H. Farag, D.D. Whitehurst, K. Sakanishi, and I. Mochida, *Catal. Today* 50 **(1999)** 9-17.
- [76] H. Farag, D.D. Whitehurst, and I. Mochida, *Ind. Eng. Chem. Res.* 37 **(1998)** 3533-3539.
- [77] E. Furimsky, *Carbons and carbon supported catalysts in hydroprocessing*. RSC Publishing, Cambridge, **(2008)**.
- [78] V.H.J. de Beer, J.C. Duchet, and R. Prins, *J. Catal.* 72 **(1981)** 369-372.
- [79] A. Centeno, V. CH, R. Maggi, and B. Delmon, in: A.V. Bridgwater, (Ed.), *Developments in thermochemical biomass conversion*, Blackie Academic & Professional London. 602-610.
- [80] M. Ferrari, S. Bosmans, R. Maggi, B. Delmon, and P. Grange, *Catal. Today* 65 **(2001)** 257-264.
- [81] M. Ferrari, B. Delmon, and P. Grange, *Carbon* 40 **(2002)** 497-511.

- [82] K.V.R. Chary, K.S.R. Rao, G. Muralidhar, and P.K. Rao, *Carbon* 29 **(1991)** 478-479.
- [83] S. Echeandia, P.L. Arias, V.L. Barrio, B. Pawelec, and J.L.G. Fierro, *Appl. Catal., B* 101 **(2010)** 1-12.
- [84] S.T. Oyama, *Catal. Today* 15 **(1992)** 179-200.
- [85] H.O. Pierson, *Handbook of refractory carbides and nitrides*. Noyes Publications, New Jersey, **(1996)**.
- [86] D. H. Gregory, *J. Chem. Soc., Dalton Trans.* **(1999)** 259-270.
- [87] C.C. Yu, S. Ramanathan, F. Sherif, and S.T. Oyama, *J. Phys. Chem.* 98 **(1994)** 13038-13041.
- [88] M. Nagai, *Appl. Catal., A* 322 **(2007)** 178-190.
- [89] K. Miga, K. Stanczyk, C. Sayag, D. Brodzki, and G. Djega-Mariadassou, *J. Catal.* 183 **(1999)** 63-68.
- [90] E. Furimsky, *Appl. Catal., A* 240 **(2003)** 1-28.
- [91] S.T. Oyama, in: S.T. Oyama, (Ed.), *The chemistry of transition metal carbides and nitrides*, Blackie Academic & Professional, London. 1-24.
- [92] R.T. Koodali, and K.J. Klabunde, in: R. Richards, (Ed.), *Surface and nanomolecular catalysis*, Taylor & Francis Group, New York. 39-61.
- [93] J.G. Choi, R.L. Curl, and L.T. Thompson, *J. Catal.* 146 **(1994)** 218-227.
- [94] L. Volpe, and M. Boudart, *J. Solid State Chem.* 59 **(1985)** 332-347.
- [95] M. Nagai, and S. Omi, *Sekiyu Gakkaishi* 38 **(1995)** 363-373.
- [96] D.W. Kim, D.K. Lee, and S.K. Ihm, *Korean J. Chem. Eng.* 19 **(2002)** 587-592.
- [97] E.J. Markel, and J.W. Van Zee, *J. Catal.* 126 **(1990)** 643-657.
- [98] C.H. Jagers, J.N. Michaels, and A.M. Stacy, *Chem. Mater.* 2 **(1990)** 150-157.
- [99] R.S. Wise, and E.J. Markel, *J. Catal.* 145 **(1994)** 344-355.

- [100] S.W. Gong, H.K. Chen, W. Li, and B.Q. Li, *Appl. Catal., A* 279 **(2005)** 257-261.
- [101] M. Nagai, Y. Goto, O. Uchino, and S. Omi, *Catal. Today* 43 **(1998)** 249-259.
- [102] J.C. Schlatter, S.T. Oyama, J.E. Metcalfe, and J.M. Lambert, *Ind. Eng. Chem. Res.* 27 **(1988)** 1648-1653.
- [103] C.W. Colling, J.G. Choi, and L.T. Thompson, *J. Catal.* 160 **(1996)** 35-42.
- [104] B.G. Demczyk, J.G. Choi, and L.T. Thompson, *Appl. Surf. Sci.* 78 **(1994)** 63-69.
- [105] Z.B. Wei, Q. Xin, P. Grange, and B. Delmon, *J. Catal.* 168 **(1997)** 176-182.
- [106] Z.B.Z. Wei, P. Grange, and B. Delmon, *Appl. Surf. Sci.* 135 **(1998)** 107-114.
- [107] Z.B. Wei, Q. Xin, P. Grange, and B. Delmon, *Solid State Ionics* 101-103 **(1997)** 761-767.
- [108] D.S. Bem, C.P. Gibson, and H.C. zur Loye, *Chem. Mater.* 5 **(1993)** 397-399.
- [109] C.C. Yu, and S.T. Oyama, *J. Solid State Chem.* 116 **(1995)** 205-207.
- [110] C.C. Yu, and S.T. Oyama, *J. Mater. Sci.* 30 **(1995)** 4037-4042.
- [111] C.C. Yu, S. Ramanathan, and S.T. Oyama, *J. Catal.* 173 **(1998)** 1-9.
- [112] D.W. Kim, D.K. Lee, and S.K. Ihm, *Catal. Lett.* 43 **(1997)** 91-95.
- [113] K. Hada, M. Nagai, and S. Omi, *J. Phys. Chem. B* 105 **(2001)** 4084-4093.
- [114] M. Nagai, and T. Miyao, *Catal. Lett.* 15 **(1992)** 105-109.
- [115] M. Nagai, T. Miyao, and T. Tuboi, *Catal. Lett.* 18 **(1993)** 9-14.
- [116] M. Nagai, A. Irisawa, and S. Omi, *J. Phys. Chem. B* 102 **(1998)** 7619-7626.
- [117] M. Nagai, Y. Goto, O. Uchino, and S. Omi, *Catal. Today* 45 **(1998)** 335-340.
- [118] M. Nagai, Y. Goto, H. Ishii, and S. Omi, *Appl. Catal., A* 192 **(2000)** 189-199.
- [119] K. Hada, M. Nagai, and S. Omi, *J. Phys. Chem. B* 104 **(2000)** 2090-2098.
- [120] H. Ishii, M. Kiyoshi, and M. Nagai, *Top. Catal.* 52 **(2009)** 1525-1534.

- [121] C.W. Colling, and L.T. Thompson, *J. Catal.* 146 **(1994)** 193-203.
- [122] P.A. Aegerter, W.W.C. Quigley, G.J. Simpson, D.D. Ziegler, J.W. Logan, K.R. McCrea, S. Glazier, and M.E. Bussell, *J. Catal.* 164 **(1996)** 109-121.
- [123] K.R. McCrea, J.W. Logan, T.L. Tarbuck, J.L. Heiser, and M.E. Bussell, *J. Catal.* 171 **(1997)** 255-267.
- [124] S. Korlann, B. Diaz, and M.E. Bussell, *Chem. Mater.* 14 **(2002)** 4049-4058.
- [125] B. Diaz, S.J. Sawhill, D.H. Bale, R. Main, D.C. Phillips, S. Korlann, R. Self, and M.E. Bussell, *Catal. Today* 86 **(2003)** 191-209.
- [126] M. Nagai, J. Takada, and S. Omi, *J. Phys. Chem. B* 103 **(1999)** 10180-10188.
- [127] A. Guerrero-Ruiz, Y. Zhang, B. Bachiller-Baeza, and I. Rodriguez-Ramos, *Catal. Lett.* 55 **(1998)** 165-168.
- [128] H. Liu, H. Wang, J. Shen, Y. Sun, and Z. Liu, *J. Nat. Gas Chem.* 15 **(2006)** 178-180.
- [129] Y.J. Lee, T.H. Nguyen, A. Khodakov, and A.A. Adesina, *J. Mol. Catal. A: Chem.* 211 **(2004)** 191-197.
- [130] J. Trawczynski, *Appl. Catal., A* 197 **(2000)** 289-293.
- [131] E.J. Markel, S.E. Burdick, M.E. Leaphart, and K.L. Roberts, *J. Catal.* 182 **(1999)** 136-147.
- [132] M. Nagai, Y. Goto, H. Sasuga, and S. Omi, *Abstr. Pap. Am. Chem. Soc.* 212 **(1996)** 28-PETR.
- [133] M. Nagai, Y. Goto, K. Sasuga, and S. Omi in: C.H. Bartholomew, and G.A. Fuentes, (Eds.), *Hydrodesulfurization of dibenzothiophene on a nitrated supported molybdena-alumina catalyst.* **(1997)**, 439-445.
- [134] M. Nagai, H. Koyama, S. Sakamoto, and S. Omi in: B. Delmon, G.F. Froment, and P. Grange, (Eds.), *The nitrated CoMo catalysts for hydrodesulfurization and hydrodenitrogenation.* **(1999)**, 195-202.
- [135] J.W. Logan, J.L. Heiser, K.R. McCrea, B.D. Gates, and M.E. Bussell, *Catal. Lett.* 56 **(1998)** 165-171.

- [136] D.C. Phillips, S.J. Sawhill, R. Self, and M.E. Bussell, *J. Catal.* 207 **(2002)** 266-273.
- [137] Y.Q. Liu, C.G. Liu, and G.H. Que, *Energy Fuels* 16 **(2002)** 531-535.
- [138] M. Nagai, Y. Goto, A. Miyata, M. Kiyoshi, K. Hada, K. Oshikawa, and S. Omi, *J. Catal.* 182 **(1999)** 292-301.
- [139] M. Nagai, Y. Goto, A. Irisawa, and S. Omi, *J. Catal.* 191 **(2000)** 128-137.
- [140] M. Nagai, Y. Yamamoto, and R. Aono, *Colloids Surf., A* 241 **(2004)** 257-263.
- [141] W. Yuhong, L. Wei, Z. Minghui, G. Naijia, and T. Keyi, *Appl. Catal., A* 215 **(2001)** 39-45.
- [142] L. Senzi, and J.S. Lee, *J. Catal.* 173 **(1998)** 134-144.
- [143] S. Li, J. Sung Lee, T. Hyeon, and K.S. Suslick, *Appl. Catal., A* 184 **(1999)** 1-9.
- [144] Y.J. Zhang, Q. Xin, I. Rodriguez-Ramos, and A. Guerrero-Ruiz, *Appl. Catal., A* 180 **(1999)** 237-245.
- [145] S. Ramanathan, and S.T. Oyama, *J. Phys. Chem.* 99 **(1995)** 16365-16372.
- [146] S. Ramanathan, C.C. Yu, and S.T. Oyama, *J. Catal.* 173 **(1998)** 10-16.
- [147] U.S. Ozkan, L. Zhang, and P.A. Clark, *J. Catal.* 172 **(1997)** 294-306.
- [148] H. Abe, T.K. Cheung, and A.T. Bell, *Catal. Lett.* 21 **(1993)** 11-18.
- [149] H. Abe, and A.T. Bell, *Catal. Lett.* 18 **(1993)** 1-8.
- [150] J. Monnier, H. Sulimma, A. Dalai, and G. Caravaggio, *Appl. Catal., A* 382 **(2010)** 176-180.
- [151] A.Y. Khodakov, W. Chu, and P. Fongarland, *Chem. Rev.* 107 **(2007)** 1692-1744.
- [152] H. Schulz, *Top. Catal.* 26 **(2003)** 73-85.
- [153] H. Schulz, *Appl. Catal., A* 186 **(1999)** 3-12.
- [154] B.H. Davis, *Ind. Eng. Chem. Res.* 46 **(2007)** 8938-8945.

- [155] A. Steynberg, and M.E. Dry, Fischer-Tropsch Technology. Elsevier B.V., **(2004)**.
- [156] A.Y. Khodakov, R. Bechara, and A. Griboval-Constant, Appl. Catal., A. 254 **(2003)** 273-288.
- [157] K. Okabe, X. Li, M. Wei, and H. Arakawa, Catal. Today 89 **(2004)** 431-438.
- [158] J.G. Chen, Y.H. Sun, B. Xinhe, and X. Yide, Stud. Surf. Sci. Catal., Elsevier. 277-282.
- [159] S.-J. Jong, and S. Cheng, Appl. Catal., A 126 **(1995)** 51-66.
- [160] S. Bessell, Appl. Catal., A 126 **(1995)** 235-244.
- [161] J. van de Loosdrecht, M. van der Haar, A.M. van der Kraan, A.J. van Dillen, and J.W. Geus, Appl. Catal., A 150 **(1997)** 365-376.
- [162] R. Bechara, D. Balloy, and D. Vanhove, Appl. Catal., A 207 **(2001)** 343-353.
- [163] E. Iglesia, S.L. Soled, and R.A. Fiato, J. Catal. 137 **(1992)** 212-224.
- [164] B. Mothebe, D.J. Duvenhage, V.D. Sokolovskii, N.J. Coville, R.L.E.C.P.N.J.H.S. M. de Pontes, and M.S. Scurrrell, Stud. Surf. Sci. Catal., Elsevier. 187-192.
- [165] A.M. Saib, M. Claeys, and E. van Steen, Catal. Today 71 **(2002)** 395-402.
- [166] B. Ernst, S. Libs, P. Chaumette, and A. Kiennemann, Appl. Catal., A 186 **(1999)** 145-168.
- [167] V. Udaya, S. Rao, and R.J. Gormley, Catal. Today 6 **(1990)** 207-234.
- [168] J. Zhang, J. Chen, J. Ren, and Y. Sun, Appl. Catal., A 243 **(2003)** 121-133.
- [169] Y. Zhang, H. Xiong, K. Liew, and J. Li, J. Mol. Catal. A: Chem. 237 **(2005)** 172-181.
- [170] E.v. Steen, G.S. Sewell, R.A. Makhothe, C. Micklethwaite, H. Manstein, M. de Lange, and C.T. O'Connor, J. Catal. 162 **(1996)** 220-229.
- [171] A.K. Dalai, and B.H. Davis, Appl. Catal., A 348 **(2008)** 1-15.

- [172] Y. Wang, M. Noguchi, Y. Takahashi, and Y. Ohtsuka, *Catal. Today* 68 **(2001)** 3-9.
- [173] Y. Ohtsuka, T. Arai, S. Takasaki, and N. Tsubouchi, *Energy Fuels* 17 **(2003)** 804-809.
- [174] H.L. Li, S.G. Wang, F.X. Ling, and J.L. Li, *J. Mol. Catal. A: Chem.* 244 **(2006)** 33-40.
- [175] A.Y. Khodakov, A. Griboval-Constant, R. Bechara, and V.L. Zholobenko, *J. Catal.* 206 **(2002)** 230-241.
- [176] Y. Ohtsuka, Y. Takahashi, M. Noguchi, T. Arai, S. Takasaki, N. Tsubouchi, and Y. Wang, *Catal. Today* 89 **(2004)** 419-429.
- [177] O. González, H. Pérez, P. Navarro, L.C. Almeida, J.G. Pacheco, and M. Montes, *Catal. Today* 148 **(2009)** 140-147.
- [178] J. Hong, P.A. Chernavskii, A.Y. Khodakov, and W. Chu, *Catal. Today* 140 **(2009)** 135-141.
- [179] D. Song, and J. Li, *J. Mol. Catal. A: Chem.* 247 **(2006)** 206-212.
- [180] E. Lira, C.M. Lopez, F. Oropeza, M. Bartolini, J. Alvarez, M. Goldwasser, F.L. Linares, J.F. Lamonier, and M.J.P. Zurita, *J. Mol. Catal. A: Chem.* 281 **(2008)** 146-153.
- [181] O. Borg, P.D.C. Dietzel, A.I. Spjelkavik, E.Z. Tveten, J.C. Walmsley, S. Diplas, S. Eri, A. Holmen, and E. Ryttera, *J. Catal.* 259 **(2008)** 161-164.
- [182] A.Y. Khodakov, R. Bechara, and A. Griboval-Constant in: R. Aiello, G. Giordano, and F. Testa, (Eds.), *Structure and catalytic performance of cobalt Fischer Tropsch catalysts supported by periodic mesoporous silicas.* **(2002)**, 1133-1140.
- [183] H.L. Li, J.L. Li, H.K. Ni, and D.C. Song, *Catal. Lett.* 110 **(2006)** 71-76.
- [184] G.L. Bezemer, J.H. Bitter, H. Kuipers, H. Oosterbeek, J.E. Holewijn, X.D. Xu, F. Kapteijn, A.J. van Dillen, and K.P. de Jong, *J. Am. Chem. Soc.* 128 **(2006)** 3956-3964.
- [185] J.P. den Breejen, P.B. Radstake, G.L. Bezemer, J.H. Bitter, V. FrÃ,se, A. Holmen, and K.P.d. Jong, *J. Am. Chem. Soc.* 131 **(2009)** 7197-7203.

- [186] R. Srinivasan, R.J. De Angelis, P.J. Reucroft, A.G. Dhere, and J. Bentley, *J. Catal.* 116 **(1989)** 144-163.
- [187] D.I. Enache, B. Rebours, M. Roy-Auberger, and R. Revel, *J. Catal.* 205 **(2002)** 346-353.
- [188] A.Y. Khodakov, J. Lynch, D. Bazin, B. Rebours, N. Zanier, B. Moisson, and P. Chaumette, *J. Catal.* 168 **(1997)** 16-25.
- [189] O. Kitakami, H. Sato, Y. Shimada, F. Sato, and M. Tanaka, *Phys. Rev. B: Condens. Matter Mater. Phys.* 56 **(1997)** 13849.
- [190] O. Ducreux, B. Rebours, J. Lynch, M. Roy-Auberger, and D. Bazin, *Oil Gas Sci. Technol.* 64 **(2009)** 49-62.
- [191] Q.H. Tang, P. Wang, Q.H. Zhang, and Y. Wang, *Chem. Lett.* 35 **(2006)** 366-367.
- [192] C.T. Kresge, M.E. Leonowicz, W.J. Roth, J.C. Vartuli, and J.S. Beck, *Nature* 359 **(1992)** 710-712.
- [193] P.T. Tanev, and T.J. Pinnavaia, *Science* 267 **(1995)** 865-867.
- [194] D.Y. Zhao, J.L. Feng, Q.S. Huo, N. Melosh, G.H. Fredrickson, B.F. Chmelka, and G.D. Stucky, *Science* 279 **(1998)** 548-552.
- [195] A. Sampieri, S. Pronier, J. Blanchard, M. Breyse, S. Brunet, K. Fajerweg, C. Louis, and G. Perot, *Catal. Today* 107-08 **(2005)** 537-544.
- [196] A.Y. Khodakov, A. Griboval-Constant, R. Bechara, and F.o. Villain, *J. Phys. Chem. B* 105 **(2001)** 9805-9811.
- [197] K. Schumacher, M. Grun, and K.K. Unger, *Microporous Mesoporous Mater.* 27 **(1999)** 201-206.
- [198] D.H. Yin, W.H. Li, W.S. Yang, H.W. Xiang, Y.H. Sun, B. Zhong, and S.Y. Peng, *Microporous Mesoporous Mater.* 47 **(2001)** 15-24.
- [199] K. Soni, K.C. Mouli, A.K. Dalai, and J. Adjaye, *Catal. Lett.* 136 **(2010)** 116-125.
- [200] E. van Steen, and M. Claeys, *Chem. Eng. Technol.* 31 **(2008)** 655-666.
- [201] R. Ravishankar, M.M. Li, and A. Borgna, *Catal. Today* 106 **(2005)** 149-153.

- [202] A.Y. Khodakov, *Catal. Today* 144 **(2009)** 251-257.
- [203] A. Martinez, and G. Prieto, *J. Catal.* 245 **(2007)** 470-476.
- [204] W. Chu, P.A. Chernavskii, L. Gengembre, G.A. Pankina, P. Fongarland, and A.Y. Khodakov, *J. Catal.* 252 **(2007)** 215-230.
- [205] G. Prieto, A. Martínez, R. Murciano, and M.A. Arribas, *Appl. Catal., A* 367 **(2009)** 146-156.
- [206] C.-Y. Chen, H.-X. Li, and M.E. Davis, *Microporous Mater.* 2 **(1993)** 17-26.
- [207] A. Tuel, *Microporous Mesoporous Mater.* 27 **(1999)** 151-169.
- [208] Z.H. Luan, M. Hartmann, D.Y. Zhao, W.Z. Zhou, and L. Kevan, *Chem. Mater.* 11 **(1999)** 1621-1627.
- [209] D.Y. Zhao, J.Y. Sun, Q.Z. Li, and G.D. Stucky, *Chem. Mater.* 12 **(2000)** 275-+.
- [210] J.B.R. Rosenholm, H.; Puputti, J.; Stathopoulos, V.; Pomonis, P.; Beurroies, I.; Backfolk, K. , *Colloids Surf. A Physicochem. Eng. Asp* 250 **(2004)** 289-306.
- [211] H. Golinska, P. Decyk, M. Ziolek, J. Kujawa, and E. Filipek, *Catal. Today* 142 **(2009)** 175-180.
- [212] D. Fuentes-Perujo, J. Santamaría-González, J. Mérida-Robles, E. Rodríguez-Castellón, A. Jiménez-López, P. Maireles-Torres, R. Moreno-Tost, and R. Mariscal, *J. Solid State Chem.* 179 **(2006)** 2182-2189.
- [213] Y. Xia, and R. Mokaya, *J. Mater. Chem.* 14 **(2004)** 3427-3435.
- [214] B. Dragoi, E. Dumitriu, C. Guimon, and A. Auroux, *Microporous Mesoporous Mater.* 121 **(2009)** 7-17.
- [215] T. Chiranjeevi, G.M. Kumaran, J.K. Gupta, and G.M. Dhar, *Thermochim. Acta* 443 **(2006)** 87-92.
- [216] N. Kob, R.S. Drago, and V. Young, *Inorg. Chem.* 36 **(1997)** 5127-5131.
- [217] M.T. Bore, R.F. Marzke, T.L. Ward, and A.K. Datye, *J. Mater. Chem.* 15 **(2005)** 5022-5028.

- [218] M.T. Bore, M.P. Mokhonoana, T.L. Ward, N.J. Coville, and A.K. Datye, *Microporous Mesoporous Mater.* 95 **(2006)** 118-125.
- [219] G. Xomeritakis, C.Y. Tsai, Y.B. Jiang, and C.J. Brinker, *J. Membr. Sci.* 341 **(2009)** 30-36.
- [220] S. Battersby, S. Smart, B. Ladewig, S. Liu, M.C. Duke, V. Rudolph, and J.o.C.D.d. Costa, *Sep. Purif. Technol.* 66 **(2009)** 299-305.
- [221] S. Brunauer, P.H. Emmett, and E. Teller, *J. Am. Chem. Soc.* 60 **(1938)** 309-319.
- [222] E.P. Barrett, L.G. Joyner, and P.P. Halenda, *J. Am. Chem. Soc.* 73 **(1951)** 373-380.
- [223] M. Kruk, M. Jaroniec, and A. Sayari, *Langmuir* 13 **(1997)** 6267-6273.
- [224] J. van de Loosdrecht, B. Balzhinimaev, J.A. Dalmon, J.W. Niemantsverdriet, S.V. Tsybulya, A.M. Saib, P.J. van Berge, and J.L. Visagie, *Catal. Today* 123 **(2007)** 293-302.
- [225] A.M. Saib, D.J. Moodley, I.M. Ciobîca, M.M. Hauman, B.H. Sigwebela, C.J. Weststrate, J.W. Niemantsverdriet, and J. van de Loosdrecht, *Catal. Today* 154 **(2010)** 271-282.
- [226] A.M. Saib, A. Borgna, J. van de Loosdrecht, P.J. van Berge, J.W. Geus, and J.W. Niemantsverdriet, *J. Catal.* 239 **(2006)** 326-339.
- [227] B.H. Toby, *J. Appl. Crystallogr.* 34 **(2001)** 210-213.
- [228] A.C. Larson, and R.B. Von Dreele, *General Structure Analysis System (GSAS) Manual*. LANSCE, MS-H805, Los Alamos National Laboratory, Los Alamos, NM, **(1994)**.
- [229] R. Speight, A. Wong, P. Ellis, T. Hyde, P.T. Bishop, and M.E. Smith, *Solid State Nucl. Magn. Reson.* 35 **(2009)** 67-73.
- [230] A. Martinez, C. Lopez, F. Marquez, and I. Diaz, *J. Catal.* 220 **(2003)** 486-499.
- [231] A.Y. Khodakov, V.L. Zholobenko, R. Bechara, and D. Durand, *Microporous Mesoporous Mater.* 79 **(2005)** 29-39.
- [232] T.J. Regan, H. Ohldag, C. Stamm, F. Nolting, J. Luning, J. Stohr, and R.L. White, *Phys. Rev. B* 64 **(2001)** 214422.

- [233] F.M.F. de Groot, J.C. Fuggle, B.T. Thole, and G.A. Sawatzky, Phys. Rev. B 42 **(1990)** 5459.
- [234] F.M.F. de Groot, M. Abbate, J.v. Elp, G.A. Sawatzky, Y.J. Ma, C.T. Chen, and F. Sette, J. Phys.: Condens. Matter 5 **(1993)** 2277-2288.
- [235] F. de Groot, Coord. Chem. Rev. 249 **(2005)** 31-63.
- [236] A. Martinez, G. Prieto, and J. Rollán, J. Catal. 263 **(2009)** 292-305.
- [237] E. Iglesia, S.L. Soled, J.E. Baumgartner, and S.C. Reyes, J. Catal. 153 **(1995)** 108-122.
- [238] E. Iglesia, Appl. Catal., A 161 **(1997)** 59-78.
- [239] H. Xiong, Y. Zhang, K. Liew, and J. Li, J. Mol. Catal. A: Chem. 295 **(2008)** 68-76.
- [240] R.B. Anderson, W.K. Hall, A. Krieg, and B. Seligman, J. Am. Chem. Soc. 71 **(1949)** 183-188.
- [241] H. Xiong, Y. Zhang, K. Liew, and J. Li, Journal of Molecular Catalysis A: Chemical 295 **(2008)** 68-76.
- [242] A.M. Saib, A. Borgna, J.V. De Loosdrecht, P.J. Van Berge, and J.W. Niemantsverdriet, J. Phys. Chem. B 110 **(2006)** 8657-8664.
- [243] E. van Steen, M. Claeys, M.E. Dry, J. van de Loosdrecht, E.L. Viljoen, and J.L. Visagie, J. Phys. Chem. B 109 **(2005)** 3575-3577.
- [244] X.J. Yin, K. Peng, A.P. Hu, L.P. Zhou, J.H. Chen, and Y.W. Du, J. Alloys Compd. 479 **(2009)** 372-375.
- [245] X.Q. Zhao, S. Veintemillas-Verdaguer, O. Bomati-Miguel, M.P. Morales, and H.B. Xu, Phys. Rev. B: Condens. Matter Mater. Phys. 71 **(2005)** 024106
- [246] C. Desgranges, and J. Delhommelle, J. Phys. Chem. B 111 **(2007)** 1465-1469.
- [247] V. Dureuil, C. Ricolleau, M. Gandais, and C. Grigis, Eur. Phys. J. D 14 **(2001)** 83-88.
- [248] V.F. Puentes, K.M. Krishnzn, and A.P. Alivisatos, Science 291 **(2001)** 2115.
- [249] A. Martinez, G. Prieto, and J. Rollan, Journal of Catalysis 263 **(2009)** 292-305.

- [250] D. Schanke, S. Vada, E.A. Blekkan, A.M. Hilmen, A. Hoff, and A. Holmen, *J. Catal.* 156 **(1995)** 85-95.
- [251] C. Sepúlveda, K. Leiva, R. García, L.R. Radovic, I.T. Ghampson, W.J. DeSisto, J.L.G. Fierro, and N. Escalona, *Catal. Today* 172 **(2011)** 232-239.
- [252] D.J. Sajkowski, and S.T. Oyama, *Appl. Catal., A* 134 **(1996)** 339-349.
- [253] T. Nimmanwudipong, R. Runnebaum, D. Block, and B. Gates, *Catal. Lett.* 141 **(2011)** 779-783.
- [254] P.E. Ruiz, K. Leiva, R. Garcia, P. Reyes, J.L.G. Fierro, and N. Escalona, *Appl. Catal., A* 384 **(2010)** 78-83.
- [255] Y. Li, Y. Zhang, R. Raval, C. Li, R. Zhai, and Q. Xin, *Catal. Lett.* 48 **(1997)** 239-245.
- [256] E. Laurent, and B. Delmon, *J. Catal.* 146 **(1994)** 281-291.
- [257] A. Popov, E. Kondratieva, J.M. Goupil, L. Mariey, P. Bazin, J.-P. Gilson, A. Travert, and F. Maugele, *J. Phys Chem. C* 114 **(2010)** 15661-15670.
- [258] A. Centeno, O. David, C. Vanbellinthen, R. Maggi, and B. Delmon, in: A.V. Bridgwater, (Ed.), *Developments in thermochemical biomass conversion*, Blackie Academic & Professional, London. 589-601.
- [259] G. de la Puente, A. Centeno, A. Gil, and P. Grange, *J. Colloid Interface Sci* 202 **(1998)** 155-166.
- [260] G. de la Puente, and J.A. Menendez, *Solid State Ionics* 112 **(1998)** 103-111.
- [261] J.G. Chen, *Chem. Rev.* 96 **(1996)** 1477-1498.
- [262] I.T. Ghampson, C. Sepúlveda, R. Garcia, B.G. Frederick, C.M. Wheeler, N. Escalona, and W.J. DeSisto, *Appl. Catal. A. Accepted* **(2011)**.
- [263] J.P. Olivier, *Carbon* 36 **(1998)** 1469-1472.
- [264] M. Kruk, M. Jaroniec, and K.P. Gadkaree, *J. Colloid Interface Sci.* 192 **(1997)** 250-256.
- [265] C.D. Wagner, L.E. Davis, M.V. Zeller, J.A. Taylor, R.H. Raymond, and L.H. Gale, *Surf. Interface Anal.* 3 **(1981)** 211-225.

- [266] R. Cid, and G. Pecchi, Appl. Catal. 14 **(1985)** 15-21.
- [267] J.L. Figueiredo, M.F.R. Pereira, M.M.A. Freitas, and J.J.M. Órfão, Carbon 37 **(1999)** 1379-1389.
- [268] Y. Otake, and R.G. Jenkins, Carbon 31 **(1993)** 109-121.
- [269] U. Zielke, K.J. Hüttinger, and W.P. Hoffman, Carbon 34 **(1996)** 983-998.
- [270] G. Lagos, R. García, A.L. Agudo, M. Yates, J.L.G. Fierro, F.J. Gil-Llambías, and N. Escalona, Appl. Catal., A 358 **(2009)** 26-31.
- [271] J.M. Calo, D. Cazorla-Amorós, A. Linares-Solano, M.C. Román-Martínez, and C.S.-M. De Lecea, Carbon 35 **(1997)** 543-554.
- [272] H.P. Boehm, Carbon 32 **(1994)** 759-769.
- [273] H.P. Boehm, Carbon 40 **(2002)** 145-149.
- [274] B. Stöhr, H.P. Boehm, and R. Schlögl, Carbon 29 **(1991)** 707-720.
- [275] J.P.R. Vissers, S.M.A.M. Bouwens, V.H.J. de Beer, and R. Prins, Carbon 25 **(1987)** 485-493.
- [276] S. Biniak, G. Szymanski, J. Siedlewski, and A. Swiatkowski, Carbon 35 **(1997)** 1799-1810.
- [277] S.D. Gardner, C.S.K. Singamsetty, G.L. Booth, G.-R. He, and C.U. Pittman, Carbon 33 **(1995)** 587-595.
- [278] E. Riedo, F. Comin, J. Chevrier, F. Schmithusen, S. Decossas, and M. Sancrotti, Surf. Coat. Technol. 125 **(2000)** 124-128.
- [279] E. D'Anna, M.L. De Giorgi, A. Luches, M. Martino, A. Perrone, and A. Zocco, Thin Solid Films 347 **(1999)** 72-77.
- [280] S.W. Yang, C. Li, J. Xu, and Q. Xin, J. Phys. Chem. B 102 **(1998)** 6986-6993.
- [281] R.J.J. Jansen, and H. van Bekkum, Carbon 33 **(1995)** 1021-1027.
- [282] J. Li, L. Ma, X. Li, C. Lu, and H. Liu, Ind. Eng. Chem. Res. 44 **(2005)** 5478-5482.

- [283] A. Calafat, J. Laine, A. LopezAgudo, and J.M. Palacios, *J. Catal.* 162 **(1996)** 20-30.
- [284] S. Gong, H. Chen, W. Li, and B. Li, *Catal. Commun.* 5 **(2004)** 621-624.
- [285] C. Sepúlveda, N. Escalona, R. Garcia, D. Laurenti, and M. Vrinat, Torremolinos-Málaga, Spain **(2011)**.
- [286] G.M. Dolce, P.E. Savage, and L.T. Thompson, *Energy Fuels* 11 **(1997)** 668-675.
- [287] I.T. Ghampson, C. Newman, L. Kong, E. Pier, K.D. Hurley, R.A. Pollock, B.R. Walsh, B. Goundie, J. Wright, M.C. Wheeler, R.W. Meulenberg, W.J. DeSisto, B.G. Frederick, and R.N. Austin, *Appl. Catal., A* 388 **(2010)** 57-67.
- [288] R. Nava, B. Pawelec, P. Castaño, M.C. Álvarez-Galván, C.V. Loricera, and J.L.G. Fierro, *Appl. Catal., B* 92 **(2009)** 154-167.
- [289] R.A. Pollock, B.R. Walsh, J. Fry, I.T. Ghampson, Y.B. Melnichenko, H. Kaiser, R. Pynn, W.J. DeSisto, M.C. Wheeler, and B.G. Frederick, *Chem. Mater.* 23 **(2011)** 3828-3840.
- [290] R.A. Pollock, B.R. Walsh, J. Fry, I.T. Ghampson, H. Kaiser, R. Pynn, Y.B. Melnichenko, M.C. Wheeler, W.J. DeSisto, and B.G. Frederick, *In prep.* **(2012)**.
- [291] S.J. Gregg, and K.S.W. Sing, *Adsorption, Surface Area and Porosity*. Academic Press, London, **(1982)**.
- [292] R. Nava, B. Pawelec, J. Morales, R.A. Ortega, and J.L.G. Fierro, *Microporous Mesoporous Mater.* 118 **(2009)** 189-201.
- [293] H.K. Park, J.K. Lee, J.K. Yoo, E.S. Ko, D.S. Kim, and K.L. Kim, *Appl. Catal., A* 150 **(1997)** 21-35.
- [294] C. Shi, A.M. Zhu, X.F. Yang, and C.T. Au, *Appl. Catal., A* 276 **(2004)** 223-230.
- [295] T. Nagata, G. Koblmuller, O. Bierwagen, C.S. Gallinat, and J.S. Speck, *Appl. Phys. Lett.* 95 **(2009)**.
- [296] J.S. Girardon, E. Quinet, A. Griboval-Constant, P.A. Chernavskii, L. Gengembre, and A.Y. Khodakov, *J. Catal.* 248 **(2007)** 143-157.
- [297] I.T. Ghampson, C. Sepulveda, R. Garcia, B.G. Frederick, L.R. Radovic, J.L.G. Fierro, N. Escalona, and W.J. DeSisto, *In prep.* **(2012)**.

- [298] G. Caglioti, A. Paoletti, and F.P. Ricci, Nuclear Instruments 3 **(1958)** 223-228.
- [299] H.S. Fogler, Elements of chemical reaction engineering. Prentice Hall, Inc, Upper Saddle River, New Jersey, **(1999)**.
- [300] R.M. Felder, and R.W. Rousseau, Elementary principles of chemical processes. John Wiley & Sons Inc, New York, NY, **(2005)**.
- [301] B.E. Poling, J. O'Connell, and J.M. Prausnitz, Properties of Gases and Liquids. McGraw-Hill Professional Publishing, New York, NY, USA, **(2000)**.

APPENDIX A

X-RAY DIFFRACTION DATA ANALYSIS

This section of the Appendix gives an overview of the line profile analysis of the XRD data of Fischer-Tropsch cobalt catalyst.

In the GSAS program, the refinement of the structure was performed by varying the unit-cell lattice constants, background coefficients, scale factors, phase fractions and profile-function coefficients using the method of least squares performed by the program *GENLES* [224-226]. The atomic thermal motion parameters, fractional occupancy of the atom site, and atomic coordinates within the cell were kept fixed during the refinements. The effects of preferred orientation and shape anisotropy were significant for the Co_{hcp} phase. The fits were performed using a variation of the pseudo-Voigt peak profile function (Continuous wave (CW) peak profile function 2 in GSAS).

The particle size and strain broadening for Co_3O_4 , Co_{fcc} and Co_{hcp} phases were calculated from the Lorentzian broadening of the CW peak profile function described in Eq. A.1, while the particle size for CoO was calculated from the Gaussian broadening of CW peak profile function described in Eq. A.2. Particle size for Co_3O_4 and Co_{fcc} , $p = 1800K \lambda / \pi X$, was estimated from the $1/\cos(\theta)$ dependent term, while particle size calculations for anisotropic Co_{hcp} were in two components relative to the c axis. The particle size parallel to the c axis, $p_{\perp} = 1800K \lambda / \pi X$, was determined from the Lorentzian Scherrer term $1/\cos(\theta)$, while the size perpendicular to the c axis, $p_{\parallel} = 1800K \lambda / \pi (X + X_e)$, was calculated from the

$\cos(\phi)/\cos(\theta)$ term. The particle size for CoO , $p=18000K\lambda/\pi\sqrt{(8\ln 2)P}$, was estimated from the $1/\cos^2\theta$ component of the Gaussian broadening. The cobalt metal particle size (from Stage 1) expected after reduction was calculated by scaling the Co_3O_4 particle size by 0.75 [227, 228]. The isotropic Lorentzian strain broadening term ($\tan(\theta)$) was varied. However, the calculated strain was only a few percent. The Lorentzian component, is given by:

$$\gamma = \frac{X + X_e \cos \phi}{\cos \theta} + (Y + Y_e \cos \phi + \gamma_L d^2) \tan \theta \quad (\text{A.1})$$

$$\sigma^2 = U \tan^2 \theta + V \tan^2 \theta + W + \frac{P}{\cos^2 \theta} \quad (\text{A.2})$$

where X is the particle size broadening contribution, Y is the strain broadening contributions, d is the d-spacing, and X_e and Y_e are anisotropic coefficients for particle size and strain respectively. From Eq. A.2, U , V , and W terms are refinable parameters described by Caglioti, Pauletti and Ricci [298].

APPENDIX B

FISCHER-TROPSCH CALCULATIONS

Calculations done for chapter 2 are illustrated in this section. They include calculations for conversion, reaction rates, particle sizes, mole fraction of multiple Co phases, and internal mass transfer limitations. The catalyst sample used for these illustrations is Co/Silica gel no. 646.

Table B.I Properties of Catalyst

Quantity	Value
BET specific surface area (S_{BET})	302 m ² g ⁻¹
Total Pore Volume (TPV)	1.18 cm ³ g ⁻¹
Pore Diameter (d_{pore})	21.7 nm
Percent Metal (χ)	9.06 %
Catalyst particle size	180-450 μ m

Calculation of Reaction Rates

The conversion was calculated from the change in signals of CO/He and H₂/Ar ratios, using the inert gases as internal standards.

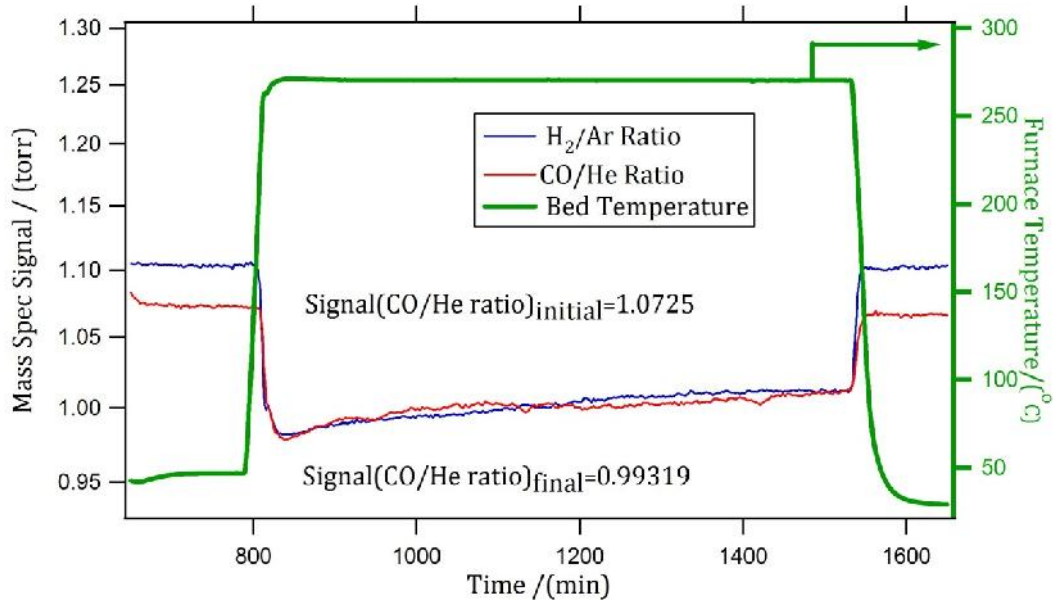


Figure B.1 Mass Spec signals of reactants (10%CO/He and 10% H₂/Ar) during FTS

$$\begin{aligned} \text{Conversion}(X) &= \frac{\text{Signal}(\text{CO/He ratio})_{\text{initial}} - \text{Signal}(\text{CO/He ratio})_{\text{final}}}{\text{Signal}(\text{CO/He ratio})_{\text{initial}}} \\ &= \frac{1.0725 - 0.99319}{1.0725} = 0.08 \end{aligned}$$

$$\text{Reaction Rates} \left(\frac{\mu\text{mol}}{\text{gCobalt}\cdot\text{s}} \right) = \frac{F_{A0} \cdot X}{\chi \cdot W}$$

where X is the conversion (0.08), χ is percent Co in the catalyst (0.0906), W is the weight of the catalyst used (0.1251 g), and F_{A0} is the molar flow rate of entering carbon monoxide:

$$F_{A0} = \frac{\nu_0 \cdot P}{R \cdot T}$$

$$\begin{aligned} v_0 &= \text{Percent CO in Gas Mixture} \times \text{Total Flowrate of CO} : \text{Heratio} \\ &= 0.1 \times 48 \text{ cm}^3 \text{ min}^{-1} \end{aligned}$$

P is the standard pressure (1 atm), X is the conversion, R is the universal gas constant ($82.057 \text{ cm}^3 \text{ atm mol}^{-1} \text{ K}^{-1}$), and T is the standard temperature (273 K):

$$\Rightarrow F_{A0} = \frac{(0.1 \times 48 \text{ cm}^3 \text{ s}^{-1}) \cdot (1 \text{ atm})}{(82.057 \text{ cm}^3 \text{ atm mol}^{-1} \text{ K}^{-1}) \cdot 273 \text{ K}} = 3.569 \mu\text{mol s}^{-1}$$

Thus, Reaction rates \rightarrow

$$\text{Reaction Rates} \left(\frac{\mu\text{mol}}{\text{g Co}_3\text{O}_4 \cdot \text{s}} \right) = \frac{(3.569 \mu\text{mol s}^{-1}) \times 0.08}{0.0906 \times 0.1251 \text{ g}} = 25.19 \mu\text{mol g}_{\text{Co}_3\text{O}_4}^{-1} \text{ s}^{-1}$$

Estimation of Particle Size and Strain

The particle sizes of the different cobalt phases at different stages of catalyst history were calculated from refined profile parameters using GSAS. The particle sizes of Co_3O_4 and Co_{fcc} were calculated from the Lorentzian Scherrer broadening:

$$p = \frac{18000K\lambda}{\pi(X - X_{\text{LaB6}})}$$

while the particle size of CoO was calculated from the Gaussian Scherrer broadening:

$$p = \frac{18000K\lambda}{\pi\sqrt{(8\ln 2)(P - P_{\text{LaB6}})}}$$

The particle sizes for anisotropic Co_{hcp} were in two components relative to the c axis:

The particle size parallel to the c axis:

$$p_{\perp} = \frac{18000K\lambda}{\pi(X - X_{\text{LaB6}})}$$

and the size perpendicular to the c axis includes an anisotropic coefficient X_e :

$$p_{\parallel} = \frac{18000K\lambda}{\pi \left[(X - X_{LaB6}) + (X_e - X_{e,LaB6}) \right]}$$

where X and P are the particle size broadening contribution (Lorentzian and Gaussian respectively), K is a constant (taken as 0.9), λ is the wavelength of Cu radiation (1.5405 Å), and X_{LaB6} and P_{LaB6} are the instrumental contribution to the particle size broadening. The strain contribution to Lorentzian broadening is given as:

$$S = \frac{\pi}{18000} (Y - Y_{LaB6}) \cdot 100\%$$

where Y is the strain broadening contribution and Y_{LaB6} is the instrumental contribution to strain.

Stage 1- after air calcination to produce Co_3O_4 :

From GSAS profile parameters for Co_3O_4 :

$$X = 53.8254, X_{LaB6} = 9.661$$

$$p = \frac{18000 \times 0.9 \times 1.5405 \text{ \AA}}{\pi (53.8254 - 9.661)} = 179 \text{ \AA} = 17.9 \text{ nm}$$

There were no strain contributions.

Cobalt metal particle size was estimated from Co_3O_4 crystallite size:

$$d_{Co} = 0.75 \cdot d_{Co_3O_4} = 0.75 \times 17.9 \text{ nm} = 13.5 \text{ nm}$$

Stage 2- after H_2 reduction to produce Co_{fcc} , Co_{hcp} , and CoO phases

From GSAS profile parameters for the Co_{fcc} phase:

$$X = 45.7777, X_{LaB6} = 9.661$$

$$p = \frac{18000 \times 0.9 \times 1.5405 \text{ \AA}}{\pi(45.7777 - 9.661)} = 219.9 \text{ \AA} = 22 \text{ nm}$$

From GSAS profile parameters for the Co_{hcp} phase:

$$X = 137.607, X_{Lab6} = 9.661, X_e = 85.007, X_{e,Lab6} = 0$$

$$p_{\perp} = \frac{18000 \times 0.9 \times 1.5405 \text{ \AA}}{\pi(137.607 - 9.661)} = 62.1 \text{ \AA} = 6.2 \text{ nm}$$

$$p_{\parallel} = \frac{18000 \times 0.9 \times 1.5405 \text{ \AA}}{\pi[(137.607 - 9.661) + (85.007 - 0)]} = 37.3 \text{ \AA} = 3.7 \text{ nm}$$

From GSAS profile parameters for the CoO phase:

$$P = 1892.31, P_{Lab6} = 0$$

$$p = \frac{18000 \times 0.9 \times 1.5405 \text{ \AA}}{\pi \sqrt{(8 \ln 2) \times 189.231}} = 77.5 \text{ \AA} = 7.8 \text{ nm}$$

The strain for the Co_{hcp} phase:

$$Y = 150.2, Y_{Lab6} = 2.5476$$

$$S = \frac{\pi}{18000} \cdot (150.2 - 2.5476) \cdot 100\% = 2.6\%$$

Estimation of the Mole Fraction of the Different Phase

The weight fraction of phase α is given by:

$$W_{\alpha} = \frac{(S_{\alpha} Z_{\alpha} MW_{\alpha} V_{\alpha})}{\sum_i (S_i Z_i MW_i V_i)}$$

where S is the scale factor, Z is the number of formula units per unit cell, MW is the molecular weight and V is the unit cell volume.

First, calculating the unit cell volumes:

$$V_{hcp} = a_{hcp}^2 \cdot \sin(60) \cdot c_{hcp} = \left(2.48 \overset{\circ}{\text{Å}}\right)^2 \cdot \sin(60) \cdot \left(4.12 \overset{\circ}{\text{Å}}\right) \\ = 21.945 \overset{\circ}{\text{Å}}^3$$

$$V_{fcc} = a_{fcc}^3 = \left(3.51 \overset{\circ}{\text{Å}}\right)^3 = 43.244 \overset{\circ}{\text{Å}}^3$$

$$V_{CoO} = a_{CoO}^3 = \left(4.28 \overset{\circ}{\text{Å}}\right)^3 = 78.403 \overset{\circ}{\text{Å}}^3$$

where a_α and c_α are the lattice parameters.

Stage 2- after H₂ reduction to produce Co_{fcc}, Co_{hcp}, CoO phases

From GSAS data for the Co_{fcc} phase ($Z= 4$ atoms per unit cell, $MW= 58.93$ g mol⁻¹),

$S = 19750$,

$$M_{fcc} = (0.19750) \cdot 4 \cdot (58.93) \cdot (43.244)$$

From GSAS data for the Co_{hcp} phase ($Z= 2$ atoms per unit cell, $MW= 58.93$ g mol⁻¹),

$S = 0.85080$,

$$M_{hcp} = (0.85050) \cdot 2 \cdot (58.93) \cdot (21.945)$$

From GSAS data for CoO ($Z= 4$ atoms per unit cell, $MW= 74.93$ g mol⁻¹),

$S = 0.012957$,

$$M_{CoO} = (0.012957) \cdot 4 \cdot (74.93) \cdot (78.403)$$

Weight fraction \rightarrow

$$W_{fcc} = \frac{M_{fcc}}{M_{fcc} + M_{hcp} + M_{CoO}} = 0.444 = 44.4\%$$

$$W_{hcp} = \frac{M_{hcp}}{M_{fcc} + M_{hcp} + M_{CoO}} = 0.489 = 48.9\%$$

$$W_{CoO} = \frac{M_{CoO}}{M_{fcc} + M_{hcp} + M_{CoO}} = 0.0668 = 6.7\%$$

Moles of phase α :

$$moles_{\alpha} = \frac{W_{\alpha} \cdot \text{Mass of Catalyst}}{MW_{\alpha}}$$

$$\Rightarrow moles_{fcc} = \frac{0.444 \cdot (0.1251 \text{ gm})}{58.93 \text{ g mol}^{-1}} = 0.00094 \text{ mol}$$

$$\Rightarrow moles_{hcp} = \frac{0.489 \cdot (0.1251 \text{ gm})}{58.93 \text{ g mol}^{-1}} = 0.00104 \text{ mol}$$

$$\Rightarrow moles_{CoO} = \frac{0.0668 \cdot (0.1251 \text{ gm})}{74.93 \text{ g mol}^{-1}} = 0.00011 \text{ mol}$$

$$\text{mole fraction}_{fcc} = \frac{moles_{fcc}}{moles_{fcc} + moles_{hcp} + moles_{CoO}} = 0.450 = 45\%$$

$$\text{mole fraction}_{hcp} = \frac{moles_{hcp}}{moles_{fcc} + moles_{hcp} + moles_{CoO}} = 0.497 = 50\%$$

$$\text{mole fraction}_{CoO} = \frac{moles_{CoO}}{moles_{fcc} + moles_{hcp} + moles_{CoO}} = 0.053 = 5\%$$

Estimation of Dispersion

Cobalt dispersion is the ratio of the number of surface Co metal atoms to the total number of Co metal present in the bulk of a catalyst.

$$D = \frac{\text{No of Co surface atoms}}{\text{No of Co in catalyst}} = \frac{A \times \text{surface site density} (\text{atoms nm}^{-2})}{V \times \frac{\rho}{MW} \times N_A}$$

where A is the surface area, V is the volume, ρ is the solid density, MW is the molecular weight of the metal, and N_A is the Avogadro's number. For Co, the surface site density is assumed to be $14.6 \text{ atoms nm}^{-2}$. Thus, Co dispersion corrected for units is simplified to:

$$D = \frac{A}{V} \left[\frac{(14.6 \text{ atoms nm}^{-2}) \times (58.93 \text{ g mol}^{-1})}{(8.9 \text{ g cm}^{-3}) \times (6.02 \times 10^{23} \text{ atoms mol}^{-1})} \right]$$

$$= \frac{A}{V} \times 0.16051 \text{ nm}$$

Assuming spherical particles (e.g. Co_3O_4 , Co_{fcc} and CoO particles),

$$\frac{A}{V} = \frac{4\pi r^2}{\frac{4}{3}\pi r^3} = \frac{3}{r} = \frac{6}{d}$$

$$\Rightarrow D_{\text{sphere}} = \left(\frac{6}{d}\right) \cdot 0.16051 \text{ nm}$$

$$D_{\text{sphere}} = \frac{0.963 \text{ nm}}{d(\text{nm})}$$

Assuming cylindrical particles (Co_{hcp} particles),

$$\frac{A}{V} = \frac{\frac{\pi d_{\perp}^2}{2} + \pi d_{\perp} \cdot d_{\parallel}}{\frac{\pi d_{\perp}^2}{4} \cdot d_{\parallel}} = \frac{2d_{\perp}^2 + 4d_{\perp} \cdot d_{\parallel}}{d_{\perp}^2 d_{\parallel}} = \frac{2d_{\perp} + 4 \cdot d_{\parallel}}{d_{\perp} d_{\parallel}}$$

$$\Rightarrow D_{\text{cylindrical}} = \left(\frac{2d_{\perp} + 4 \cdot d_{\parallel}}{d_{\perp} d_{\parallel}}\right) \cdot 0.16051 \text{ nm}$$

$$\Rightarrow D_{\text{cylindrical}} = \frac{0.321d_{\perp}(\text{nm}) + 0.642 \cdot d_{\parallel}(\text{nm})}{d_{\perp}(\text{nm})d_{\parallel}(\text{nm})}$$

Stage 1- after air calcination to produce Co_3O_4 :

$$D = \frac{0.963 \text{ nm}}{13.5 \text{ nm}} = 0.071 = 7.1\%$$

Stage 2- after H₂ reduction to produce Co_{fcc}, Co_{hcp}, CoO phases

$$D_{Co_{fcc}} = \frac{0.963\text{nm}}{22\text{nm}} = 0.0434 = 4.3\%$$

$$D_{Co_{hcp}} = \frac{(0.321\text{nm} \times 6.2\text{nm}) + (0.642\text{nm} \times 3.7\text{nm})}{(6.2\text{nm} \times 3.7\text{nm})} = 0.189 = 19\%$$

Weighted Sum of the dispersion of cobalt is calculated from dispersions of Co_{hcp} and Co_{fcc} particles:

$$\begin{aligned} \text{Wtd Dispersion} &= \frac{(D_{Co_{fcc}} \cdot \text{mole fraction}_{Co_{fcc}}) + (D_{Co_{hcp}} \cdot \text{mole fraction}_{Co_{hcp}})}{\text{mole fraction}_{Co_{fcc}} + \text{mole fraction}_{Co_{hcp}}} \\ \text{Wtd Disp} &= \frac{(0.043 \times 0.45) + (0.19 \times 0.50)}{0.45 + 0.50} = 0.12 = 12\% \end{aligned}$$

Estimation of Turnover Frequency

Turnover frequency is given by:

$$TOF = \frac{\text{Reaction rates} \left(\frac{\text{moles}}{\text{gCo} \cdot \text{s}} \right)}{\frac{\text{moles surface Co atoms}}{\text{gCo metal}}} = \frac{\text{Reaction rates} \left(\frac{\text{moles}}{\text{gCo} \cdot \text{s}} \right)}{\frac{(\text{mole fraction}_{Co_{fcc}} + \text{mole fraction}_{Co_{hcp}}) \cdot \text{Wtd Disp}}{MW}}$$

From Stage 3 data:

$$TOF = \frac{(25.19 \times 10^{-6} \text{ mol g}_{Co}^{-1} \text{ s}^{-1})}{\frac{((0.35 + 0.64) \times 0.158)}{58.93 \text{ g mol}^{-1}}} = 95.2 \times 10^{-4} \text{ s}^{-1}$$

B.6. The Rate Limiting Step in FT reaction

The Weisz-Prater criterion was used to estimate whether the reaction was pore-diffusion limited [299]:

$$C_{WP} = \frac{-r_{CO} \cdot \rho_C \cdot R_p^2}{D_e C_{As}}$$

If $C_{WI} = 1$ then there are no diffusion limitations, and if $C_{WI} < 1$ then the reaction is internal diffusion limited.

- $r_{CO} = 2.28 \cdot 10^{-6} \text{ mol } g_{catalyst}^{-1} \text{ s}^{-1}$ (Observed reaction rates per gram of catalyst and not per gram of Co for Co/Silica gel no. 646)

- $\rho_c = \chi \cdot \rho_{Co} + (1 - \chi) \rho_{silica}$ (catalyst density with Co loading, $\chi = 0.0906$, $\rho_{Co} = 8.86 \text{ g cm}^{-3}$ and $\rho_{silica} = 2.25 \text{ g cm}^{-3}$ [300]):

$$\rho_c = (0.0906 \cdot 8.86 \text{ g cm}^{-3}) + (0.9094 \cdot 2.25 \text{ g cm}^{-3}) = 2.849 \text{ g cm}^{-3}$$

- $R_p = (180 + 420) \mu\text{m} / 4 = 150 \mu\text{m}$ (Average particle radius is estimated from the average particle diameter from the sieve used)
- D_e is the effective diffusivity given by:

$$D_{eff} = \frac{1}{\frac{1}{D_{AB,eff}} + \frac{1}{D_{K,eff}}}$$

$$\text{where } D_{K,eff} = D_K \varepsilon / \tau \text{ and } D_{AB,eff} = D_{AB} \varepsilon / \tau$$

D_K is the Knudsen diffusivity given by:

$$D_K = 9700 \sqrt{\frac{g}{\text{mol} \cdot K}} \cdot \frac{\text{cm}}{\text{s}} \times r_{pore} \times \sqrt{\frac{T}{MW}}$$

where $r_{pore} = d_{pore} / 2 = 21.5 \text{ nm} / 2 = 10.75 \text{ nm}$ (the pore radius)

$T = 543 \text{ K}$ is the reaction temperature and $MW = 28 \text{ g mol}^{-1}$ is the molecular weight of carbon monoxide). Thus,

$$D_K = 4.579 \times 10^{-6} \text{ m}^2 \text{ s}^{-1}$$

$$\Rightarrow D_{K,eff} = \frac{(4.579 \times 10^{-6} \text{ m}^2 \text{ s}^{-1}) \cdot 0.5}{3} = 7.632 \times 10^{-7} \text{ m}^2 \text{ s}^{-1}$$

D_{AB} is the bulk diffusivity (taken for CO:N₂ and corrected for 10 atm

$$D_{AB} = \frac{0.3}{10} m^2 s^{-1},$$

$$D_{AB,eff} = \frac{(0.03 m^2 s^{-1}) \cdot 0.5}{3} = 5 \times 10^{-3} m^2 s^{-1}$$

Therefore,

$$D_{eff} = \frac{1}{\frac{1}{5 \times 10^{-3} m^2 s^{-1}} + \frac{1}{7.632 \times 10^{-7} m^2 s^{-1}}} = 7.632 \times 10^{-7} m^2 s^{-1}$$

The effective diffusivity is dominated by Knudsen diffusivity.

- C_{As} is the concentration of CO at the surface, and it is given by:

$$C_{As} = y_{CO} \cdot \frac{P}{R \cdot T}$$

y_{CO} is the mole fraction of CO:

$$y_{CO} = \frac{0.10 \cdot 1}{1 + 2.1} = 0.032$$

$$\Rightarrow C_{As} = \frac{0.032 \cdot 10 atm}{(8.205 \times 10^{-5} m^3 \cdot atm mol^{-1} K^{-1}) \cdot 543 K} = 7.24 mol m^{-3}$$

Therefore,

$$C_{WP} = \frac{(2.28 \cdot 10^{-6} mol g^{-1} s^{-1}) \cdot (2.849 g cm^{-3}) \cdot (150 \mu m)^2}{(7.632 \times 10^{-7} m^2 s^{-1}) \cdot (7.24 mol m^{-3})} = 8.645 \times 10^{-4}$$

Since $8.645 \times 10^{-4} \ll 1$, there are no pore diffusion limitation, and the surface reaction is the rate limiting step.

APPENDIX C

HYDRODEOXYGENATION OF GUAIACOL CALCULATIONS

Calculations done for chapters 3-5 are illustrated in this section. They include calculations for conversion, reaction rates, and internal and external mass transfer limitations. The catalyst sample used for these illustrations is MoN/CGran-NH.

Table C.I Properties of Catalyst

Quantity	Value
BET specific surface area (S_{BET})	571 m ² g ⁻¹
Total Pore Volume (TPV)	0.47 cm ³ g ⁻¹
Pore Diameter (d_{pore})	3.2 nm
Percent Metal (χ)	11.25 %
Catalyst particle size	180-450 μ m

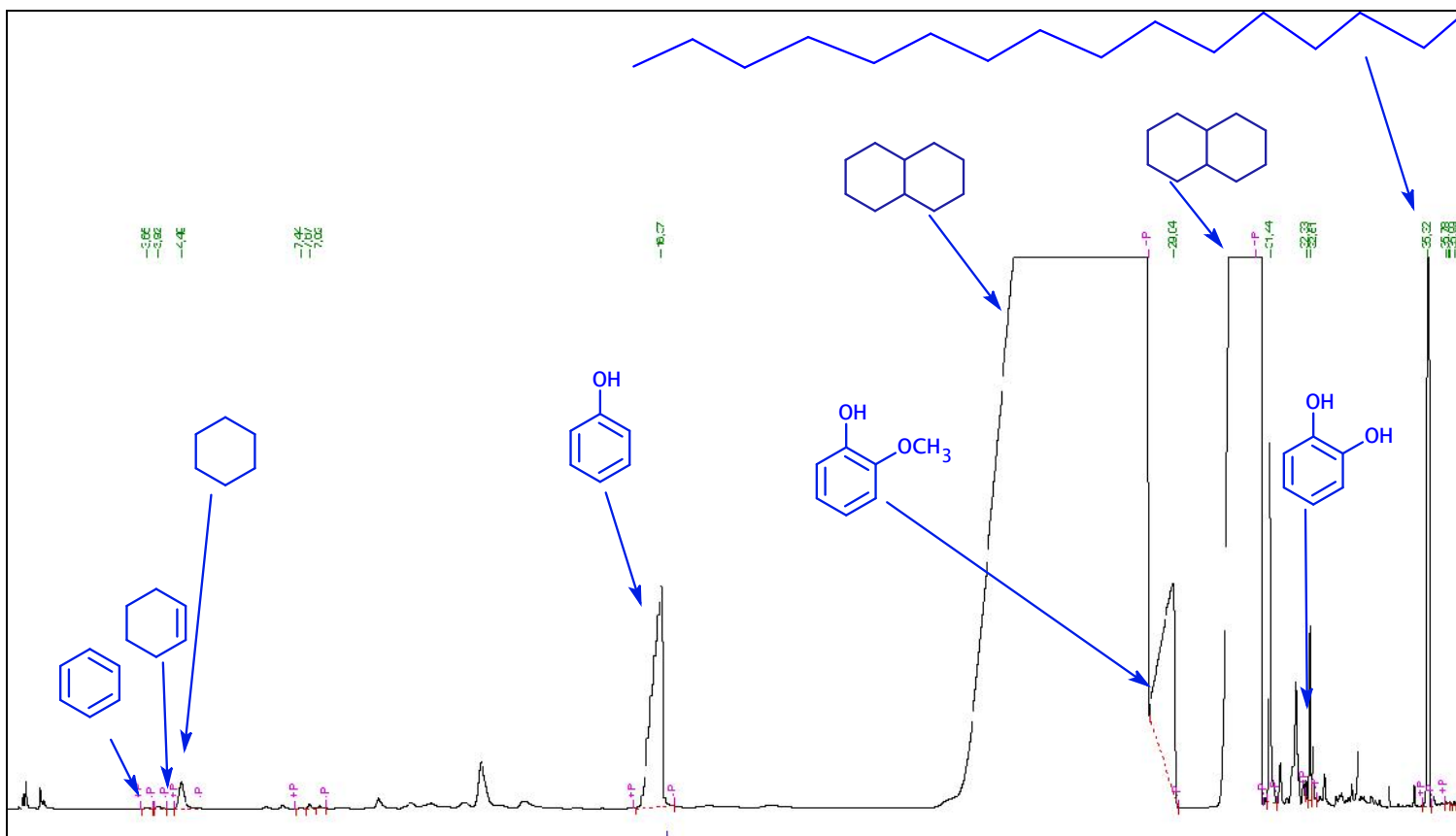


Figure C.1 The GC spectrum of products from hydrodeoxygenation of guaiacol for MoN/CGran-NH catalyst

Calculation of Conversion of Guaiacol and Yield of Products

The conversion of guaiacol and the yield of products were calculated from changes in the peak areas of guaiacol and products in the GC spectrum using hexadecane as an internal standard. Table B.1 shows integrated areas of the reactants and products after 0 and 180 min of reaction.

Table C.2 Calculated areas from GC spectrum

Compound	Integrated Peak Areas	
	t = 0 min	t = 180 min
Guaiacol	20406846	8135427
Hexadecane	3925539	3953088
Catechol	203951	660234
Phenol	-	7120682
Benzene	-	561724
Cyclohexene	-	417065
Cyclohexane	-	28012

The overall conversion of guaiacol at time, t , was calculated as follows:

$$X_{Total,t} (\%) = \left[\frac{\frac{\sum_{products} (Area)}{Area_{hexadecane}}}{Area_{Guaiacol} + \frac{\sum_{products} (Area)}{Area_{hexadecane}}} \right] \times 100\% \quad (C.1)$$

And the yield of products (phenol, catechol, benzene etc) was calculated by

$$Y_{i,t} (\%) = \left[\frac{\frac{Area_i}{Area_{hexadecane}}}{Area_{Guaiacol} + \frac{\sum_{products} (Area)}{Area_{hexadecane}}} \right] \times 100\% \quad (C.2)$$

$\{i = phenol, catechol etc\}$

Thus, the guaiacol conversion at time (t = 0 and 180 min) were:

$$X_{Total,t=0min}(\%) = \left[\frac{\left(\frac{203951}{3925539} \right)}{\left(\frac{203951 + 20406846}{3925539} \right)} \right] \times 100\%$$

$$= 1.0\%$$

$$X_{Total,t=180min}(\%) = \left[\frac{\left(\frac{28012 + 417065 + 561724 + 7120682 + 660234}{3953088} \right)}{\left(\frac{28012 + 417065 + 561724 + 7120682 + 660234 + 8135427}{3953088} \right)} \right] \times 100\%$$

$$= 50.3\%$$

The yield of products at t = 180 min were calculated as follows:

$$Y_{phenol,t=180min}(\%) = \left[\frac{\left(\frac{7120682}{3953088} \right)}{\left(\frac{28012 + 417065 + 561724 + 7120682 + 660234 + 8135427}{3953088} \right)} \right] \times 100\%$$

$$= 43.5\%$$

$$Y_{catechol,t=180min}(\%) = \left[\frac{\left(\frac{660234}{3953088} \right)}{\left(\frac{28012 + 417065 + 561724 + 7120682 + 660234 + 8135427}{3953088} \right)} \right] \times 100\%$$

$$= 4.0\%$$

The total yield of deoxygenated products was based on identified deoxygenated products (i.e. benzene, cyclohexene and cyclohexane):

$$Y_{HDO,t}(\%) = \left[\frac{\frac{\sum_{\text{deoxygenated products}} (\text{Area})}{\text{Area}_{\text{hexadecane}}}}{\frac{\text{Area}_{\text{Guaiacol}} + \sum_{\text{products}} (\text{Area})}{\text{Area}_{\text{hexadecane}}}} \right] \times 100\%$$

$$Y_{HDO,t=180\text{min}}(\%) = \left[\frac{\left(\frac{28012 + 417065 + 561724}{3953088} \right)}{\left(\frac{28012 + 417065 + 561724 + 7120682 + 660234 + 8135427}{3953088} \right)} \right] \times 100\%$$

$$= 2.8\%$$

Calculation of Reaction Rates

The reaction rate was given as:

$$\text{Reaction Rates} \left(\frac{\text{mol}}{\text{g}_{\text{catalyst}} \cdot \text{s}} \right) = \frac{\text{Initial slope}_{\text{Total}} \cdot \text{moles}_{\text{Guaiacol}}}{W}$$

where $\text{moles}_{\text{Guaiacol}}$ is the moles of guaiacol in the reactant mixture, W is the weight of the catalyst and $\text{Initial slope}_{\text{Total}}$ is the slope from the conversion vs. reaction time plot (shown in Fig. C.2):

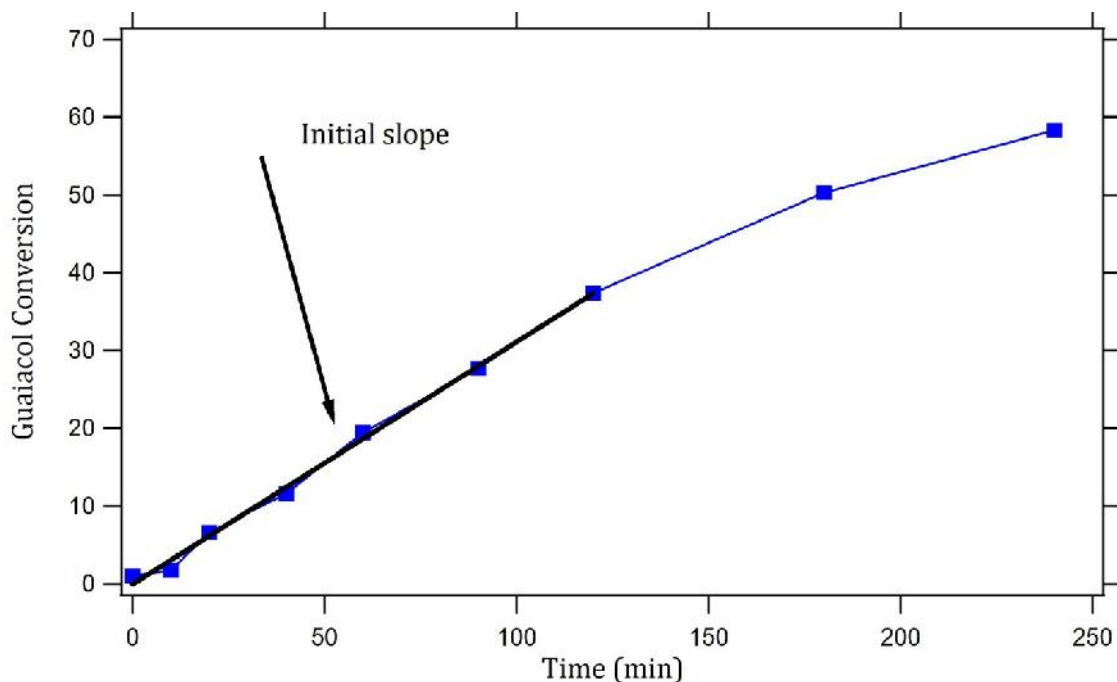


Figure C.2 Conversion of guaiacol and the formation of deoxygenated products versus time for MoN/CGran-NH catalyst.

$$\begin{aligned} \text{moles}_{\text{Guaiacol}} &= (\text{Conc}_{\text{Guaiacol}}) \cdot \text{Volume}_{\text{Solvent}} \\ &= (0.232 \text{ mol L}^{-1}) \cdot (0.08 \text{ L}) = 0.01856 \text{ mol} \end{aligned}$$

$$\begin{aligned} \text{Reaction Rates} \left(\frac{\text{mol}}{\text{g}_{\text{catalyst}} \cdot \text{s}} \right) &= \frac{(2.86998 \times 10^{-3} \text{ min}^{-1}) \cdot (0.01856 \text{ mol})}{0.250 \text{ g}} \\ &= 3.55 \times 10^{-6} \text{ mol g}_{\text{catalyst}}^{-1} \text{ s}^{-1} \end{aligned}$$

The intrinsic activity was calculated based on the molybdenum content, χ :

$$\begin{aligned} \text{Intrinsic activity} \left(\frac{\text{mol}}{\text{mol}_{\text{Mo}} \cdot \text{s}} \right) &= \frac{(\text{Reaction Rates}) \cdot \text{MW}_{\text{Mo}}}{\chi} \\ &= \frac{(3.55 \times 10^{-6} \text{ mol g}_{\text{catalyst}}^{-1} \text{ s}^{-1}) \cdot (95.94 \text{ g mol}^{-1})}{0.1125} \\ &= 3.03 \times 10^{-3} \text{ s}^{-1} \end{aligned}$$

C.3. Calculation of Phenol/Catechol Ratio

The phenol/catechol ratio was calculated at 10 % guaiacol conversion as shown in Fig. C.3.

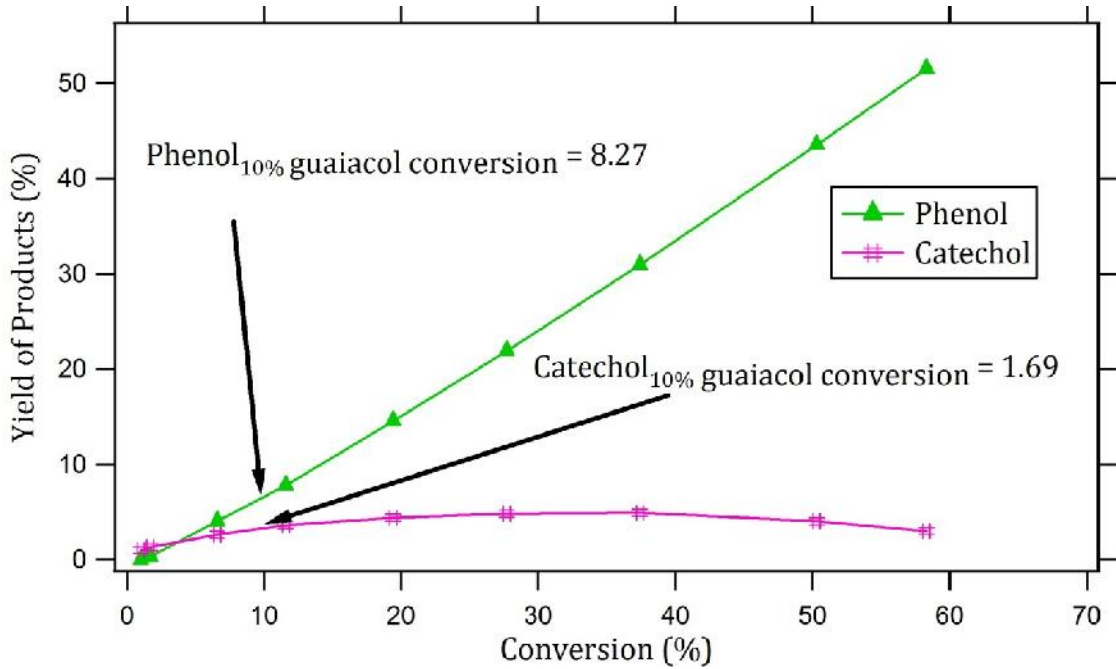


Figure C.3 Yield of phenol and catechol versus guaiacol conversion for MoN/CGran-NH catalyst.

Thus, the phenol/catechol ratio was calculated as:

$$\text{Phenol/Catechol} = \frac{8.27}{1.69} = 4.89$$

Mass Transfer Limitation Calculations

The Weisz-Prater criterion given in A.4 was used to estimate whether our reaction was limited by internal mass transfer

$$C_{WP} = \frac{-r_{GUA} \cdot \rho_c \cdot R_p^2}{D_{AB} C_{As}}$$

- $r_{GUA} = -3.55 \times 10^{-6} \text{ mol } g_{\text{catalyst}}^{-1} \text{ s}^{-1}$ (measured reaction rates per gram of catalyst)

- $$\rho_C = \left(\underbrace{0.1125}_{\chi} \cdot \underbrace{10.28 \text{ g cm}^{-3}}_{\rho_{Mo}} \right) + \left(\underbrace{0.8875}_{1-\chi} \cdot \underbrace{2.10 \text{ g cm}^{-3}}_{\rho_{ActivatedCarbon}} \right)$$

$$= 3.02 \text{ g cm}^{-3}$$

- $R_p = 150 \mu\text{m}$
- The effective diffusivity of the reactant D_{AB} was estimated from the Wilke-Chang technique for dilute solutions [301]:

$$D_{AB} = \frac{7.4 \times 10^{-8} (\phi M_B)^{1/2} T}{\eta_B V_A^{0.6}}$$

where D_{AB} ($\text{cm}^2 \text{ s}^{-1}$) is the mutual diffusion coefficient of solute A (guaiacol) at very low concentrations in solvent B (decalin), ϕ is the association factor of solvent (chosen as 1 for unassociated solvent), M_B is the molecular weight of the solvent ($M_B = M_{\text{decalin}} = 138.25 \text{ g mol}^{-1}$), η_B is the viscosity of the solvent (0.141 cP), V_A is the molar volume of the solute at its normal boiling temperature ($V_A = V_{\text{Guaiacol}} = 131.3 \text{ cm}^3 \text{ mol}^{-1}$), and T is the reaction temperature (573 K).

$$\text{Thus, } D_{AB} = 7.4 \times 10^{-8} \frac{[(1) \cdot (138.25)^{1/2} (573)]}{(0.141)(131.3)^{0.6}} = 1.894 \times 10^{-4} \text{ cm}^2 \text{ s}^{-1}$$

- The concentration of guaiacol at the surface C_{As} is assumed to be the same as the concentration of guaiacol in the bulk mixture given as 0.232 mol L^{-1}

And hence,

$$C_{WP} = \frac{-(-3.551 \cdot 10^{-6} \text{ mol g}^{-1} \text{ s}^{-1}) \cdot (3.02 \text{ g cm}^{-3}) \cdot (150 \mu\text{m})^2}{(1.894 \times 10^{-8} \text{ m}^2 \text{ s}^{-1}) \cdot (0.232 \text{ mol L}^{-1})} = 0.056$$

Since $0.056 \ll 1$, there were negligible influence of internal diffusion on the calculated reaction rate.

The potential influence of external mass transfer effects were assessed using Mears criterion C_M [299]:

$$C_M = \frac{(-r_{GUA}) \rho_c \cdot R_p \cdot n}{k_c \cdot C_A} < 0.15$$

- n is the reaction order (which is assumed to be 1)
- k_c is the mass transfer coefficient which is estimated from the modified Sherwood parameter, N_{Sh} :

$$k_c = \frac{N_{sh} \cdot D_{AB}}{2 \cdot R_p}$$

Assuming a Sherwood number of 2 [286],

$$\Rightarrow k_c = \frac{(2) \cdot (1.894 \times 10^{-4} \text{ cm}^2 \text{ s}^{-1})}{2 \cdot (150 \mu\text{m})} = 1.253 \times 10^{-4} \text{ m}^2 \text{ s}^{-1}$$

- C_A is the reactant concentration in the reactant mixture (0.232 mol L^{-1})

Thus,

$$C_M = \frac{(-3.551 \times 10^{-6} \text{ mol g}^{-1} \text{ s}^{-1}) \cdot (3.02 \text{ g cm}^{-3}) \cdot (150 \mu\text{m}) \cdot 1}{(1.253 \times 10^{-4} \text{ m}^2 \text{ s}^{-1}) \cdot (0.232 \text{ mol L}^{-1})} = 0.056$$

Since $C_M < 0.15$, the reaction rate was not controlled by mass transfer from the bulk

BIOGRAPHY OF THE AUTHOR

Isaac Tyrone Ghampson was born in Tema, Ghana. He graduated from Tema Secondary School and then attended Kwame Nkrumah University of Science and Technology in Kumasi, Ghana. Tyrone then transferred to the Jacobs University Bremen in Bremen, Germany where he received a B.S. degree in Biochemical Engineering in 2007. He began graduate school at the University of Maine in 2007. Tyrone is a candidate for the Doctor of Philosophy degree in Chemical Engineering from the University of Maine in December, 2011.